Simulation of Light-Mediated Coupling in Planar Photonic Resonators

vorgelegt vom Diplom-Physiker
Stefan Declair

Fakultät III - Naturwissenschaften
der Universität Paderborn
Department Physik
Computational Nanophotonics

Dissertation zur Erlangung des akademischen Doktorgrades Dr. rer. nat.

genehmigte Dissertation

Datum der mündlichen Prüfung: 31.05.2011

Promotionsausschuss:

Vorsitzender: Prof. Dr. rer. nat. Artur Zrenner
1. Gutachter: Dr. rer. nat. Jens Förstner
2. Gutachter: Prof. Dr. rer. nat. Torsten Meier

Simulation of Light-Mediated Coupling in Planar Photonic Resonators

vorgelegt vom Diplom-Physiker
Stefan Declair

Fakultät III - Naturwissenschaften
der Universität Paderborn
Department Physik
Computational Nanophotonics

Dissertation zur Erlangung des akademischen Doktorgrades Dr. rer. nat.

genehmigte Dissertation

Datum der mündlichen Prüfung: 31.05.2011

Promotionsausschuss:

Vorsitzender: Prof. Dr. rer. nat. Artur Zrenner
1. Gutachter: Dr. rer. nat. Jens Förstner
2. Gutachter: Prof. Dr. rer. nat. Torsten Meier

Für meinen Großvater.

Zusammenfassung

Das Hauptaugenmerk dieser Arbeit ist die lichtvermittelnde Kopplung in planaren photonischen Resonatoren unter der Benutzung der zeitaufgelösten Finite-Differenzen Methode (FDTD). Mit dieser Methode werden die dreidimensionalen Maxwellgleichungen numerisch ausgewertet. Zwei verschiedene Arten photonischer Resonatoren werden untersucht: Mikrodisk Resonatoren und photonische Kristallkavitäten. Das Ziel ist die Untersuchung der Kopplung zwischen Quantenpunkten und optischen Resonatoren über das Lichtfeld, eingesperrt in der Kavität. Zur Beschreibung der Quantenpunkte werden dynamische Bewegungsgleichungen für die Kohärenz und für die Besetzungsdichte auf einer quantenmechanischen Basis verwendet, um das optische Polarisationsfeld zu berechnen. Dieses Polarisationsfeld ist selbstkonsistent an die Maxwellgleichungen gekoppelt. Außerdem wird die Kopplung zwischen Mikrodisks und zwischen photonischen Kristallkavitäten über das Lichtfeld untersucht.
Als erstes werden Eigenmoden von Mikrodisk Resonatoren berechnet, die das Licht innerhalb eines kleinen räumlichen Gebietes nur über Totalreflektion an der Grenzfläche zwischen dem Resonator und dem umgebenden Material einsperren. Der Effekt der Form auf die Resonanz der Flüstergalleriemoden wird untersucht. Die Verwendung eines optisch uniaxial anisotropen Umgebungsmaterials läßt vermeidete Kreuzung zwischen verschiedenen Modenordnungen Flüstergalleriemoden auftreten. Zur Benutzung von uniaxialer Anisotropie als Einstellungsmechanismus für spektrale Eigenschaften eines Resonators werden numerische Daten von dreidimensionalen Simulationen eines Mikrodisk Resonators, eingebettet in eine Flüssigkristallumgebung, mit experimentellen Daten verglichen.
Als zweites werden Resonatoren basierend auf photonischen Bandlücken numerisch untersucht. Ein zweidimensionaler photonischer Kristall mit einem Liniendefekt, bestehend aus 3 fehlenden Luftlöchern, wird verwendet. Modifizierung des Defektgebietes mit der Methode der behutsamen Einschränkung erhöht die Abklingzeit der Kavitätmoden um eine Größenordnung. Für einen Liniendefekt, bestehend aus 7 fehlenden Luftlöchern wird ein Mechanismus zur permanenten Einstellung spektraler Eigenschaften durch Aufdampfen einer zusätzlichen dünneren Schicht eines zweiten Materials numerisch berechnet. Daten aus einem Experiment werden mit den numerischen Daten verglichen und diskutiert.
Starke Resonator-Resonator-Wechselwirkung zwischen Mikrodisk Resonatoren und zwischen photonischen Kristallkavitäten werden als drittes gezeigt. Hoch asymmetrische Linienaufspaltung bei kurzen Abständen ist von der Formierung von Supermoden mit ultraniedrigen und ultrahohen Q-Faktoren in jedem der beiden Systeme begleitet. Ersteres ist durch einen tight-binding-ähnlichen Ansatz erklärt, während zweiteres das Resultat von Interferenzeffekten ist. In dreifach gekoppelten Kavitäten in einem hexagonalen Gitter wird eine geeignete Anordnung vorgeschlagen, um die Kopplung effizienter zu machen. Es wird außerdem die Möglichkeit gezeigt, Licht in gekoppelten optischen Resonatorwellenleitern entlang verschiedener Symmetrierichtungen des Gitters effizient zu führen. Ein einzelner Quantenpunkt, gekoppelt an eine Kavität und mit einem intensiven Laserfeld angeregt, zeigt symmetrische Seitenbandübergänge um den Hauptübergang, ein Mollow-Triplet. Intensitäts- und Q-faktor-abhängige Rechnungen werden dazu durchgeführt.

Abstract

The focus of this thesis is the light-mediated coupling in planar photonic resonators using the Finite-Difference Time-Domain method. With this method, the three-dimensional Maxwells equations are evaluated numerically. Two different kinds of optical resonators are investigated: microdisk resonators and photonic crystal cavities. The goal is the investigation of the coupling between quantum dots and optical resonators via the light field, confined in the cavity. For the description of the quantum dots, dynamic equations of motion for the coherence and population on a quantum mechanical level are used to calculate the generated optical polarization field. This macroscopic polarization field is coupled back self-consistently to the Maxwell equations to accurately describe the coupled system. Also, coupling between microdisks and between photonic crystal cavities via the electromagnetic field is investigated.
First, eigenmodes in microdisk resonators, which confine light inside a small spatial volume only by total internal reflection at the interface between the microdisk and the surrounding environment, are calculated. The effect of the shape on the resonance of whispering gallery modes is investigated. Applying an optical, uniaxial anisotropic environment, anticrossings between different mode orders of the whispering gallery modes occur. Using uniaxial anisotropy as a tuning mechanism for spectral properties of a resonator, numerical data of a three-dimensional simulation of a microdisk, embedded in a liquid crystal environment, are compared with experimental data.
Second, photonic gad gap-based resonators are investigated numerically. A two-dimensional photonic crystal with a line defect of three missing air holes is used. Modifying the defect area with the method of gentle confinement, the cavity decay time of the defect modes is increased by one order of magnitude. For a line defect with 7 missing air holes, a permanent tuning mechanism for the spectral properties, induced by evaporation of a thin additional layer of a second material, is also evaluated numerically. Data from an experiment are compared with the numerical results and discussed.
Strong resonator-resonator interaction between microdisk resonators and between photonic crystal cavities is shown. Strongly asymmetric line splitting at short gap sizes is accompanied by the formation of ultra-low- and ultra-high-Q super-modes in each of the coupled systems. The first is explained in a tight-binding like approach, while the latter is shown to be the result from interference effects. In three-fold coupled cavities in a hexagonal lattice, a proper alignment is proposed to efficiently coupled multiple cavities. Also, the possibility to guide light in coupled resonator optical waveguides along non-symmetry directions of the lattice is proposed. A single quantum dot, coupled to a microcavity and excited by an intense laser pulse, shows symmetric side band peaks around the main transition, a Mollow triplet. Intensity- and Q-factor-dependent calculations are performed.

Contents

List of Figures

List of Tables

Chapter 1

Introduction

1.1 Motivation

In the last years, optoelectronics and photonics became a new and important field in physics. In general, optoelectronics deals with the transfer of electronically coded information into information coded in the basic quantum of the electromagnetic interaction, the photon, and vice versa. But still, this can be explained and expressed in a semiclassical way where the photons are described via electromagnetic waves according to Maxwells equations. However, more specifically, photonics deals with the nonclassical part of the optoelectronics.
To do optoelectronics, semiconductor heterostructures can be used. In general, semiconductors can have two different electronic properties: they can be either conducting or metallic, depending on several parameters like temperature, pressure, doping density, etc. In the conducting regime, valence band (VB) and conduction band (CB) are separated by a gap. Charge carriers like electrons cannot be permanently located in this gap energetically. To transfer the charge carrier from one band to the other by bridging the energetically forbidden gap, an energy carrying particle is needed. In optoelectronics, this energy is provided by the photon. Electrons falling from higher energy levels to lower energy levels of the semiconductor band structure cause the emission of light, and hence coding information of the electronic system before the electronic decay into the photon. The other way around, if a photon is absorbed by a semiconductor, an electron is excited from a lower energy state into a higher one, and information coded in the photon is then coded in the electronic system of the conducting semiconductor.
With the today available technology, semiconductor structures can be made smaller in size than the wavelength of the light, which is used to transfer the energy of the light to the electronic system or manipulate the electronic system in any way. This gives the possibility for compound structures consisting of many different semiconductor materials to use all the different properties at once and use the combined electronic band structure properties. For example, the quantum well (QW) is a thin layer of a semiconductor material sandwiched between thick layers of a semiconductor material with a larger band gap. Molecular beam epitaxy (MBE) or metal organic chemical vapor deposition (MOCVD) are exemplarily mentioned for the growing procedure. This forms a potential well, in which the charge carriers can only move within the thin layer, which can be treated as a two-dimensional electron gas. Perpendicular to the plane of the thin layer, the movement of the electrons is not allowed due to the potential walls. This phenomenon is called confinement (the effect of confinement occurs, when the confinement length is in the range of the de Broglie wavelength of the particle). The energetically allowed region for charge carriers is then no longer a continuum, but discrete energy levels. For example, the QW is used in lasing systems like the quantum cascade laser. Many layers of QWs are stacked behind each other and splitting of the energy bands occurs, hence so-called minibands are formed. The carriers fall, after being injected on one side, down the energy levels from this multiple QW structure in a cascade, emitting a photon at every change of energy. Also, QWs are used in several diode laser systems as well in Distributed Bragg Reflectors (DBR). Another representative of a semiconductor heterostructure is the quantum dot (QD). One epitaxial procedure to grow quantum dots is the Stranski-Krastanov (SK) procedure using the MBE, which results in self-assembled QDs with measures from tens to some hundreds nanometers scaling in each direction with a density of up to 10^4 atoms or molecules. Those quantum dots look like flat pyramidal structures, which confine the charge carriers in all three spatial directions. The charge carriers have then discrete energy levels in all dimensions like in in atomic systems or a particle in a box. That is why a QD is also

called an *artificial atom*. Hence, this effectively leads to a zero-dimensional structure. QDs are already widely used, e.g. in QD lasers, diodes, single electron transistors. Also, they are promising candidates for quantum information processing [5], e.g. for storage or manipulation of quantum information, since dephasing mechanisms for the charge and spin degree of freedom are already investigated and understood well, see for example [6–8].
Both, the QW and the QD can be manipulated by a light field via direct illumination, or by placing the active media in an optical resonator, a cavity, like a microdisk resonator (MD) or a photonic crystal cavity (PhCC). There, the light field is concentrated within a small spatial region. When the electronic system is placed in a high-field position in the resonator, the light can interact temporally in the range of the cavity decay time. Different cases can occur: First, when the cavity decay time is larger than the dephasing time of the QD, the spontaneous emission rate of the QD is enhanced by the Purcell factor [9–12]. This is called the weak-coupling regime. Second, the cavity decay time can be tuned by several mechanisms up to the nanosecond regime [13], even on a chip [14], which equals the dephasing time of excitons in QDs. In this case, after emission of the photon from the QD, the photon is reabsorbed again before it can leave the cavity and the so-called strong-coupling regime is reached. Hence, this results in new eigenstates, the cavity polaritons, manifested in a line splitting in the frequency domain, the Vacuum Rabi Splitting (VRS) [15]. Third, this can be pushed further, when the splitting energy of the cavity polaritons is in the same order of magnitude as the uncoupled energies and is referred as the ultrastrong coupling regime [16]. Besides coupling between the light field and a quantum mechanical oscillator like a QD, strong coupling is also observed in systems consisting of a light field and a macroscopic oscillator (e.g. in a one-dimensional cavity, one of the mirrors is fixed while the other is movable due to a small spring [17–19]). It reveals also quantum mechanical properties of macroscopic systems, like the ground state of the mechanical oscillator [20]. Further investigations on strong optomechanical coupling in photonic crystal cavity systems are described in [21–23].
Liquid crystals (LC) are know since the end of the 19th century [24] (however the designation liquid crystal was introduced by a German physicist [25]), and till now still fascinate researchers all over the world. Actually, research with LCs started about 40 years ago in the 1970's. Not only because LCs can be utilized for fundamental research, but also because LCs found their way into every days life. The most popular usage is the LC display, which makes use of the electro-optical switching properties, present in calculators, watches, cell phones, navigation systems, automatic teller machines, just to mention some of the merely infinite possibilities of usage. Also, medical and security applications are already employed. In general, LCs can exhibit special reversible or irreversible optical properties: optical anisotropy. The change from isotropic to anisotropic behavior can be induced by several external parameters like temperature, pressure or electric fields. Possible future applications can make use of the switchability between isotropy and birefringence to e.g. tune resonances [26, 27]. Also, in the new field of transformation optics [28, 29], anisotropy is used often to guide the light around small-sized objects to camouflage them. There are many different kinds of LCs, however, in this thesis only thermotropic crystals in the isotropic or nematic phase are considered.
All these mechanisms can be utilized for manipulating electronic properties of the semiconductor heterostructures or the photons itself. The range of applications is broad: those systems are already used for probing, investigating and manipulating the fundamental physics of light-matter interaction. Devices for single photon generation, high finesse filters, slow light generation, etc. are also realized. Still, this is a current research topic in modern physics in the area of nanooptics, nanophotonics and optoelectronics. But there is still a problem: if one

wants to build devices which are operating in a specific coupling regime, then this device has to be tested. One problem is to place the QDs in high-field positions, and additionally to this, to have the gap energy of the QD match exactly (or within a decay rate) the energy of the cavity mode. To overcome trial-and-error procedures, numerical analysis became a crucial tool in designing optoelectronic devices. Nowadays, large-scaled computers and computer clusters allow simulations of various problems of optoelectronics and photonics and treat the electromagnetic together with the material equations for large simulation volumes with nanoscale-leveled spatial discretization for reliable results in acceptable times.
For near-field resolved numerical analysis of optoelectronic devices, several methods can be used. Common methods are the Finite-Difference Time-Domain method (FDTD) [30–32] and the Finite Element Method (FEM) [33, 34]. In general, these two methods differ in the working domain. As the name already reveals, FDTD is a time domain method, so with one calculation one can get information over a whole frequency range. On the other hand, FEM is a frequency domain method, thus to have a spectrum, one needs to calculate the response for every single frequency. On the other hand, FEM is more flexible in the choice of the spatial grid. Both methods have their own advantages and disadvantages, and the method of choice is highly problem-dependent. Within the framework of this thesis, the FDTD method is used.
At the University of Paderborn, methodical development in this research area is done. Used methods are the finite integration method, based on the Finite Integration Technique (FIT) [35, 36] and is widely used for large-sized systems. This method solves Maxwells equations on a primary and dual grid, similar to FDTD, but the differential operators are not expressed with finite differences, but treated with a matrix formulation, resulting in (sparse) matrices with entries 0, ± 1. FIT can be used for time-domain simulations as well as for frequency domain simulations simply by replacing the time derivative $\partial_t \longrightarrow i\omega$. Also, non-orthogonal grids are supported to save a huge amount of computational effort [37]. Especially for one-dimensional (linear) problems, the Transfer Matrix Method (TMM) is the method of choice [38, 39]. Here, a two-dimensional input vector (containing the incident and reflected field) is multiplied with 2×2 transfer matrices for every interface between different isotropic dielectric/magnetic materials to get the output vector (containing the transmitted and incident field from the other side). This method can also be generalized for anisotropic materials [40, 41]. In fact, the latter is for acoustic waves in anisotropic media, but can be directly transferred to propagation of electromagnetic waves in anisotropic dielectric (dispersive) media. Since some years, also the Discontinuous Galerkin Time Domain method DGTD is widely used, which combines the advantages of FDTD and FEM [42–46].

1.2 Structure of this thesis

The structure of this thesis is divided into 6 chapters. The fundamentals are shown in Chap. 2. Starting from the basis of the whole thesis, in Sec. 2.1, Maxwells equations, the reader is guided to the numerical evaluation with the FDTD method in Sec. 2.2. The principles for the derivation of the update equations is depicted and stability, accuracy and problems of the algorithm are discussed. The need of numerical methods for averaging optical properties in a spatially discretized grid and of a finite simulation volume calls attention in this section, too. Different kinds of optical resonator, photonic crystal cavities and microdisk resonators, taken into account in the framework of this thesis, are shown in Sec. 2.3 and 2.4, respectively. As a quantum-mechanical resonator, the QD model is introduced in Sec. 2.5, including nonlinear-

ities and the embedding into the FDTD grid. Fundamentals of coupling between oscillators, going from the weak coupling regime to the ultra-strong coupling regime, is found in Sec. 2.6. For simulations including optical anisotropy, Sec. 2.7 gives basic information about LCs. The last Sec. 2.8 depicts the methods used for data analysis and special features, which can be accessed in the used FDTD implementation.
Chapter 3 validates the implementation of the FDTD method. Here, numerical results from $H1$- and $L3$-type photonic crystal cavities are compared with experimental results from relevant publications. The spectral response for different polarization are compared and mode patterns of the resonances are shown.
Chapter 4 guides the reader from two-dimensional to three-dimensional calculations of microdisk devices. A sub-μ microdisk, providing highly confined modes with a vacuum wavelength smaller than the device diameter, is used to numerically investigate the effect of imperfections, occurring e.g. in the fabrication process, in Sec. 4.1.1. Effects of a non-circular shape (Sec. 4.1.1) and edge profiles (Sec. 4.1.1) are taken into account. The subsequent Sec. 4.1.2 shows, how highly confined modes are affected in an uniaxial anisotropic environment. Anti-crossing features occur due to the applied anisotropy, especially in an experimentally accessible range for the ordinary and extraordinary refractive indices. After the study of different effects on resonances in a circular-shaped structure, a microdisk device embedded in a LC environment is simulated using uniaxial anisotropy in Sec. 4.2.1 and numerical results are compared with experimental data, which agree nicely.
The numerical results for PhCCs are given in Chap. 5. Different possibilities for manipulating resonances in line-defect PhCC in a hexagonal lattice of air holes are shown. Permanent tuning of the $L3$-type PhCC with the method of gentle confinement [3] in Sec. 5.2 and the $L7$-type PhCC with a one-side evaporated additional dielectric layer of lower permittivity in Sec. 5.3 exhibit the behavior of the defect modes and the effect on the spectral properties. The latter PhCC modification is shown to agree very well with experimental data.
Coupling of different resonators is calculated in Chap. 6. Section 6.1 shows numerical data for coupled sub-μ MDs to investigate the distant-dependent line and loss splittings. Strong resonator-resonator interaction is observed. Section 6.3 deals with the coupling between defects in photonic band gap materials, say photonic crystal cavities, where the coupling is investigated distant- and alignment-dependent. For applications, i.e. coupled resonator optical waveguides (CROWs), Sec. 6.3.2, shows, that the coupling between the defect cavities can be enhanced with a proper alignment. The last Sec. 6.4 shows the coupling between a photonic crystal cavity mode and a single quantum dot, placed at a high-field position. Effects of the nonlinearity of the QD on the QD emission are studied, depending on the exciting intensity and the cavity decay time.
The last Chap. 7 concludes the content of this thesis and gives a short outlook on possible future works.
In the appendix, numerical methods for the integration of ordinary differential equations and an interpolation scheme are shortly depicted in Sec. A and constants for the numerical investigations are listed in Sec. B.

Chapter 2

Fundamentals

2.1 Maxwell's Equations

In 1865, James Clark Maxwell published the basic set of equations for electric and magnetic fields **E** and **H**, respectively, today famously called Maxwell's Equations [47]. These equations connect the electric and magnetic properties of the fields and show, that the sources of the electric and magnetic fields are the scalar function ρ, the charge density, and the vector function **j**, the current density. Since Maxwell's equations are form-invariant under unit transformation, such transformations change definitions and constants [39, 48]. Throughout this thesis, SI units are used, if not mentioned otherwise.
The equations in their differential form can be written as [49]:

$$\nabla \times \mathbf{E}(\mathbf{r},t) = -\dot{\mathbf{B}}(\mathbf{r},t) \tag{2.1}$$

$$\nabla \times \mathbf{B}(\mathbf{r},t) = \mu_0 \mathbf{j}(\mathbf{r},t) + \mu_0 \epsilon_0 \dot{\mathbf{E}}(\mathbf{r},t) \tag{2.2}$$

$$\nabla \cdot \mathbf{B}(\mathbf{r},t) = 0 \tag{2.3}$$

$$\nabla \cdot \mathbf{E}(\mathbf{r},t) = \frac{\rho(\mathbf{r},t)}{\epsilon_0}\,, \tag{2.4}$$

where $\mathbf{E}(\mathbf{r},t)$ is the electric field strength, $\mathbf{B}(\mathbf{r},t)$ the magnetic flux density, $\rho(\mathbf{r},t)$ the charge density, $\mathbf{j}(\mathbf{r},t)$ the current density at position $\mathbf{r}$ and time t, ϵ_0 and μ_0 are the free space permittivity (vacuum permittivity) and free space permeability (vacuum permeability), respectively. Maxwell's equations can also be written in integral form [49]:

$$\oint_{\partial S} \mathbf{E}(\mathbf{r},t) \cdot d\mathbf{l} = -\partial_t \Phi_{B,S} \tag{2.5}$$

$$\oint_{\partial S} \mathbf{B}(\mathbf{r},t) \cdot d\mathbf{l} = \mu_0 I_S + \mu_0 \epsilon_0 \epsilon_r(\mathbf{r}) \partial_t \Phi_{E,S} \tag{2.6}$$

$$\oiint_{\partial V} \mathbf{B}(\mathbf{r},t) \cdot d\mathbf{A} = 0 \tag{2.7}$$

$$\oiint_{\partial V} \mathbf{E}(\mathbf{r},t) \cdot d\mathbf{A} = \frac{1}{\epsilon_0 \epsilon_r(\mathbf{r})} \rho_{\partial V}\,. \tag{2.8}$$

Here, $\Phi_{B,S}$ and $\Phi_{E,S}$ are the magnetic and electric flux through a surface S, I_S is the electric current through surface S and $\rho_{\partial V}$ is the charge density inside the boundary of volume V. The vectorial length and area elements are $d\mathbf{l}$ and $d\mathbf{A}$, respectively.
The differential forms of Maxwell's equation (2.1)-(2.4) can be transformed into the integral forms (2.5)-(2.8) with vector-analytical methods using Kelvin-Stokes' and Gauss' theorem, see [48, 49]. Equations (2.1)-(2.4) have to be extended to obey optical and magnetic properties of material on a non-atomic level. Calculations on the atomic level are utterly impossible to perform. Therefore, an averaged quantity of the electric and magnetic response of the considered material is introduced, which flattens possible fluctuations in the fields due to atomic-sized objects. Thus, the electric field is modified with the dielectric constant ϵ_r and the magnetic field is modified with magnetic permeability μ_r, which typically depend on position $\mathbf{r}$. Actually, these two quantities are tensors of second second rank and frequency-dependent. The space dependency and tensor characteristic will be mentioned in the later chapters in more detail. Since the interest lies on nonmagnetic materials, μ_r is always equal to 1. $\mu_r(\mathbf{r})$ only differs weakly from unity, so that approximation to 1 is justified. For the sake

of completeness, $\mu_r(\mathbf{r})$ will still appear in the following equations. Therefore, eqs. (2.1)-(2.4) extend to the macroscopic Maxwell's Equations via the constitutive relationships [48]:

$$\mathbf{B}(\mathbf{r},t) = \mu_0\mu_r(\mathbf{r})\mathbf{H}(\mathbf{r},t) + \mathbf{M}(\mathbf{r},t), \qquad \mathbf{D}(\mathbf{r},t) = \epsilon_0\epsilon_r(\mathbf{r})\mathbf{E}(\mathbf{r},t) + \mathbf{P}(\mathbf{r},t)\,, \tag{2.9}$$

where $\mathbf{H}$ and $\mathbf{D}$ are the magnetic field strength and dielectric displacement field at position $\mathbf{r}$ at time t. Magnetization $\mathbf{M}(\mathbf{r},t)$ and polarization $\mathbf{P}(\mathbf{r},t)$ are not taken into account here. With this, eqs. (2.1)-(2.4) transform to the macroscopic Maxwell equations

$$\nabla \times \mathbf{E}(\mathbf{r},t) = -\dot{\mathbf{B}}(\mathbf{r},t) \tag{2.10}$$

$$\nabla \times \mathbf{H}(\mathbf{r},t) = \mathbf{j}(\mathbf{r},t) + \dot{\mathbf{D}}(\mathbf{r},t) \tag{2.11}$$

$$\nabla \cdot \mathbf{B}(\mathbf{r},t) = 0 \tag{2.12}$$

$$\nabla \cdot \mathbf{D}(\mathbf{r},t) = \rho(\mathbf{r},t)\,, \tag{2.13}$$

where $\rho(\mathbf{r},t)$ and $\mathbf{j}(\mathbf{r},t)$ are now macroscopic charge and current densities, respectively. The time-dependent Maxwell's curl equations (2.1) and (2.2) together with the constitutive relationships (2.9), and assuming that the fields are known at an initial position in time and space, form a hyperbolic partial differential equations (PDE). This set of hyperbolic PDEs has a unique solution, uniquely depending on the initial values. For numerical evaluation, one uses the curl equations with $\mathbf{E}(\mathbf{r},t)$ and $\mathbf{H}(\mathbf{r},t)$ for reasons which can be found in Sec. 2.2:

$$\nabla \times \mathbf{E}(\mathbf{r},t) = -\frac{1}{\mu_0\mu_r(\mathbf{r})}\dot{\mathbf{H}}(\mathbf{r},t) \tag{2.14}$$

$$\nabla \times \mathbf{H}(\mathbf{r},t) = \mathbf{j}(\mathbf{r},t) + \epsilon_0\epsilon_r(\mathbf{r})\dot{\mathbf{E}}(\mathbf{r},t)\,. \tag{2.15}$$

Discretization of eqs. (2.14) and (2.15) is fundamentally shown in Sec. 2.2.1 for numerical evaluation. For further information, see [30, 32].

2.2 Numerics With Maxwell's Equations: The Finite-Difference Time-Domain Method

To numerically evaluate eqs. (2.10)-(2.13), one needs to discretize time and space, since continuous problems cannot be solved on computers due to limited computational resources like memory. The discretization scheme in space is based on the idea of Yee [50], where the different field components of different field quantities are placed at different positions on a staggered grid, the so-called *Yee*-Cube (see Fig. 2.1, left). Electric field components are centered on the edges of the *electric grid*, the primary grid, whereas magnetic field components are centered on the edges of the *magnetic grid*, the secondary grid. The structure of eqs. (2.5)-(2.8) gives rise, that the magnetic field has to be on a grid, which has its corner in the center of the grid for the electric field. For example, in eq. (2.5) one has to calculate the line integral of the electric field along a closed curve to obtain the magnetic flux through area bounded by this closed curve (see also Fig. 2.1, right). The proposal from Yee exactly fulfills the conditions, given by the integral forms of Maxwell's equations. Namely, the secondary grid is shifted half a grid edge length in each direction, so that the magnetic field components centered on the surfaces of the primary grid and vice versa. This section only provides a short sketch of how to discretize Maxwell's equations and follows the work of [30, 32]. For further information and reading, the interested reader is referred to these references.

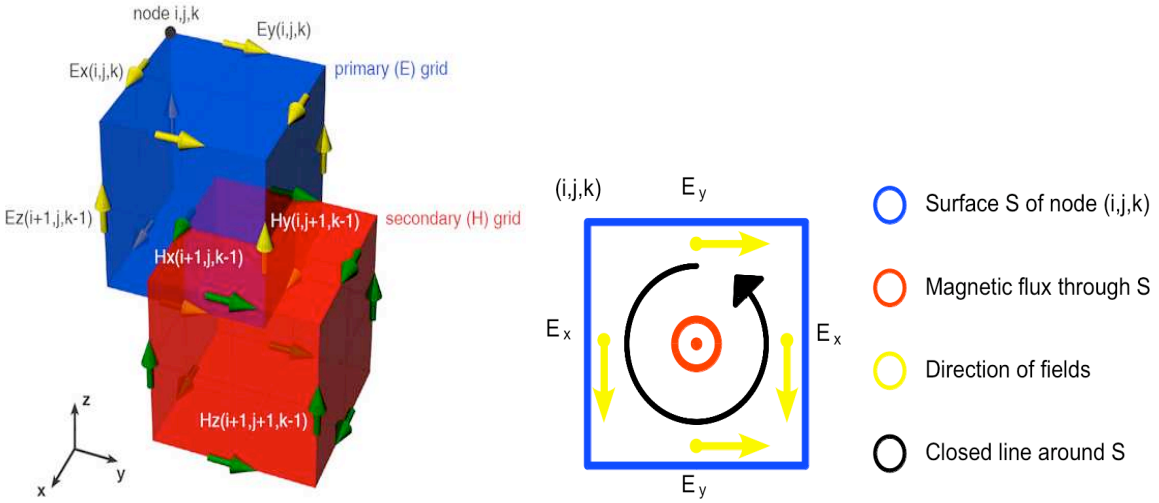

Figure 2.1: Left: Primary and secondary grid of the Yee-cube at node (i, j, k). Electric field components live on the edges of the primary grid (blue), while magnetic fields live on the edges of the secondary grid (red). The arrangement of both grids, staggered half a cell length in all directions, let electric field be localized face-centered on the secondary grid, and magnetic field be located face-centered on the primary grid. Right: Scheme of the line integral at node (i, j, k). Due to the staggered arrangement, the line integral, exemplarily for eq. (2.5) can be evaluated easily.

2.2.1 Update Equations of the FDTD

Spatially the computational volume is separated into voxels, the three-dimensional analogue to the two-dimensional pixel, which are indexed with natural number triples (i, j, k) for the x, y, z-direction. Neighboring cells have incremented or decremented indices depending on the direction. An edge length of a grid cell is $\Delta\mu$, $\mu = x$, y, z, so that neighboring field quantities are separated by one discretization length. Now, to address the field components in a numeric scheme, the following nomenclature is used:

$$(\mathbf{E}(\mathbf{r}))_\mu = E_{\mu\, ijk,t} = E_\mu \left((i + \frac{1}{2}\delta_{\mu x})\Delta x, (j + \frac{1}{2}\delta_{\mu y})\Delta y, (k + \frac{1}{2}\delta_{\mu z})\Delta z \right) \tag{2.16}$$

$$(\mathbf{H}(\mathbf{r}))_\mu = H_{\mu\, ijk} = H_\mu \left((i + \frac{1}{2}(1 - \delta_{\mu x}), t)\Delta x, (j + \frac{1}{2}(1 - \delta_{\mu y}))\Delta y, (k + \frac{1}{2}(1 - \delta_{\mu z}))\Delta z) \right) , \tag{2.17}$$

where $\delta_{\mu\nu}$ is the Kronecker-symbol, which is equal to 1 if $\mu = \nu$ and 0 otherwise. Required field components on positions on the Yee-cube, where they are not defined, like $E_{x\, i+\frac{1}{2}j+\frac{1}{2}k}$, have to be averaged arithmetically from known field components, e.g.

$$E_{x\, i+\frac{1}{2}j+\frac{1}{2}k} = \frac{1}{2}\left(E_{x\, i+\frac{1}{2}jk} + E_{x\, i+\frac{1}{2}j+1k} \right) \tag{2.18}$$

$$\begin{aligned} H_{x\, i+\frac{1}{2}j+\frac{1}{2}k} &= \frac{1}{2}\left(H_{x\, ij+\frac{1}{2}k} + H_{x\, i+1j+\frac{1}{2}k} \right) \\ &= \frac{1}{4}\left(H_{x\, ij+\frac{1}{2}k-\frac{1}{2}} + H_{x\, i+1j+\frac{1}{2}k+\frac{1}{2}} \right) . \end{aligned} \tag{2.19}$$

With this spatial discretization scheme and the possibility to average field components at positions on the Yee-Cube, where the desired field component is not defined, one can now

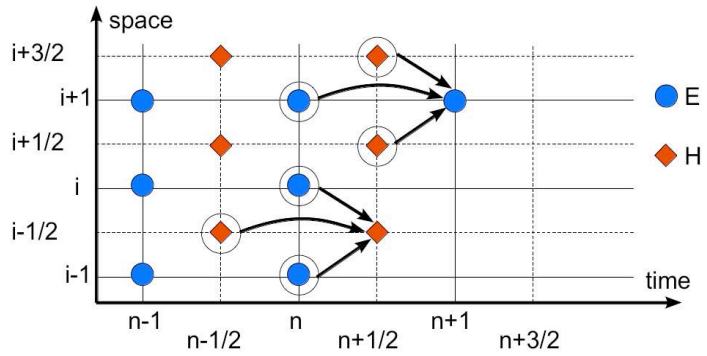

Figure 2.2: Update scheme for the fields (leapfrog scheme). Time stepping is in horizontal direction, while spatial stepping is in vertical direction (direction according to arrows). To update the magnetic field $H_{i-\frac{1}{2}}^{n+\frac{1}{2}}$, the field one full time step Δt earlier, $H_{i-\frac{1}{2}}^{n-\frac{1}{2}}$, and the electric fields half a time step before and half a space step back and forth each, E_{i-1}^{n} and E_{i+1}^{n}, is needed. Update of the electric field is similar, but fields are exchanged and half a step has to be added to time and space (Here, two half steps in time and space is shown to have the update scheme separated).

discretize the spatial differential operator ∂_μ. Since the derivative is a quantity obtained by a limes, discretization is needed to let the differential operator fit on the spatial grid. So the derivative is now written like in its derivation, but with central differences. Exemplarily, $\partial_x(\mathbf{H}(\mathbf{r},t))_y$ then yield

$$\partial_x H_{y\,i+\frac{1}{2}jk+\frac{1}{2}} = \frac{1}{\Delta x}(H_{y\,i+1jk+\frac{1}{2}} - H_{y\,ijk+\frac{1}{2}})\,. \tag{2.20}$$

The macroscopic Maxwell's equations (2.10)-(2.13) now have to be discretized in time with central differences, too, due to the partial derivatives in time. Temporal integration is then done with the so-called *Leap-Frog*-algorithm, where electric field quantities at time t are calculated from neighboring field quantities from the magnetic quantities at $t+\frac{1}{2}\Delta t$ and $t-\frac{1}{2}\Delta t$, where Δt is the discretization in time. See Fig. 2.2 for a coarse scheme. Therefore, the numerical scheme for all the field components is extended with another natural numbered index, n, for the time, i.e.

$$(\mathbf{E}(\mathbf{r},t))_x = E_{x\,i+\frac{1}{2}jk}^{n} = E_x((i+\frac{1}{2})\Delta x,\, j\Delta y,\, k\Delta z,\, n\Delta t) \tag{2.21}$$

$$(\mathbf{H}(\mathbf{r},t))_x = H_{x\,ijk}^{n+\frac{1}{2}} = H_x(i\Delta x,\, (j+\frac{1}{2})\Delta y,\, (k+\frac{1}{2})\Delta z,\, (n+\frac{1}{2})\Delta t)\,. \tag{2.22}$$

A generic discretization of the partial temporal derivative with central differences of $(\mathbf{E}(\mathbf{r},t))_x$ and $(\mathbf{H}(\mathbf{r},t))_z$ then yields:

$$\partial_t E_{x\,i+\frac{1}{2}jk}^{n} = \frac{1}{\Delta t}\left(E_{x\,i+\frac{1}{2}jk}^{n+\frac{1}{2}} - E_{x\,i+\frac{1}{2}jk}^{n-\frac{1}{2}}\right) \tag{2.23}$$

$$\partial_t H_{z\,i+\frac{1}{2}j+\frac{1}{2}k}^{n+\frac{1}{2}} = \frac{1}{\Delta t}\left(H_{z\,i+\frac{1}{2}j+\frac{1}{2}k}^{n+1} - H_{z\,i+\frac{1}{2}j+\frac{1}{2}k}^{n}\right)\,. \tag{2.24}$$

With these tools one can now derive update equations to calculate the components of electric and magnetic field on all grid points at the next unknown time step. To do so, one uses the

curl equations (2.12)-(2.13) and replaces the derivatives in time and space like eq. (2.20) and (2.23)-(2.24). This yields the following update equations exemplarily for the x-component of the electric and magnetic field:

$$E^{n+1}_{x\,i+\frac{1}{2}jk} = E^{n}_{x\,i+\frac{1}{2}jk} - \frac{\Delta t}{\epsilon_0 \epsilon_{i+\frac{1}{2}jk}} \times \left(\frac{1}{\Delta y}(H^{n+\frac{1}{2}}_{z\,i+\frac{1}{2}j+\frac{1}{2}k} - H^{n+\frac{1}{2}}_{z\,i+\frac{1}{2}j-\frac{1}{2}k}) - \frac{1}{\Delta z}(H^{n+\frac{1}{2}}_{y\,i+\frac{1}{2}jk+\frac{1}{2}} - H^{n+\frac{1}{2}}_{y\,i+\frac{1}{2}jk-\frac{1}{2}}) - j^{n+\frac{1}{2}}_{x\,i+\frac{1}{2}jk} \right) \tag{2.25}$$

$$H^{n+\frac{1}{2}}_{x\,ij+\frac{1}{2}k+\frac{1}{2}} = H^{n-\frac{1}{2}}_{x\,ij+\frac{1}{2}k+\frac{1}{2}} - \frac{\Delta t}{\mu_0} \times \left(\frac{1}{\Delta y}(E^{n}_{z\,ij+1k+\frac{1}{2}} - E^{n}_{z\,ijk+\frac{1}{2}}) - \frac{1}{\Delta z}(E^{n}_{y\,ij+\frac{1}{2}k+1} - E^{n}_{y\,ij+\frac{1}{2}k}) \right), \tag{2.26}$$

from which one can calculate the unknown $(\mathbf{E})_\mu$ at time $t + \Delta t$ using $(\mathbf{E})_\mu$ at time t at the same position in the Yee cube and $\mathbf{H}$ on the surrounding positions.
These update equations are now based on a centered difference scheme in time as well as in space. As one may have already noticed, the spatial derivatives $\partial_\mu(\mathbf{E}(\mathbf{r},t))_\mu$ did not emerge. The reason is, that this update scheme based on the Yee-cube naturally fulfills the divergence equations (2.12)-(2.13). Hence, the full set of electrodynamic equations (2.10)-(2.13) is complete with temporally and spatially update eqs. (2.25)-(2.26) of the FDTD.

2.2.2 Accuracy and Stability

Discretization of the Maxwell eqs. (2.14) and (2.15) induces mistakes in the temporal and spatial derivatives, since they are continuous, but the FDTD grid in time and space is discrete. A Taylor expansion shows the order of the error in terms of the spatial discretization. Assume a function $f(x)$ probed by a grid with discretization Δx and use central differences to express a derivative in x. For the left-aligned (right-aligned) function values, $f\left(x - \frac{\Delta x}{2}\right)$ $(f\left(x + \frac{\Delta x}{2}\right))$, the Taylor expansion equals

$$f\left(x + \frac{\Delta x}{2}\right) = f(x) + \frac{\Delta x}{2} f^{(1)}(x) + \frac{1}{2}\left(\frac{\Delta x}{2}\right)^2 f^{(2)}(x) + \frac{1}{6}\left(\frac{\Delta x}{2}\right)^3 f^{(3)}(\chi_+) \tag{2.27}$$

$$f\left(x - \frac{\Delta x}{2}\right) = f(x) - \frac{\Delta x}{2} f^{(1)}(x) + \frac{1}{2}\left(\frac{\Delta x}{2}\right)^2 f^{(2)}(x) - \frac{1}{6}\left(\frac{\Delta x}{2}\right)^3 f^{(3)}(\chi_-)\,, \tag{2.28}$$

$$\tag{2.29}$$

where $f^{(n)}$ is the n$^{\text{th}}$ derivative of f and $\chi_\pm \in [x, x \pm \frac{\Delta x}{2}]$. Now, subtracting (2.28) from (2.27) and dividing by Δx, one gets

$$f^{(1)}(x) = \frac{f\left(x + \frac{\Delta x}{2}\right) - f\left(x - \frac{\Delta x}{2}\right)}{\Delta x} - \frac{1}{3}\left(\frac{\Delta x}{2}\right)^3 f^{(3)}(\chi)\,, \tag{2.30}$$

with $\chi \in [x - \frac{\Delta x}{2}, x + \frac{\Delta x}{2}]$. So the centered first derivative approximation eq. (2.30) is of $\mathcal{O}(\Delta x^2)$.
The time integration to get $\mathbf{E}(\mathbf{r},t)$ and $\mathbf{H}(\mathbf{r},t)$ for the new time steps in eqs. (2.25) and (2.26) is done according to Fig. 2.2. Here, $\mathbf{E}(\mathbf{r},t)$ $(\mathbf{H}(\mathbf{r},t))$ at time $t = (n+1)\Delta t$ (for $\mathbf{H}(\mathbf{r},t)$:

$t = (n+\frac{1}{2})\Delta t)$ is calculated with the previous value at $t = (n-1)\Delta t$ (for $\mathbf{H}(\mathbf{r},t)$: $t = (n-\frac{1}{2})\Delta t$) and the surrounding $\mathbf{H}(\mathbf{r},t)$ ($\mathbf{E}(\mathbf{r},t)$) at time $t = (n+\frac{1}{2})\Delta t$ (for $\mathbf{E}(\mathbf{r},t)$: $t = n\Delta t$). Expressing this procedure with the functions $f(t)$ and $g(t)$, which are defined at temporal positions $t = n\Delta t$ and $t = (n+\frac{1}{2})\Delta t$, respectively, and assuming that $\mathcal{F}(\cdot)$ is some functional, the update scheme looks like

$$f\left((n+1)\Delta t\right) = f(n\Delta t) + \mathcal{F}\left(g\left((n+\frac{1}{2})\Delta t\right)\right) \tag{2.31}$$

$$g\left((n+\frac{1}{2})\Delta t\right) = g\left((n-\frac{1}{2})\Delta t\right) + \mathcal{F}\left(f(n\Delta t)\right) . \tag{2.32}$$

Since the time integration is of second order in the discretization, too, the stability criterium for the FDTD implementation, the so-called Courant-criterium, can be exploited to the maximum. The Courant-criterium says, that

$$\Delta t \leqslant s \cdot \frac{1}{c_0\sqrt{\Delta x^{-2} + \Delta y^{-2} + \Delta z^{-2}}} \tag{2.33}$$

ensures stability of the implementation. In the case of different orders of accuracy for the time and space derivative approximations, the factor s has to be $s << 1$, resulting in a small temporal discretization. In the FDTD case, s is mostly chosen to be ≈ 1.
If s equals 1, (2.33) is called the magic time step. In a one-dimensional FDTD implementation, the simulation equals the analytic solution exactly. The reason is the numerical dispersion, which is induced by the spatial grid. Numerical dispersion in general means, that a wave propagating in the spatial grid will be slowed down compared to its *natural* speed, c_0. In a one-dimensional case, one can choose the time step according to the magic time step, $\Delta t = \frac{\Delta x}{c_0}$. Hence, the time, which is needed for a propagating wave to go $c_0\Delta t$ equals exactly eq. (2.33) with $s = 1$, and the speed of the wave is exactly c_0, so no numerical dispersion occurs. In higher-dimensional FDTD simulations, the magic time step would only ensures no numerical dispersion along the principle axes of the simulation volume (if a uniform grid is provided). The other directions then *carry* a numerical dispersion, which are calculated via

$$\left[\frac{1}{c_0\Delta t}\sin\left(\frac{\omega\Delta t}{2}\right)\right]^2 = \sum_{\mu=x,y,z}\left[\frac{1}{\Delta\mu}\sin\left(\frac{\tilde{k}_\mu\Delta\mu}{2}\right)\right]^2 , \tag{2.34}$$

where $\tilde{k}_\mu$ are the components of the numerical wave vector (see [30]).
In other words, the temporal discretization is determined by the spatial discretization and s. Since eq. (2.34) is of the same order of accuracy as eq. (2.32), the numerical dispersion can be reduced drastically when a smaller spatial discretization is used. The problem is, that when reducing the the spatial discretization by $\Delta\mu_{\text{coarse}} = m \cdot \Delta\mu_{\text{fine}}$, memory raises with $\mathcal{O}(m^3)$ and computational time raises with $\mathcal{O}(m^4)$. Accordingly, a blind reduction of $\Delta\mu$ has no use, in fact one has to think about the problem one wants to solve. A good value to start with is $\Delta\mu = 0.1\lambda_0$, with λ_0 being the smallest wavelength in the material with the highest dielectric permittivity and the highest conductivity one wants to detect. However, this is of course no rule, but a rule of thumb. Another point to think of is, what is the smallest geometrical shape one wants to resolute. Usually, curvatures need a higher resolution to let the waves in the computational domain interpret the structure as a curved structure. In cartesian grids, curvatures always result in staircasing, Fig. 2.4, which affects resonant

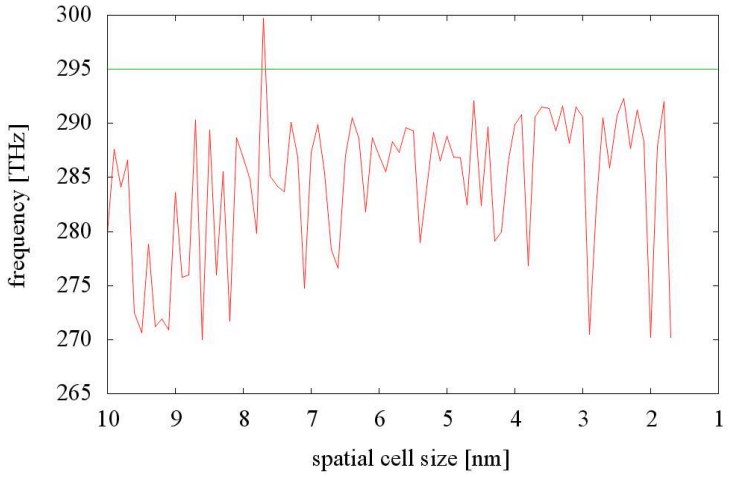

Figure 2.3: Staircasing effect on the resonance of an eigenmode in a circular resonator (two-dimensional calculation, [51]). A cartesian (uniform) grid is used to map the perfectly circular structure. The spatial cell size is decreased from 10 nm down to 1.7 nm in 0.1 nm steps. The vertical axes shows the resonant frequency for a certain eigenmode. Red: numerically calculated resonance. Green: analytical value.

frequencies drastically [52, 53]. Non-cartesian grids can be applied to solve the problem. For cylindrical structures, the best choice is a cylindrical coordinate system (if one has point symmetry to the origin). Therefore, transform eqs. (2.12)-(2.13) into cylindrical coordinates and then perform the discretization in the new coordinate system, like in the free available software package *MEEP* [31]. Another method is to use a polygonal mesh without orthogonal principal axis like in the frequency-domain method FEM [33, 34] or the DGTD method [42–46]. To overcome a lack in accuracy due to staircasing effects, one can use an averaging method for the permittivity within the cells (Sec. 2.2.3).
Figure 2.3 shows the dependency of the numerical frequency of a perfectly circular resonator structure in a metallic environment on the size of the spatial grid, used in a two-dimensional FDTD [51]. The radius of the resonator structure is set to $R = 361$ nm and the permittivity is set to the GaAs value of $\epsilon = 11.56$. The usage of a cartesian grid yields the mapping of the dielectric structure to be staircased at the boundary. Therefore, an increase or decrease of the cell size changes the effective resonator shape, hence the frequency of the resonance changes. The analytically calculated value of the 4^{th} resonance is $f = 295$ THz (green). As can be seen, the numerically calculated values for the resonances (red) approach asymptotically the analytical value, in fact it stays below the exact value, even for cell sizes much smaller than the expected wavelength. Thus, convergence for a curved structure in a cartesian grid is not expected along this thesis, but sufficiently small spatial probing will be chosen to e.g. ensure experimentally unmeasurable frequency changes.

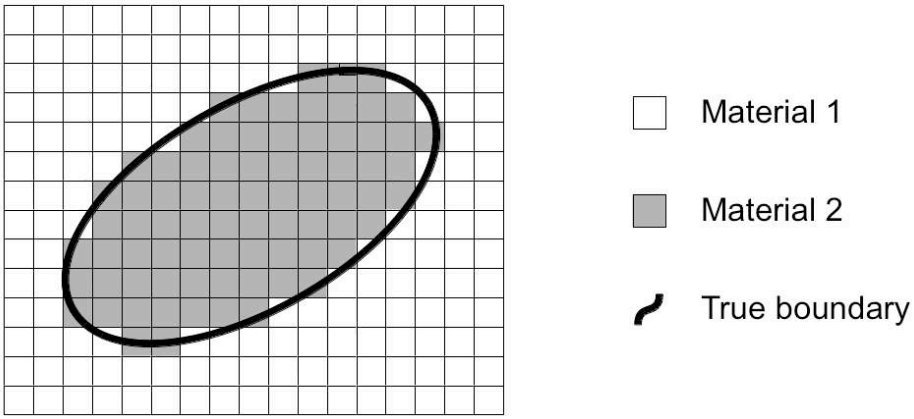

Figure 2.4: Two-dimensional scheme of the staircasing. The black line shows the interface between two media with different dielectric permittivity (white and grey). Spatial cells, which contain the interface, are filled with only one of the two materials, if no averaging routine is provided. The shape of the originally curvatures object gets staircased.

2.2.3 Subpixel-Averaging for Isotropic Dielectric Media

In the setup of the spatial grid and the implantation of dielectric material in arbitrary shape, it happens that Yee-cells are not filled totally with one and the same dielectric material, hence one cell has two or even more different values for the dielectric permittivity. The question arising is, what value is assigned to this cell. Obviously, one can, e.g. in the case of two dielectric materials in one cell, calculate the amount of each material filling this cell, and then fill the whole cell with the most frequently present. This results, especially for circular structures, in a staircasing, see Fig. 2.4. Also, this reduces the accuracy of the algorithm to 1^{st} order. To overcome this problem, one uses an averaging method for the permittivity, based on the filling factor of the different permittivities in the corresponding cell. In general, such averaging schemes can drop the accuracy down to 1^{st} order in the spatial discretization. For two reasons, the method of choice is the subpixel averaging scheme developed in [54]. First, the averaging scheme is chosen to be in a way that, treating the problem in a pertubative approach with pertubative parameter s, for $s \to 0$ the 1^{st} error vanishes, providing 2^{nd} order accuracy. In fact, the result is then an enhanced accuracy, up to 2^{nd} order for special cases and specific fields, but in general a higher accuracy than without averaging. Second, this averaging scheme can be extended to full anisotropic materials, too [55].

The performance of the averaging process is shown in Fig. 2.5. Here, a two-dimensional FDTD calculation with a cylindrical dielectric object with a radius of $r = 3\ \mu$m, embedded in vacuum, is done. The behavior of a specific mode around $\varepsilon = 0.806$ eV is chosen to be tracked, while the cylindrical object is shifted in subpixel steps over 4 cells (right part of Fig. 2.5, shown schematically). The spatial discretization correspond to $\Delta x = \Delta y = 40$ nm. Spectral data are extracted with the *Harmonic Inversion* tool (see Sec. 2.8). In the top case, no ϵ-averaging routine is used in the simulation. A periodic shifting up to $\Delta\varepsilon = 1$ meV in the resonant energy of the system with a periodicity of the cell length, as well as a modification in the intensity of the resonance is observed. In fact, shifting the dielectric object in subpixel steps changes the geometry, since cells, which were filled before, are no longer filled (or vice versa) after the shift. The lower case, where the ϵ-averaging procedure is applied, shows no shift in the resonance.

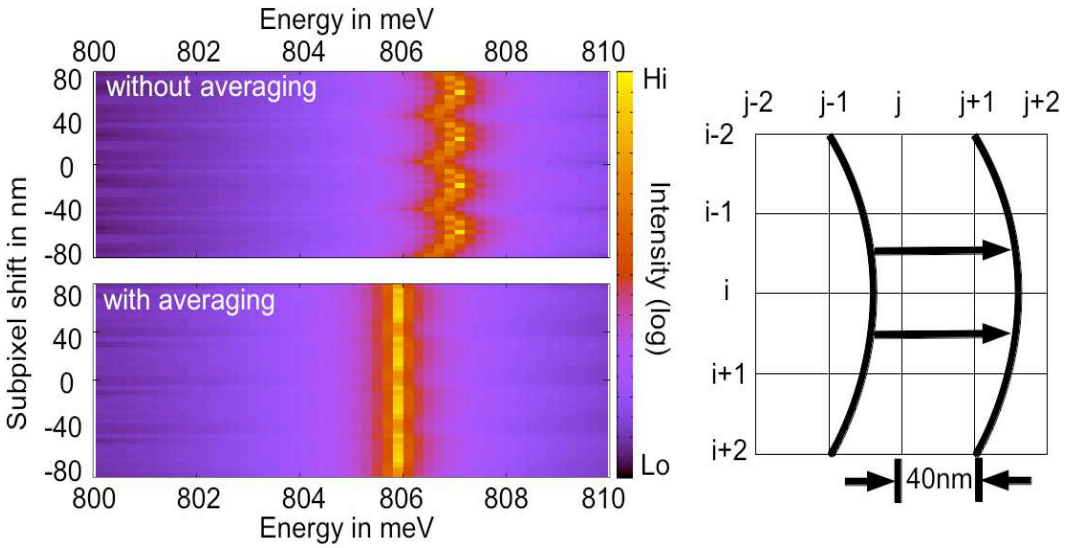

Figure 2.5: Left: Comparison of a simulation of a cylindrical object with a radius of $r = 3$ μm. Top: no ϵ-averaging. Bottom: with ϵ-averaging. Chasing the resonance occurring at $\varepsilon = 0.806$ eV, one can clearly see blue-shift of the resonance up to $\Delta\varepsilon = 1$ meV with a periodicity of 40 nm, equal to the spatial discretization, resulting from an efficiently smaller object due to staircasing. Right: scheme of the subpixel shift of the dielectric cylindrical object. As the true boundary passes a cell, the cell itself is either full filled or half filled.

Still, the intensity in the resonance changes with a periodicity as before without the averaging process, but the deviation is of lower order.

2.2.4 CPML: Truncate the Computational Volume

Since the computational resources are limited, one has to, next to temporal and spatial discretization, truncate the computational volume in space. Setting all the field values out of the simulation volume hard to zero would end up as a perfect electric (magnetic) conductor, PEC (PMC). Hence, all fields inside the computational volume are then reflected from the boundary, since no fields would be able to penetrate the outer regions. The result then is that the implanted energy will stay inside the simulation volume forever (despite usage of lossy materials). Since this is unphysical, one at best needs absorbing boundary conditions (ABC) which totally absorb the energy of incident waves, independent of the polarization, frequency and incident angle, in fact are 100% transmittive. Furthermore, the absorbing boundary should be effective when scattering objects or sources, especially point sources, are close. Additionally, since the ABC area also consists of cells which need to update $\mathbf{E}(\mathbf{r}, t)$ and $\mathbf{H}(\mathbf{r}, t)$ in every time step with additional effort, the absorbing area should not be too large to not unnecessarily enlarge the computational domain and hence increase the computation time.
The first widely used numerically stable, second-order accurate ABC was formulated by Mur [56], but the disadvantage is that it only absorbs specific polarization well. Berenger then introduced a highly efficient ABC [57], the so-called perfectly matched layer (PML), based on formulation of split fields, which are orthogonal to each other, resulting in 12 coupled 1^{st} PDEs with loss parameters. The big advantage of the PML is the universal applicability to cut the simulation volume consisting not only of isotropic lossless dielectric material, but also

anisotropic, nonlinear and dispersive materials, just to mention some. Later, a formulation with stretched coordinates was developed. This gave the possibility to also apply the PML concept to other orthogonal coordinate systems than the cartesian one. The split-field PML proposed by Berenger and its stretched analogue is based on a mathematical model. The uniaxial PML (UPML) based on an anisotropic PML yields a physical formulation [58]. The performance of Berengers split-field PML and the UPML is the same, but they differ in Gauss' law. Since the use of a classical tensor coefficient can lead to large reflection errors in the low frequency range, the complex-frequency shifted (CFS) PML overcomes this problem [59, 60]. However, Roden and Gedney implemented a more efficient version using strechted coordinates from Berenger based on a recursive-convolution formulation, the convolutional PML (CPML). The result is more efficient, more accurate than the UPML, and provides better applicability to terminate regions with generalized media.
The strechted coordinates are built with the CFS tensor coefficient $s_\mu = \kappa_\mu + \frac{\sigma_\mu}{\alpha_\mu + i\omega\epsilon_0}$, where the parameter ranges are $\kappa_\mu \geqslant 1$, $\sigma_\mu \geqslant 0$ and $\alpha_\mu \geqslant 0$ and $\mu = x, y, z$. Berengers strechted coordinates metrics is obtained for $\kappa_\mu = 1$ and $\alpha_\mu = 0$. The update equation within the CPML material exemplarily for the x-component of the electric field yields

$$\begin{aligned} E^{n+1}_{x\,i+\frac{1}{2}jk} &= E^{n}_{x\,i+\frac{1}{2}jk} \\ &- \frac{\Delta t}{\epsilon_0 \epsilon_{i+\frac{1}{2}jk}\mu_0}\left(\frac{1}{\kappa_{yj}\Delta y}\left(H^{n+\frac{1}{2}}_{z\,i+\frac{1}{2}j+\frac{1}{2}k} - H^{n+\frac{1}{2}}_{z\,i+\frac{1}{2}j-\frac{1}{2}k}\right) - \frac{1}{\kappa_{zk}\Delta z}\left(H^{n+\frac{1}{2}}_{y\,i+\frac{1}{2}jk+\frac{1}{2}} - H^{n+\frac{1}{2}}_{y\,i+\frac{1}{2}jk-\frac{1}{2}}\right)\right) \\ &- \frac{\Delta t}{\epsilon_0 \epsilon_{i+\frac{1}{2}jk}\mu_0}\left(\Psi^{\;n+\frac{1}{2}}_{E_{x,y}\,x\,i+\frac{1}{2}jk} - \Psi^{\;n+\frac{1}{2}}_{E_{x,z}\,x\,i+\frac{1}{2}jk}\right) \end{aligned} \tag{2.35}$$

$$\tag{2.36}$$

with

$$\Psi^{\;n+\frac{1}{2}}_{E_{x,y}\,x\,i+\frac{1}{2}jk} = b_{yj}\Psi^{\;n-\frac{1}{2}}_{E_{x,y}\,x\,i+\frac{1}{2}jk} + \frac{c_{yj}}{\Delta y}\left(H^{n+\frac{1}{2}}_{z\,i+\frac{1}{2}j+\frac{1}{2}k} - H^{n+\frac{1}{2}}_{z\,i+\frac{1}{2}j-\frac{1}{2}k}\right) \tag{2.37}$$

$$\begin{aligned} \alpha_\mu &= \alpha_{\mu,\,\max}\left(1 - \frac{x}{d}\right)^{m_\alpha} \\ b_\mu &= e^{-\left(\frac{\sigma_\mu}{\kappa_\mu} + \alpha_\mu\right)\frac{\Delta t}{\epsilon_0}} \\ c_\mu &= \frac{\sigma_\mu}{\kappa_\mu(\sigma_\mu + \kappa_\mu\alpha_\mu)}(b_\mu - 1)\,, \end{aligned} \tag{2.38}$$

where $0 \leqslant x \leqslant d$, the boundary to the CPML is located at 0, d is the thickness of the CPML and m_α determines the scaling order. A detailed derivation can be found in [60].
Within this thesis, open boundary conditions are used, utilizing a CPML with parameters as given in Tab. B.4, if not mentioned otherwise.

2.3 The Photonic Crystal

In nature, the concept of photonic crystals is not a new feature. One of the most famous representatives is the butterfly *Morphus rhodopteron* with its shiny blue wings or the opal, which can please every womans' temper. The effect is no biological or chemical pigmentation, rather a physical one. Multiple reflections of incident light on successive layers lead to constructive and destructive interference, depending on wavelength and angle of incidence.

	Quantum mechanics	Electrodynamics
Field	$\Psi(\mathbf{r})e^{-\frac{iEt}{\hbar}}$	$\mathbf{H}(\mathbf{r}) \cdot e^{-i\omega t}$
Eigenvalue Problem	$\hat{H}\Psi = E\Psi$	$\hat{\Theta}\mathbf{H} = \left(\frac{\omega}{c_0}\right)^2 \mathbf{H}$
Hermetian Operator	$-\frac{\hbar^2}{2m}\nabla^2 + V(\mathbf{r})$	$\nabla \times \epsilon_r(\mathbf{r})^{-1}\nabla\times$
Potential	$V(\mathbf{r})$	$\epsilon_r(\mathbf{r})$

Table 2.1: Quantum Mechanics vs. Electrodynamics: A comparison. After [62].

Within the last decades, PhCs have inspired great interest not only due to their applications in research, but also in various commercial areas accessible in the future. The most used phrase in this context for sure is optical information processing. There, electronic manipulation of data is then substituted by optical or optoelectronical manipulation [61]. Also, since speed of light (in vacuum) is the highest velocity known by mankind, data transfer speed can be drastically increased. Scientists all over the world deal with the experimental realization of optical and optoelectronical devices, miniaturization, integrability and usability. Therefore, PhC is a promising candidate, since, once a device is characterized, the characteristics can be scaled up and down in size, because Maxwell's equations (2.14)-(2.15) scale with length [62].
What is a photonic crystal? A crystal is a periodic arrangement of atoms (molecules) within a certain pattern of repetition, forming the crystal lattice, which provides a potential. Thereby it does not matter, if this potential is of electronic or optical kind. Charge carriers, i.e. electrons in a lattice of a conducting crystal can propagate resistance-free (if no defects like impurities are present), because electrons do not behave just like particles, which would be scattered by the atomic bodies, but also like waves. When those waves match particular criteria, they can propagate through the crystal without being scattered. On the other hand, they can also be prohibited from propagating through the crystal lattice. Normally, there is not only one criterium for a prohibition of propagation. In this way, different energetically forbidden areas emerge, called the electronic band gap, which divides the valence band from the conduction band and is basis for many important inventions in semiconductor physics [63–71]. In a PhC, the optical analogue to a conductive crystal for charge carriers, photons behave in the same manner [72–74]. The atomic (molecular) lattice is then substituted by different dielectric materials, which form the crystal, hence the potential for the photons. The compound material can then form a photonic band gap for the light for a specific frequency range. The prohibition of propagation can be manipulated to be in all directions, for all polarization, for smaller or larger frequency ranges, depending on the designing rules applied to the compound material [62, 75, 76] (see Fig. 2.6 as an example). Thus, manipulation of light can be performed on the nanoscale, which is the basic key for small-sized photonic devices for future quantum information processing computers.
To derive an equation to access the fields in arbitrarily shaped and arbitrarily composited dielectric structures, one explicitly needs spatial variation of the dielectric constant even on small length scales (in the range of the material wavelength, or even smaller). Therefore, $\epsilon_r \equiv \epsilon_r(\mathbf{r})$. Attention needs to be paid in eq. (2.13), since the divergence is taken from the dielectric displacement field $\mathbf{D}(\mathbf{r}, t)$ to get the charge density. Now, inserting eq. (2.9) results in

$$\nabla \cdot \mathbf{D}(\mathbf{r}, t) = \nabla \cdot (\epsilon_r(\mathbf{r})\mathbf{E}(\mathbf{r}, t)) = \rho(\mathbf{r}, t)\,, \tag{2.39}$$

while eqs. (2.12), (2.14) and (2.15) remain unchanged. If one wants now to derive the wave equation for the time-harmonic fields $\mathbf{H}(\mathbf{r},t) = \mathbf{H}(\mathbf{r}) \cdot e^{-i\omega t}$ and $\mathbf{E}(\mathbf{r},t) = \mathbf{E}(\mathbf{r}) \cdot e^{-i\omega t}$ and without any sources of electromagnetic radiation in the standard way [48, 77, 78] one ends up with [62]

$$\nabla \times \left(\epsilon_r(\mathbf{r})^{-1} \nabla \times \mathbf{H}(\mathbf{r})\right) = \hat{\Theta}_H \mathbf{H}(\mathbf{r}) = \left(\frac{\omega}{c_0}\right)^2 \mathbf{H}(\mathbf{r})\,, \tag{2.40}$$

$$\epsilon_r(\mathbf{r})^{-1} \nabla \times \nabla \times \epsilon_r(\mathbf{r})^{-1} \mathbf{D}(\mathbf{r}) = \hat{\Theta}_D \mathbf{D}(\mathbf{r}) = \left(\frac{\omega}{c_0}\right)^2 \epsilon_r(\mathbf{r})^{-1} \mathbf{D}(\mathbf{r})\,. \tag{2.41}$$

Maxwell's equations are now rewritten as an eigenvalue problem with the linear operator $\hat{\Theta}_H$ ($\hat{\Theta}_D$), corresponding eigenvalue $\left(\frac{\omega}{c_0}\right)^2$ and eigenvector $\mathbf{H}(\mathbf{r})$ ($\mathbf{D}(\mathbf{r})$). Equation (2.41) was divided by an extra $\epsilon_r(\mathbf{r})$ to keep the $\hat{\Theta}_D$ hermitian. This is an important point, because the eigenvalues are then real positive semi-definite, say larger or equal to zero. Additionally, the fact that $\hat{\Theta}_X$ is a linear operator, cannot be underrated, since (linear) superpositions of found solutions are also solutions. For mathematical convenience, eq. (2.40) is normally used with $\hat{\Theta}_H = \hat{\Theta}$. Access to $\mathbf{D}(\mathbf{r},t)$ is gained by solving eq. (2.40), and subsequently using eq. (2.11) in its time-harmonic form. The solutions of eq. (2.40) have some more interesting and useful properties. For example, the analogy to quantum mechanics, *Schrödinger's equation*, which allows to transfer some properties from quantum mechanics directly to classical electrodynamics (find a comparison in Tab. 2.1), like symmetries and orthogonality of the solutions of eq. (2.40). The latter one is the consequence of the hermitian property of $\hat{\Theta}_H$. For two different solutions labeled with 1 and 2, one gets

$$0 = (\omega_1^2 - \omega_2^2)\,(\mathbf{H}_2(\mathbf{r}), \mathbf{H}_2(\mathbf{r}))\,, \tag{2.42}$$

where $(\,\cdot\,,\cdot\,)$ denotes the inner product as defined in a *Hilbert*-space. So either the inner product has to be zero, then the two solutions are orthogonal, or the eigenvalues have to be the same, then the two solutions are degenerate. In real systems, degeneracy normally is lifted due to e.g. broken symmetries.

Due to the astonishing similarities between the electronic and electromagnetic eigenvalue problem, methods known from electronic system can be used for the electromagnetic problem, too, like a tight-binding formalism [79, 80]. This answers directly the question for the origin of the electromagnetic band gap.

Another way to understand the origin of the band gap is to locate the points of high energy of the harmonic modes $\mathbf{H}(\mathbf{r}) \cdot e^{-i\omega t}$ [62]. A variational principle ansatz shows, that the harmonic mode with the lowest frequency in the band gap concentrates its energy density mostly in the material with the highest permittivity (often called a dielectric band), while others locate less energy density in these regions, but in the material with lower permittivity (often called air band). This is why the modes (band) at the low side of the first band are called dielectric modes (band), while the modes locates above the band gap are called air modes (band). A collection of different band structures is depicted in Sec. 2.4.2 for two- and three-dimensional systems.

Depending on the application, for which a photonic band gap material is designed, one wants to modify the size of the band gap and/or the spectral position of the band gap. This can be done by various modifications, for example change of the periodicity, modification of the permittivities, combine more than two materials with different permittivities, etc. [62]. Figure

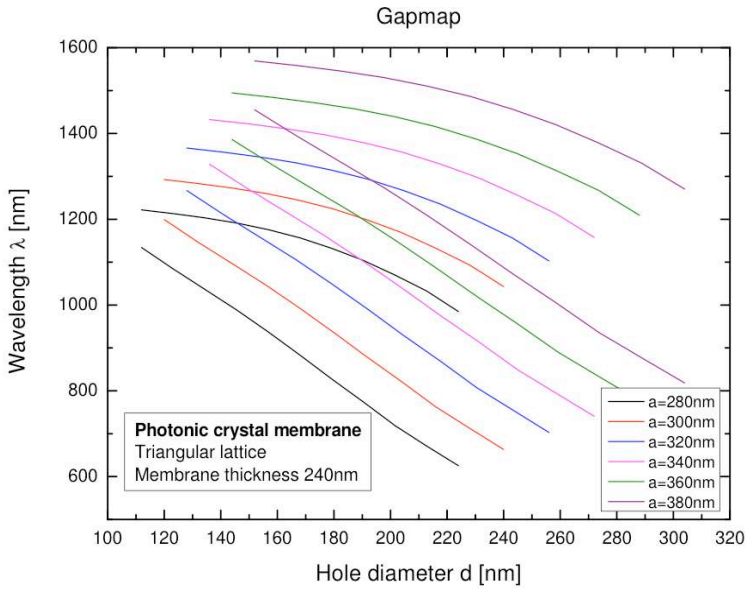

Figure 2.6: Band gap size vs. hole diameter for different lattice constants a (see right inset) in a triangular lattice of air holes in a dielectric slab ($\epsilon = 11.56$) of fixed thickness ($t = 240$ nm). Data are extracted from *MPB* [82], the upper lines denote the upper band edge of the 1st photonic band, the lower lines denote the lower band edge of the 2nd photonic band [81].

2.6 shows the variation of the band gap size with the hole diameter d of the air holes in a triangular lattice in a dielectric slab with $\epsilon = 11.56$ of fixed thickness ($t = 240$ nm) and different lattice constants a [81]. The wavelength in nm is given on the vertical axis, the hole diameter is on the horizontal axis. Lines of the same color belong to a setup of the PhC with the lattice constant shown in the inset. Upper and lower lines are extracted from numerical data, calculated with *MPB* [82], and denote the band edge of the 1st photonic band and the low band edge of the 2nd photonic band. One can see, that the width of the photonic band gap changes with changing lattice constant. To be more precise, the band gap increases with increasing lattice constant. The hole diameter also affects the band gap size. A maximum of the gap size emerges for every lattice constant, close to the maximal size of the hole diameter for a fixed lattice constant (compare the gap size for $a = 280$ nm (black) and $a = 380$ nm (purple) for large hole diameters). So the width of the gap size is primary controlled by the hole diameter, while the spectral position is controlled primary by the lattice constant.

Last but not least one has to mention the photonic density of states (PhDoS), which gives the number of allowed photonic modes per frequency interval $\delta\omega$. Inside a PBG (yellow region in Fig. 2.7), the density of states is zero, because no propagating states are allowed within this frequency range. Photonic states which would be in the PBG region are pushed away and are localized above and below the PBG (blue areas in Fig. 2.7). But modes with an imaginary wave vector are allowed in the PBG region, since these modes are not propagating modes, but evanescent ones. Localization of evanescent modes in the PBG can be done with a defect in the periodicity of the crystal, as is depicted as the red line in Fig. 2.7. Section 2.4.2 shows how one can make use of the photonic band gap and the enlarged PhDoS, to store light in a small volume (comparable to the cubic material wavelength of the confined photons) over a long time, when introducing a defect in the PhC, a PhC cavity (PhCC).

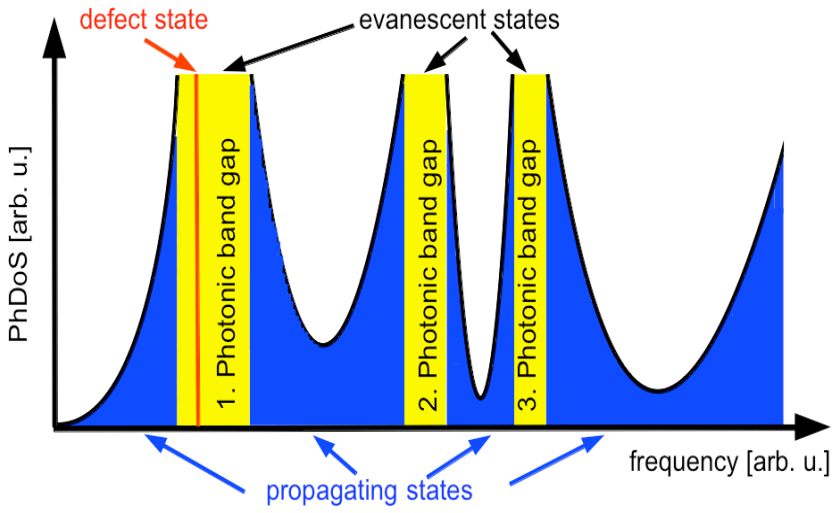

Figure 2.7: Photonic density of states (PDoS) vs. frequency in arbitrary units. The blue region shows propagating modes with a real wave vector **k**. Near the photonic band gaps (yellow parts), the photonic density of states raises, since the states from the band are pushed outside, hence increasing the PDoS. Here, only modes with an imaginary wave vector are allowed, since they represent evanescent modes, which only decay and show no propagate. In these regions, one can confine the light introducing a defect, like a point or line defect, thus increasing the density of states for a certain frequency matching the resonance of the defect. After [62].

Nowadays, this concept has already been applied to various kinds of PhCs. Just to mention some, examples are the two-dimensional dielectric slabs with periodic arrangements of air holes exhibiting a hexagonal symmetry, the three-dimensional *Yablonovite*, a woodpile stack of layers of parallel oriented dielectric columns, alternating in height in a 90° angle or the inverse opal structure.

2.4 Nanoscale Optical Resonators

There are various kinds of optical resonators. The focus is on microcavities, so this thesis concentrates on optical resonators in the (sub-) micrometer range. In general, there are two different kinds of optical microresonators: first, a material without a PBG like a micro-toroid or a microdisk (Sec. 2.4.1), purely relying on the principle total internal reflection (TIR), and second, a PBG material (Sec. 2.4.2) with a defect to confine the light, like a PHCC.

2.4.1 The Microdisk Resonator

The MD resonator is a good example for a resonant structure without a PBG, because periodicity is not provided. As will be seen in this chapter, the electromagnetic problem of a (perfectly) cylindrical dielectric object can be solved analytically, if one omits the post on which the MD is standing to separate the dielectric layer forming the disk from the substrate material. As will be seen later, the post will not affect the field distribution in the microdisk. The ratio between thickness of the microdisks membrane and radius can thereby vary over some orders of magnitude [26, 83].
Regarding Maxwell's equations in their time harmonic form, utilizing the curl equations and

assume, that no free charges or currents are present ($\mathbf{j}(\mathbf{r},t) = \rho(\mathbf{r},t) \equiv 0$) , one can rewrite eqs. (2.1) and (2.2) with usage of (2.9) to

$$\nabla \times \mathbf{E}(\mathbf{r},\omega) = -\frac{i\omega}{\epsilon_0 c_0^2}\mathbf{H}(\mathbf{r}) \cdot e^{-i\omega t} \tag{2.43}$$

$$\nabla \times \mathbf{H}(\mathbf{r},\omega) = -i\omega\epsilon_0\epsilon_r(\mathbf{r})\mathbf{E}(\mathbf{r}) \cdot e^{-i\omega t}\,. \tag{2.44}$$

Decoupling (2.43) and (2.44) results in wave equations for $\mathbf{E}$ and $\mathbf{H}$

$$\nabla \times \nabla \times \mathbf{E}(\mathbf{r}) = \epsilon_r(\mathbf{r}) \left(\frac{\omega}{c_0}\right)^2 \mathbf{E}(\mathbf{r})\,, \tag{2.45}$$

$$\nabla \times \epsilon_r(\mathbf{r})^{-1} \nabla \times \mathbf{H}(\mathbf{r}) = \left(\frac{\omega}{c_0}\right)^2 \mathbf{H}(\mathbf{r})\,, \tag{2.46}$$

which can be used to derive the *Helmholtz*-equation, exemplarily for the electric field $\mathbf{E}$ (in areas of constant $\epsilon_r(\mathbf{r})$) using standard vector calculus:

$$(\triangle + n^2\mathbf{k}^2)\,\mathbf{E}(\mathbf{r}) = 0\,. \tag{2.47}$$

The dispersion relation $\mathbf{k}^2 = \left(\frac{\omega}{c}\right)^2$, is used here, $\mathbf{k}$ is the wave vector, $\triangle = \sum_{\mu=x,y,z} \partial_\mu^2$ denotes the Laplacian operator and it is assumed, that $\epsilon_r(\mathbf{r}) = n^2$, since the focus lies on investigating pure dielectric materials without resonances.
Without loss of generality, one now assumes an infinitely extended dielectric slab in the $x-y$-plane, whose permittivity is piecewise constant at the interfaces, a finite thickness t in z-direction and propagating fields in the x-direction. The thickness is an important quantity if one is interested in single-mode operating devices, whose basis is a planar waveguiding system. Total internal reflection keeps the light within the thin dielectric slab. Using the fields propagating in x-direction (with wave vector k_x) and eq. (2.47), one gets for the TE-case ($E_y = \tilde{E}_y(z) \cdot e^{ik_x x}$)

$$\left(\partial_z^2 + \underbrace{\left(\epsilon_r \left(\frac{\omega}{c_0}\right)^2 - k_x^2\right)}_{(*)}\right) \tilde{E}_y = 0\,. \tag{2.48}$$

For the permittivity, $\epsilon_r = \epsilon$ for $\mid z \mid < \frac{t}{2}$ and $\epsilon_r = 1$ for $\mid z \mid > \frac{t}{2}$ applies. So for both spatial domains, one can rewrite the $(*)$-marked part in eq. (2.48) into

$$(*) = \kappa^2 = \epsilon \left(\frac{\omega}{c_0}\right)^2 - k_x^2\,, \text{ for } \mid z \mid < \frac{t}{2} \tag{2.49}$$

$$(*) = (i\gamma)^2 = i^2 \left(k_x^2 - \left(\frac{\omega}{c_0}\right)^2\right) \text{ for } \mid z \mid > \frac{t}{2}. \tag{2.50}$$

Since this problem has spatial symmetry in z-direction, symmetric as well as antisymmetric solution can be derived. To obtain exponentially decaying solutions outside and standing waves inside the slab, κ and γ need to be larger than 0. Using the boundary conditions at

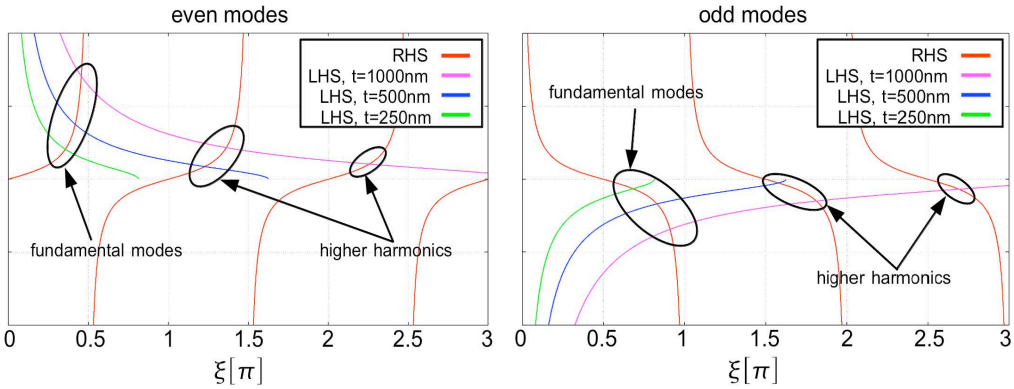

Figure 2.8: Graphical solution of eqs. (2.51) and (2.52). The intersections show the valid values for κ, hence for γ. The RHS is shown in red. The used parameters are: $\epsilon = 11.56$, $\lambda_0 = 1000$ nm, $t = 250$ nm (green), 500 nm (blue), 1000 nm (magenta). For increasing thickness, more modes (higher harmonics)are occupied.

the interface of the two different dielectric media (the field and its derivative with respect to space have to be continuous), one derives the transcendental equations in order to calculate the wave vector

$$\tan\xi = \frac{\gamma d}{2\xi}\,, \text{ for even modes and} \tag{2.51}$$

$$\cot\xi = -\frac{\gamma d}{2\xi}\,, \text{ for odd modes } . \tag{2.52}$$

where $\xi = \frac{\kappa d}{2}$. Rewriting $\gamma d = d^2\left(\left(\frac{\omega}{c_0}\right)^2(\epsilon - 1) - \kappa^2\right)$ using some algebraic transformations, the graphical solution for eqs. (2.51) and (2.52) result in Fig. (2.8), respectively, where every intersection is a valid value for κ and γ for the given system (the used parameters are given in the caption).
For the in-plane solution one considers a dielectric cylinder with permittivity $\epsilon_r = \epsilon$ and radius R, infinitively extended in z-direction, to calculate the field distribution, hence to understand the in-plane confinement of electromagnetic radiation. Since the slab is assumed to be in the $x-y$-plane, one uses now the *Helmholtz* equation (2.47) and transforms the problem into cylindrical coordinates $(x, y) \longrightarrow (r, \phi)$ yielding

$$\left(\frac{1}{r}\partial_r(r\partial_r) + \frac{1}{r^2}\partial_\phi^2 + \epsilon\left(\frac{\omega}{c_0}\right)^2\right) E_y(r,\phi) = 0\,. \tag{2.53}$$

Here, one uses a product ansatz for $(\mathbf{E})_y(r,\phi) = R(r)\cdot\Phi(\phi) = R(r)\cdot e^{\pm iM\phi}$ (ϕ-harmonic with azimuthal order M; the $\pm$ occurs because of double degeneracy for propagation clockwise or counterclockwise) to separate the variables r and ϕ. Utilizing the product ansatz and the common substitution to a unitless, effective radius ρ, $r \longrightarrow \frac{c_0}{n\omega}\rho$, one finally finds the differential equation for the radial component of $(\mathbf{E})_y$ to be a *Bessel* differential equation

$$\left(\partial_\rho^2 + \frac{1}{\rho}\partial_\rho + \left(1 - \left(\frac{M}{\rho}\right)^2\right)\right) R(\rho) = 0\,, \tag{2.54}$$

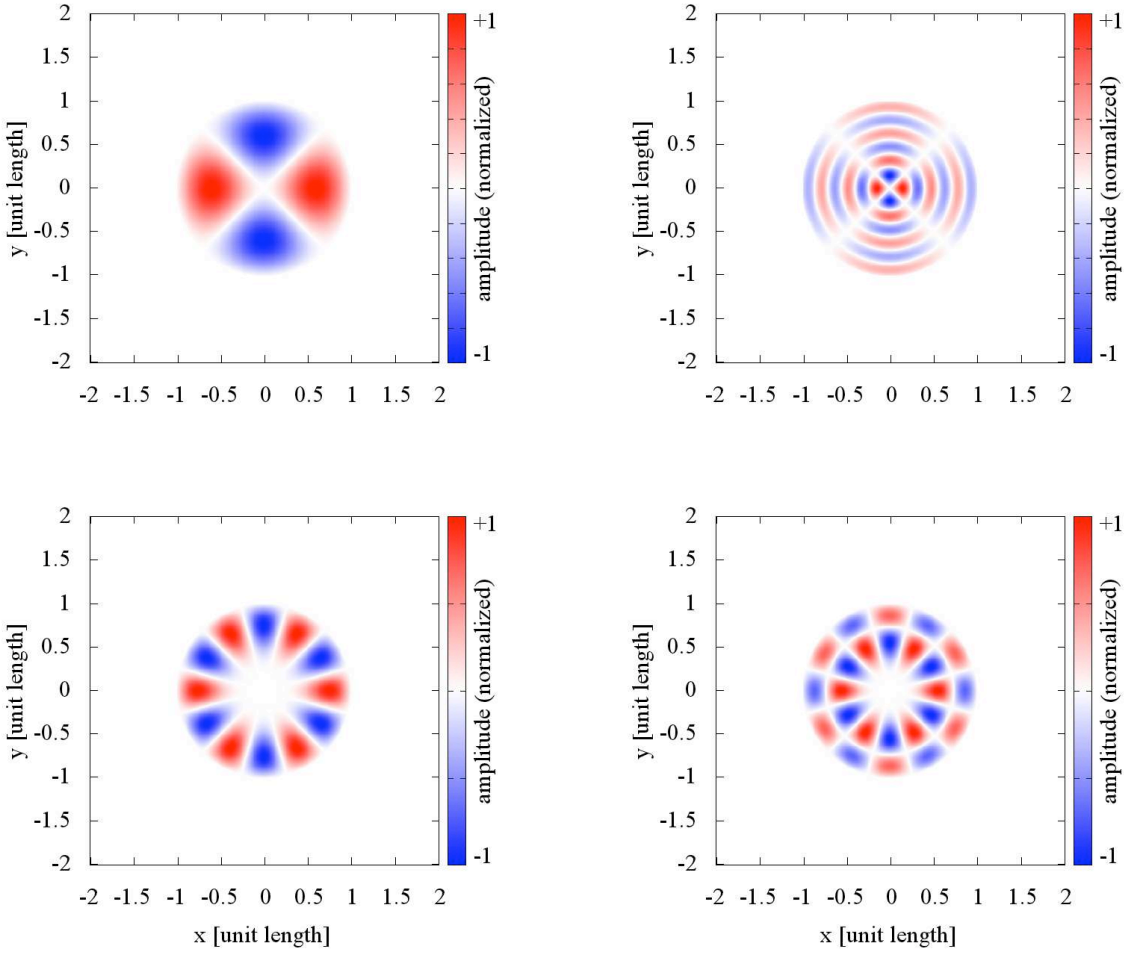

Figure 2.9: Analytic solution of eq. (2.54) for the case of a metallic environment or different cases of N and M: $N = 1$, $M = 2$ (top left), $N = 6$, $M = 2$ (top right), $N = 1$, $M = 6$ (bottom left), $N = 2$, $M = 6$ (bottom right). The radius of the disk is 1.

whose solutions are the M$^{\text{th}}$ order *Bessel* function of first kind $J_M(\rho)$ inside the cylinder ($\rho \leqslant R$) and a (complex) superposition of the M$^{\text{th}}$ order *Bessel* functions of first kind $J_M(\rho)$ and second kind $Y_M(\rho)$, the M$^{\text{th}}$ order *Hankel*-function $H_M(\rho) = J_M(\rho) + iY_M(\rho)$, outside the cylinder ($\rho > R$). The radial mode order is coded in the effective radius ρ, where the wave vector enters as $k_N = \frac{n\omega_N}{c_0}$. The order N now depends on which solution one chooses from the equation, resulting from the continuity at the interface between the disk and the environment. Figure 2.9 shows the analytical field distributions for a cylinder with metallic environment ($(\mathbf{E})_y \equiv 0$ outside) and different combinations of M, N. As can be seen, the field is mostly concentrated in the rim of the cylinder (except for large radial orders and / or small azimuthal mode orders). That motivates the assumption that the post, on which the microdisk is standing freely, has (almost) no influence on the field distribution.
Figure 2.10 shows the absolute value of the field (in the disk plane, normalized to 1) for the fundamental modes (radial mode order $N = 1$) in a sub-μ microdisk resonator in a metallic

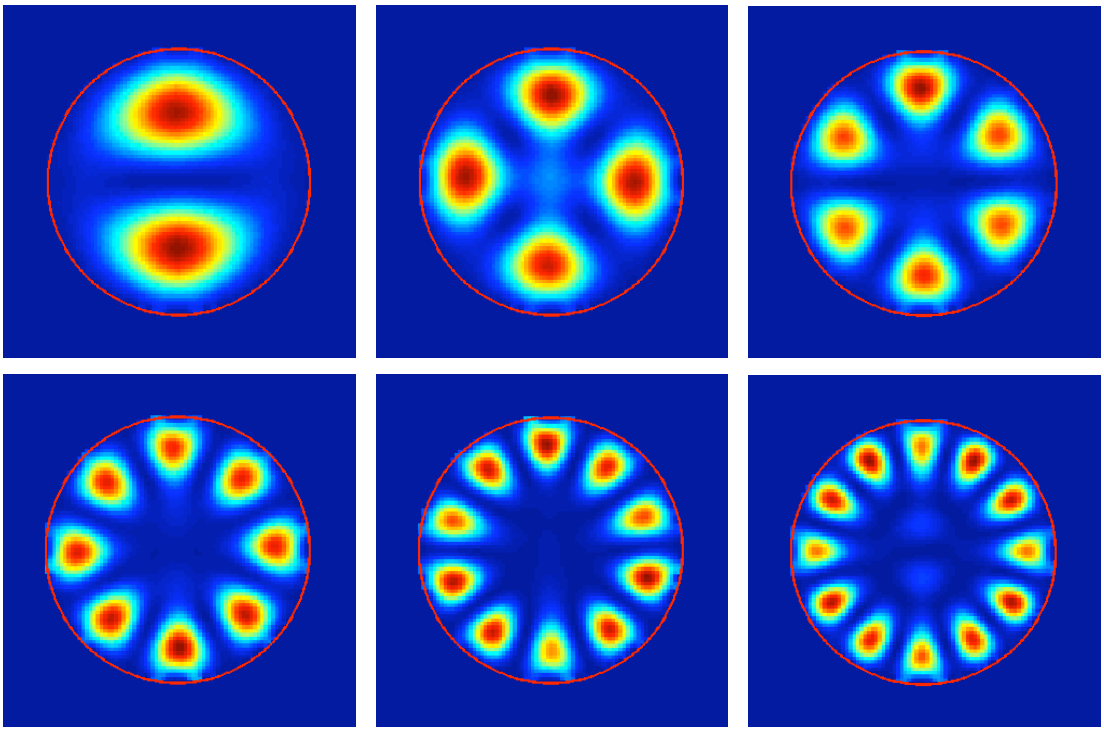

Figure 2.10: Numerical solution, calculated with a two-dimensional FDTD code (implemented in MATLAB [51]) on a cartesian grid (cell size $\Delta x = \Delta y = 10$ nm), for a dielectric microdisk (dielectric permittivity $\epsilon = 11.56$ and radius $R = 361$ nm) in a metallic environment (the red line denotes the interface between dielectric disk and the PEC) for the first fundamental (radial mode order $N = 1$) modes: $1 \leqslant M \leqslant 3$ in the top line and $4 \leqslant M \leqslant 6$ in the bottom line (from left to right). The intensity is color-coded (red: 1, black: 0).

environment (the red circle denotes the boundary of the microdisk), calculated with the two-dimensional FDTD code implemented in MATLAB [51]. A cartesian grid with a spatial cell size of $\Delta x = \Delta y = 10$ nm is used. The permittivity and the radius of the disk are chosen to be $\epsilon = 11.56$ and $R = 361$ nm, respectively. In the top line, the first 3 modes (azimuthal mode orders $1 \leqslant M \leqslant 3$) are depicted. Note, that the absolute value is plotted here, therefore the double amount of maxima are visible, compared to the azimuthal mode order. The subsequent azimuthal mode orders $4 \leqslant M \leqslant 6$ are shown in the bottom line.

2.4.2 The Photonic Crystal Cavity

In a Photonic Crystal Cavity, PhCC, one makes use of the increased density of states around the PBG. Evanescent modes, so harmonic modes with a purely complex wave vector, are allowed to penetrate the PBG region. In a defect, like a missing hole in a periodic arrangement of air holes in a two-dimensional dielectric slab, this evanescent mode can manifest itself and become a highly confined mode, a cavity mode. Cavity modes in general reflect the symmetry of the PhC, for example a rotational symmetry of the lattice leads to degenerate modes, say these modes have the same frequencies, but are not necessarily orthogonal. This degeneracy can be lifted by destroying a symmetry property, for example the air holes are not perfectly circular shaped, but more of elliptical shape [2]. Then, the lifted degeneracy manifests itself

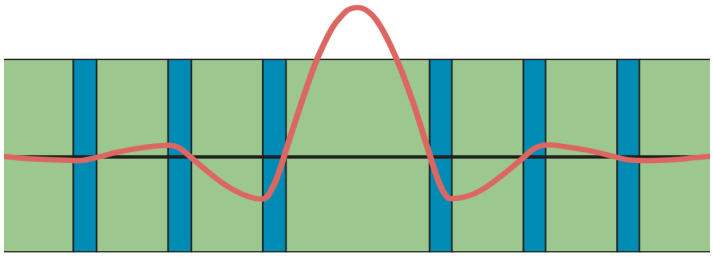

Figure 2.11: $\lambda/2$-defect in the center of a distributed Bragg reflector (material 1 (green): low ref. index, material 2 (blue): high ref. index). The layer thickness of the DBR is determined via $d_i = \lambda/4n_i$, $i = 1, 2$ and the electric field (red) is concentrated in the defect area. After [62].

in polarization properties of the harmonic modes. The degenerate spectral line splits into two polarization-dependent modes.
The most simple model of a PhCC is a cavity in a one-dimensional DBR (Fig. 2.11). Here, the periodicity is broken with a $\lambda/2$ layer (center) in the low dielectric medium instead of the $\lambda/4$ thickness (λ is the wavelength in the material), acting as a defect which is able to confine light (as described in Sec. 2.3).
As a two-dimensional example for a PhCC, the H-, L and hybrid-type cavities are mentioned. The basis for all kinds can be for example a square, hexagonal or honey-comb lattice of circular air holes in a dielectric slab, extended infinitively perpendicular to the whole plane. But one can also imagine a lattice of square holes in a certain lattice. As long as the periodicity is provided, all kinds can be combined. In these systems, confinement is based on fulfilling the Bragg condition of reflection, like in the DBR case, but here in all directions. Figure 2.12 (top) shows the band structures for two different kinds of lattices [62]. In a two-dimensional simulation case, there is always a TE and a TM solution. Here, the square lattice of dielectric rods in air show a TM gap, while the air holes in a dielectric slab show a TE gap [62]. Also, simultaneous occurrence (meaning in the same frequency range) of both gaps can be realized, too, when using a hexagonal lattice of air holes in a dielectric slab.

In reality, one always deals with a three-dimensional device. The confinement in the third dimension is provided by total internal reflection (TIR). The thickness t of the device is normally chosen to be in the range of $t \approx \frac{\lambda}{2}$, λ is the vacuum wavelength, divided by the refractive index of the desired material, to have only the lowest optical mode in this direction occupied (single mode operation, see Sec. 2.4.1). Thus, all components mix and one cannot uncouple the different polarization. Hence, only TE- and TM-like band gaps occur, see Fig. 2.12, bottom. Since hexagonal lattices provide larger band gaps, they are often preferred and for the rest of this thesis, the hexagonal lattice is taken into account for PhCs. A defect is now introduced by leaving away an air hole in a hole-array, or a rod in a rod-array. Typically, in the H-case, one leaves for example a single air hole , yielding a $H1$-cavity or every next neighbors of this single defect to get a $H2$-cavity. The light is confined in the defect region, where it can be concentrated in the material part, referring to modes located energetically near the material band (band below gap) or in the air part, referring to modes located energetically close to the air band (band above gap) [62]. Its evanescent parts then leak out into the non-cavity region, where the Bragg condition of reflection is fulfilled, hence they are reflected back. Exemplarily, mode patterns for material modes for a $H1$-, $H2$-cavity and a $L3$-cavity, meaning leaving away a line of three air holes in a hexagonal lattice, in the x-y-plane are shown in Fig. 2.13

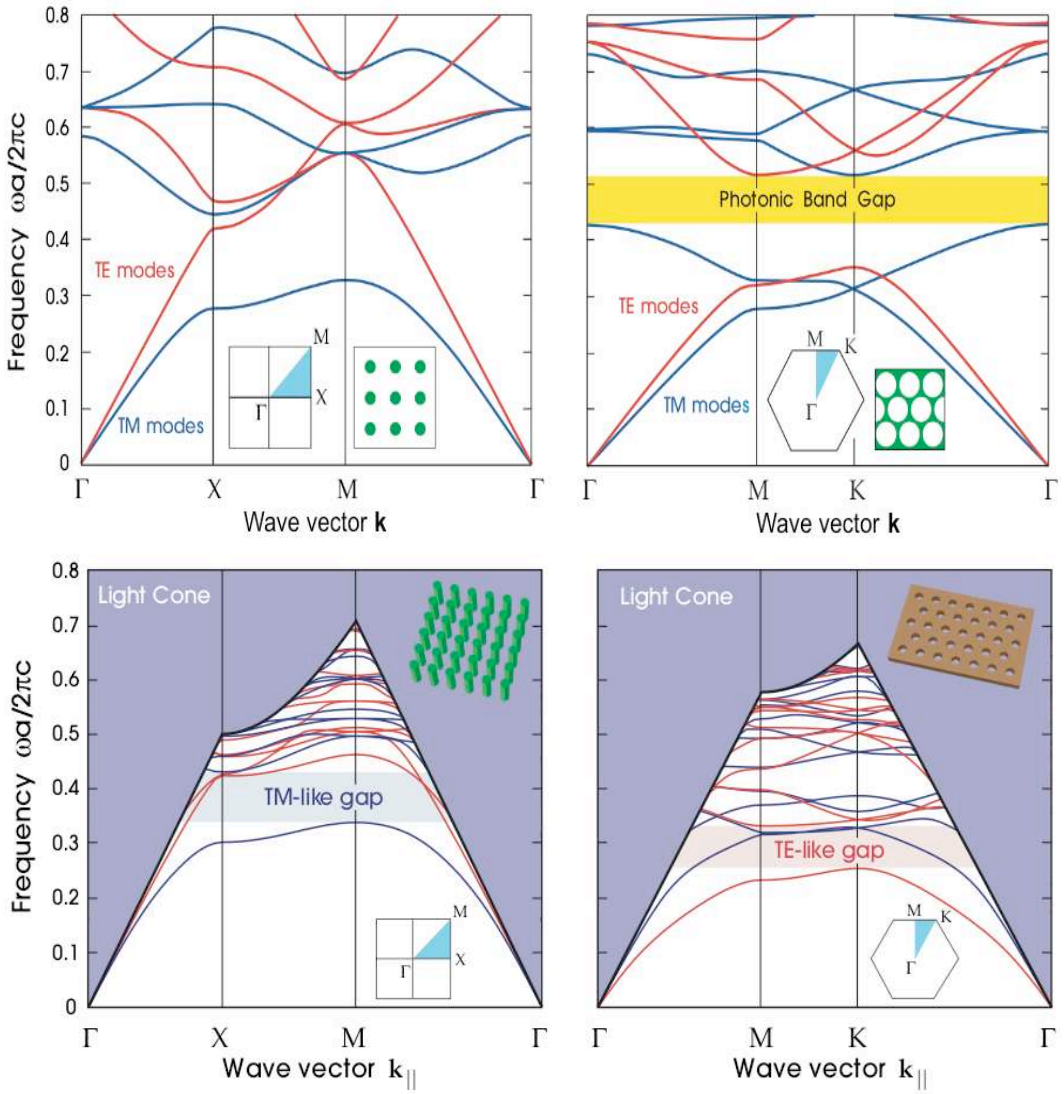

Figure 2.12: Band structures for a two- and three-dimensional PhCC with a square lattice of dielectric rods in air (left) and with a hexagonal lattice of air hole in a dielectric slab (right). The insets show the assumed real-space geometry as well as the irreducible Brillioun zone (blue) in the reciprocal lattice. Points of high symmetry are marked. In the band structure (frequencies, normalized to the lattice constant, over the wave vector). Top: No photonic band gap occurs in left geometry, while for the right, a full band gap (TE- and TM-band at the same frequencies). Bottom: For the left geometry, a TM-like band gap occurs, while the right geometry provides a TE-like band gap. After [62].

(from left to right). The black thin lines represent the air hole lattice in the dielectric slab and color-coded one finds the amplitude of the y-component of the electric field. The largest contributions are found to be inside the defect, hence in the material. The used parameters for the simulations can be found in [1–3]. The $L3$-cavity will gain more interest in the later Chaps. 5 and 6, since tuning mechanisms are present to enhance the life time of the mode. Strong cavity-cavity interaction (strong interaction means, the line splitting exceeds the line width) between resonant and detuned $L3$-cavities is investigated in Chap. 6.

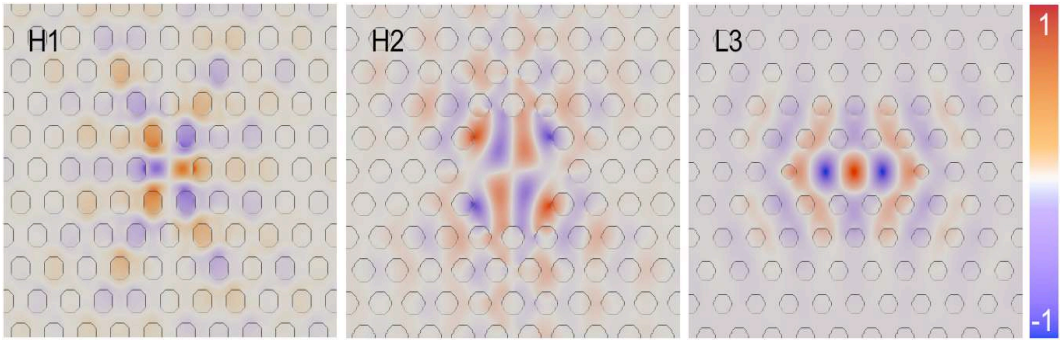

Figure 2.13: Mode patterns for the $H1$-, $H2$- and $L3$-type cavity (from left to right). In each plot, the plane shows the x-y-plane and color-coded the amplitude of the electric field (y-component). Used Parameters are taken from [1–3], including modifications of the first outer air holes for the $L3$-type defect (see Sec. 5.2 for details).

2.5 The Quantum Dot Model

A QD can be considered as a two-level system (TLS) like an atom with only two energetically allowed levels: a ground state and an excited state. The excited state normally is due to an exciton resonance. An exciton, in fact, is a bound electron-hole pair, which can be excited optically. The electron from the valence band is excited into the conduction band via the incident optical field and a hole is left where the electron was before. Now, since the two particles have opposite charge (and momentum), the Coulomb interaction bounds them together. Like in an atom, a *Bohr*-radius a_{0_X} is defined by $a_{0_X} = \frac{4\pi\epsilon_0\epsilon_r\hbar^2}{\mu e^2}$, e is the elementary charge (defined positive). The excited state will be denoted with $|1\rangle$ while the ground state will be denoted by $|0\rangle$. The main reason for this notation is the possible usage of quantum dot exciton states for quantum information, where the logical *bits* 0 and 1 are mapped to the quantum-logical *qubits* $|0\rangle$ and $|1\rangle$ on the Bloch sphere [61] (the quantum-logical states $|0\rangle$ and $|1\rangle$ are referred as the poles of the sphere).
For the derivation of the equations of motions for the microscopic polarization and the conduction band density of the QD, the formalism of second quantization is used [66, 68]. Therefore, fermionic ladder operators (creation operator $a_\mu^\dagger$, annihilation operator a_μ) are defined. The subscript μ labels the bands. Since no dispersion of the bands or spin for the electrons is assumed, labels for the wave vector or spin are omitted. A coherence, or microscopic polarization, between the ground and excited state is then given by $a_{\mathrm{vb}}^\dagger a_{\mathrm{cb}}$, where an electron in the valence band is destroyed and and electron is created in the conduction band at the same time. The two bands are coupled via a dipole matrix element $\mathbf{d}_{\mu\mu'}$. Generally, for a n-level resonator with normalized wave functions Ψ_μ for the carriers, $\mathbf{d}_{\mu\mu'}$ is defined as

$$\mathbf{d}_{\mu\mu'} = -e \int_{\mathbb{R}^3} d\mathbf{r} \Psi_\mu^*(\mathbf{r})\, \mathbf{r}\, \Psi_{\mu'}(\mathbf{r})\,. \tag{2.55}$$

where $\mathbf{r}$ is the spatial coordinate and * means complex conjugation.
To calculate the time dynamics of such a quantum mechanical system, one needs the *Hamilton* operator $\hat{H}_{\mathrm{tot}}$, which lets the system evolve in time according to the *Heisenberg* equation of

motion of a time-dependent operator $\hat{A}$

$$\frac{d}{dt}A = -\frac{1}{i\hbar}[\hat{H}_{\text{tot}}, \hat{A}]_- + \partial_t \hat{A}\,, \tag{2.56}$$

where $[A,B]_- = AB - BA$ is the commutator. The last term vanishes for not explicitly time-depending operators (which is the case for the coherence and density). For the QD system, the Hamilton operator with only the free part and light-matter interaction is given by

$$\begin{aligned}\hat{H}_{\text{tot}} = &\quad \hat{H}_{\text{free}} \quad + \quad \hat{H}_{\text{light-matter}} \\ &= \overbrace{\hbar \sum_{\mu} \omega_\mu a_\mu^\dagger a_\mu} + \overbrace{\frac{i}{\hbar}\mathbf{E}(t) \cdot \sum_{\mu\mu'} \mathbf{d}_{\mu\mu'} a_\mu^\dagger a_{\mu'}}\,.\end{aligned} \tag{2.57}$$

$\mathbf{E}(t)$ is the exciting light field. For the coherence p and conduction band density n one gets with eq. (2.57)

$$\dot{p} = i\omega_{\text{gap}} p + i\Omega_R(1-2n) - \gamma_p p \tag{2.58}$$

$$\dot{n} = -2\Im\left(\Omega_R p^*\right) - \gamma_n n \qquad \text{with} \tag{2.59}$$

$$\text{with } \Theta(t) = \int_{-\infty}^{t} dt' \Omega_R(t') \text{ and } \Omega_R(t') = \frac{\mathbf{d}_{\mu\mu'} \cdot \overline{\mathbf{E}}(t')}{\hbar}\,. \tag{2.60}$$

The quantity $\Theta(t')$ is the pulse area at a time t', Ω_R is the *Rabi* frequency, $\overline{\mathbf{E}}$ is the envelope function of the exciting electric field (defined via $\mathbf{E} = \overline{\mathbf{E}} \cdot \cos(\omega t + \phi)$, ϕ is the phase), ω_{gap} is the gap frequency of the QD material, γ_p and γ_n are the phenomenologically introduced dephasing rates for the coherence p and the conduction band density n, respectively. In the calculations, $\gamma_n = 2\gamma_p$ (coherent limit).

2.5.1 Quantum Dots in the FDTD: Back-Coupling to the Electromagnetic Field and Limits

A QD provides a microscopic polarization after optical or electronic excitation. This microscopic polarization couples back to the surrounding light field via the macroscopic polarization, which enters Maxwell's equation (2.11) via an additional term in the dielectric displacement field $\mathbf{D}(\mathbf{r},t) = \epsilon_0\epsilon_r(\mathbf{r})\mathbf{E}(\mathbf{r},t) + \mathbf{P}(\mathbf{r},t)$:

$$\nabla \times \mathbf{H}(\mathbf{r},t) = \mu_0\mu_r(\mathbf{r})\mathbf{j}(\mathbf{r},t) + \frac{\mu_r(\mathbf{r})}{c_0^2}\dot{\mathbf{D}}(\mathbf{r},t) \tag{2.61}$$

$$= \mu_0\mu_r(\mathbf{r})\mathbf{j}(\mathbf{r},t) + \frac{\mu_r(\mathbf{r})}{c_0^2}(\epsilon_r(\mathbf{r})\dot{\mathbf{E}}(\mathbf{r},t) + \dot{\mathbf{P}}(\mathbf{r},t)) \tag{2.62}$$

where the macroscopic polarization $\mathbf{P}(\mathbf{r},t)$ is calculated by the sum of all microscopic polarizations, say coherences, of the QDs, weighted with the corresponding dipole matrix element:

$$\mathbf{P}(\mathbf{r},t) = \sum_{\mu\mu'} \mathbf{d}_{\mu\mu'} \langle a_\mu^\dagger a_{\mu'} \rangle \Psi_\mu^*(\mathbf{r}) \Psi_{\mu'}(\mathbf{r})\,. \tag{2.63}$$

This macroscopic polarization feeds the light field which itself again excites the QD.

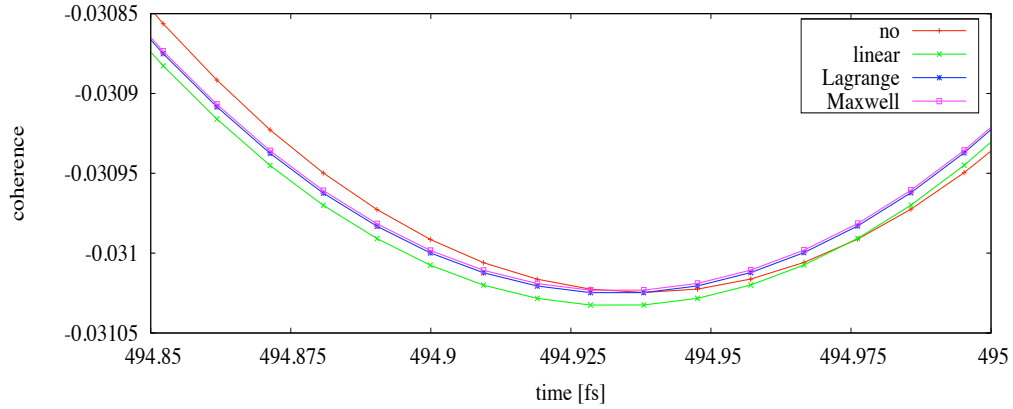

Figure 2.14: Comparison of different extrapolation schemes for calculating future values for the electric field for the 4th Runge-Kutta integrator (Sec. A.1, [84]). Coherence of the QD vs. time on a very short time window in fs. Red: no extrapolation, $E^{n+\frac{1}{2}} = E^{n+1}$. Green: linear extrapolation. Blue: Lagrange extrapolation of 3rd order. Magenta: Extrapolation via FDTD update with Maxwell's equations. The Lagrange and Maxwell extrapolation scheme agree nicely, while no and only linear extrapolation show comparably large deviations.

Since the QD is embedded in the spatial and temporal FDTD grid, the stepping for the update equation needs to be matched. The spatial stepping is done straight forward. For the temporal stepping an extrapolation method needs to be used. Exemplarily, for a one-dimensional case, the modified update equation for $\mathbf{E}(\mathbf{r},t)|_i$ at Yee-cell i and time $(n+\frac{1}{2})\Delta t$, taking the macroscopic polarization $\mathbf{P}(\mathbf{r},t)|_i$ from the QD into account, is

$$E_i^{n+1} = E_i^n - \frac{\Delta t}{\epsilon_0 \epsilon_i \Delta x}\left(H_{i+\frac{1}{2}}^{n+\frac{1}{2}} - H_{i-\frac{1}{2}}^{n+\frac{1}{2}}\right) - \left(P_i^{n+1} - P_i^n\right) . \tag{2.64}$$

As can be seen from eq. (2.64), the values for the polarization at $t = (n+1)\Delta t$ are necessary to update the electric field, because both quantities are defined on the same temporal grid. Using a standard 4th order Runge-Kutta integrator (see Sec. A.1) [84] to integrate the equations of motion for the QD, the electric field at times $t = (n+\frac{1}{2})\Delta t$ and $t = (n+1)\Delta t$ are needed, but not provided by the FDTD method. The missing values can be obtained by standard extrapolation methods, like linear extrapolation or nth polynomial Lagrange extrapolation, shortly depicted in Sec. A.2 [84]. In the used code, a field update utilizing the FDTD update scheme is performed to calculate the electric field at the unknown time steps. A comparison of the performance of different extrapolation schemes is shown in Fig. 2.14. The plot shows the coherence of the QD on a very short time scale only covering some time steps, but nicely shows the differences between the schemes. No extrapolation (red), meaning a constant electric field is used, and linear extrapolation (green) show comparably strong deviations from the more accurately working 3rd order Lagrange extrapolation scheme (blue). The extrapolation scheme taken from the FDTD update (magenta) is consistent with the Lagrange scheme.
As described in the Sec. 2.5.2, the coherence and conduction band density have to be damped to describe a physically senseful picture. In the presence of the fields, occupying the spatial FDTD grid, the QD starts to decay radiatively once excited. The decay constant can be calculated analytically [85], assuming an infinitely thin QW structure and linear excitation,

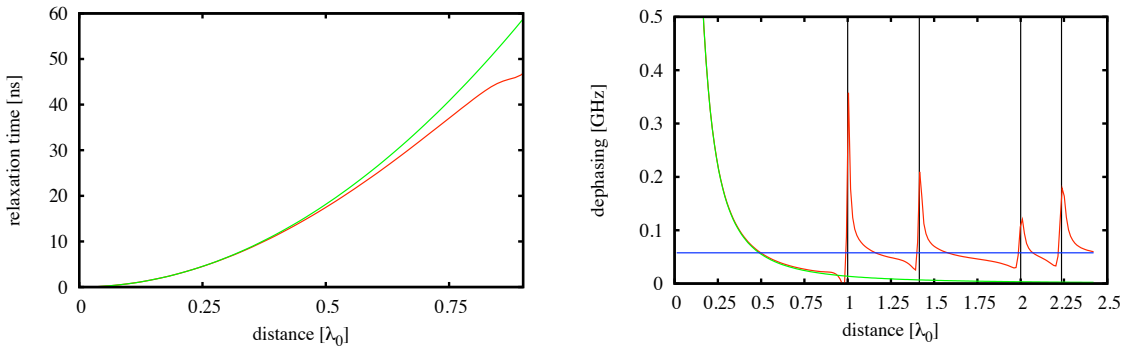

Figure 2.15: Left: Relaxation time in ns vs. QD distance in units of the resonant wavelength λ_0. Green: QW limit, calculated via (2.65). Red: numerical data. Clear deviations from the QW-limit can be seen with the bare eye to emerge at QD distances larger than $0.3\lambda_0$. Right: Radiative dephasing in GHz of the QD array vs. QD distance in λ_0 (red). Clear resonance features are visible due to the radiative coupling between the QDs. The non-integer resonances emerge from coupling in diagonal directions ($\sqrt{3}$, $\sqrt{5}$...). Green: QW limit [85]. Blue: analytical value for an isolated QD [86].

yielding

$$\Gamma_{\text{rad}}^{QW} = \frac{\omega \mathbf{d}_{\text{VC}}^2}{2\epsilon_0 c_0 \hbar a_{0_x}^2}\,, \tag{2.65}$$

where, ω is the angular frequency. This result is valid for a dense grid of QDs in two dimensions, simulating a quantum well like structure. If a delta-like QD is assumed, the radiative decay constant can be derived analytically [86]. There, Maxwell equations for the full electric field are solved in the reciprocal space with a Greens tensor approach and using the *Lippmann-Schwinger* equation to determine the frequency-dependent electric field in real space. Calculating the averaged electric field at the QD position and inserting it into the macroscopic polarization with a renormalized susceptibility (renormalized to the exciting electric field at the QD position), the radiative decay constant of the quantum dot yields

$$\Gamma_{\text{rad}}^{QD} = \frac{2\omega^3 \mathbf{d}_{\text{VC}}^2}{3c_0^3}\,. \tag{2.66}$$

Figure 2.15 depicts the numerical performance of a QD array in the three-dimensional FDTD grid, depending on the distance between the QDs. In x-direction, the computational domain is set to 800 nm with CMPL boundary (10 cells). Periodic boundary condition are applied in y- and z-direction and the edge length of the computational domain was gradually increased in the same manner (horizontal axis, in units of the (vacuum) emission wave length λ_0 of the quantum dot) with the QD placed in the center to get an infinitively extended square lattice of QDs. On the left side, the relaxation time of the QD array in ns is depicted over the resonant wavelength λ_0. Green shows the QW limit, see eq. (2.65), while red shows the numerical data. One can clearly see the deviation from the QW limit, starting above $0.3\lambda_0$. On the right side, the dephasing in GHz is plotted vs. the distance in λ_0. The blue line shows the analytical value for an isolated QD, in green the QW limit is shown and red shows the numerical data, extracted from the QD. At all integer distances, clear dips and resonant features occur. The

radiative coupling (constructive interference of the emitted spherical waves) between the QDs suppress the emission, hence the dephasing drops. The resonant features emerging at non-integer distances arise from the radiative coupling between QDs which are not next-neighbored [85].

2.5.2 Nonlinearities in Quantum Dots: Rabi Oscillations

Eqs. (2.58)-(2.59) are also called the Optical Bloch Equations. The Bloch equations are often discussed in a somehow more intuitive and graphical way: as a dynamic three-dimensional vector $\mathbf{s}$ in the Bloch sphere. As components of $\mathbf{s}$, the inversion of the QD $-w = 1 - 2n$ and absorptive part u (dispersive part v) of the coherence $p = u - iv$ appear:

$$\mathbf{s} = \begin{pmatrix} u \\ v \\ w \end{pmatrix} = \begin{pmatrix} u \\ v \\ 2n-1 \end{pmatrix} . \tag{2.67}$$

As can be seen, $|\mathbf{s}| = 1$ for all possible u, v , w. So the possible orbit for the Bloch vector is a unit sphere, on which it rotates with angular velocity ω around the w-axis (can be eliminated with the rotating wave approximation, RWA).
Under certain assumptions, the coupled eqs. (2.58) and (2.59) can be solved analytically. First assumption is, that one can write eqs. (2.58) and (2.59) in RWA, eliminating the fast oscillations of the exciting laser field and the coherence and just leaves the slowly varying envelopes (denoted with a bar). This yields a new set of differential equations:

$$\dot{\overline{p}} = i\overline{\Omega}_R(1-2n) \tag{2.68}$$

$$\dot{(1-2n)} = -2\Im\left(\overline{\Omega}_R p^*\right) . \tag{2.69}$$

The Rabi frequency $\overline{\Omega}_R$ is defined as Ω_R in Sec. 2.5 (since there is used already the envelope of the field). As a second condition for solvability, the phenomenologically introduced dephasing rates are set to zero and $\Omega_R \in \mathbb{R}$ (for resonant excitation). This set of equations is now solvable analytically with

$$\overline{p} = \frac{i}{2}\sin\frac{\Theta(t)}{2} , \quad 1-2n = \cos\frac{\Theta(t)}{2} \tag{2.70}$$

resulting in

$$n = \sin^2\frac{\Theta(t)}{2} . \tag{2.71}$$

If the pulse area $\Theta(t \to \infty) = 2\,m\,\pi$, the system performs m full flops of the upper density, means inverting the QD and destroying occupancy again m times. In the picture of the Bloch sphere this means, that the Bloch vector $\mathbf{s}$ rotates m times on the edge of the sphere and returns to his originating position where it started.

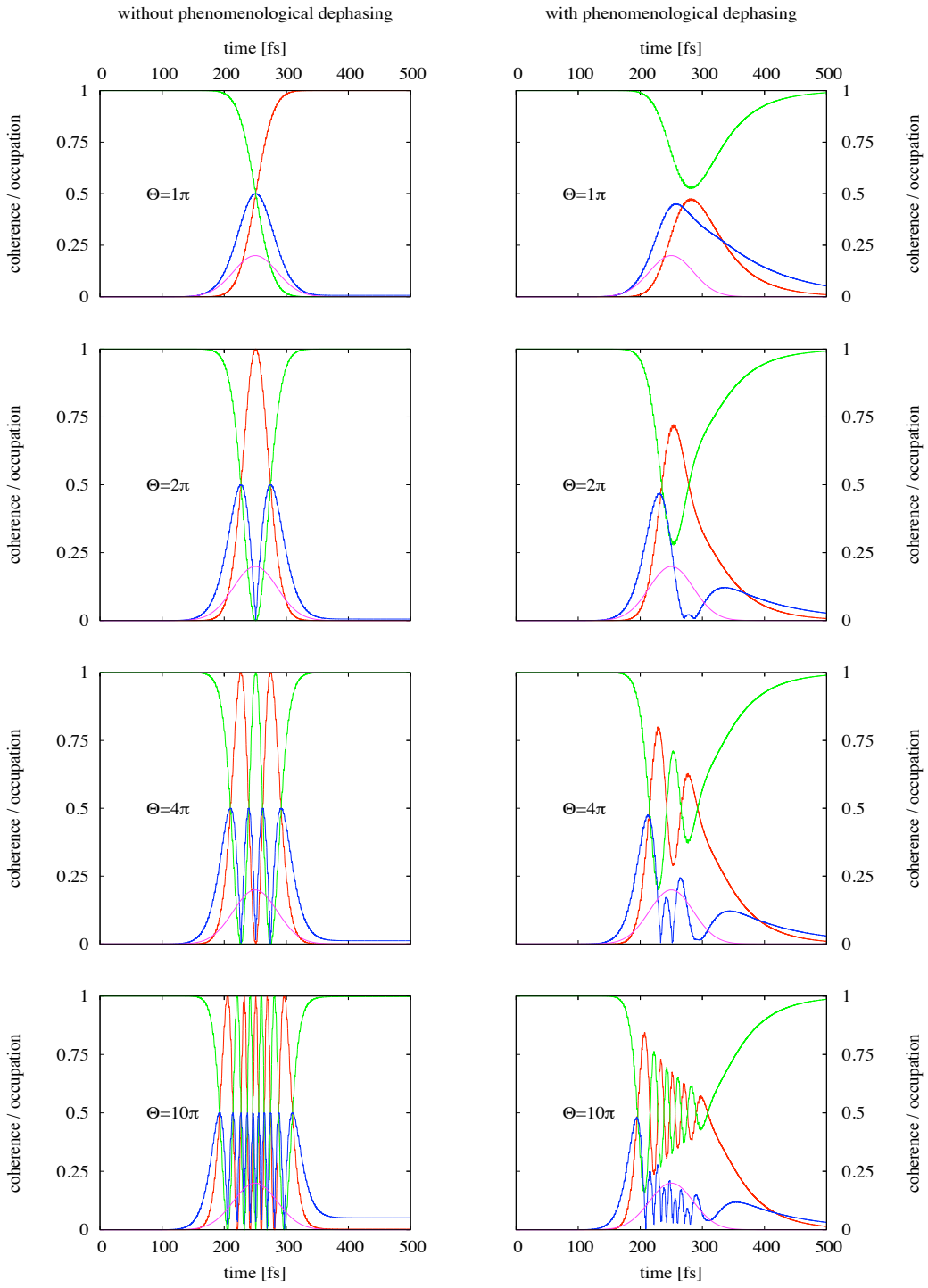

Figure 2.16: Rabi Oscillations in a TLS, calculated with the FDTD method and self-consistent backcoupling. From top to bottom: densities of conduction (red) band, valence band (green), coherence between conduction and valence band (blue) and the exciting pulse (magenta). Parameters for the TLS are: dipole matrix element $d_{\mathrm{cv}} = 3$ e$\mathring{A}$, gap energy $\varepsilon_{\mathrm{gap}} = 1.5$ eV, phenomenological dephasing $\gamma = 10$ THz (right). Radius of Gaussian wave function for the carriers $r = 30$ nm. Parameters for the exciting pulse are: center time $t_0 = 250$ fs, pulse width $\tau = 50$ fs, energy $\varepsilon = 1.5$ eV. The slight oscillations, covering the whole dynamics of p and n, are a no-RWA effect.

Introducing a phenomenological dephasing rate γ affects the Rabi oscillations. The flops of the conduction band density is not complete and after the exciting light pulse vanishes, the n stays at a finite value. In the Bloch sphere picture, $\mathbf{s}$ would remain somewhere on the Bloch sphere and not return to his starting pole. Dephasing always occurs in such systems, because the QDs are never isolated, but coupled to e.g. phonons of the substrate. As discussed in the last Section 2.5.1, a QD will decay radiatively in the FDTD without a phenomenologically introduced dephasing. Hence, a physical picture is obtained. Figure 2.16 depicts the dynamics of eqs. (2.58) and (2.59), calculated in a three-dimensional simulation. Red (green) show the CB density (VB density), blue the coherence between VB and CB and the envelope of the exciting light field is shown in magenta to show the temporal presence of the field. The left row is calculated without a phenomenological damping for the QD, while the right row has a damping rate of $\gamma = 10$ THz, which is chosen to be quite large to show the effect on a short time scale. The inset denotes the pulse area, accordingly, the system performs the expected number of density flops of the QD in the undamped case. In the damped case, the density flopping is suppressed.

2.6 Coupling of Oscillators

Considering a system of two oscillators in the states $|\Psi_1\rangle$ and $|\Psi_2\rangle$, coupled with the coupling constant J and eigenenergies ε_1 and ε_2, the result is a beating between those two oscillators when the eigenfrequencies are equal. The problem can be formulated as

$$\begin{pmatrix} \varepsilon_1 & J \\ J & \varepsilon_2 \end{pmatrix} \begin{pmatrix} \Psi_1 \\ \Psi_2 \end{pmatrix} = \begin{pmatrix} \varepsilon + J & 0 \\ 0 & \varepsilon - J \end{pmatrix} \begin{pmatrix} \Psi_+ \\ \Psi_- \end{pmatrix} \tag{2.72}$$

for $\varepsilon_1 = \varepsilon_2 = \varepsilon$. Diagonalizing the matrix, thus uncoupling the oscillations into two orthogonal normal oscillations Ψ_+ and Ψ_-, yields an energy splitting Δ, depending on the coupling strength, $\Delta = 2\ J$.
In quantum optics, the *Jaynes-Cummings* ladder (JC ladder) describes the interaction between a single mode field with frequency in a cavity ω_0 with an embedded TLS with frequency ω_{21} between upper ($|2\rangle$) and lower level ($|1\rangle$) [87]. The JC Hamilton operator reads

$$\hat{H}_{\mathrm{JC}} = \underbrace{\hbar\omega_0 c^\dagger c}_{\text{field}} + \underbrace{\frac{\hbar\omega_{21}}{2}\sigma_z}_{\text{TLS}} + \underbrace{\hbar(gc\sigma_+ + g^* c^\dagger \sigma_-)}_{\text{interaction}}, \tag{2.73}$$

where $c^\dagger$ (c) are the bosonic creation (annihilation) operators for the single mode field,σ_z is the occupancy difference of the two levels $|1\rangle$ and $|2\rangle$ and σ_+ (σ_-) are the creation (annihilation) operators of the TLS. The interaction constant is denoted by g. Neglecting the interaction part of eq. (2.73) and assuming that $\omega_0 = \omega_{21} = \omega$ and n photons in the system, the eigenenergies of the two possible configurations of the system are degenerate: the state with $n-1$ photons in the system and an excited TLS has the same energy as a system with $n$photons and a TLS in the ground state. Switching on the interaction part between, TLS and single mode field, this degeneracy is lifted, resulting in the new eigenenergies

$$\varepsilon_{\mathrm{n},\pm} = \left(n + \frac{1}{2}\right)\hbar\omega \pm \frac{1}{2}\hbar\Omega_n\,, \quad \Omega_n = 2\sqrt{n}g\,. \tag{2.74}$$

For $n \equiv 1$, this is called Vacuum Rabi Splitting (VRS). With the semi-classical FDTD approach, where the field is treated classically and a TLS is treated quantum-mechanically, the normal mode splitting, which equals the line splitting for the limit $n = 1$ in the quantum-optical picture, can be calculated, too (see Sec. 6.2).
A detuning Δ between the single mode frequency ω_0 and the TLS frequency ω_{21} enters eq. (2.74) in $\Omega_n = \sqrt{4ng^2 + \Delta^2}$. Now, two important cases are distinguished:
First, the weak coupling regime, or Stark regime. Here, $2\sqrt{n}|g| \ll |\Delta|$. That means, that even with a strong field, hence large number of photons, the coupling regime can still be weak. Rewriting and tailoring Ω_n yields

$$\Omega_n = |\Delta|\sqrt{\frac{4ng^2}{\Delta^2} + 1} \approx |\Delta|(1 + \frac{4ng^2}{\Delta^2}) \,, \tag{2.75}$$

one can calculate the new eigenenergies of the coupled system to be

$$\varepsilon_{\mathrm{n},\pm} = \left(n + \frac{1}{2}\right)\hbar\omega \pm \frac{1}{2}\hbar\omega_{21} + \frac{\hbar n g^2}{|\Delta|} \,, \tag{2.76}$$

which shows a red shift for both states, called the 2^{nd} order Stark effect, since eq. (2.75) is quadratic in the electric field.
Second, the strong coupling regime. Here, $2\sqrt{n}|g| \gg |\Delta|$ is fulfilled. Neglecting the detuning in eq. (2.74), the new eigenenergies in the coupled system read

$$\varepsilon_{\mathrm{n},\pm} = \left(n + \frac{1}{2}\right)\hbar\omega \pm \hbar\sqrt{n}|g| \,. \tag{2.77}$$

So the new eigenstates, the dressed states, are first non-degenerate due to the light -matter coupling, and second are split by $\Delta\varepsilon = 2\sqrt{n}|g|$, which means, that the coupling can be enhanced via the photon number n. This splitting is linear in the field, hence referred to the linear or dynamical Stark effect [88].
Above the strong coupling regime, there also exists a ultrastrong coupling regime. This regime is reached, when the splitting $\Delta\varepsilon \approx \hbar\omega$. In this regime, the RWA, often used in the weak and strong coupling regime, breaks down. Also, additional terms in the Hamiltonian have to be considered, which are proportional to $(a^\dagger + a)^2$, the creation and annihilation operators for the TLS, yielding a violation in energy conservation. Since this topic is not discussed in this thesis, the interested reader is referred to [89–91].
As an example of coupling between two photonic resonators, Fig. 2.17 shows coupled dielectric cavities, sandwiched between DBRs, the corresponding field patterns of the electric field (normalized to 1) and the spectral response (transmission spectrum) of the coupled systems [93] (calculated with the FDTD method [94], taken from [92]). At the top, as a reference, a single cavity surrounded by 15 layers of alternating lambda-quarter plates with different permittivities is shown. The left side shows the spectral response, the right side shows the spatiotemporal response in a short time window. The cavity length corresponds to a lambda-half plate for 1.5 eV ($\lambda_0 \approx 826$ nm). Deviations from the exact value of 1.5 eV originate from rounding errors of the layer thicknesses due to spatial discretization, since Yee-cells are filled completely with a permittivity. The incident wave travels from left to right (on the left side the reflections from the first DBR layers are clearly visible). The middle part of Fig. 2.17 shows two coupled cavities. The eigenstates of the coupled system can be regarded as in atomic physics, like a bonding and an anti-bonding state, where the bonding state has a

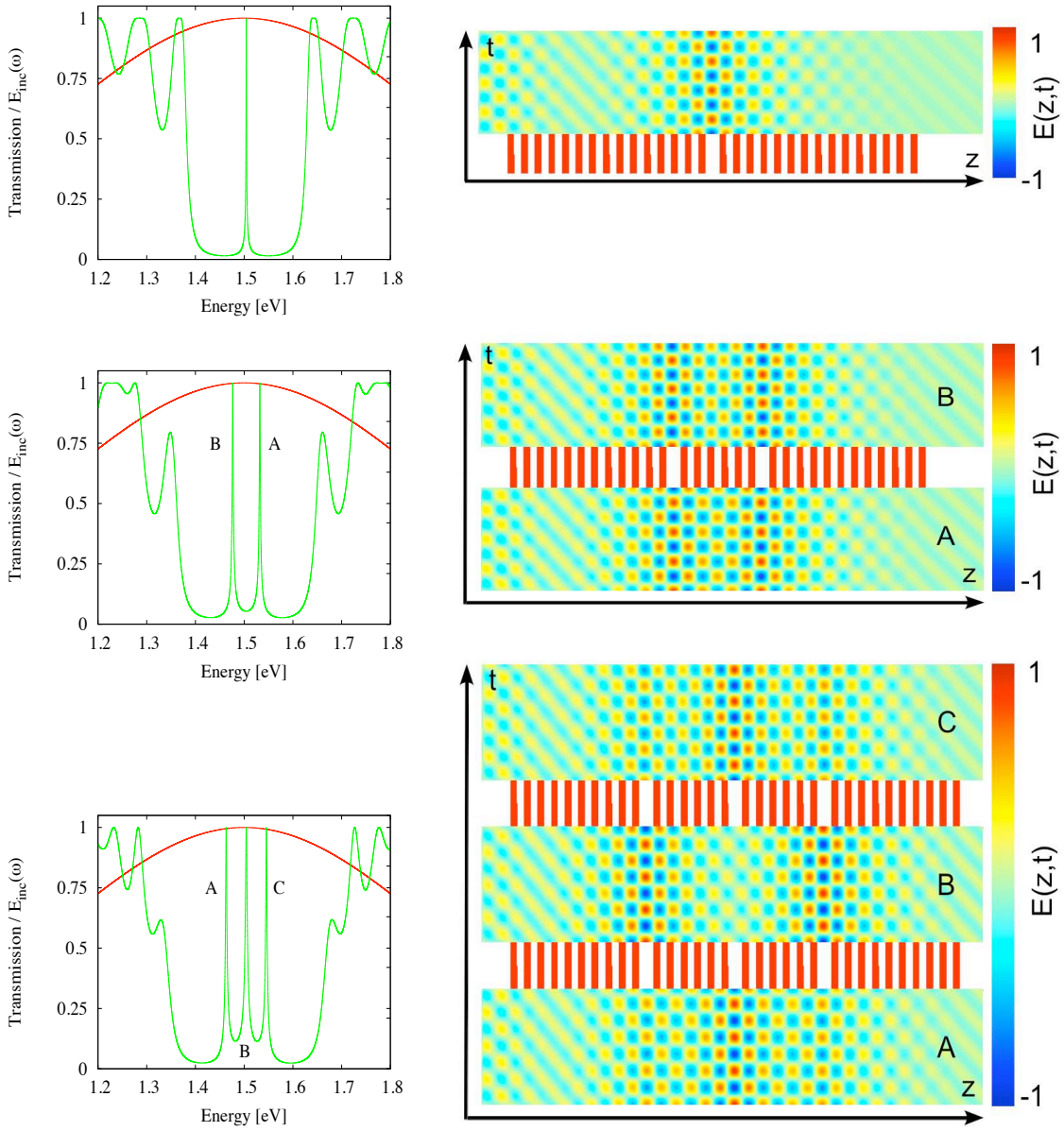

Figure 2.17: Coupling between two and three cavities. Left: Spectral response (transmission). Red shows the spectral width of the incident pulse. Right: Spatiotemporal response. The DBR structure is shown as alternating red/white bars (red: $\epsilon_r = 13$, white $\epsilon_r = 8.7$). Top: Reference spectrum from a single cavity (resonance at $\varepsilon = 1.5$ eV). Middle: 2 coupled (identical) cavities. The transmission spectrum shows a clear line splitting (strong cavity-cavity interaction). Bottom: 3 coupled (identical) cavities. Three distinct peaks appear in the transmission. The corresponding spatiotemporal responses are labeled with capital letters. From [92].

decreased energy due to the *binding energy*, while the anti-bonding state has an increased energy compared to the uncoupled state. This is reflected in the field patterns: the formation of anti-symmetric (bonding) and symmetric (anti-bonding) modes, see labels A and B. At the bottom side of Fig. 2.17 three coupled dielectric cavities with their corresponding spatiotem-

poral response are depicted. The spectral response exhibits a third resonance, corresponding to field pattern with zero amplitude in the central cavity (exactly in the center), while the other two resonances correspond to the bonding and anti-bonding field profiles.

2.7 The Liquid Crystal Model: Uniaxial Anisotropy

Optical anisotropy is a common tool in current research (resonance tuning, transformation optics, etc. [26, 27, 95–97]) and used already in a broad range of commercial applications (i.e. LC-displays [98, 99]). LCs exhibit different phases for different environmental parameters, like temperature, pressure or applied electric fields [26, 95] which can be applied. In the scope of this thesis, LCs with the following two phases are taken into account: an isotropic phase and an anisotropic phase. Phase transition between a liquid crystalline and an isotropic phase of a liquid crystal can be observed even with the naked eye. Figure 2.18 [100] shows the wavelength-dependent refractive indices (left) for a temperature of $T = 25.1$ °C. Open and closed circles (extraordinary and ordinary refractive index, respectively) are experimental data, the solid and dashed lines are results from different theories proposed in [100], which agree both very well. For large wavelengths, both curves go into saturation. Therefore, for the wavelength range used in Sec. 4.2.1, the same values can be used. In the middle of Fig. 2.18, the dependency of the refractive indices from the temperature are shown. Again, open and closed circles (extraordinary and ordinary refractive index, respectively) are experimental data for different wavelengths (triangle: 450 nm, circle: 550 nm, square: 650 nm), the solid line is a result from theory, proposed in [100]. Again, both curves agree very well. Both branches approach a saturation value for increasing wavelengths. The situation is summed up in the right part of Fig. 2.18 [101]. The diagram shows the temperature-dependency of the refractive indices for $\lambda = 4.45$ μm. Therefore, extrapolation of the curves from the diagram on the right from high wavelengths up the wavelength range of interest is satisfied. In the high temperature regime, the LC behaves optically isotropic (refractive index n). Below the clearing temperature T_C is the nematic phase. The optical properties of liquid crystals depend strongly on the confinement due to the anchoring conditions on surfaces and the form (geometry) of the surrounding. In this theoretical work, the liquid crystal is treated as a medium, where uniaxial birefringence can be induced by homogeneous electric fields. This model is somewhat inspired by solid media like $LiNbO_3$, but assumes a considerably higher electric response by means of the absolute value of the induced birefringence. This simple approach leads to a qualitative understanding of the optical phenomena, investigated in this thesis, although LC filled specimen can have a highly complex spatial dependence of the refractive index tensor, especially near walls in dielectric systems. Applying the electric field results in a splitting of the isotropic curve into two branches, the ordinary n_o and the extraordinary branch n_eo. As temperature decreases, the level of birefringence, say the difference between the ordinary and the extraordinary refractive index, increases until a saturation regime is reached. At this point, the maximal alignment of the LC molecules is reached.

Calculations performed within this thesis concerning LCs are using a uniaxial anisotropic dielectric medium without subpixel averaging routine and without magnetic properties. Hence, the dielectric permittivity is treated as a second rank tensor $\underline{\underline{\epsilon}}$ with diagonal elements, while magnetic permeability μ is still treated as a scalar equal to 1. The off-diagonal elements are responsible for the component mixture and have to be taken into account if one wants to use biaxial anisotropic dielectric materials. Liquid crystal properties like molecule shape,

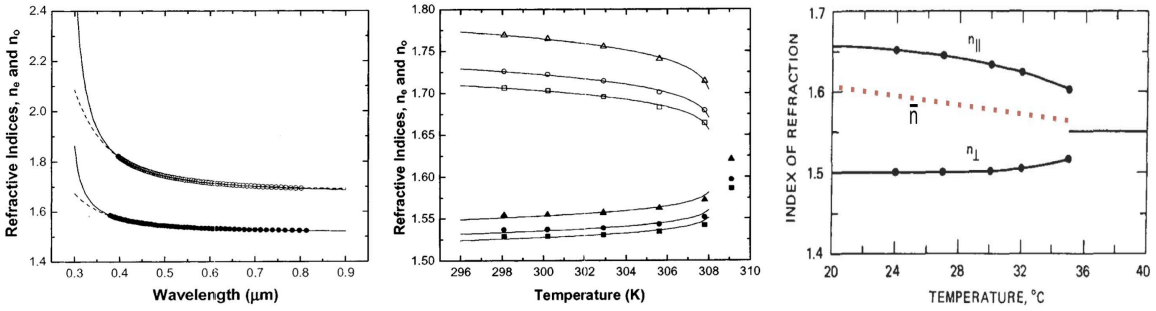

Figure 2.18: Characteristics of the liquid crystal 5CB [100, 101]. Left: wavelength dependency of the refractive indices (ordinary: close circles, extraordinary: open circles) at a constant temperature of $T = 25.1$ °C. Solid and dashed lines are from different theoretical models in [100]. Middle: temperature dependency of the refractive indices (ordinary: close symbols, extraordinary: open symbols) for different wavelengths (triangle: 450 nm, circle: 550 nm, square: 650 nm). The solid lines are fitting curve according to [100]. Right: Used temperature profile of the refractive indices [101]. For the isotropic case below the clearing temperature $T_C \approx 35$ °C, $\bar{n}$ is the averaged refractive index in the nematic phase without external field.

polarizability, special anchoring mechanisms of the molecules on a surface, loss mechanisms, local orientation features like twist, splay or bend and coherence lengths of the LC molecules are not taken into account.

2.8 Analysis Tools, Methods and Special Features

All the simulations shown in this thesis are performed with an in-house FDTD code, *Maexle*, implemented in the Junior Research group *Computational Nanophotonics*. *Maexle* numerically evaluates the three-dimensional Maxwell equations with the methods explained in Section 2.2. For data analysis and post-processing of data, quite a lot of tools are available directly within the program. Next to the standard discrete Fourier Transform (DFT), spectral analysis is also possible with the Filter Diagonalisation Method (FDM) *Harmonic Inversion* [102–105] or the Fast Fourier Transform (FFT) [106]. The first method relies on the fact, that one can transform the spectral analysis of a time-evolving dataset $f(t)$ of finite, exponentially decaying sum of oscillations into a matrix equation, which can be diagonalized to efficiently extract spectral properties from time data like resonant frequencies f, phases ϕ and decay rates γ:

$$f(t) = \sum_{k<\infty} A_k e^{-i(2\pi f_k - i\gamma_k)t + \phi_k} \,, \tag{2.78}$$

where A_k is the (complex) amplitude of the oscillation with index k. In general, the computational performance of the *Harmonic Inversion* is essentially better than of the DFT, but one has to be careful with large sets of oscillations. The great advantage of the FDM is, that the time signal does not need to decay to zero to get a fully converged spectrum. The complexity of the FDM, for N time points and J frequencies, i $\mathcal{O}(NJ + J^3)$. Compared, the DFT uses orthogonality relations of oscillations of different frequency. The complexity here is $\mathcal{O}(N^2)$. The latter method, the FFT, is a quite complicated algorithm and should be left for those who invented it and work with it every day. But it should be mentioned, that compared again with the DFT, the performance is greatly increased. The complexity here is $\mathcal{O}(N \log_2 N)$.

Additionally, a uniaxial anisotropic material is provided, which is used to model the LC material described in the Section 2.7. Uniaxial anisotropy is easy to implement, because the field components do not mix as they do when one wants to implement full anisotropy. This mixture of field components results in needed fields at positions, where they are not defined. Also, the subpixel averaging procedure described in Section 2.2.3 cannot be easily applied to both, the uniaxial and full anisotropic materials.

Chapter 3

Validation of *Maexle*

3.1 Validation of the FDTD Implementation

Validation of the implementation is a crucial point before using a program for research. In this case, the validation is done by comparing numerical results with results from four high-impact publications with the PhCC topic. For this purpose, three-dimensional calculations are performed, investigating the spectral and spatiospectral response of the two-dimensional $H1$-type cavity from [1] and [2], and $L3$-type from PhCC [3] and [4]. The planar photonic structures are located in the x-y-plane of the computational volume. Computational details about the simulation volume and time are: $V_{\text{sim}} = 19a \times 9.5\sqrt{3}a \times 2a$, $\Delta x = \Delta z = \frac{a}{16}$, $\Delta y = \frac{\sqrt{3}}{2}\Delta x$ and $t_{\text{sim}} = 5$ ps for all cases. These settings are sufficiently enough to gain reliable results from the simulation. Also, the extension of the first photonic band gap of the referenced structures are calculated with the *MPB* package [82]. For every investigated structure, the general form of the graphics are the same: the spectral properties are collected in the first figure, containing the band structure, spectral information from the publication and the spectrum calculated by *Maexle*. The second (third) figure shows the spatiospectral response of the structure in the TE-plane for the different resonances within the first band gap for x- and y-polarization.

3.1.1 $H1$-type PhCC

At first, the $H1$-type cavity from [1] is rebuild. A full investigation of the resonances located within the first band gap can be found in [1] in dependence of the outward shift s of the outer air holes away from the defect and modulating the radius Δr of the holes. The parametric set for the $H1$-cavity is a lattice constant of $a = 350$ nm, slab thickness $t = 0.71 \times a$, air hole radius $r = 0.31 \times a$ and a dielectric permittivity for a GaAs slab, $\epsilon_r = 11.56$. Modifications, as shown in the publication, are not applied. The top left of Fig. 3.1 shows the band structure, the right side shows the experimental data from [1]. As can be seen, the 1$^{\text{st}}$ band gap extends from roughly $f_{\text{min}} = 220$ THz to $f_{\text{min}} = 290$ THz and contains ten modes, depending on s and Δr. The focus for the validation purpose lies on the case for no modification, therefore $\Delta r = s = 0$. Calculations with *MPB* [82] confirm the spectral extension of the band gap (middle). The figures below depict the spectral response for the x-component (middle) and y-component (bottom) of the electric field, calculated with *Maexle*, in a broader range to also show that outside of the band gap no other resonances occur. The intensity in arbitrary units is plotted over the frequency (the upper horizontal axis shows in frequencies normalized to the lattice constant for better comparison with the upper figures, the lower axes shows the frequency in THz). The grey-shaded region (1$^{\text{st}}$ band gap) contains three resonances A, B and C. Resonance A is identified with the dipole-like mode, as shown in [1]. Resonances B and C are higher order modes, pushed into the band gap (grey-shaded region). Deviations in the spatial grid and possible differences in the ϵ-averaging process cause the differences to [1]. Nevertheless, the additionally visible modes are no artifacts, since depending on the radius-to-lattice constant more modes move into the photonic band gap (see next paragraph). Figure 3.2 shows the spatiospectral response of the defect in-plane ($\mathbf{r}_{\text{ip}}$) of the PhCC for the peaks A, B and C. The electric field pattern $E_{x/y}(\mathbf{r}_{\text{ip}}, \omega)$ (left), the absolute square $|E_{x/y}(\mathbf{r}_{\text{ip}}, \omega)|^2$ (middle) and the absolute square of the spatial Fourier transform $|E_{x/y}(\mathbf{k}_{\text{ip}}, \omega)|^2$ (right), where $\mathbf{k}_{\text{ip}}$ is the in-plane component of the wave vector. The grey lines in the field patterns show the boundaries of the air-to-material interfaces. All patterns are normalized to 1. The electric field concentrates in the defect region in different patterns, depending on symmetry and frequency.

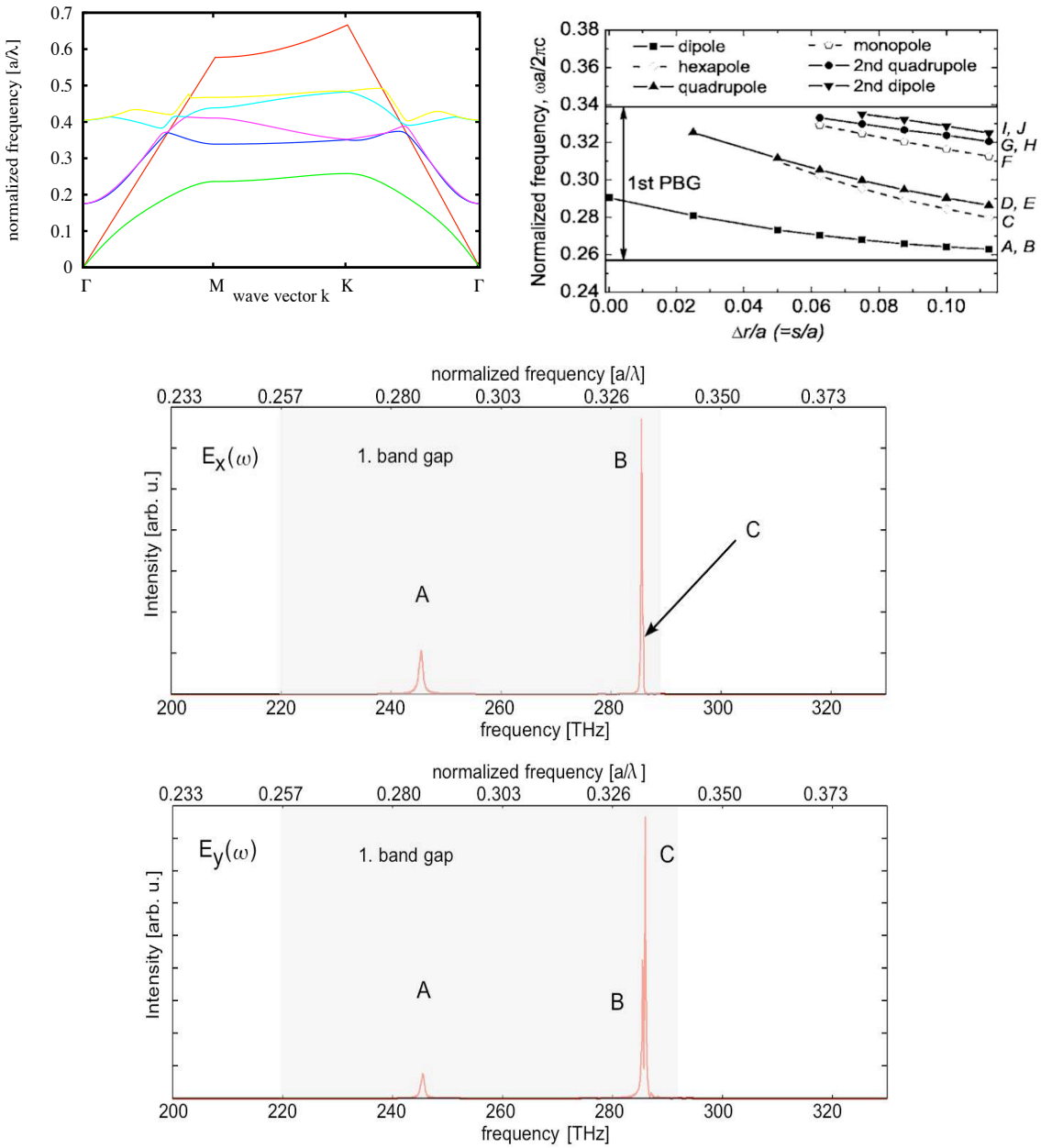

Figure 3.1: Spectral response for the $H1$ PhCC, after [1]. Top left: Band structure of the PhC, containing the first 5 photonic bands and the light cone (red line). Normalized frequencies are plotted vs. the wave vector. High-symmetry points of the reciprocal space are marked. Note the 1st band gap between the first two bands. Calculated with *MPB* [82]. Top right: data from [1]. The spectral region around the 1st band gap allows 10 different modes. The focus lies on the modes for no modification of the PhCC, thus $\Delta r = s = 0$. The normalized frequencies are plotted over the modification. Middle and bottom: Spectral response (middle: x-component, bottom: y-component), calculated with *Maexle*. Intensity in arbitrary units over the frequency in THz is shown (the top horizontal axes also provides normalized frequencies for better comparison). The 1st band gap is marked with a grey shade. The dipole-like resonance A is clearly identified. B and C are higher-order modes, pushed into the bandgap.

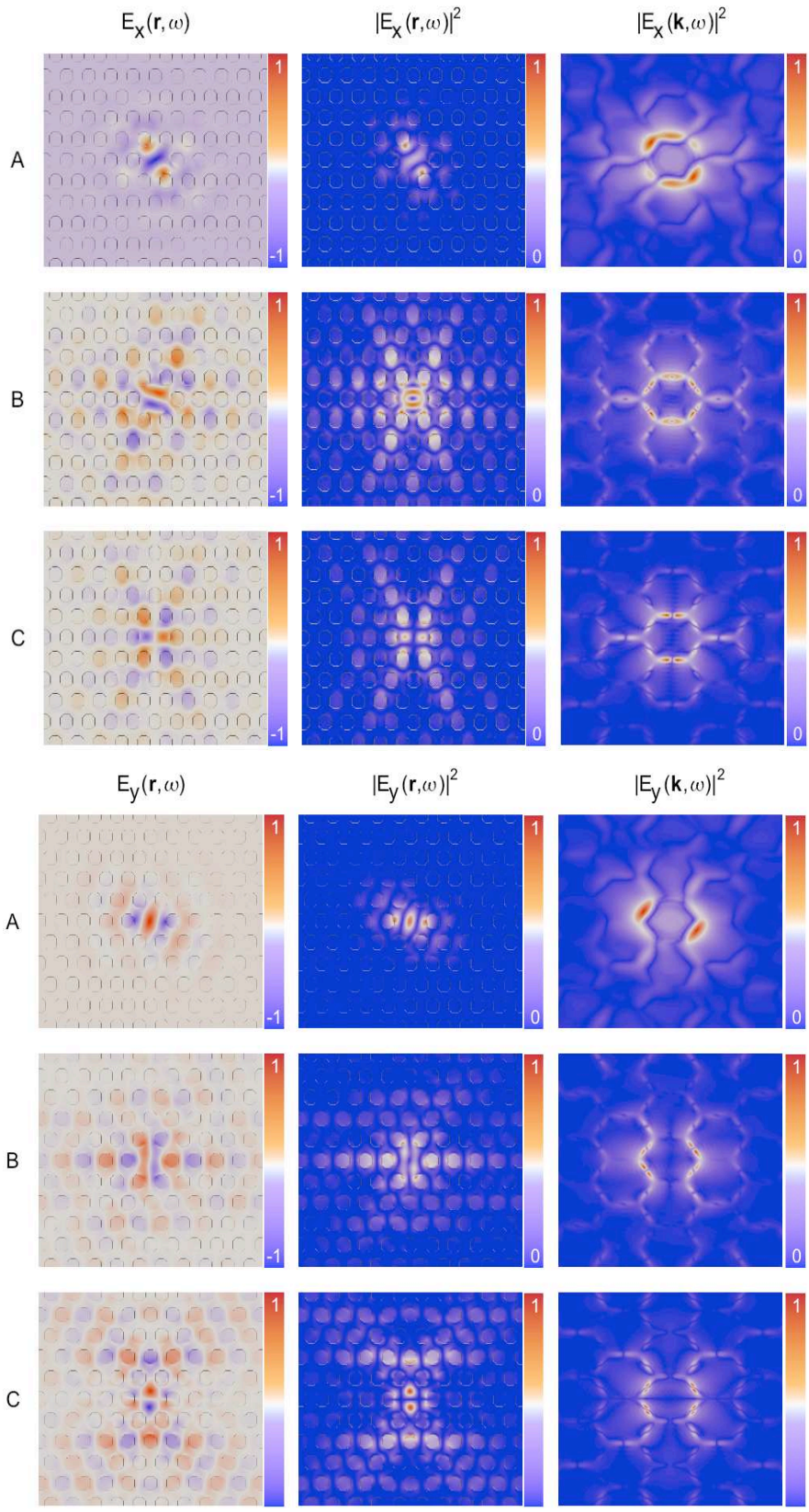

Figure 3.2: Spatiospectral response, calculated with *Maexle*. From top to bottom: mode patterns belonging to the peaks A-C in Fig. 3.1, middle and bottom. From left to right: electric field pattern $E_\mu(\mathbf{r}_{\mathrm{ip}},\omega)$, absolute square $|E_\mu(\mathbf{r}_{\mathrm{ip}},\omega)|^2$ and spatial Fourier transform $|E_\mu(\mathbf{k}_{\mathrm{ip}},\omega)|^2$ in-plane of the slab ($\mu = x,\ y$).

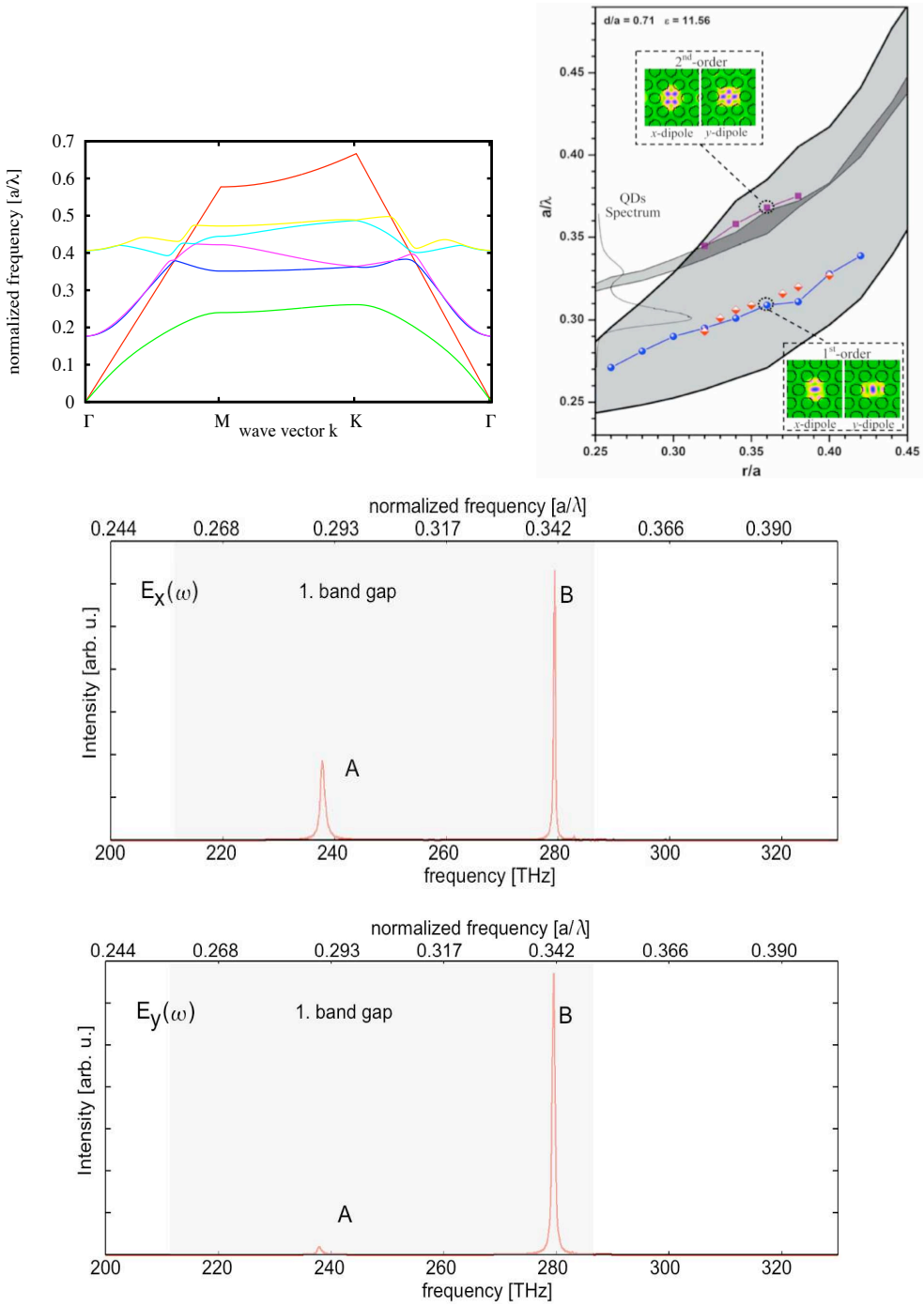

Figure 3.3: Spectral response for the $H1$ PhCC, after [2]. Top left: Band structure of the PhC, containing the first 5 photonic bands and the light cone (red line). Normalized frequencies are plotted vs. the wave vector. High-symmetry points of the reciprocal space are marked. Note the 1st band gap between the first two bands. Calculated with *MPB* [82]. Top right: Experimental and numerical data from [2]. Two modes are shown in the 1st band gap (grey-shaded area). Normalized frequencies are plotted vs. r/a. Middle and bottom: Spectral response (middle: x-component, bottom: y-component), calculated with *Maexle*. Intensity in arbitrary units over the frequency in THz is shown (the top horizontal axes also provides normalized frequencies for better comparison). The 1st band gap is marked with a grey shade. The dipole-like resonances A (1st-order) and B (2nd-order) are clearly identified.

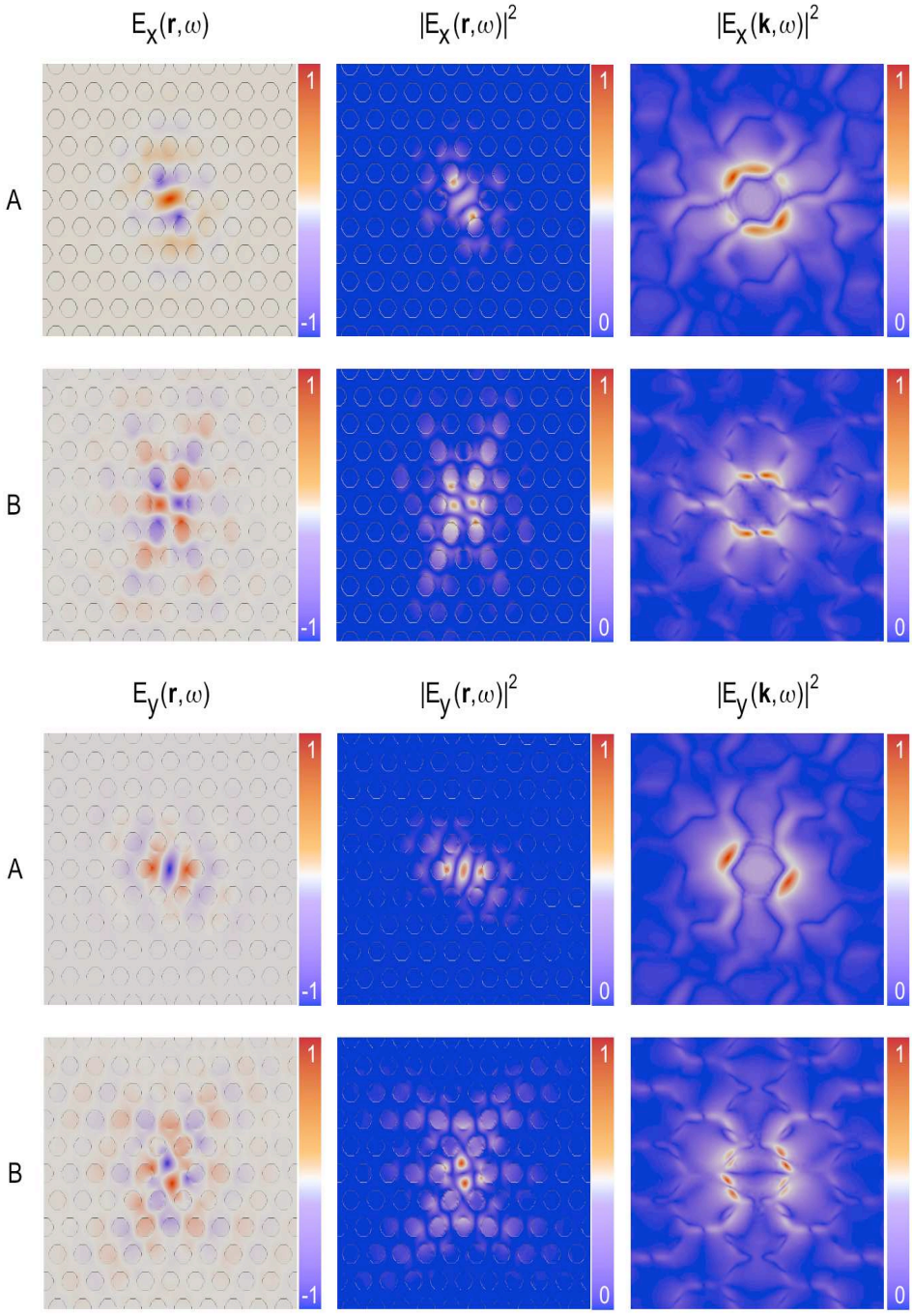

Figure 3.4: Spatiospectral response, calculated with *Maexle*. From top to bottom: mode patterns belonging to the peaks A and B in Fig. 3.3, middle and bottom. From left to right: electric field pattern $E_\mu(\mathbf{r}_{\mathrm{ip}},\omega)$, absolute square $|E_\mu(\mathbf{r}_{\mathrm{ip}},\omega)|^2$ and spatial Fourier transform $|E_\mu(\mathbf{k}_{\mathrm{ip}},\omega)|^2$ in-plane of the slab ($\mu = x,\, y$).

Next, the $H1$-type cavity from [2] is calculated with *Maexle*. The PhCC parameters are a lattice constant of $a = 366$ nm, slab thickness $t = 0.71 \times a$, air hole radius $r = 0.32 \times a$ and a dielectric permittivity for GaAs, $\epsilon_r = 11.56$. A comparison of the numerical results and the experimental data is depicted in Fig. 3.3. The only slightly different radius-to-lattice constant ratio compared with the previous case give rise for a similar extension of the band gap, as it is confirmed via a *MPB* calculation (left). On the right side data from [2] are shown. Normalized frequencies are shown on the vertical axes over the radius-to-lattice constant ratio r/a. The grey-shaded areas distinguish between the 1$^{\text{st}}$ band gap for quasi-TE-like modes (thin boundaries) and quasi-TM-modes (thick boundaries). Half-filled diamonds are results from the experiment for the 1$^{\text{st}}$-order dipole mode, all other points are calculated. In the insets the electric energy is depicted for the 1$^{\text{st}}$- and 2$^{\text{nd}}$-order dipole modes. Since the defect structure is the same as in the prior case, and only the resonant frequencies are scaled with the altered lattice constant and shifted due to a different r/a. The mode patterns are given in Fig. 3.3 for the sake of completeness.

3.1.2 $L3$-type PhCC

The next case follows the data from [3]. Here, a $L3$ cavity with a lattice constant of $a = 420$ nm, air hole radius-to-lattice constant ratio $r/a = 0.29$, a slab thickness-to-lattice constant ratio of $t/a = 0.6$ is systematically investigated. For the dielectric permittivity, again $\epsilon_r = 11.56$ is chosen. The case of highest Q is chosen to be verified with *Maexle*, therefore the shift of the outer air holes are shifted outward by $s/a = 0.15$. The photonic band structure is calculated with *MPB*, see Fig. 3.5 (top left). Normalized frequencies are plotted over the wave vector, where high-symmetry points in the reciprocal space are marked. Note the photonic band gap between the first (green) and second (blue) band (the light cone is shown in red). Experimental data from [3] are shown in the top right corner. Spectral responses over (vacuum-) wavelength is shown for different outward shifts s of the outer air holes. The calculated spectral responses of the x-component (y-component) of the electric field are depicted in the middle (bottom). Each spectrum shows 6 peaks within the band gap (grey-shaded). The mode patterns and corresponding spatial FTs for the x-component and y-component of the electric field are depicted in Fig. 3.6 and Fig. 3.7, respectively. In comparison, the frequency of the desired resonance agrees nicely with the fundamental mode (mode A). The fundamental mode A will be focus of investigation in Chaps. 5 and 6.
In [4], also a $L3$-type defect is investigated for the use in strong-coupling experiments with single QDs. The set of parameters describing the PhCC are $a = 300$ nm, of $r = 0.27 \times a$ and $t = 0.9 \times a$ with $\epsilon_r = 11.56$. An outward shift $s/a = 0.2$ is used for investigations [3]. Like in the previous cases, a photonic band structure is calculated with *MPB*. Note the band gap between the first two bands in the top left of Fig. 3.8, where normalized frequencies are plotted over the wave vector. High symmetry points in the irreducible Brillouin zone are marked. In the top left, experimental data from [4] are depicted. The spectrum of the active layer in the samples over the (vacuum-) wavelength is shown on the left, while on the right side spectra of the emission of three different samples are shown. Note the deviations, occurring due to slight differences in the samples, e.g. deviating sizes of the air holes, distributed over the whole sample. Calculations of the spectral response with *Maexle* are shown in the middle (x-component) and bottom (y-component) part. Also, the agreement is good. The intensity (logarithmic scale) vs. frequency in THz (bottom axes; the top axes provides normalized frequencies for better comparison with the band structure) is plotted. The five occurring resonances are marked from A to E.

Corresponding field patterns and spatial FTs are shown in Fig. 3.9 for the x-component and in Fig. 3.10 for the y-component.

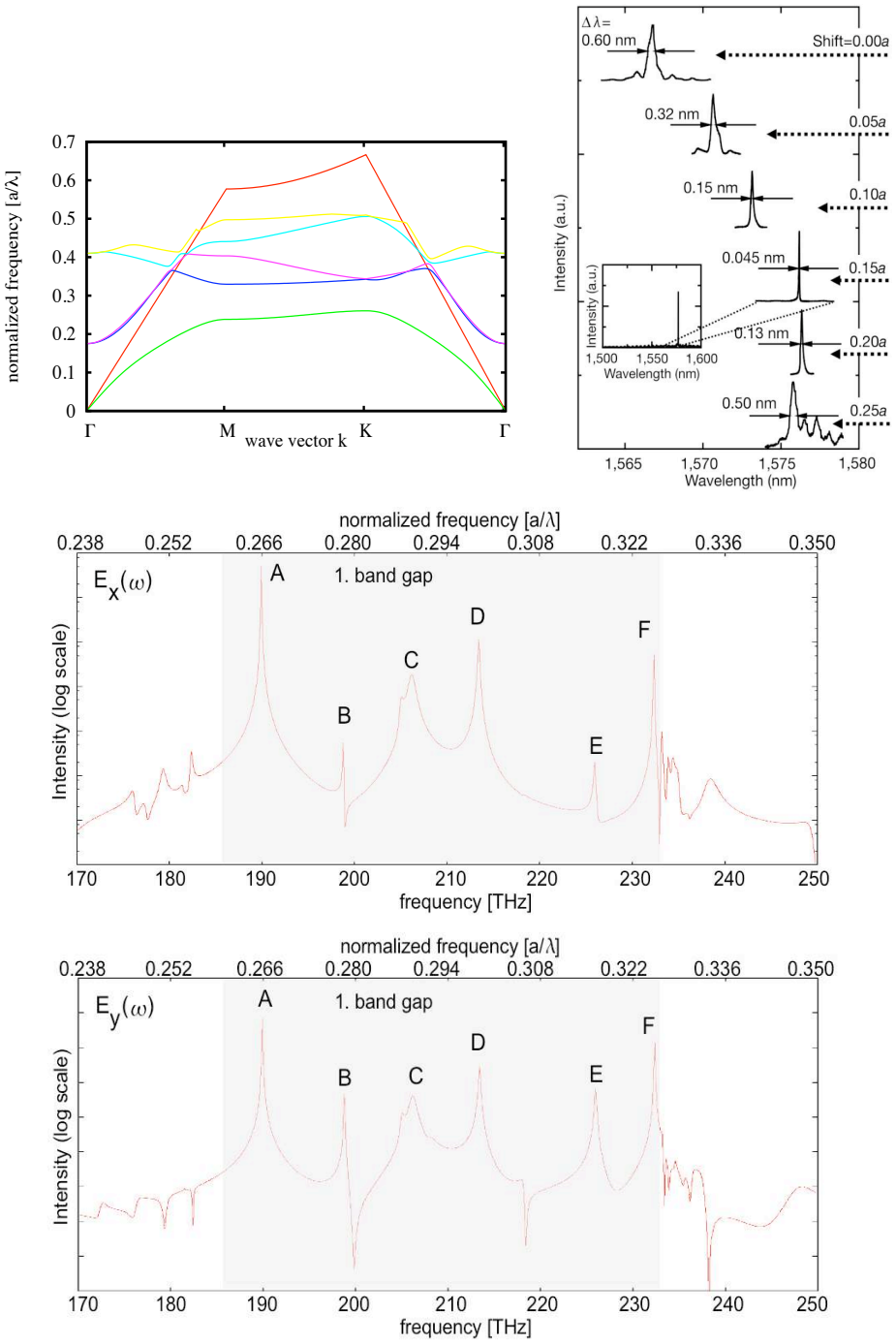

Figure 3.5: Spectral response for the *L*3 PhCC, after [2]. Top left: Band structure of the PhC, containing the first 5 photonic bands and the light cone (red line). Normalized frequencies are plotted vs. the wave vector. High-symmetry points of the reciprocal space are marked. Note the 1st band gap between the first two bands. Calculated with *MPB* [82]. Top right: Experimental data from [3]. The (vacuum-) wavelength of fundamental mode is shown for different shifts s of the outer air holes. For comparison, the case for $s/a = 0.15$ is chosen. Middle and bottom: Spectral response (middle: x-component, bottom: y-component), calculated with *Maexle*. Intensity on a logarithmic scale over frequency in THz is shown (the top horizontal axes also provides normalized frequencies for better comparison with the band structure). The 1st band gap is marked with a grey shade. Six resonances are marked from A to F.

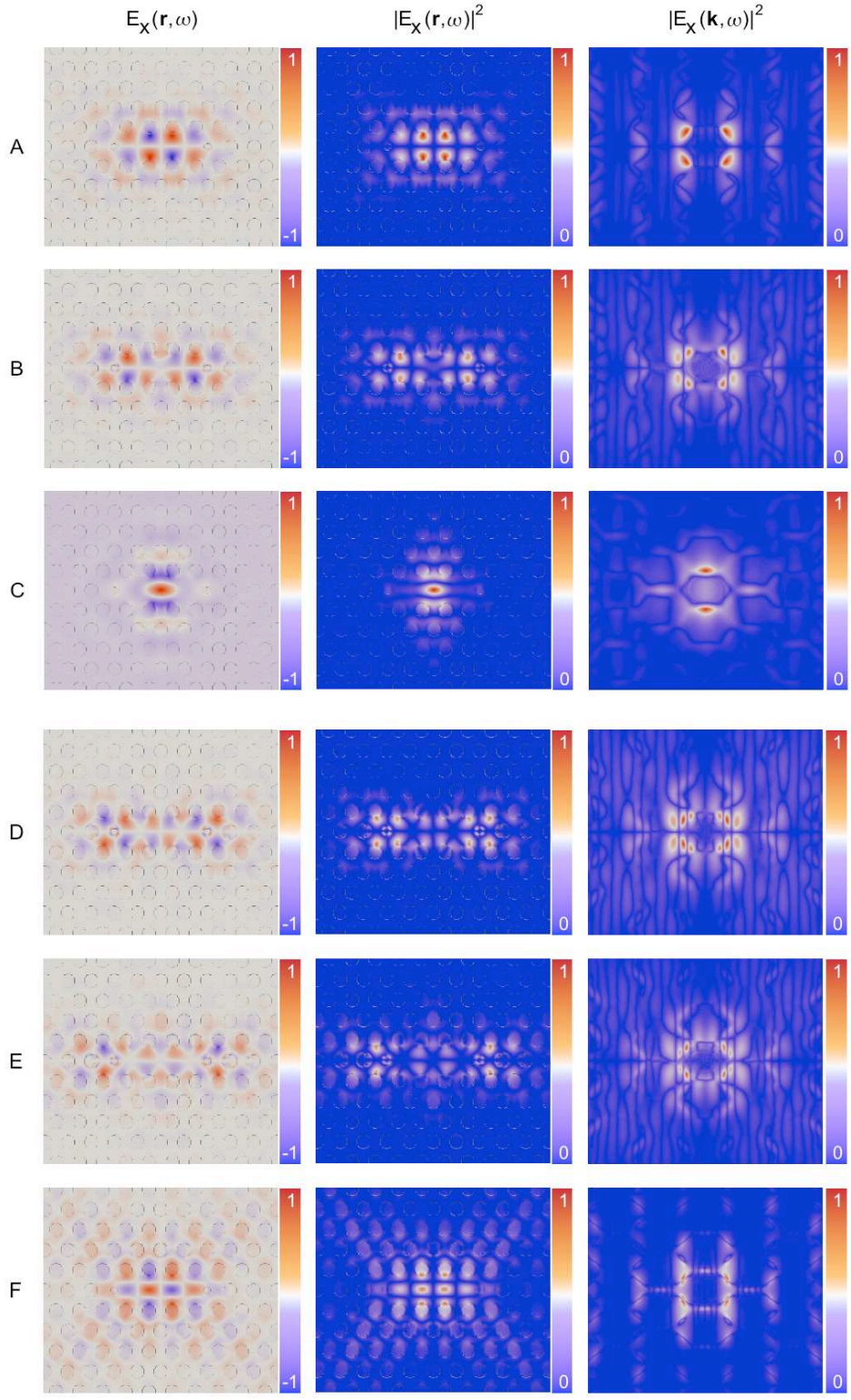

Figure 3.6: Spatiospectral response, calculated with *Maexle*. From top to bottom: mode patterns belonging to the peaks A-F in Fig. 3.5, middle. From left to right: electric field pattern $E_x(\mathbf{r}_{\mathrm{ip}},\omega)$, absolute square $|E_x(\mathbf{r}_{\mathrm{ip}},\omega)|^2$ and spatial Fourier transform $|E_x(\mathbf{k}_{\mathrm{ip}},\omega)|^2$ in-plane of the slab.

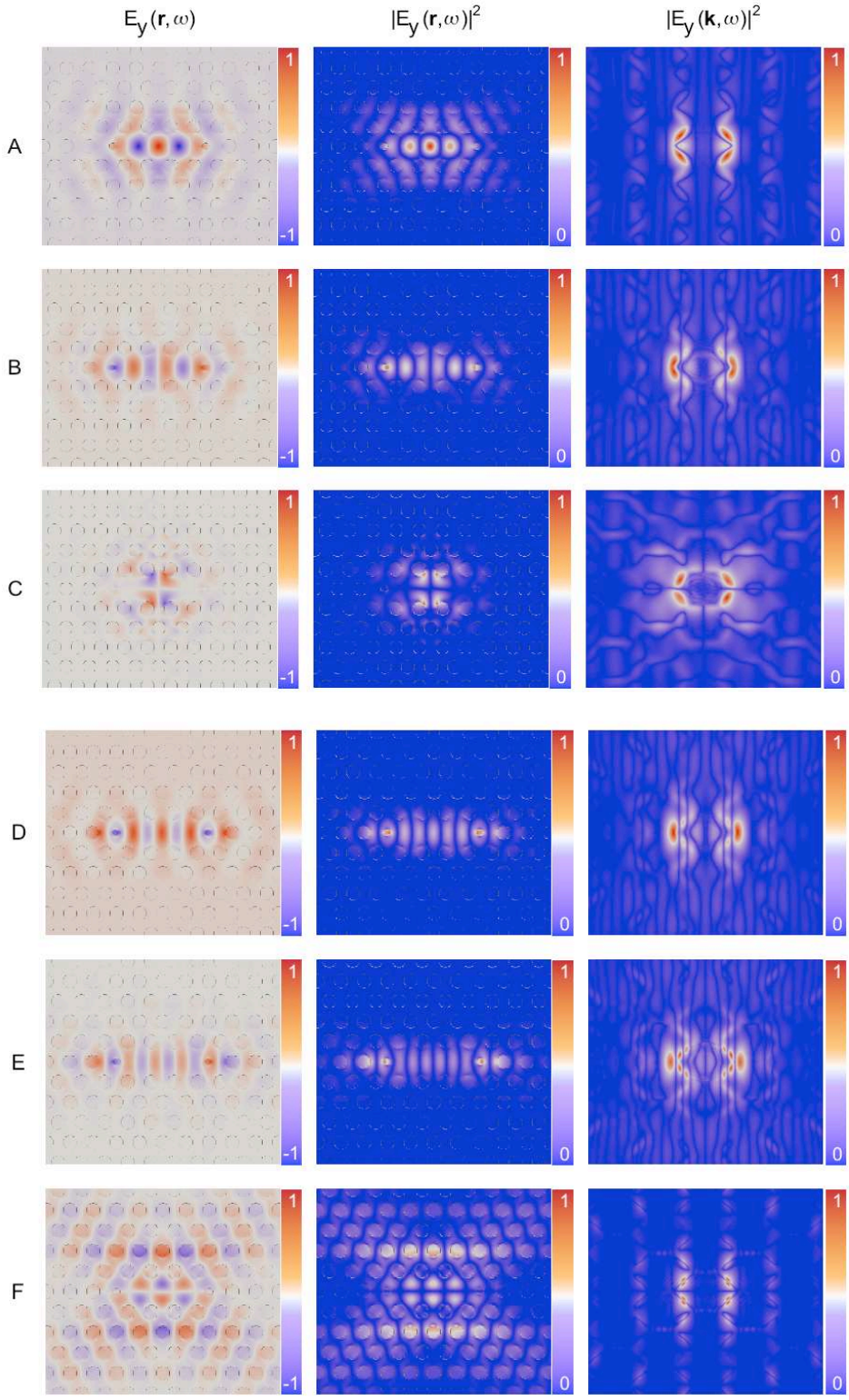

Figure 3.7: Spatiospectral response, calculated with *Maexle*. From top to bottom: mode patterns belonging to the peaks A-F in Fig. 3.5, bottom. From left to right: electric field pattern $E_y(\mathbf{r}_{\mathrm{ip}},\omega)$, absolute square $|E_y(\mathbf{r}_{\mathrm{ip}},\omega)|^2$ and spatial Fourier transform $|E_y(\mathbf{k}_{\mathrm{ip}},\omega)|^2$ in-plane of the slab.

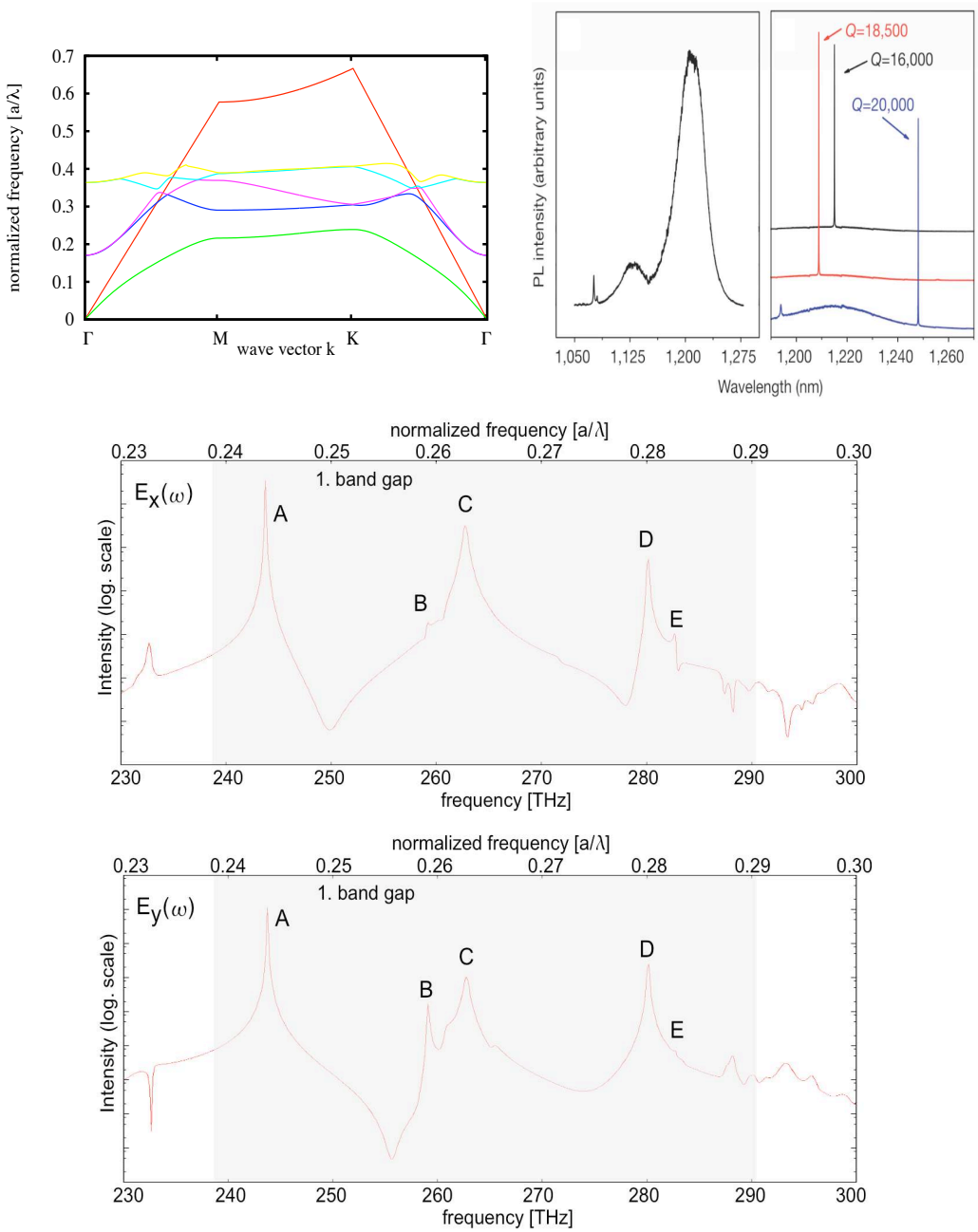

Figure 3.8: Spectral response for the $L3$ PhCC, after [4]. Top left: Band structure of the PhC, containing the first 5 photonic bands and the light cone (red line). Normalized frequencies are plotted vs. the wave vector. High-symmetry points of the reciprocal space are marked. Note the 1st band gap between the first two bands. Calculated with *MPB* [82]. Top right: Experimental data from [4]. Spectrum of the active layer in the sample (left). Photoluminescence of the samples. A modification (shift of the outer air holes $s/a = 0.2$) is applied. The (vacuum-) wavelength for three different samples are shown, including the corresponding Q-factors. Note the different resonances due to fabrication inaccuracies. Middle and bottom: Spectral response (middle: x-component, bottom: y-component), calculated with *Maexle*. Intensity on a logarithmic scale over frequency in THz is shown (the top horizontal axes also provides normalized frequencies for better comparison with the band structure). The 1st band gap is marked with a grey shade. Due to a slightly different r/a, only five resonances occur (compared to Fig. 3.5), which are marked from A to E.

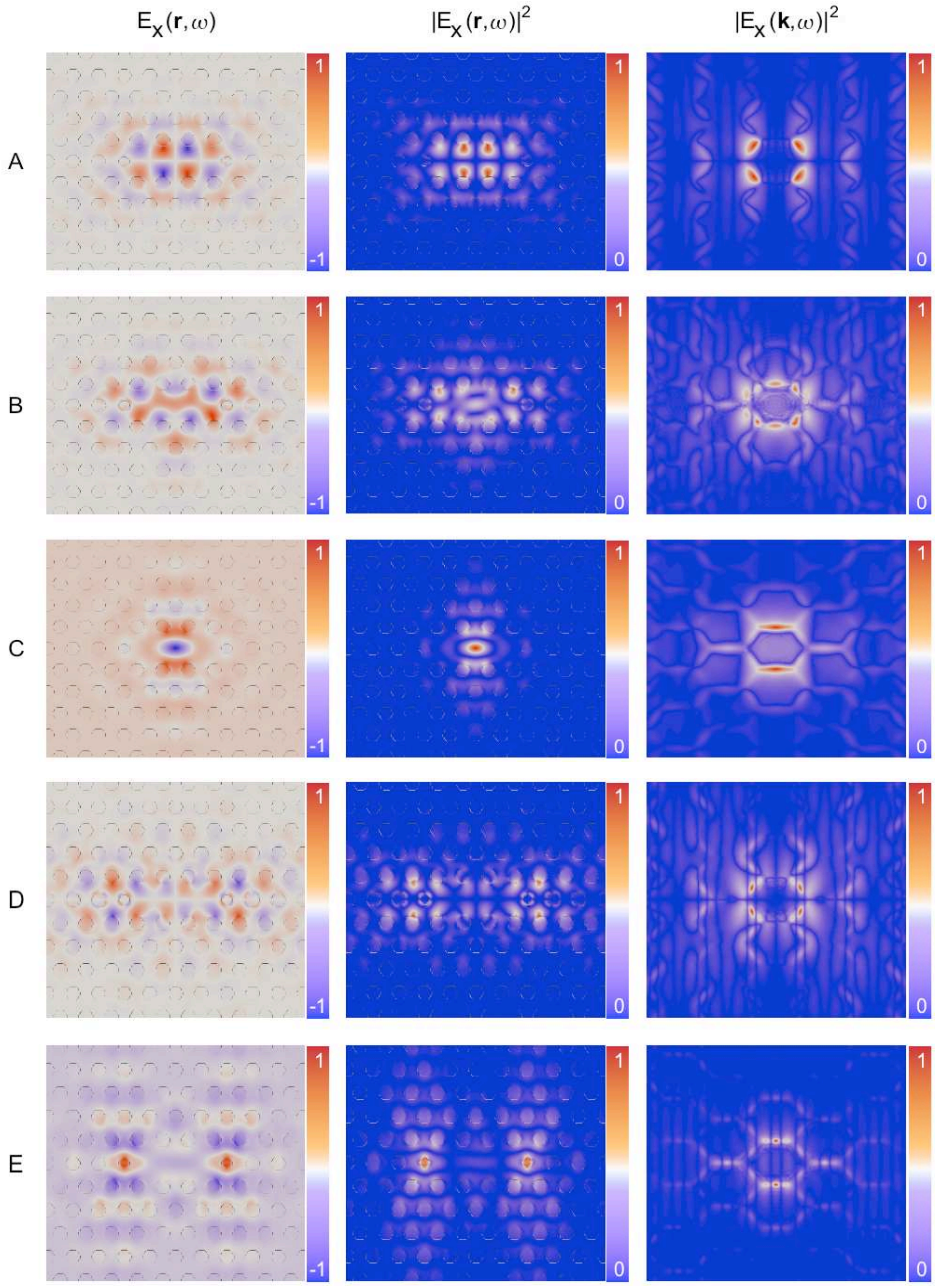

Figure 3.9: Spatiospectral response, calculated with *Maexle*. From top to bottom: mode patterns belonging to the peaks A-E in Fig. 3.8, middle. From left to right: electric field pattern $E_x(\mathbf{r}_{\mathrm{ip}},\omega)$, absolute square $|E_x(\mathbf{r}_{\mathrm{ip}},\omega)|^2$ and spatial Fourier transform $|E_x(\mathbf{k}_{\mathrm{ip}},\omega)|^2$ in-plane of the slab.

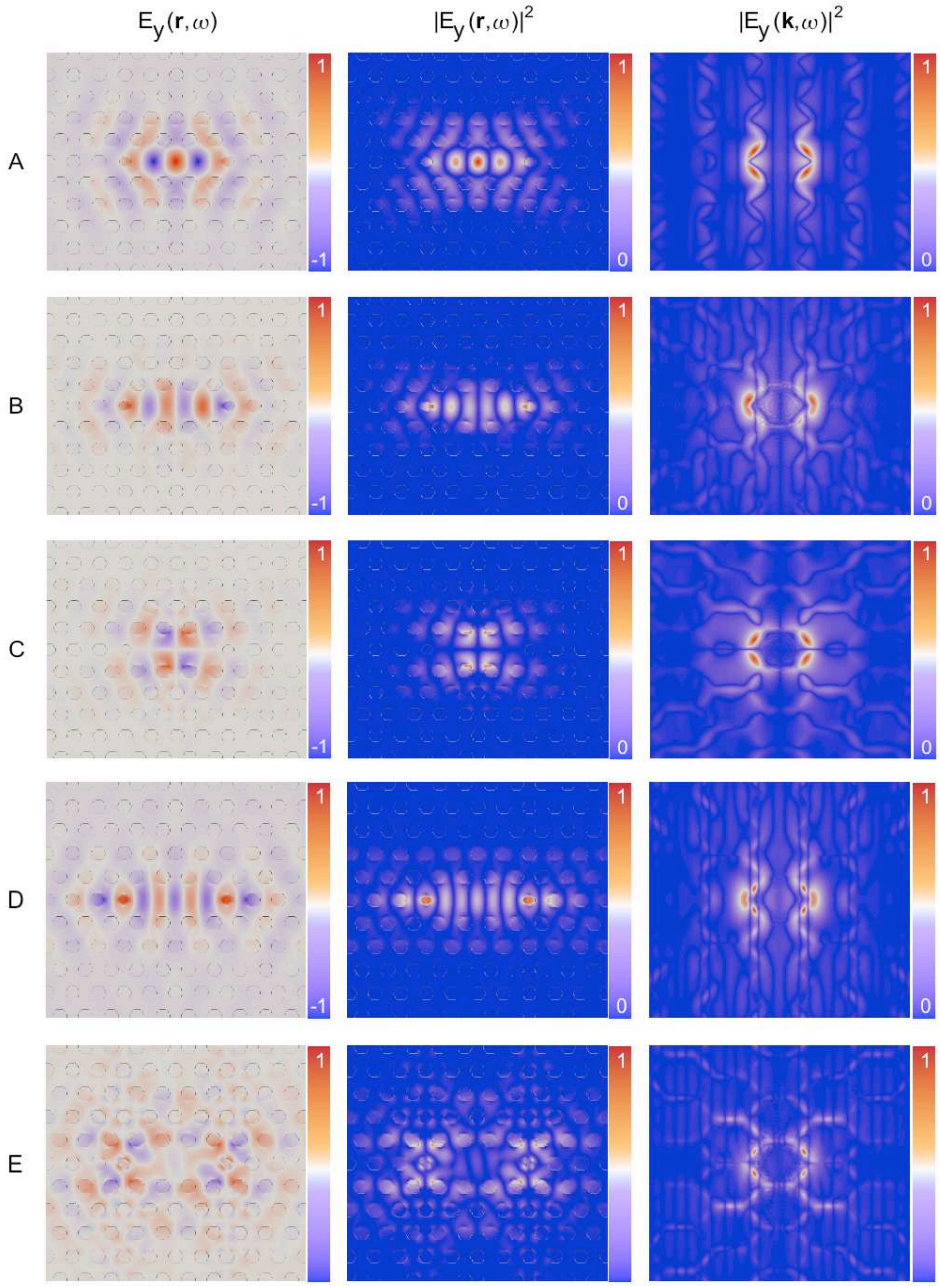

Figure 3.10: Spatiospectral response, calculated with *Maexle*. From top to bottom: mode patterns belonging to the peaks A-E in Fig. 3.8, bottom. From left to right: electric field pattern $E_y(\mathbf{r}_{\mathrm{ip}},\omega)$, absolute square $|E_y(\mathbf{r}_{\mathrm{ip}},\omega)|^2$ and spatial Fourier transform $|E_y(\mathbf{k}_{\mathrm{ip}},\omega)|^2$ in-plane of the slab.

Chapter 4

Microdisk Resonator

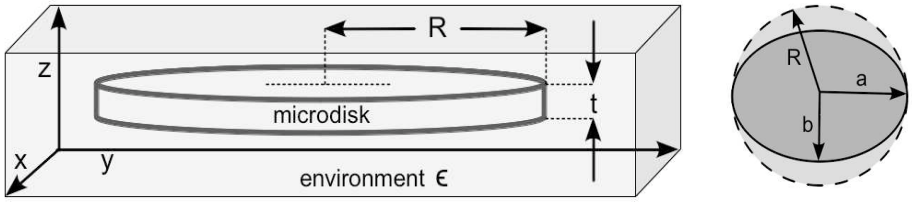

Figure 4.1: Sub-μ Microdisk: Geometrical Setup. The main axes of the MD is parallel to the z-axes, the thickness is denoted by t, the radius of the device is denoted by R and the microdisk has an isotropic dielectric permittivity. For the environment, the dielectric permittivity is ϵ. Left: side view. Right: top view. a and b are the big and small halfaxis, respectively.

Microdisk resonators in general provide ultra-high Q-factors [107], corresponding photon life times up to the millisecond regime. In fact, the higher the azimuthal mode order, the higher is the Q-factor. The reason is the reduction of bending loss of the confined electromagnetic wave in the rim of the microdisk. Consequences, which one can take advantage from, are for example extremely high energy densities and intensities and ultra-narrow line widths, which can be used e.g. for ultra-fine sensing. Experimentally interesting, and also interesting for (commercial) applications, is the usability for accurate displacement measurements with ultra-fine environmental sensing and high-resolution spectroscopy. Also, they can be used for quantum non-demolishing measurements, optical switches and in integrated optical devices [26, 108–110].
In this chapter, the focus lies on two different microdisk devices. First, a sub-μ microdisk resonator is investigated (after [83]). The effects of a non-perfect circular shape and of a uniaxial anisotropic environment on the spectral response is numerically analyzed. Second, a microdisk device with a radius of 3 μm, embedded in a LC environment (modeled with the uniaxial anisotropic material), is calculated and compared with the experimental realization [26, 111, 112]. The microdisk device itself is modeled with a pure dielectric material, thus no absorption is taken into account. Substrates and microposts are also neglected. Due to the fact that the field distribution for a resonance is concentrated in the rim of the device, a post does not affect the spectral response. The general geometrical setup is depicted in Fig. 4.1. The main axis of the cylindrically shaped resonator is perpendicular to the x-y-plane. Parameters used in the simulations are given in the corresponding sections.

4.1 Sub-μ Microdisk Resonator

The general parameters for the numerical investigation of the sub-μ microdisk resonator are taken from [83], hence the radius is $R = 361$nm, thickness of the resonator is $t = 265$ nm and the value for the dielectric permittivity (only real part) is taken for GaAs, hence $\epsilon_D = 11.56$. A spatial resolution of $\Delta x = 7.3529$ nm is chosen. Since no absorption is taken into account, the fact that GaAs is absorbing below 800 nm is ignored. Note that this is a model study. Also, materials like Gallium Nitride with a larger band gap than GaAs, having a comparable dielectric permittivity in this spectral region, can be used.
In Sec. 2.4.1, the analytic solution for a microdisk resonator surrounded with a PEC material, as well as for a dielectric material is shown. Numerically, using the FDTD method, one can get the spectral response from a broadband excitation with a point source located near

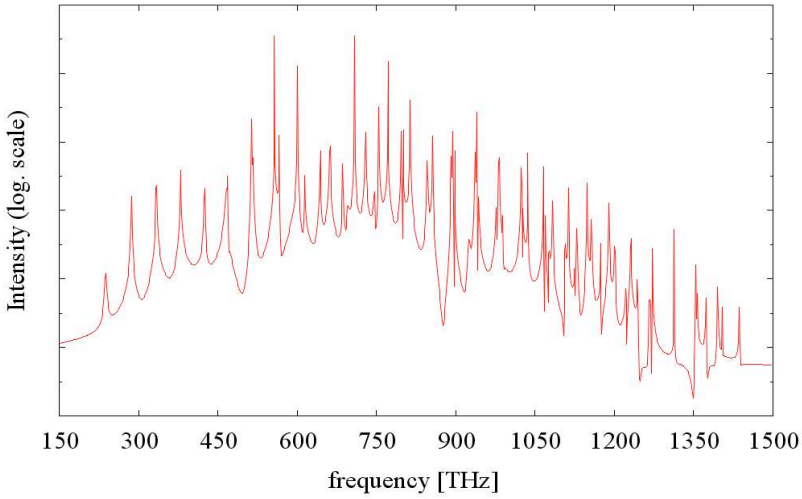

Figure 4.2: Broadband spectral response from the microdisk device, simulation parameters after [83]. Intensity (logarithmic scale) vs. frequency in THz is plotted. Equidistant peaks belong to the same radial mode order.

the interface of the microdisk with its isotropic environment, shown in Fig. 4.2 from a two-dimensional calculation volume, where open boundaries (CPML, see Sec. 2.2.4) in-plane and periodic boundary condition in z-direction are used. The vertical axis shows the intensity of the TE response ($|H_z|^2$) on a logarithmic scale over frequencies in THz. Equidistant peaks with different spacings occur over the whole spectral range. Starting from the low-frequency side, the azimuthal mode order increases with each peak for a radial mode order of 1 (fundamental modes in-plane). For higher radial modes, this applies, too. Figure 4.3 illustrates this exemplarily in the spectral range from 500 THz to 600 THz, covering 5 modes (see spectral response in the top part on a logarithmic scale, plotted over the frequency in THz). The high-intensity peaks belong to the modes with a radial mode order of 1, while the low-intensity modes have a radial mode order of 2. Starting at the low-frequency edge, the azimuthal mode order is incremented from 9 (therefore, the mode label is $\mathrm{TE}_{1,9}$) to 11 ($\mathrm{TE}_{1,11}$) for the high-intensity and high-Q modes, and from $\mathrm{TE}_{2,6}$ to $\mathrm{TE}_{2,7}$ for the low-intensity and also low-Q modes. The effect of additional lobes in radial direction is visible in the mode patterns for the modes with radial mode order 2. Due to increased bending loss, the mode pattern also expands strongly into the environment. Therefore, the Q-factor is reduced. The spatial field distribution in the mirror plane $z = 0$ (quasi-TE) for these modes are depicted in the bottom part of Fig. 4.3, where the field intensity is color-coded (negative: red, positive: blue, normalized to 1) and the grey circle shows the interface between the microdisk and the environment. The normalized absolute value of the spatial FT (color-coded: black: zero, white: 1) of the mode patterns in the k_x-k_y-plane are directly below the real-space patterns. Here, one directly sees the reason for the lower Q-factor of the modes with higher radial order and higher Q-factor for modes with high azimuthal mode order. The consequence of the second order in radial direction is a second lobe in the spatial FT as well, yielding large contributions inside the light cone, $|\mathbf{k}| \leqslant k_{\mathrm{lc}} = \frac{2\pi}{\lambda_0}$ (λ_0 is the vacuum wavelength of the resonance). For waves with contributions

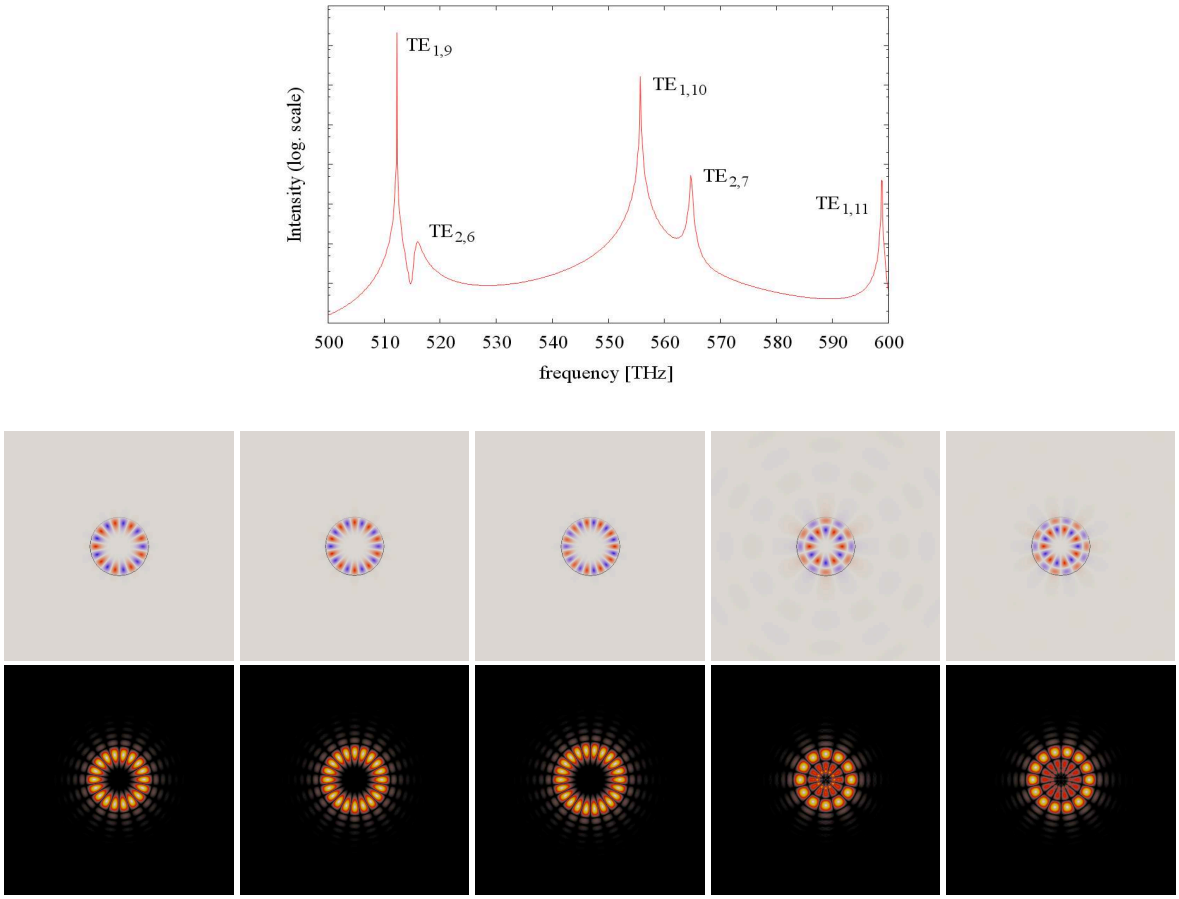

Figure 4.3: Spatial field distribution and intensity in reciprocal space from a two-dimensional calculation. Top: Spectrum, intensity in a logarithmic scale over frequency in THz. The labels denote the corresponding mode order $\mathrm{TE}_{N,M}$, where N is the radial mode order and M the azimuthal mode order. Note, that peaks belonging to higher modes in z-direction do not occur due to the periodic boundary condition. Middle: mode patterns (normalized, red: $+1$, blue: -1). Bottom: intensity in reciprocal space (dark: low, bright: high) of the $\mathrm{TE}_{N,M}$ modes in the spectrum. The spatiospectral responses in reciprocal space have the same number of lobes as the field patterns in real space.

inside the light cone, the conservation law for the parallel wave vector component is fulfilled. Thus, they are not confined due to TIR, but are diffracted. On the other side, modes with high radial mode orders have reduced components inside the light cone. Thus, the condition for TIR is fulfilled for mostly all the waves and the Q-factor increases.

4.1.1 Geometrical Variations

The effect of slight deviations of the parameters from a perfectly circular microdisk resonator is significant and cannot be underestimated, when one wants to utilize the spectral properties of the microdisk eigenmodes. In the following sections, the influence of the variation of the radius of a perfectly circular device, of a numerical excentricity, of an elliptically shaped device as well as an edge profile is investigated numerically.

Regarding this from a positive point of view, proper shaping of a microdisk resonator leads to the possibility to tune resonances to the interval of interest. Also, switching the mode order can be achieved with relatively small changes of the geometry. Contrary, this has a negative side effect. Slight deviations of the perfectly cylindrical structure result in shifts of resonances, detuning afore properly tuned QDs for example. Numerical calculations are helpful to properly predict the effect of geometrical changes. An analytic solution for WGMs with a perturbated circular shape is not available, because the variables cannot be separated as in [113] for the perfectly circular shape.

Radius

The modification of the resonance via a radius variation is used in the later Sec. 6.1 to tune coupled MD resonators into resonance. Figure 4.4 shows the shift of the spectral response. Every line corresponds to another radius of the considered MD, denoted on the right side. The absolute square of the TE mode is plotted over the frequency in THz. From the bottom to the top, the radius of the microdisk device is increased in steps of a spatial discretization from $R-10\Delta x = 287.471$ nm up to $R+10\Delta x = 434.529$ nm. First, one notices the strong shift of the modes with even a slight radius variation. This is due to the fact, that the size of the device is small compared to the wavelength of the modes, as well as due to the chosen spectral range, where the azimuthal mode orders are small. For increasing radius, the frequencies are collectively red-shift. A larger radius includes a larger effective radius of the WGM due to the continuity condition at the interface between microdisk and environment (see Sec. 2.4.1). Therefore, the wave vector decreases and the frequency is red-shifted.
The fairly large amount of eigenmodes, available in the shown tuning range, ranging from $\mathrm{TE}_{1,7}$ for $R-10\Delta x$ to $\mathrm{TE}_{1,13}$ for $R+10\Delta x$ for modes with a radial order of 1 and from $\mathrm{TE}_{2,5}$ for $R-10\Delta x$ to $\mathrm{TE}_{2,10}$ for $R+10\Delta x$ for modes with a radial order of 2, can be used to investigate the coupling between modes with different mode orders. In [114], this coupling behavior is investigated and explained with the radiation patterns of the eigenmodes. For a more detailed explanation of the coupling between eigenmodes with equivalent mode order, see Sec. 6.1.
In large microdisks, for example like the MD in Sec. 4.2, the spectral density of modes is fairly high, since all kinds of azimuthal and radial mode orders are present. This makes it difficult to experimentally distinguish between the different peaks emerging in the spectrum and identify the mode order. A coarse estimation is presented to identify first order radial modes. However, if other disturbing factors like ovality or an edge profile are present, the estimation is not valid.

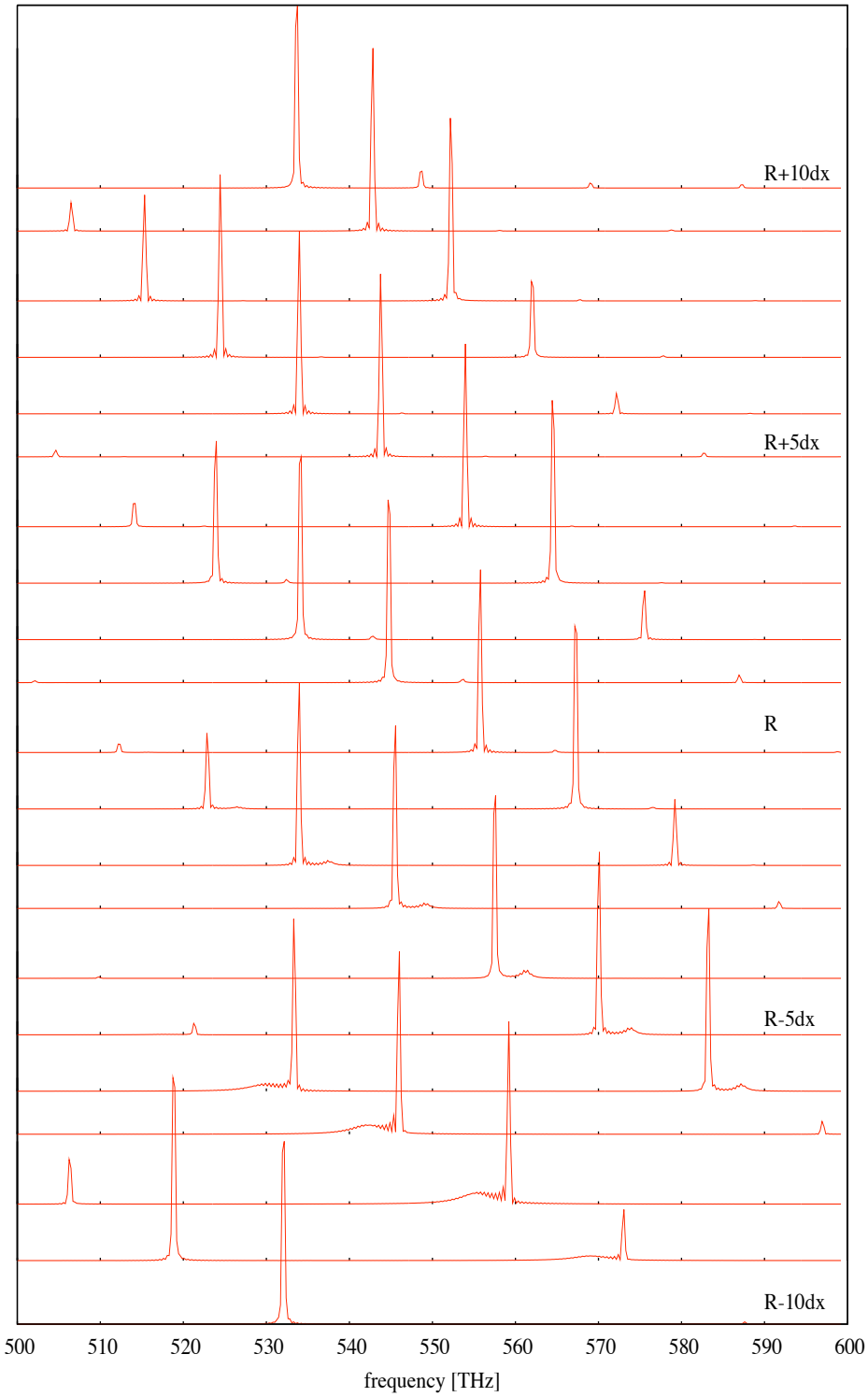

Figure 4.4: Shift of the resonances with varying radius of the MD. Each line shows the intensity in arbitrary units versus the frequency in THz. From bottom to top: Radius increases from $r_< = R-10\Delta x$ to $r_> = R+10\Delta x$. A slight variation of the radius about $dR = \Delta x$ results in a tremendous frequency shift of more than 10 THz. Note the spectral separation of the different modes.

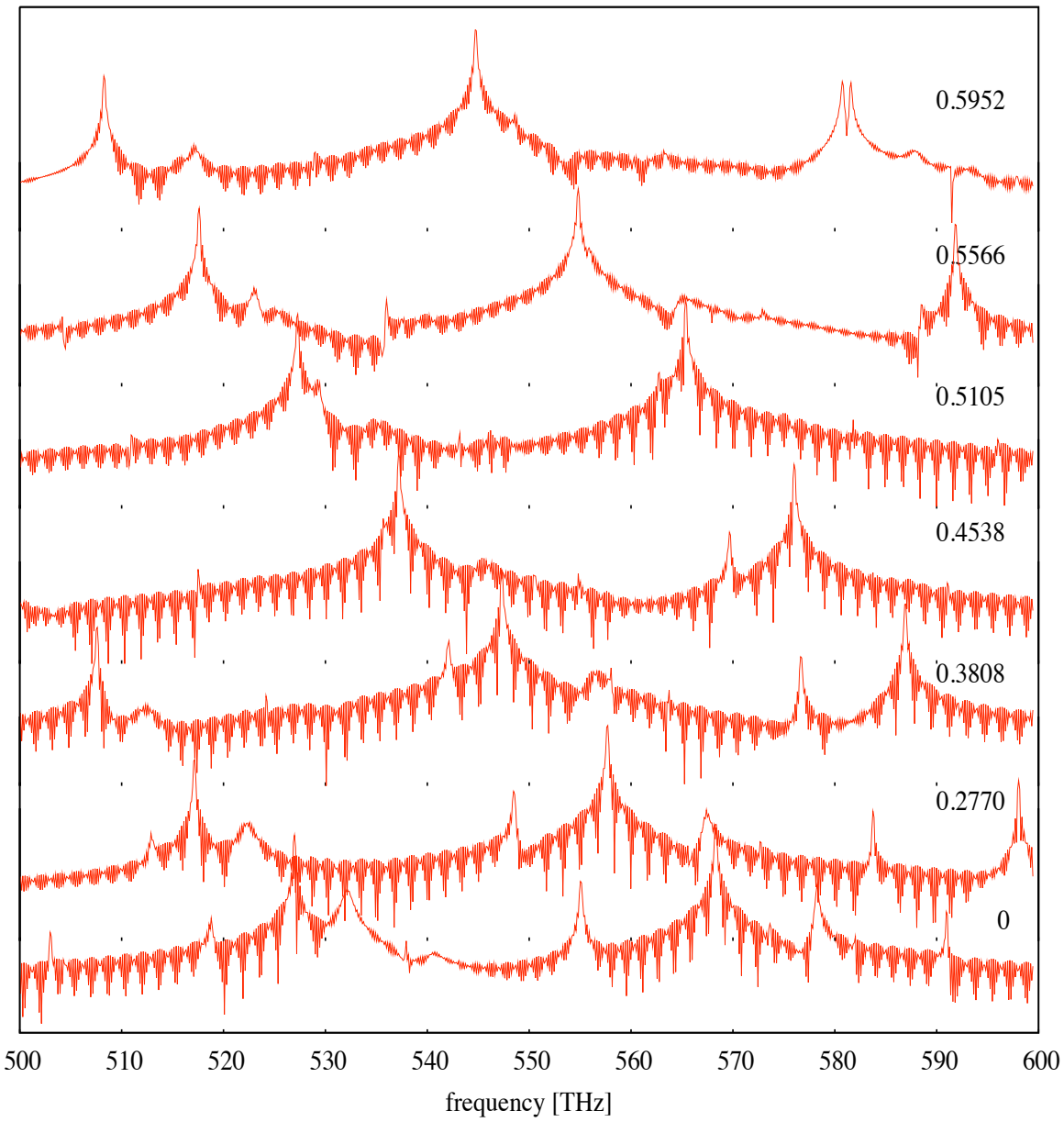

Figure 4.5: Spectral response of a MD with different halfaxis, calculated in a three-dimensional simulation. Every line corresponds to the labeled numerical excentricity $\epsilon = \sqrt{1+(b/a)^2}$ (a: large halfaxis, b: small halfaxis). Intensity on a logarithmic scale is plotted over the frequency in THz. A collective red-shift with increasing ϵ is observed.

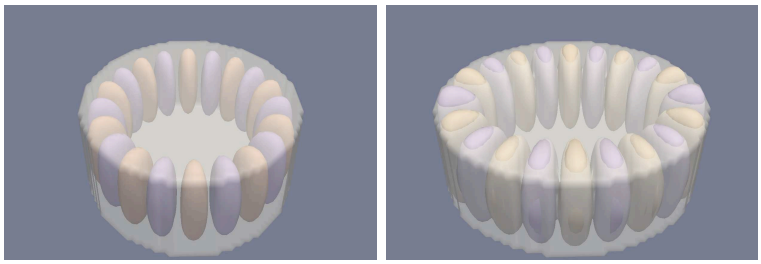

Figure 4.6: Spatiospectral response of $TE_{1,10,1}$ in a MD with numerical excentricity $\epsilon = 0$ (left) and $\epsilon = 0.5952$ (right). The amplitude is color-coded (red: +1, blue: -1) and the MD is shown in transparent grey. Stretching of the mode pattern concentrates the field in the left and right corner. Bending loss is increased there, while contrary bending loss is decreased in the front and back side.

Ellipticity

Figure 4.5 shows the numerical results from the variations of the numerical excentricity, defined as $\epsilon = \sqrt{1-(b/a)^2}$, where a and b are the big and small halfaxis, respectively (refer to Fig. 4.1 for a sketch of the geometry). Due to the radial symmetry with respect to the x- and y-axis, only the radius in x-direction is altered without loss of generality. Different numerical excentricities are plotted. From bottom to top, $\epsilon = 0$, $\epsilon = 0.2770$, $\epsilon = 0.3808$, $\epsilon = 0.4538$, $\epsilon = 0.5105$, $\epsilon = 0.5566$ and $\epsilon = 0.5952$, corresponding to a fixed small halfaxis $b = 361$ nm (along y) and a big halfaxis $a = 361$ nm, 375.7 nm, 390.4 nm, 405.1 nm, 419.8 nm, 434.5 nm and $a = 449.2$ nm, respectively. Intensity on a logarithmic scale is plotted over the frequency in THz. It is apparent, that first all modes are red-shifted and second that different modes experience a different shift. To be more precisely, modes with radial mode order $N = 1$ shift stronger than higher order modes. Due to the strong spatial confinement, a perturbation of the radial symmetry also perturbates the confinement and strong localization of the field inside the rim of the MD. Exemplarily, the spatiospectral response of WGM $TE_{1,10,1}$ is plotted in Fig. 4.6 (red: +1, blue: -1). The MD is shown in a grey shade. On the left, the case with zero ellipticity is depicted. One can see the strong spatial confinement of the TE-like mode inside the resonator structure. On the right side, contrary, the case for $\epsilon = 0.5952$ is shown. The mode pattern is clearly stretched along the x-axis, thus increasing bending loss on the left and right side and decreasing bending loss at the front and back side. A drop of the Q-factor from $Q_0 = 28200$ down to $Q_{0.5952} = 1050$ accompanies the spectral shift of $\Delta f = 61.1$ THz.

Edge Profile

As another frequency-altering effect, the edge profile comes into play. Assume the bottom and top of the MD to have different radii, forming a linear edge profile. Now, the propagating WGMs in the MD are altered due to an effectively larger device thickness. In Sec. 2.4.1, the Helmholtz equation for an infinitely extended dielectric slab was derived, eq. (2.48). Standing waves inside the layer and exponential decaying tails outside are the solutions, when a wave is assumed to propagate perpendicular to the normal of the layer (guided mode). In the case of a WGM in a MD resonator, the propagating wave is guided along the rim of the MD (clockwise and counterclockwise because of degeneracy of the angular equation). With an oblique wall (formed due to i. e. a larger bottom radius R_b compared to the top radius R_t), the WGM snuggles up into the small-angle corner. This increases the effective radius, on which the WGMs

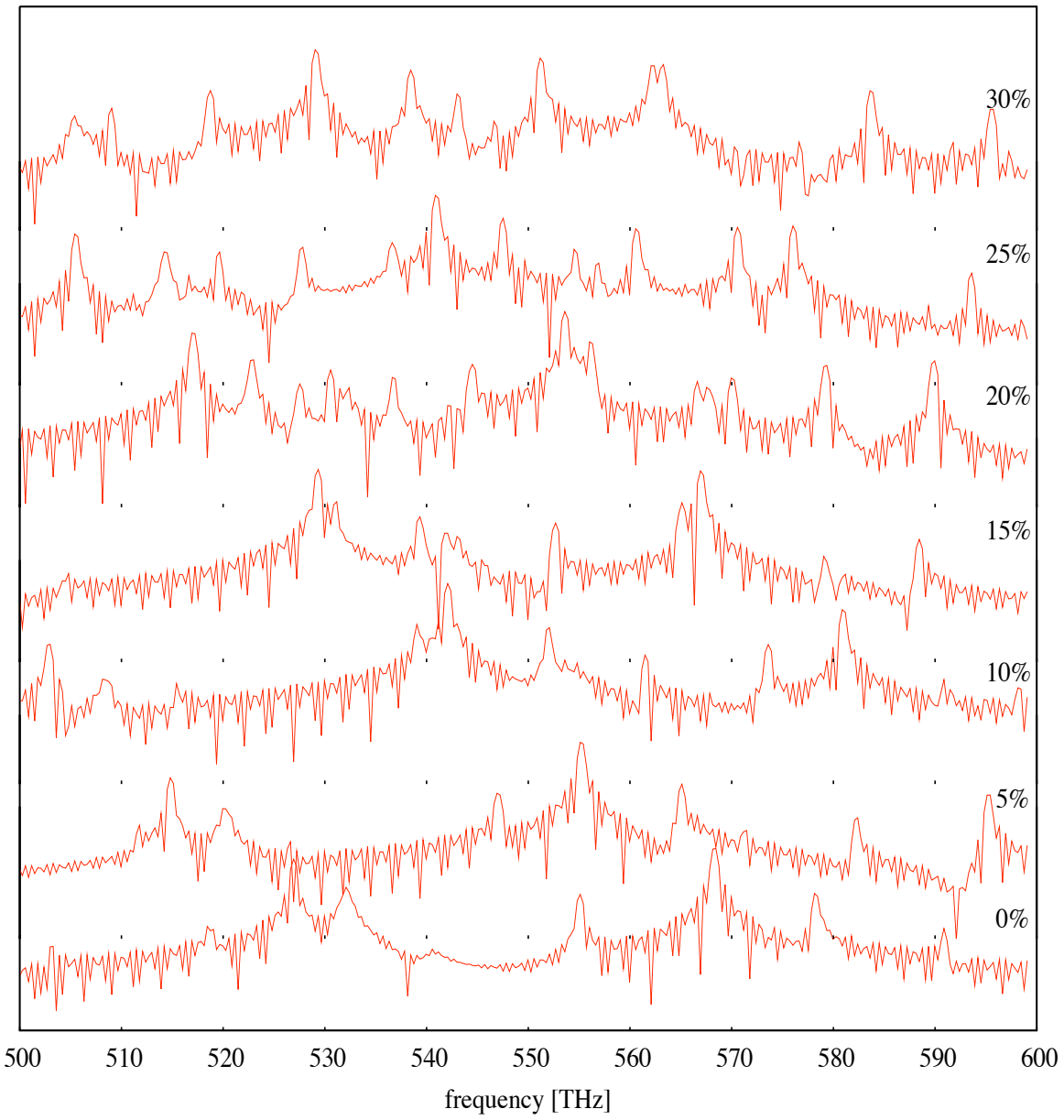

Figure 4.7: Spectral response of a MD with an applied edge profile, calculated in a three-dimensional simulation. Every line corresponds to the labeled increase of the bottom radius with respect to the top radius. Intensity on a logarithmic scale is plotted over the frequency in THz. A collective red-shift with increasing ϵ is observed. An effectively thicker membrane results in higher order modes in z-direction.

are propagating, thus increasing the wavelength. The shift to smaller frequencies is observed in the numerical data, too. Figure 4.7 shows the variation of the bottom radius with respect to the top up to $R_\mathrm{b} = 1.3R_\mathrm{t}$. Every line shows the intensity on a logarithmic scale over frequency in THz. The black labels denote the corresponding increase of R_b. Collectively, all modes are red-shifting. Also, due to the increased effective radius for propagation, higher-order modes

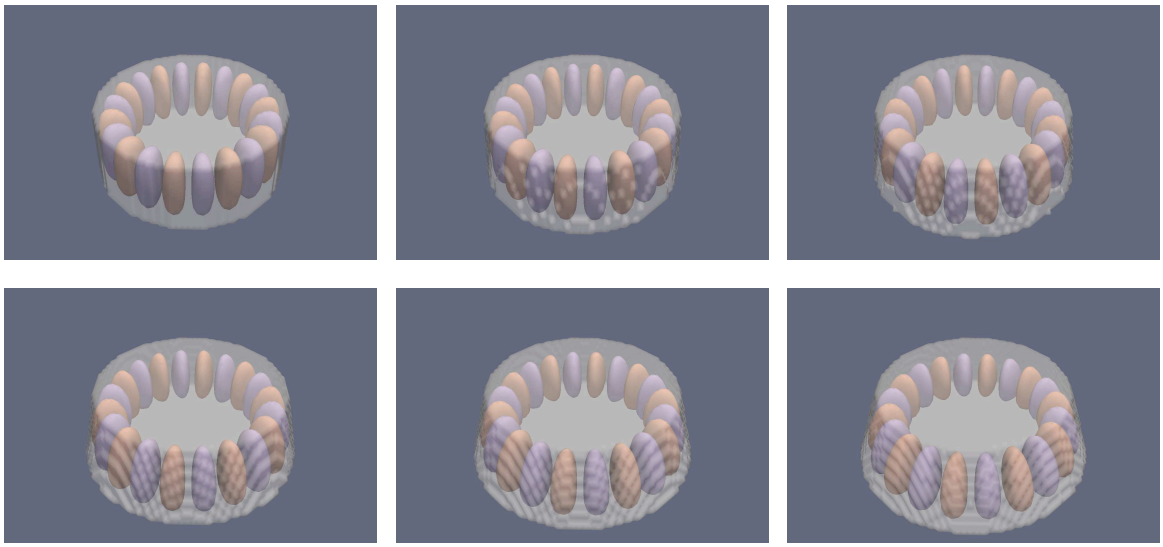

Figure 4.8: 3D spatial field distributions of $TE_{1,10,1}$ for different edge profiles. Top: $R_b = R_t$, $R_b = 1.05R_t$, $R_b = 1.1R_t$(from left to right). Bottom: $R_b = 1.15R_t$, $R_b = 1.2R_t$, $R_b = 1.25R_t$ (from left to right). With increasing edge profile, the maximum of the lobes moves towards the bottom, thus the field is concentrated more in the small-angled corner.

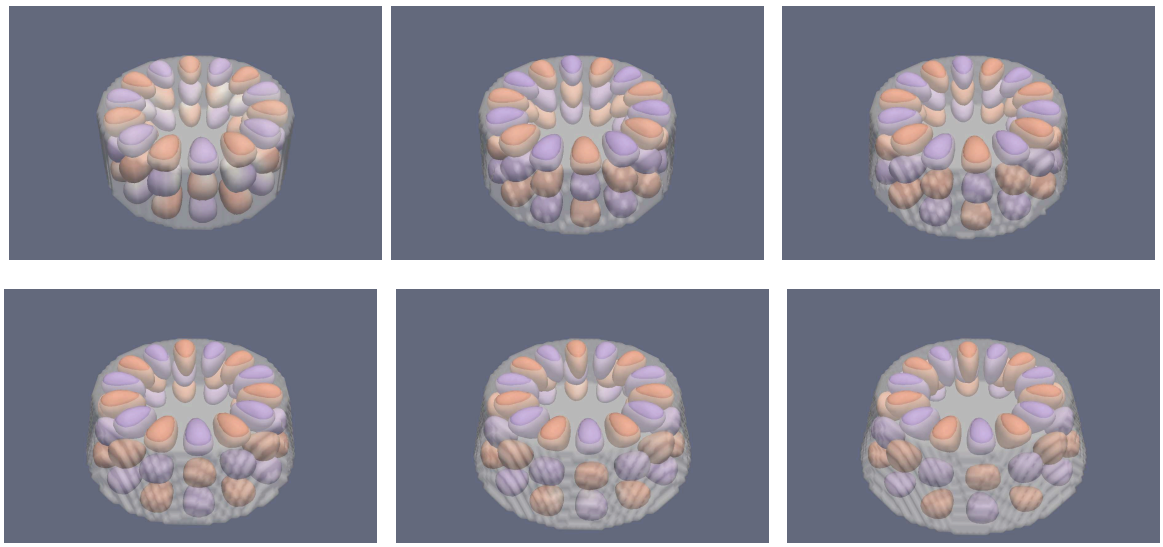

Figure 4.9: 3D spatial field distributions of $TE_{1,7,3}$ for different edge profiles. Top: $R_b = R_t$, $R_b = 1.05R_t$, $R_b = 1.1R_t$(from left to right). Bottom: $R_b = 1.15R_t$, $R_b = 1.2R_t$, $R_b = 1.25R_t$ (from left to right). With increasing edge profile, the maximum of the lobes moves towards the top, thus the field is concentrated more in the large-angled corner.

in z-direction emerge, since the oblique side wall includes an effectively thicker MD device. Spatiospectral responses for the $TE_{1,10,1}$ and $TE_{1,7,3}$ WGM are depicted in Figs. 4.8 and 4.9, respectively, with frequencies $f_{0,1,10,1} = 568$ THz and $f_{0,1,7,3} = 592$ THz (without applied edge profile). In the top lines from left to right, the bottom radius is increased by 0%, 5% and 10%, while in the bottom line from left to right, the bottom radius is further increased to 15% 20%

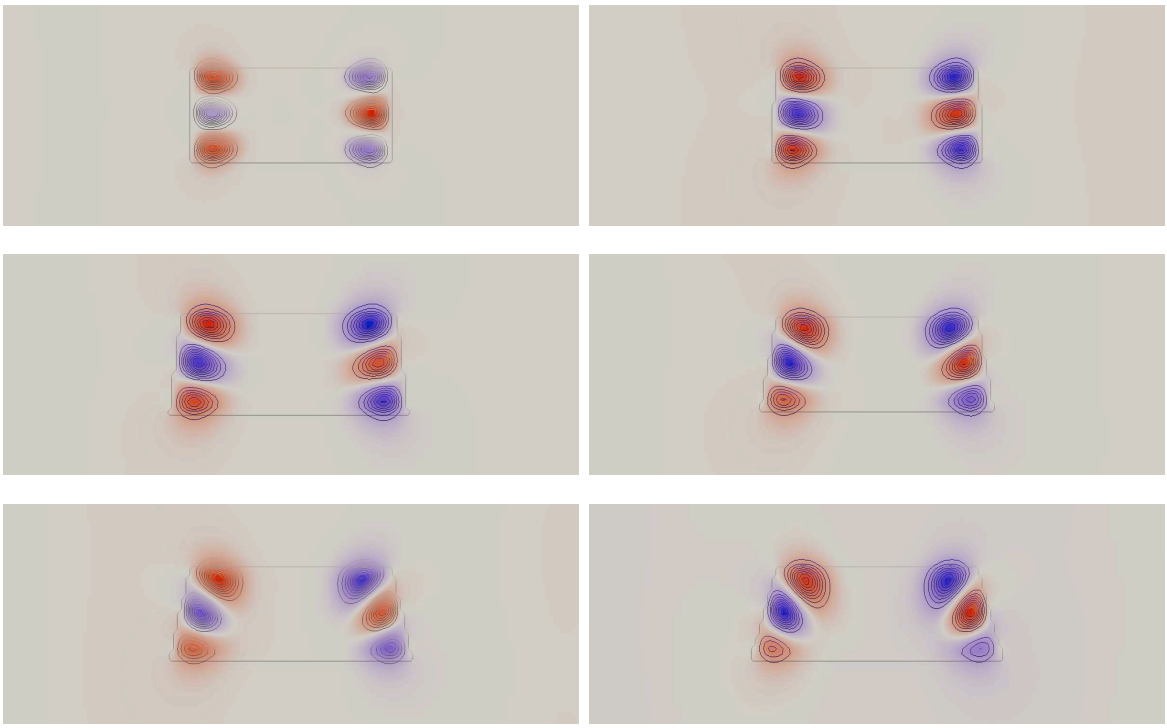

Figure 4.10: Spatial field distributions of $TE_{1,7,3}$ for different edge profiles in the y-z-plane. Top: $R_b = R_t$, $R_b = 1.05R_t$, $R_b = 1.1R_t$(from left to right). Bottom: $R_b = 1.15R_t$, $R_b = 1.2R_t$, $R_b = 1.25R_t$ (from left to right). Concentration of the field in the upper corner is clearly visible.

and 25%. With increasing bottom radius, the WGMs are aligned along the oblique side wall, while maintaining the mode order.
Additionally to Fig. 4.9, a cut along the y-z-plane shows Fig. 4.10. The grey box denotes the MD, field amplitudes are color-coded (red: +1, blue: -1) and black lines are iso-intensity surfaces. One can clearly see, that the intensity of the $TE_{1,7,3}$ is concentrated in the large-angled corner. Due to edge profile and the comparably weak spatial confinement of the high-order mode in z-direction, field in the small-angle corner couples to the environment more easy, resulting in diffraction and hence reducing of the concentration of field. In contrast, the WGM $TE_{1,10,1}$ concentrates the field in the small-angle corner (note the downward shifted maxima of the lobes in z-direction).

4.1.2 Mode Tuning with a Uniaxial Anisotropic Liquid Crystal Environment

Providing a dynamical tuning procedure is of great importance for both, current research and commercial applications. A microdisk resonator is embedded in an artificial uniaxial anisotropic environment. The quantity n_z is varied from $n_z = 1$ to $n_z = 3.5$, thus it exceeds the refractive index of the MD, while the other components are fixed to $n_x = n_y = 1$. Due to the penetration depth of the evanescent tail of the WGM, leaking into the surrounding of the MD, the coupling of the electromagnetic field to the environment can be controlled. Hence, WGMs can be spectrally tuned. Exemplarily, the accessible range for the difference between the ordinary and extraordinary refractive index of the LC 5CB is about $|n_o - n_{eo}| = 0.2$

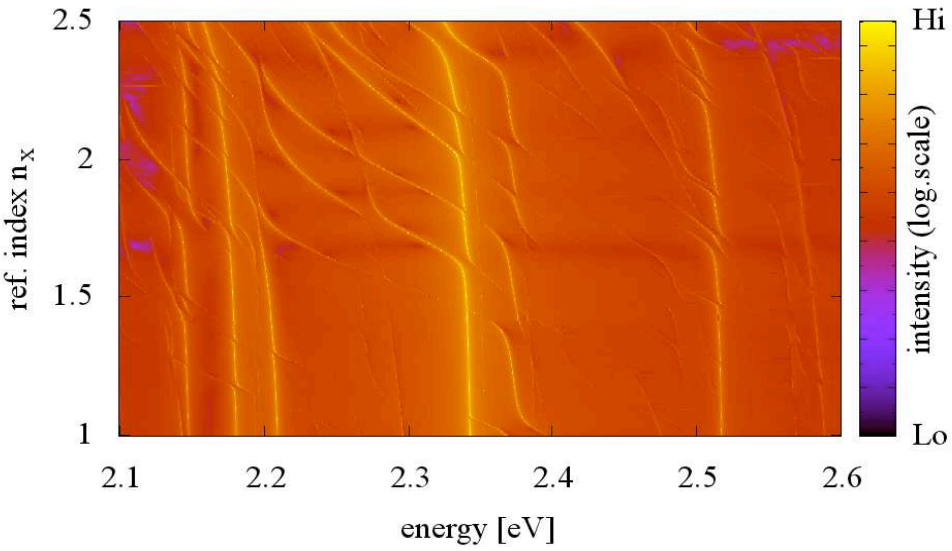

Figure 4.11: Mode map of WGMs in a microdisk resonator, embedded in an artificial uniaxial anisotropic environment. The intensity is color-coded (logarithmic scale, bright: high, dark: low), the refractive index n_z is on the vertical axis and the energy in eV is on the horizontal axis. Several anticrossing points are observed due to coupling of WGMs via the anisotropic environment.

from ≈ 1.5 to ≈ 1.7, easily controllable via an external electric field, which provides a large tuning range. Possible future materials, i.e. meta materials, may provide an even larger range. Therefore it is interesting to investigate the effect of anisotropy on the spectral properties of a resonator [115].
Figure 4.11 shows the quasi-TE spectral response of a broad energetic range for different values of n_z (vertical axis) on a mode map. The intensity on a logarithmic scale is color-coded (dark: low intensity, bright: high intensity). Two global properties are observed, when n_z is increased. First, all modes in the investigated range shift slighty to lower energies. WGMs with lower azimuthal mode order (low energy side) shift stronger than WGMs with high azimuthal mode order. Second, strong red-shifts occur, when modes of different mode order approach each other. Anticrossings emerge at the suspected crossing points and the line widths are divided equally between both resonances. Thus, the WGMs couple to each other indirectly via the uniaxial anisotropic environment. All these features are located in an experimentally accessible range for the birefringence.
An interesting fact occurs, when n_z approaches and exceeds the refractive index of the MD. As shown in Fig. 4.12, where intensity (normalized) on a logarithmic scale is plotted over the energy in meV, the usage of a uniaxial anisotropic environment (top) differs substantially from the usage of an isotropic environment. Four spectra are collimated for each case. The corresponding regime of n_z is shown on the right side. For the case of an isotropic environment, the increase of n_z results in suppression of all WGM before the value for the MD is exceeded. The condition for TIR cannot be fullfilled for this regime, therefore the confinement is lost. In contrast, when a uniaxial anisotropic environment is used, confinement is still maintained

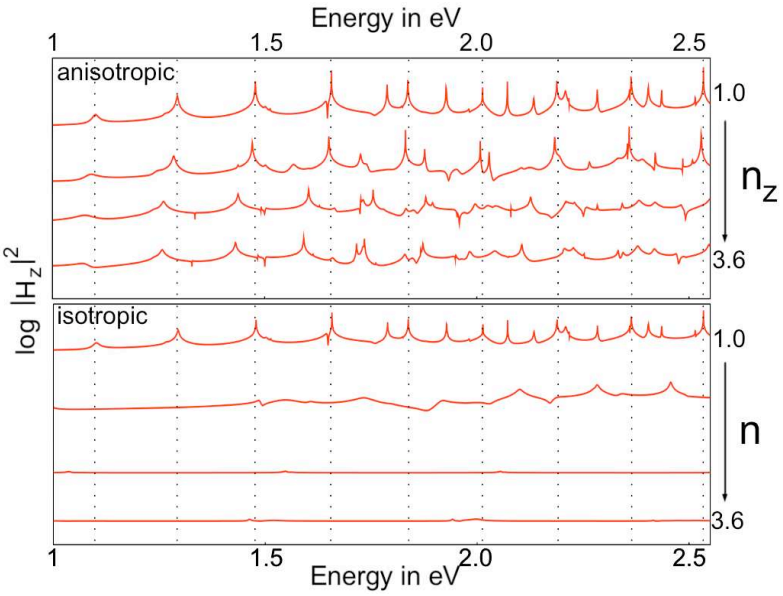

Figure 4.12: Comparison between isotropic and uniaxial anisotropic variation of the environmental dielectric permittivity. Intensity on a logarithmic scale is plotted over the energy in eV for n_z (top) and $n = 1$, 1.8, 3.4, 3.6 (bottom), respectively. In the isotropic case, no confinement is provided for $n > 1.8$, because the condition for total internal reflection cannot be fulfilled. In contrast, the anisotropic case still maintains confinement even for exceeding the refractive index of the MD. Dotted lines are a guide for the eye, showing the spectral position of selected WGMs for $n_z = 1$.

and clear peaks are observed in the spectrum. Since the resonances are only TE-like, all components of one kind of field drive the other field via the time-dependent Maxwell equations eq. (2.13). Thus, dielectric permittivities act like a potential for the electromagnetic waves (see Tab. 2.1) and the confinement is provided by the TE-components, but the coupling between the WGMs, the anticrossings in other words, are due to the interaction of the non-TE components with z-component of the environmental permittivity.

4.2 3μ Microdisk Resonator

In the previous section, a microdisk resonator with a large radius-to-thickness ratio is investigated. Now, attention is shifted towards more common circular devices. Thicknesses of some hundreds of nanometers are used to still have only the fundamental modes occupied perpendicular to the microdisk plane, so only one field maximum concentrated in the quasi-TM plane at $z = 0$ (see also Sec. 2.4.1). The radius is chosen to be comparably large to ensure, that a post does not affect the propagation of the WGM along the rim of the device. Here, the radius is $R = 3.05$ μm, thickness $t = 240$ nm and the dielectric permittivity for the disk is $\epsilon = 11.56$, corresponding to GaAs at room temperature. Figure 4.13, top, shows a spectrum of the considered MD resonator. Intensity in arbitrary units is plotted over the energy in eV. Several equidistant modes of different amplitude are observed. For first order modes, the energetic distance between modes with neighbored azimuthal mode orders $M \to M \pm 1$ can be estimated via [116]

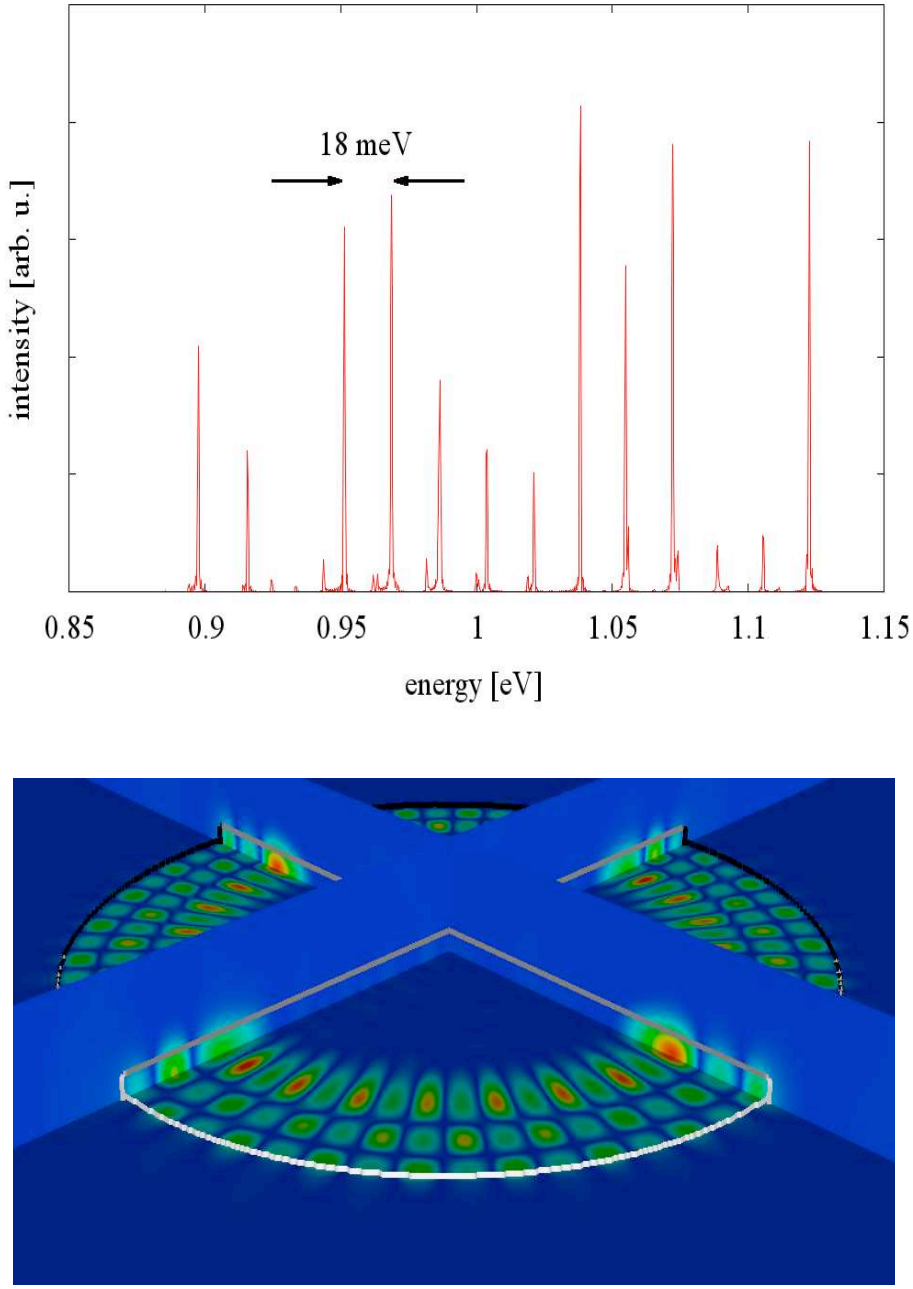

Figure 4.13: Top: Spectrum of a MD resonator ($R = 3.05$ μm) in vacuum, intensity in arbitrary units is plotted over the energy in eV. Several equidistant modes are observed. First order modes in radial direction exhibit highest intensities and shortest distance, followed by second order modes. Third order modes are not visible on the linear scale. Bottom: Spatiospectral intensity (normalized) of the WGM $TE_{3,30,1}$ (blue: low, red: high) in a 3 μm microdisk resonator, denoted by the white lines (interface between MD and environment). The mode pattern indicates, that a centered post has no influence on the field distribution due to vanishing field components in the center of the microdisk.

$$\Delta\varepsilon_{\mathrm{M}\to\mathrm{M}\pm1} = \frac{\hbar c}{nR}, \tag{4.1}$$

where n is the refractive index of the microdisk device. For the present device, the energy distance is calculated to be $\Delta\varepsilon_{\mathrm{M}\to\mathrm{M}\pm1} = 19.04$ meV. Compared to the simulated spectral response in Fig. 4.13, top, the difference between the high-intensity peaks is ≈ 18 meV, which nicely agrees. Though the values fit nicely, one has to keep in mind, that in a real system the energetic distance is smaller than the calculated value with eq. (4.1) and only approaches the calculated value for increasing energy, hence with increasing azimuthal mode order. The bottom side of Fig. 4.13 shows the normalized intensity pattern (blue: low, red: high) for the WGM $\mathrm{TE}_{3,30,1}$ of a microdisk resonator, obtained from a three-dimensional simulation. For the calculation, a slightly modified set of parameters is used. A thickness of $t = 240$ nm, radius of $R = 3\mu$m and a dielectric permittivity of $\epsilon_{\mathrm{MD}} = 11.56$, similar to GaAs at room temperature in the desired frequency range, is assumed. White lines show the interface between the microdisk and the isotropic environment (vacuum, $\epsilon = 1$). As can be seen, the intensity is concentrated along the rim of the device and therefore, neglecting a post in the simulations is justified.
The following section deals with a MD, embedded in a uniaxial anisotropic environment, mimicking a LC. Numerical results are shown, compared with the experimental data [26] and discussed.

4.2.1 Mode Tuning with a Uniaxial Anisotropic Liquid Crystal Environment: Comparison with the Experiment

The geometrical setup in the simulation is equal to Fig. 4.1. Modifications, perturbating the perfect, round shape, are not applied here. To take the birefringence of a LC environment into account, the ordinary and extraordinary refractive indices are supposed to be in the range of $1.5 \leqslant n \leqslant 1.68$, respectively [26, 101], to model rod-like, polar LC-molecules. Thus, the extraordinary refractive index is applied along the molecules, while the ordinary refractive index applies in the plane perpendicular to the disk. The computational domain has a volume of $V_{\mathrm{sim}} = 4 \times 4 \times 1R^3$ (x-, y-, z-extensions) with a spatial cell size of $\Delta x = R/100$ (cubic) with a simulation time of $t_{\mathrm{sim}} = 10$ ps. A subpixel averaging process is not applied for both, the microdisk and the environment, since the implemented algorithm supports only subpixel averaging for isotropic, dielectric media. However, these setting are sufficient to reproduce the experimental results.
Uniaxial anisotropy means, that the dielectric permittivity tensor has only non-zero diagonal elements, hence the electric field components are not mixing. As a simple model, it is assumed, that TE-like modes populate the microdisk device. Hence, E_z and $H_{x,y}$ vanish in the TE plane at $z = 0$. Therefore, the displacement field (see Sec. 2.1, eq. (2.9), neglecting the polarization field $\mathbf{P}(\mathbf{r}, t)$) can be written as:

$$\mathbf{D}(\mathbf{r}, t) = \epsilon_0 \underline{\underline{\epsilon}}(\mathbf{r})\mathbf{E}(\mathbf{r}, t) = \epsilon_0 \begin{pmatrix} n_o^2 & 0 & 0 \\ 0 & n_o^2 & 0 \\ 0 & 0 & n_{eo}^2 \end{pmatrix} \mathbf{E}(\mathbf{r}, t)\,. \tag{4.2}$$

Magnetic field components are altered by the dielectric tensor via eqs. (2.13) indirectly.
Now, applying an external electric field forces a rotation of the polar LC molecules, to align the dipole axis along the electric field. In reality, the molecules are not rotating homogeneously

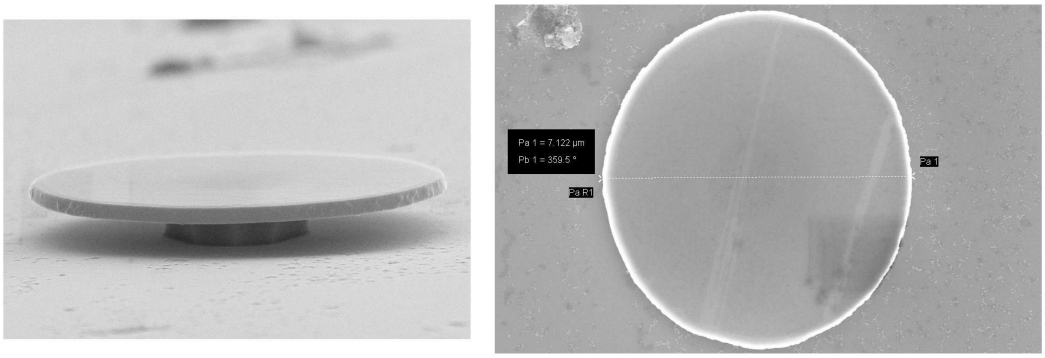

Figure 4.14: Scanning Electron Microscope image of the microdisk device, used in the experiment [81, 112]. Left: Side view. The microdisk circumference in the microdisks plane is apart enough from the post, that the influence of the post on the WGMs can be neglected. Note the perturbated rim and the edgeprofile, which significantly affects the frequency of a WGM due to non-vanishing fields. Right: Top view. The shape shows slight ellipticity and a rough interface between the microdisk device and the environment.

in the whole volume. Especially around the MD, the molecules are anchored to the surface of the device. Anchoring mechanisms of LC molecules in photonic devices is investigated in detail in [95] for LC-infiltrated photonic crystal fibers. Therefore, the area near a surface has to be treated differently. Note that within the numerical evaluation, no special treatment is applied to take effects like bend or splay from anchored molecules into account. However, the whole simulation volume is filled homogeneously with the uniaxial anisotropic material, to simulate the birefringence.
The introduction of an orientation parameter o will act as a map for the progress of orientation of the LC molecules. Assuming, that parallel orientation with respect to the TE-plane is given by $o = -1$, the orientation perpendicular to the TE-plane is equal to $o = +1$. The intermediate state, meaning a quasi-isotropic case with disordered orientation, is mapped with $o = 0$. The suggestion of an orientation parameter is closely related to a simple picture of the director field $\mathbf{n}$ and the ordering parameter S, which describes a state of a LC. Thus, $\{\mathbf{n}, S\} \rightarrow o$. Figure 4.15, top, shows the meaning of the orientation parameter schematically. From left to right, $o = -1 \rightarrow o = 0 \rightarrow o = +1$. The red rods depict the LC molecules, while blue depicts the shape of the MD.
A comparison between the experimental data (Fig. 4.15, left) and the numerical data (right) shows the intensity in arbitrary units, plotted over the energy in eV. For the sake of clarity, the numerical data show the spectral response only for the three cases of o, shown at the top. On the left, every line belongs to a higher bias (from top to bottom). Zero bias, 30 V and 100 V are marked. A strong collective shift of the WGMs is observed, for increasing the bias voltage from 0 V to 30 V. The effect of the altered orientation of the LC molecules is affecting all resonances. Above 30 V, a saturation in the spectral shift occurs, after a spectral repositioning of $\Delta\varepsilon \approx 5$ meV. The numerical data (right) cannot reproduce the saturation effect properly, since the orientation parameter is only defined between $o = -1$ (parallel) and $o = +1$ (perpendicular). However, the trend of the spectral shift is in very good agreement with the experiment. A global shift of all WGMs is clearly visible. Assuming, that the corresponding WGM, observed

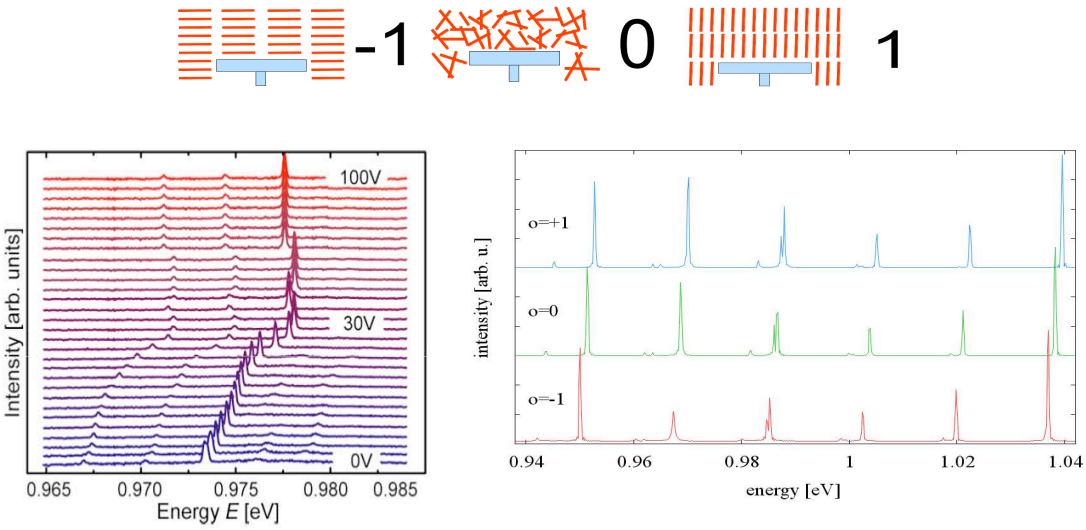

Figure 4.15: Top: Alignment of the LC molecules according to the orientation parameter o: $o = -1$, parallel orientation of the LC molecules. $o = 0$, quasi-isotropic case. $o = +1$, perpendicular orientation of the LC molecules. Bottom left: Experimental data. Intensity in arbitrary units is plotted over the energy in eV. The chosen energy range shows 5 different modes. Two main features are observable. First, with increasing bias, starting at 0 V up to 100 V (labels on the right), all modes collectively shift towards higher energies. Second, above 30 V, a saturation effect emerges. Bottom right: Numerical data from the FDTD simulation. Intensity in arbitrary units is plotted over the energy in eV. Special values of the orientation parameter o are chosen: $o = -1$, parallel orientation of the LC molecules (red). $o = 0$, quasi-isotropic case (green). $o = -1$, perpendicular orientation of the LC molecules (blue). The trend of the (collective) spectral shift is reproduced nicely.

in the experiment, agrees with the numerically calculated WGM at $\varepsilon = 967.408$ meV, the reorientation of the LC shifts the resonance to $\varepsilon = 970.196$ meV, resulting in a shift $\Delta\varepsilon = 2.788$ meV.

A detailed view shows, that first order radial modes shift less than higher order radial modes. Additionally, the higher the azimuthal mode order, the less is the shift. Due to a stronger spatial confinement, first order modes in radial direction have less field in the environment compared the higher order modes. Therefore, the coupling of the electromagnetic field to the LC environment is weaker. Figure 4.16 shows the shift of 1^{st}-order WGMs with low (left) and high (right) azimuthal mode order, $TE_{1,35,1}$ and $TE_{1,48,1}$, respectively. Intensity in arbitrary units is plotted over the energy in eV. For both cases, the energy range is chosen to be the same size to show the difference in the shift from the parallel orientation (red) to the perpendicular orientation (blue), passing the disordered state (green). As can be seen, both modes shift differently. According to the penetration depth of the evanescent tail into the LC environment, which is shorter for the WGM with higher azimuthal order, the resonance in the right graph shifts less than the resonance in the left graph. Black labels denote the shift of the blue curve with respect to the red curve. For low azimuthal mode order, the shift yields $\Delta\varepsilon = 3.21$ meV, while the shift for the high azimuthal mode order is $\Delta\varepsilon = 2.88$ meV. Hence, the azimuthally low-ordered mode can be tuned 10% more.

Due to the observed shift compared with the experiment, it is concluded that the LC initially was in a parallel alignment, at least within coherence length around the microdisk. With bias applied, the LC molecules start to rotate due to their dipole moment to orientate along the

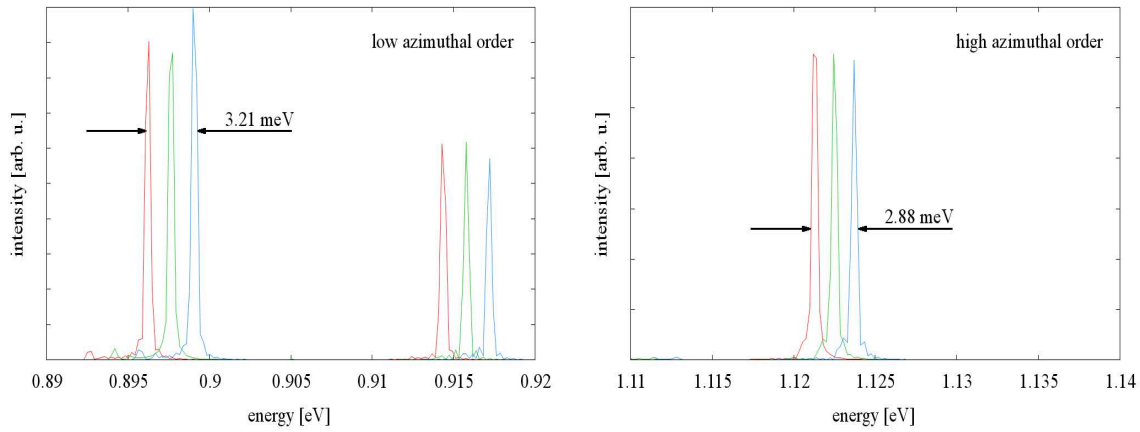

Figure 4.16: Spectral response of the MD with uniaxial anisotropic environment. Intensity in arbitrary units is plotted over the energy in eV. Red: $o = -1$, green: $o = 0$, blue: $o = +1$.Left: spectral shift of $TE_{1,35,1}$ (left) and $TE_{1,36,1}$ (right). A shift of $\Delta\varepsilon = 3.21$ meV occurs. Right: spectral shift of $TE_{1,48,1}$. A shift of $\Delta\varepsilon = 2.88$ meV occurs.

electric field. According to the progress of the orientation, the refractive index background changes, affecting the evanescent field of the WGMs. With increasing twist, ordinary and extraordinary refractive index exchange due to the perpendicular alignment or the LC molecules. The simple model using the orientation parameter o gives a satisfying explanation for the spectral shift of the resonance and reproduces the experimental data very well.
However, two main differences emerge. First, the spectral shift of the WGM due to the orientation of the LC molecules in the experiment is approximatively twice as large as in the theory. Second, the spectral position of the investigated eigenmodes are different. Both differences are explained by a non-perfect shape of the microdisk. In Sec. 4.1.1, the effect of a non-perfect cylindrical shape on the resonance of the microdisks eigenmodes is discussed. All kinds of introduced perturbations on the perfect shape have significant influence on the frequency. A view on Fig. 4.14, showing a SEM image of the device, used for the experiment [26, 81, 112], reveals a rough circumference, as well as a slight elliptically shape. While the rough surface acts as a scatterer for the electromagnetic field and therefore induces additional loss and frequency shifts, the latter introduces additional modes with increasing mode orders in z-direction when the slope of the side wall decreases. Thus, the possibility for comparing different modes in the experimental and numerical data is at place. The estimation eq. 4.1, however, is only valid for first order radial modes, but gives a good approximation, for which modes one has to look for in the experimental data.

Chapter 5

Photonic Crystal Cavities

This chapter deals with the tuning possibilities of PhCC modes in two-dimensional PhC structures. Tuning in this sense means, to change the spectral properties of a resonance, say the frequency and the cavity decay time. Therefore, different aspects are taken into account. First, mode tuning is possible via the modification of the PhC slab itself. The effect is a permanent tuning, mostly effecting all resonances in the system. Permanent tuning can be realized in different ways. One can locally modify the slab properties, the PhC parameters like lattice constant or the air hole radius for example. Another way is to evaporate (or with other epitaxial methods) an additional layer, either only on the top surface of the PhC slab, or on all surfaces. The latter would have a significantly larger effect on the whole system, since the conditions for not only the TIR are changed, but also for the Bragg conditions for the in-plane confinement of the light.
The goal of the tuning mechanism addresses some different points: first, modifying the cavity decay time. To have high Q-factors is essential to investigate strong coupling between a cavity mode and a single QD [4, 117] or i. e. a nitrogen vacancy center [118]. Ultra-high Q-factors can be realized with a double heterostructure, say a waveguide with a locally changed lattice constant and air hole radii [13]. On the other hand, when coupling cavities among themselves, the injection of the photons from one to another cavity is important. Therefore, cavities with a lower Q-factor are already utilized for trapping from a coupled waveguide to a single defect cavity, and subsequent emission of the photon [119]. There is already a proposed method to dynamically change the Q-factor for efficient in- and outcoupling of photons into a cavity from a close waveguide [120]. Additionally, the usage of the optoelectronical device also dictates the importance of the tuning range of the resonance. Other tuning mechanisms can be realized via nonlinearities, where local variations of the refractive index occur due to the Kerr effect or thermo-optical effects [121].

5.1 Preparations

To obtain reasonable results from the simulations, calculations concerning the spatial discretization, spatial and temporal simulation domain are performed. The discretization is a crucial point when calculating structures with strong curvatures, like in the case of the PhC, since the air hole radii in general are smaller than the wavelength of the light in the PhCC. Hence, when the spatial resolution is not sufficiently good, the waves in the PhC cannot sample the curvature sufficiently, thus the structure is not interpreted as a circle. This dramatically changes the spectral properties, because small deviations from the perfect circular structure mean to simulate a different geometry. The spatial computational domain has, if chosen too small, influence on the spectral response of the geometry, too. A resonant mode in a cavity has evanescent field contributions, which penetrate the surroundings in all three dimensions. When the evanescent parts pierce the CMPL, the fields are leeched out of the simulation volume, meaning to reduce the energy in the system and hence to e.g. reduce the Q-factor. For the spectral analysis, the *Harmonic Inversion*, see Sec. 2.8, is used [105]. Despite this method provides converged results for short simulation times, this is not independent of the decay time of a resonance, for example. Figure 5.1 shows the behavior of a specific resonance and its decay, thus Q-factor, in dependence of the in-plane size of the simulation domain and the spatial grid resolution. A $L3$-type PhCC in a hexagonal lattice with a lattice constant of $a = 260$ nm, air hole radius $r = 0.35 \times a$ ($= 91$ nm), slab thickness $t = 0.692 \times a$ ($= 180$ nm) made from GaAs ($\epsilon = 11.56$) is considered. A size- and resolution-stable frequency and Q-

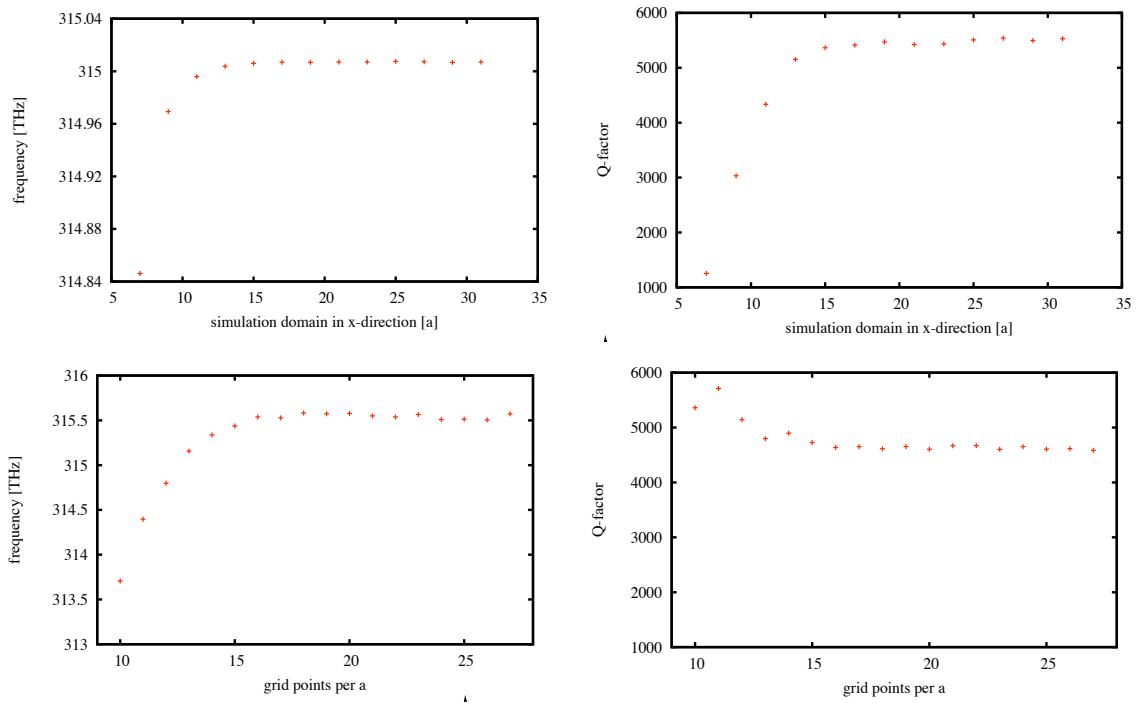

Figure 5.1: Determination of the simulation domain parameters. Top: minimum size determination along the x-direction. Frequency (left) and Q-factor (right) are plotted versus the length in units of the lattice constant. A size of 15 lattice constants is found to be necessary to obtain sufficient results. Bottom: determination of the sampling rate per lattice constant. Frequency (left) and Q-factor (right) are plotted versus the number of grid points per lattice constant. Most influencing factor here is the sampling rate of the air holes, to let a propagating wave interpret the interfaces to be perfectly circular shaped. A sampling rate of 16 grid points per lattice constant is found to be sufficient.

factor is obtained for a sampling rate of 16 grid points per lattice constant (spatial resolution $dx = a/16$) and at least 15 lattice constants extension in x-direction. To be sure, 19 lattice constants extension are chosen for further investigations. The y-direction is supposed to have the same number of air holes. For the z-direction, a size of $2 \times a$ is chosen, which is sufficient for the numerical calculations (not shown).

5.2 Permanent Mode Tuning of the $L3$ Photonic Crystal Cavity

The method of choice to tune the spectral properties of resonances from a cavity in a two-dimensional PhC slab is the method of gentle confinement [3]. There, the Q-factor is increased by almost one order of magnitude, while maintaining the effective modal volume V_{eff}. Both quantities, the Q-factor and the effective modal volume, enter the Purcell-factor as the fraction Q/V_{eff}, which determines the enhanced spontaneous emission in a weakly coupled cavity-quantum dot system [9]. Hence, the cavity decay time directly influences the Purcell factor.
To understand the method of gentle confinement, a k-space analysis is performed. Assume a one-dimensional dielectric slab with a finite extension of length L in x-direction and thickness t in z-direction, surrounded by perfect mirrors for $|x| \leqslant L/2$ and vacuum for $|z| \leqslant L/2$. Two

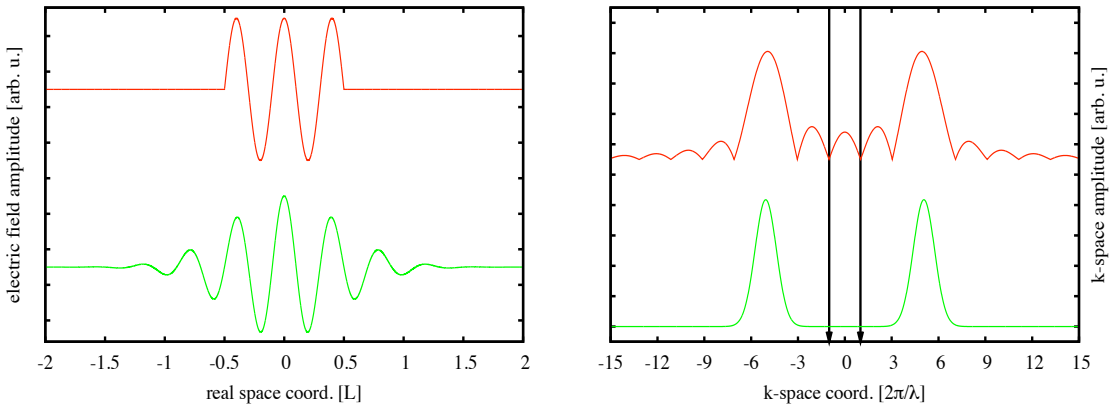

Figure 5.2: Principle of the method of gentle confinement, after [3]. Left: two different kinds of (hypothetical) wave functions, confined in a one-dimensional cavity of length L, cladded by vacuum: a step-like envelope function (red) and a Gaussian envelope function (green), modulated with a cosine with wavelength $\lambda = L/2.5$. Amplitude in arbitrary units is plotted over the spatial coordinate in cavity lengths L. Right: spatial FT of wave functions on the left. Absolute value in arbitrary units is plotted versus the wave vector in units of $2\pi/\lambda$. The black arrows indicate the left and right border of the light cone. For the FT of the step-like envelope, large contributions inside the light cone appear, while for the Gaussian envelope function, almost no contributions are located inside the light cone.

cases concerning the wave function of the confined field, shown in Fig. 5.2, are now considered. The left side shows the electric field distribution in x-direction. A step-like envelope function (red curve) and a Gaussian envelope function (full width at $1/e$, green curve), modulated with a cosine function with wavelength $\lambda = L/2.5$ are used. Note that the step-like envelope has a discontinuous transition at the interface $\pm L$, while the Gaussian envelope has a smooth profile and is continuous at the interface. The right side depicts the spatial FT (absolute value) of the field profiles in arbitrary units. Black arrows indicate the light cone barriers for $\lambda = L/2.5$ at $k = \pm 1$ (in units of $2\pi/\lambda$). The FT of the step-like function has non-zero contributions for all wave vectors, while the Gaussian profile has only contributions around the resonance.
Regarding the conservation law for the wave vector $\mathbf{k}$, a wave can leak out of the cavity, when the tangential component of $\mathbf{k}$ (here $|k_x|$) is $0 \leqslant |k_x| \leqslant k_0$ [3]. The condition for TIR at the cavity-vacuum interface is not fulfilled. For $|k_x| > k_0$, the conservation law is violated, hence the wave cannot leak out of the cavity and is highly confined. Thus, generating a more gentle envelope for a field distribution of a confined mode yields a higher Q-factor.

Utilizing the method of gentle confinement to the $L3$-type PhCC (the PhC slab is laying in the x-y-plane and the cavity is aligned along the x-axes), the geometrical setup results in Figure 5.3. The two-dimensional dielectric slab (grey block) with a hexagonal array air holes in a three-dimensional computation volume (white box) is shown. A line defect is introduced by leaving away three air holes in a line (center), a $L3$-type cavity. On the left side, the unmodified geometry can be seen, while on the right, the modified geometry is depicted. The outer holes on the left and right side of the line defect are shifted away from the cavity center by a shift-to-lattice constant ratio $s/a = 0.3$ to make the modification clearly visible. The lattice constant of the hexagonal air hole array is $a = 300$ nm (hole-to-hole distance along x-direction), the slab thickness-to-lattice constant ratio is $t/a = 0.6$ and the hole radius-to-lattice constant ratio is $r/a = 0.3$. As a dielectric permittivity for the slab, a value of $\epsilon = 10.595$ is chosen, which is

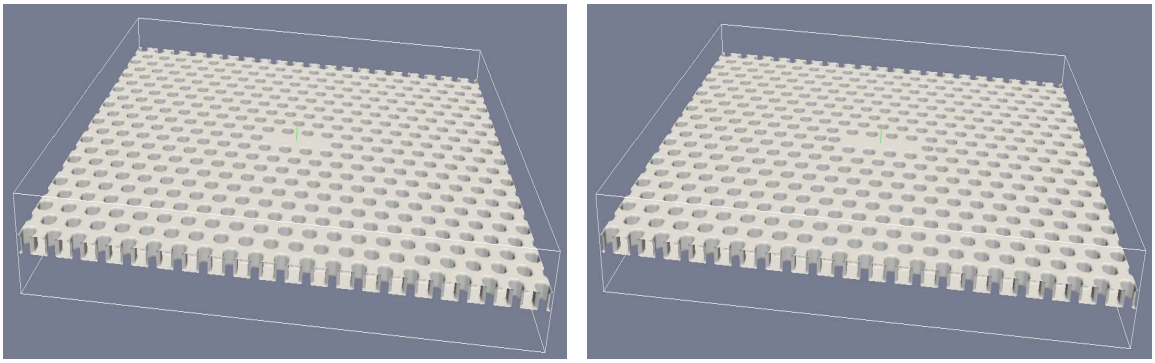

Figure 5.3: Modification process of the Q-optimization of the $L3$-type PhCC. Left: Unmodified geometrical setup of the simulation volume (white box). The dielectric slab (light grey block), permittivity $\epsilon = 10.595$, is perforated with air holes in a hexagonal lattice with a lattice constant $a = 300$ nm, slab thickness $t = 180$ nm (=$0.6a$) and air hole radius $r = 90$ nm (= $0.3a$). Three missing air holes in a line in the center introduce the $L3$-type cavity (along x-direction). Right: Air hole shift of the nearest holes located left and right at the ends of the cavity (x-direction). For clarity, a shift of $s = 90$ nm (= $0.3a$) is chosen.

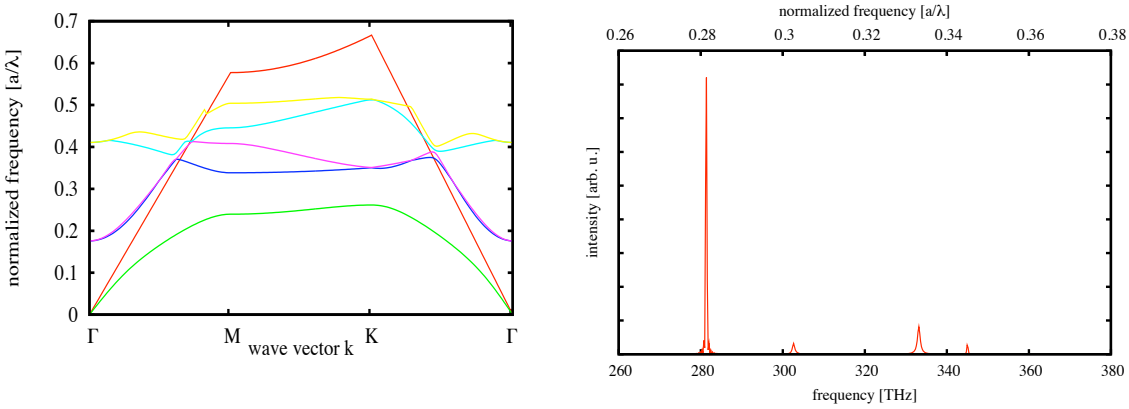

Figure 5.4: Left: Band structure for the investigated PhC (normalized frequencies vs. the wave vector). High-symmetry points in the irreducible Brillouin zone are marked. The first 5 bands (1: green, 2: blue, 3: magenta, 4: turquoise, 5: yellow), including the light cone (red) are plotted. Note the band gap between the first two bands. Calculations are performed with *MPB* [82]. Right: Spectral response of the PhCC. Intensity in arbitrary units is plotted vs. frequency in THz (lower axes; the upper axes shows normalized frequencies in units of a/λ_0, λ_0 is the vacuum wavelength). Used parameters are $a = 300$ nm, slab thickness $t = 180$ nm (=$0.6a$) and air hole radius $r = 90$ nm (= $0.3a$). For the band structure calculations, supercell of 4 unit lengths in z-direction, 16 points per lattice constant for the real space sampling and 64 k-points between high-symmetry points are used.

similar to a GaAs slab at $T = 4$ °K [122]. The corresponding photonic band structure is shown in Fig. 5.4, where normalized frequencies are plotted over the wave vector. High-symmetry points in the irreducible Brillouin zone are marked. Note the band gap between the first two bands.

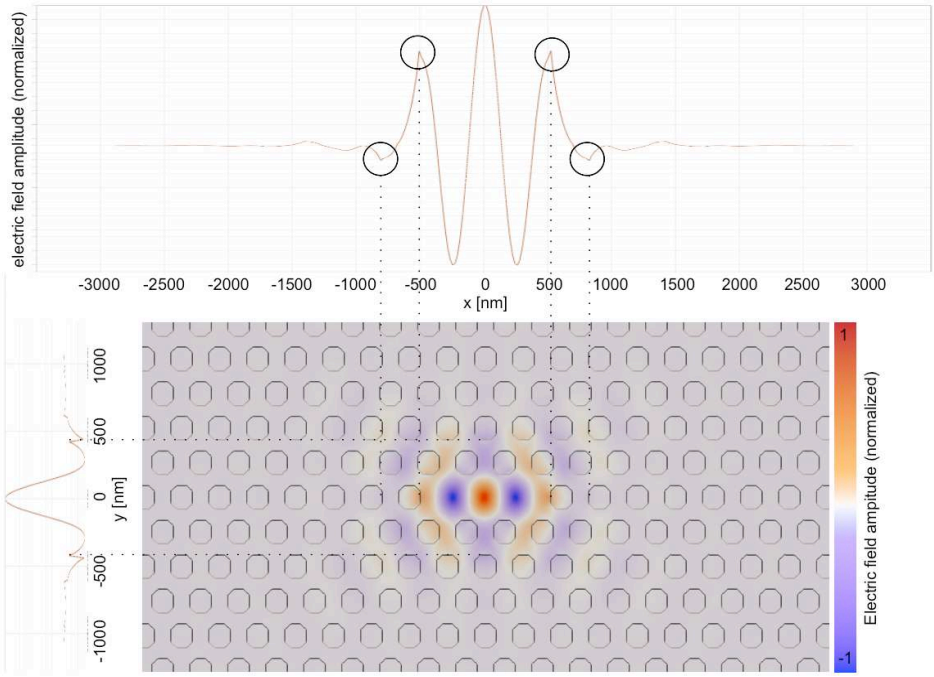

Figure 5.5: Field distribution in the TE-plane of the y-component for the fundamental mode for the unmodified $L3$-type PhCC. Cutting along the y-axes at $x = 0$ (left) and along the x-axis at $y = 0$ (top) shows discontinuities at the interfaces between the air holes and the defect region in the dielectric slab (black circles). The dotted lines are a guide for the eye.

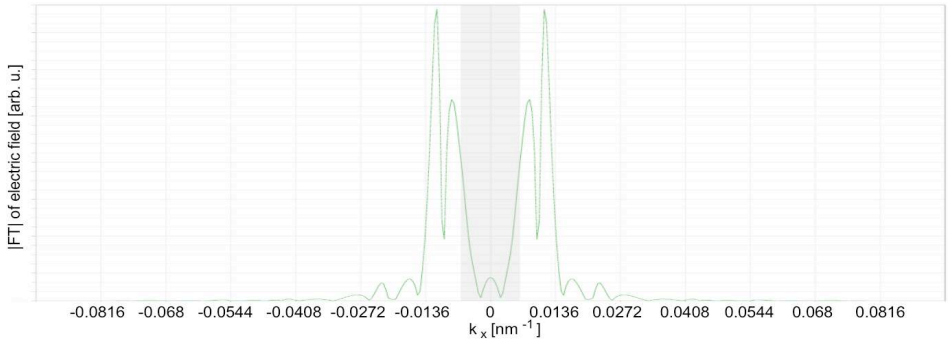

Figure 5.6: Intensity in reciprocal space of the fundamental mode for the unmodified PhCC. **k**-space intensity (vertical axis, arbitrary units) is plotted over the x-component of the wave vector in reciprocal nm. The grey-shaded area denotes the light cone. Note the contributions of the **k**-space intensity within the light cone.

In this chapter, the focus lies on the fundamental mode, since this mode provides already the highest Q-factor even without modification. Spectrally, this mode is located at the low frequency side of the band gap at $f = 281.3$ THz (see Fig. 5.4) with a decay rate of $\Gamma = 219.77$ GHz, resulting in a Q-factor of slightly above $Q = 4000$. The spatial field distribution of the y-component of the electric field in the TE-plane of the slab (at $z = 0$) is shown in Fig. 5.5. The two-dimensional, color-coded plot shows the field distribution normalized to 1 (red: 1, blue: -1) with a superimposed PhCC lattice (grey circles). Note that this is only a part

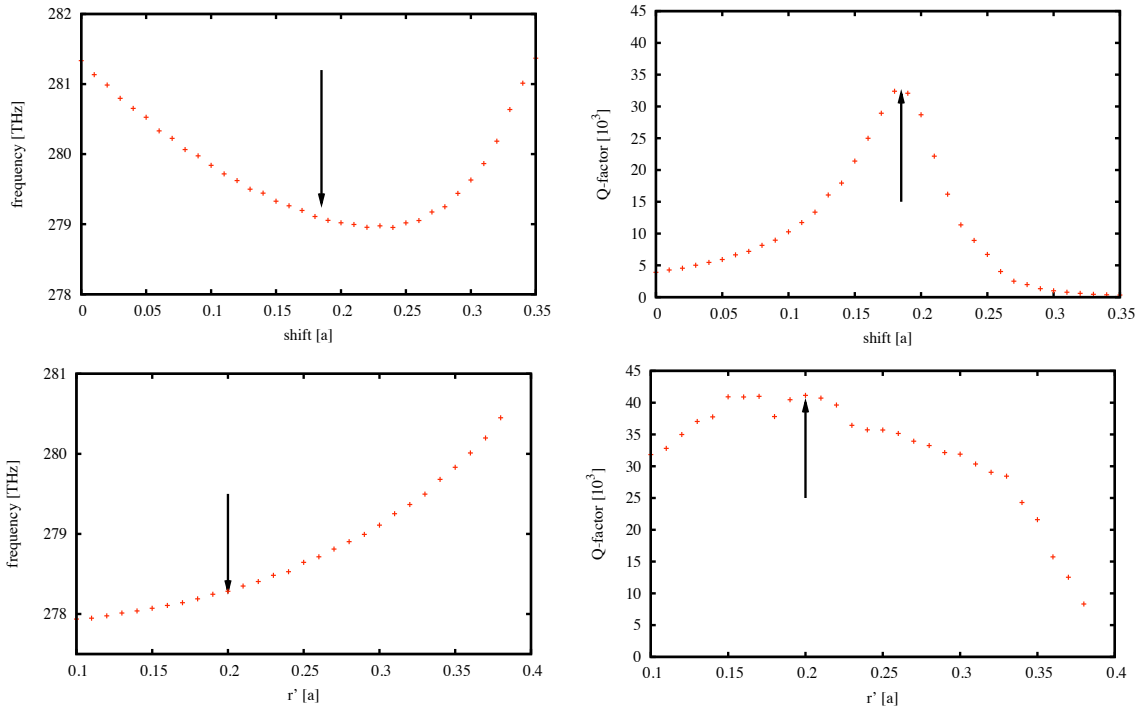

Figure 5.7: Modification of the PhCC of $L3$-type for Q-optimization: shift (s) and radius variation (r') of the first outer air hole. Top line: resonance (left) and Q (right) alteration due to the first air hole shift-to-lattice constant ratio $0 \leqslant s/a \leqslant 0.35$, $\Delta s/a = 0.01$. The resonance is shifted successively towards the upper band edge of the first band gap, where it reaches its minimum at $s/a = 0.23$. The maximum in the Q-factor, $Q \approx 3.3 \times 10^4$, is reached at for $s/a = 0.185$, indicated by black arrows. Bottom line: resonance (left) and Q (right) alteration du to the first air hole radius-to-lattice constant ratio $0.1 \leqslant r'/a \leqslant 0.38$, $\Delta r'/a = 0.01$. A continuous increase in the resonance is observed. The Q-factor reaches his maximum at $r'/a = 0.2$, $Q \approx 41500$, marked with a black arrow.

of the simulation volume. Following the dotted line to the left side, a cut along the y-axes ($x = 0$) is shown, while when following the dotted lines upwards, a cut along the x-axes ($y = 0$) is depicted. The spatial extent is given in nm. The field is spatially concentrated in the defect area, as it is expected, and the envelope of the electric field distribution has already a Gaussian-like shape. When the field reaches a discontinuous change in the permittivity (the dotted line are a guide for the eye), the slope changes drastically, too. Therefore, the Gaussian behavior is perturbated. Figure 5.6 depicts the absolute value of the spatial FT of the x-cut from Fig. 5.5 in arbitrary units, plotted over the wave vector in x-direction in inverse nm. The grey-shaded area denotes the light cone for the fundamental mode. Non-zero contributions are locate within the light cone.

Following the method of gentle confinement, the defect area will be modified. Like in [3], the focus lies on the first-neighbored air holes. The outer air holes are successively shifted away from the cavity center in steps of $\Delta s/a = 0.01$ from $0 \leqslant s/a \leqslant 0.35$. This modifies also the effective length of the cavity (along x), hence an additional effect is obviously a decrease in the resonance frequency. Thus, the hole shift pushes the resonance closer towards the upper edge of the 1$^{\text{st}}$ band. Figure 5.7 shows the effect of the modification of the first air hole on the spectral properties. In the top line, the resonance and Q-factor change is plotted versus

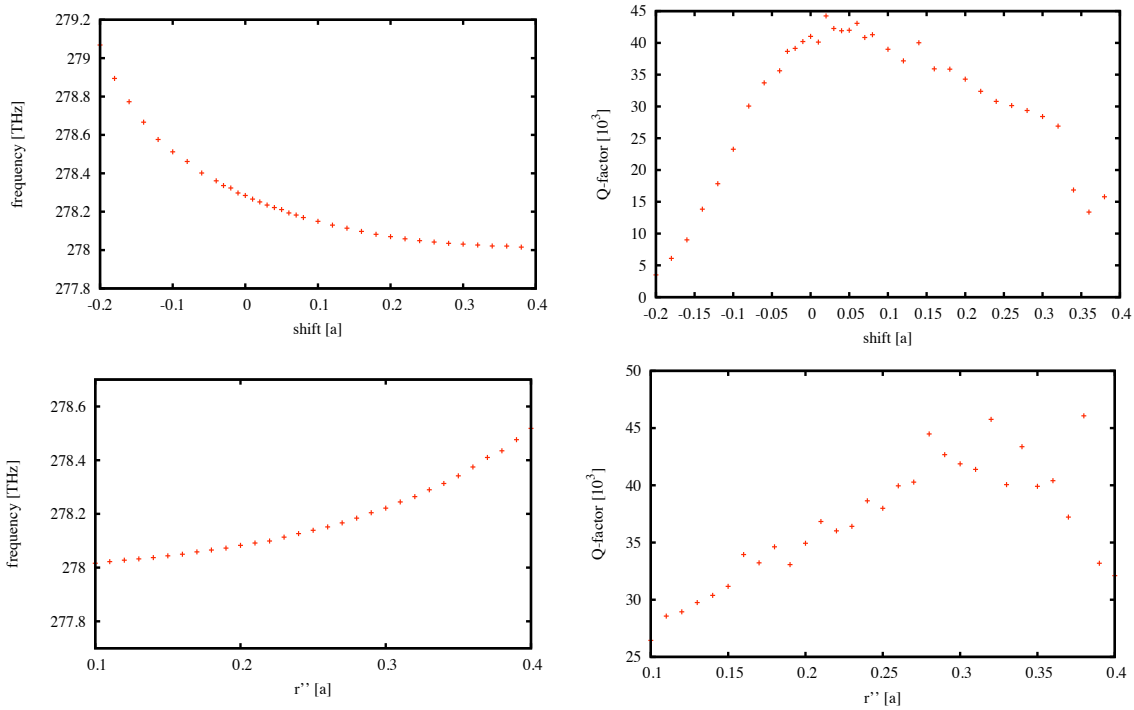

Figure 5.8: Modification of the PhCC of $L3$-type for Q-optimization: shift (s) and radius variation (r') of the second outer air hole. Top line: resonance (left) and Q (right) alteration due to the second air hole shift-to-lattice constant ratio $0 \leqslant s/a \leqslant 0.35$, $\Delta s/a = 0.01$. The resonance is shifted successively towards the upper band edge of the first band gap, where it undergoes saturation for $s/a = 0.4$. The maximum in the Q-factor appears slightly above $s/a = 0$ with strong deviations, altering around the maximum reached with the first air hole modification (a more fine sampling of the region around $s/a = 0$ did not show any clear maximum). Bottom line: resonance (left) and Q (right) alteration due to the second air hole radius-to-lattice constant ratio $0.1 \leqslant r''/a \leqslant 0.38$, $\Delta r''/a = 0.01$. A continuous increase in the resonance is observed. The Q-factor starts spreading for $r'/a \geqslant 0.15$, hence no clear maximum is found. Numerical uncertainties are assumed to be the reason.

the shift of the air hole in units of the lattice constant, starting from $s/a = 0$ to $s/a = 0.35$. A decrease of the resonance is observed, about 0.7%, accompanied by a drastic change of the cavity decay time. The Q-factor increases from approximatively 4000 to 33000 for a shift-to-lattice constant ratio of s/a=0.185. Furthermore, a decrease of the radius-to-lattice constant ratio r' decreases the frequency by an amount of approximatively 1 THz, while increasing the Q-factor to 41500. Hence, the modification of the first air hole results in an overall increase of the photon life time about one order of magnitude. In [123], an expanded method of the gentle confinement is proposed, regarding the next-nearest neighbors of the $L3$ defect. Second and third air hole modification yield an improvement of 166% compared with [3]. However, numerical evaluations of further modifications, the shift and radius variation of the second air hole show no further improvement for the chosen set of parameters. Figure 5.8 plots the frequency change and Q-factor variation versus the shift of the second air hole in units of the lattice constant in the top line, like in Fig. 5.7.

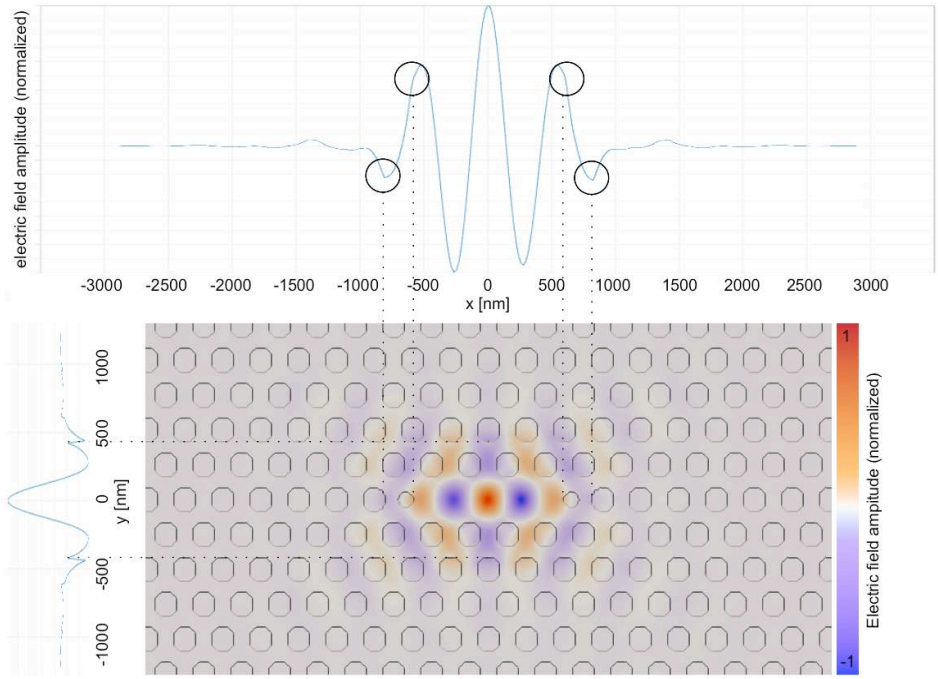

Figure 5.9: Field distribution in the TE-plane of the y-component for the fundamental mode for the modified $L3$-type PhCC. A cut along the y-axes at $x = 0$ shows no difference (left). However, cutting along x-axis at $y = 0$ (top) shows a continuous field distribution (black circles) due to the shifted air holes. The dotted lines are a guide for the eye.

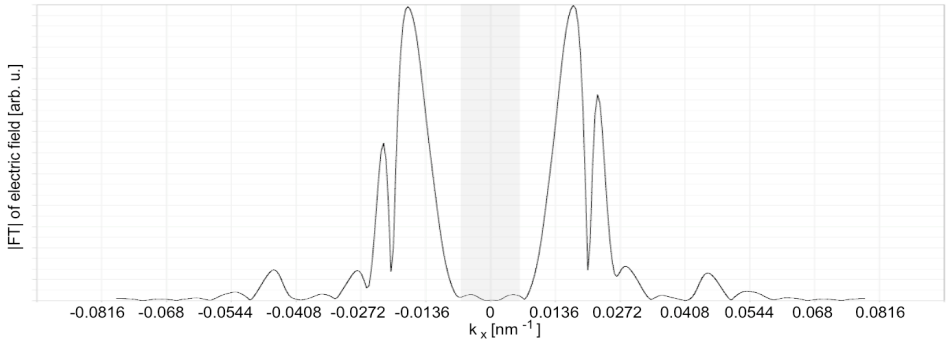

Figure 5.10: Intensity in reciprocal space of the fundamental mode for the modified PhCC. **k**-space intensity (vertical axis, arbitrary units) is plotted over the x-component of the wave vector in reciprocal nm. The grey-shaded area denotes the light cone. Though the fundamental mode is spectrally shifted, this slight deviations are not visible on this scale. Note the clear reduction of the **k**-space intensity within the light cone, compared with Fig. 5.6.

Figure 5.9 and 5.10 show the field distribution in the x-y-plane in real space and k-space, respectively, for a modified defect region, similar to Figs. 5.5 and 5.6 for the unmodified case. For modification, the parameters for the largest Q-factor are chosen, therefore $s = 0.185 \times a$ and $r' = 0.2 \times a$. The cut along the x-axes shows clear reduction of the perturbation of the envelope function from a perfect Gaussian shape (black circles), resulting in a more gentle confinement. In contrast to Fig. 5.10, the intensity of the Fourier spectrum for the modified

case (black) shows a substantial difference around the light cone: the intensity profile itself remains approximatively the same, but it is pushed away from the light cone. Thus, less contributions are inside the light cone, meaning, that less modes couple to vacuum modes. Therefore, the Q-factor is increased. For better comparison, the cuts in real and k-space along the x-axes are plotted together in Fig. 5.11, top. Note the strong differences in the black circles while the rest of the field distribution is mostly unchanged. Since the frequency shifts due to the modification, the light cone also changes. The differences between the light cone for the fundamental mode is not visible on this scale.
The reciprocal space intensity for the fundamental mode in the k_x-k_y-plane is shown in Fig. 5.11. The normalized intensity is color-coded (red:1, blue:0), leaky modes are located inside the light cone (white circle). On the left side, the k-space profile for the unmodified case is shown. Inside the light cone, non-zero contributions limit a high Q-factor (white shade, stretching along k_y). On the right side, the k-space intensity is shown for the modified structure. Significantly less contributions are located within the light cone.
In Fig. 5.12, the band structure of the given PhC is shown again, including the tuning range in a dark-grey-shade. The photonic band gap is shown in a light grey shade. Spectrally, the fundamental mode can be tuned above half the band gap size with only shifting the air holes outward of the defect area. The left part shows a more detailed band structure around the photonic band gap. Figure 5.13 compares the applied modification steps, normalized to 1 for better comparison. Red shows the resonance of the fundamental mode without modification, in green the resonance for an outward shift of the 1st air hole is depicted and blue is the resonance with outward shift with additional radius decrease. The decrease of the line width of more than one order of magnitude can be seen, resulting in an increase of the Q-factor from 4000 to 41500.

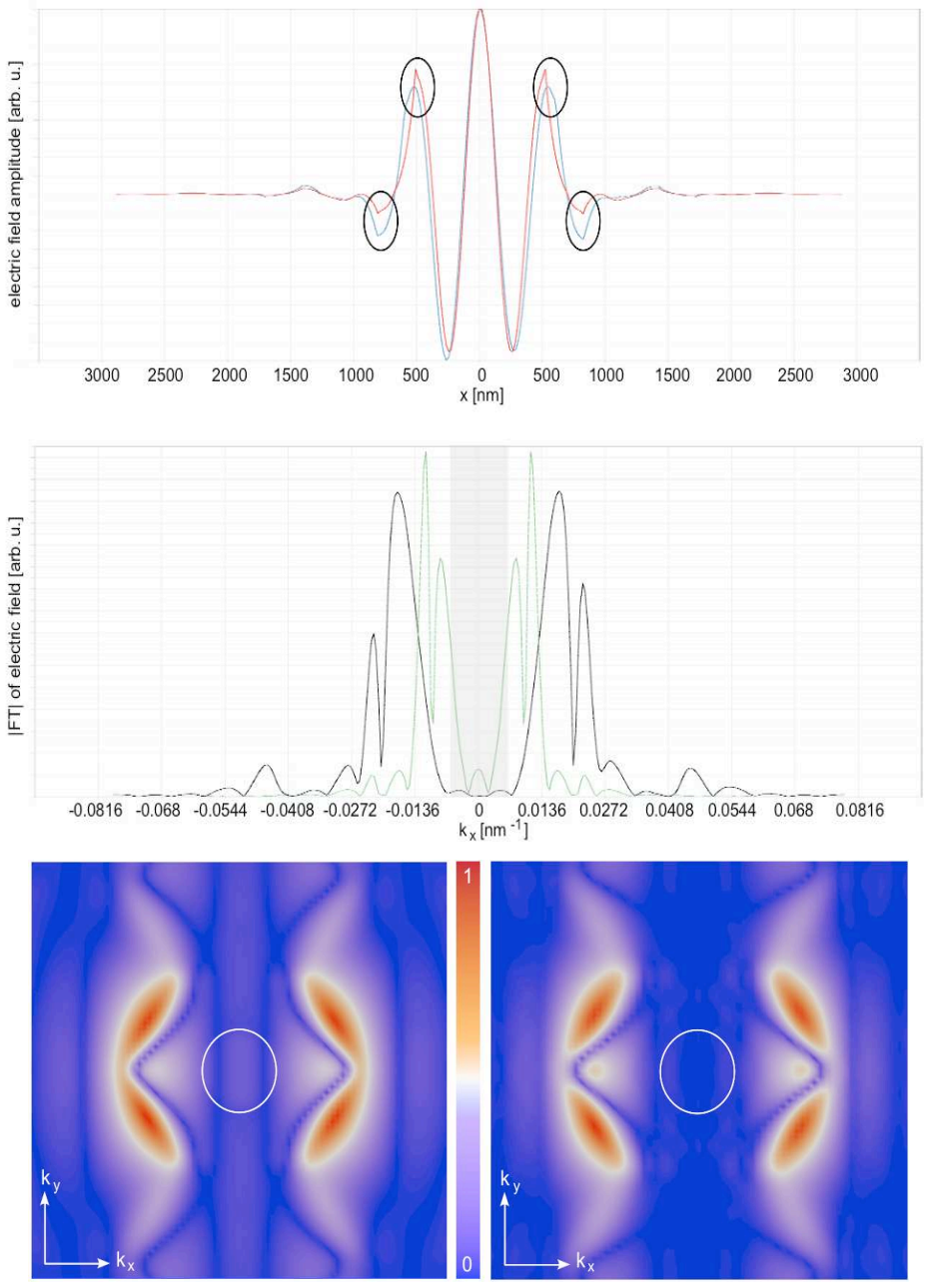

Figure 5.11: Electric field Distribution for the unmodified (red) and modified (blue) case (top), real part of $E_y(\omega, x)$ versus the x-coordinate in nanometer. The black circles show the effect of the shift of the first outer air hole. Middle: Cut through the spatial FT of the y-component of the electric field along x-direction. Intensity versus wave vector k_x in inverse nanometers, for the unmodified (green) and modified (blue) cavity. The grey shaded area denotes the light cone (since the frequencies of the fundamental mode with and without modification differ only slightly, a difference in the width of the light cone is not visible on this scale). Clearly visible is the reduction of contributions inside the light cone. Bottom: spatial FT of the y-component (intensity) of the electric field in the x-y-plane. The white circle indicates the light cone. Left: unmodified cavity, right: modified cavity. A reduction of the contributions inside the whole light cone are apparent (along the y-direction), pushed outwards along the x-direction.

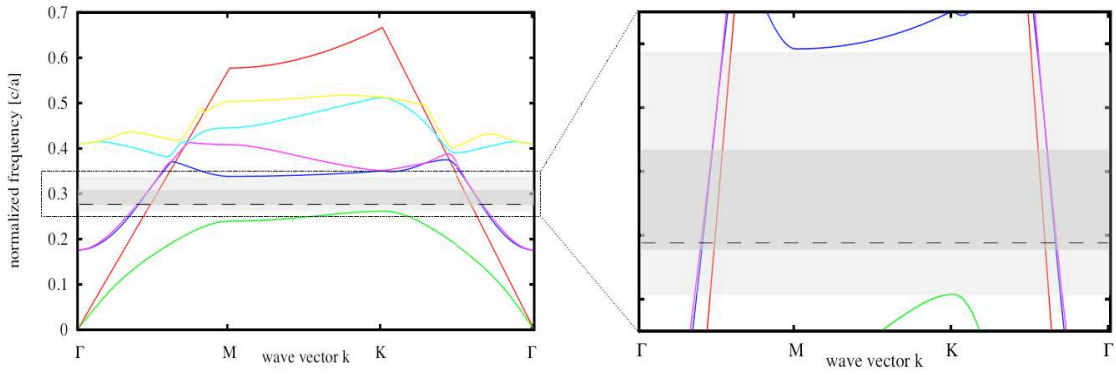

Figure 5.12: Band structure for the investigated PhC with lattice constant $a = 300$ nm, slab thickness $t = 180$ nm (=0.6a) and air hole radius $r = 90$ nm (= 0.3a). In z-direction, a supercell of 4 unit lengths is used. Left: First 5 bands (1: green, 2: blue, 3: magenta, 4: turquoise, 5: yellow), including light cone (red), plotted is a normalized frequency [c/a] vs. $|\mathbf{k}|$. Right: Zoom around the 1st band gap. High-symmetry points of the first Brillouin zone are marked on the horizontal axes. The light grey-shaded denotes the band gap, the dark grey shaded-area shows the modification range of the resonance of the fundamental mode with hole shifting and air hole radius modification of the first air hole. The black dashed line shows the optimized fundamental mode frequency with $Q \approx 41500$. Calculations are performed with *MPB* [82].

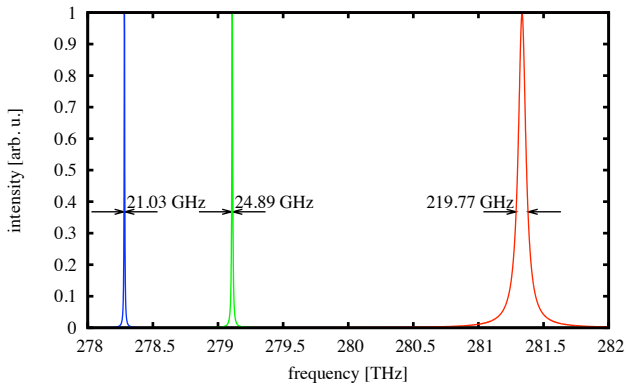

Figure 5.13: Spectral response of the unmodified cavity (red), with shift of the first air hole (green) and with radius shrinking (blue). The frequency is shifted towards the band edge of the first band, while the line width is reduces by more than one order of magnitude, resulting in an increase of the Q-factor from ≈ 4000 (without) over ≈ 33000 (shifted first outer air hole) to ≈ 41500 (shift+ shrunken first outer air hole).

5.3 Permanent Mode Tuning of the $L7$ Photonic Crystal Cavity

Generalizing the permanent tuning possibilities of resonances in a cavity, one maybe wants to retune a optical resonance to match an embedded quantum mechanical oscillator, for example a QD or a nitrogen vacancy [118]. Difficulties or inaccuracies in the fabrication process may have implicated defects in the dielectric resonant structure. For example, holes, to be expected perfectly circular in the whole sample to maintain periodicity, can get a slightly elliptical shape. The effect on the spectral properties of the sample is then a lifting of the degeneracy for double-degenerate modes, hence a splitting of the resonance. Also, the surface of a wall of a hole can be irregularly rough, resulting in disturbance of the perfectly assumed periodicity. Thus, a resonance shifts. Figure 5.14 shows the SEM image of a PhC slab in the top left corner [112], where clear deviations from a perfect circular shape and rough walls can be seen. The small black bar in the middle of the image has a length of about 20 nm. Both effects now affect e.g. the coupling to a single QD, which is located inside the resonator in a high-field position to maximize the coupling and whose parameters are chosen such, that the resonance matches the cavity resonance. The unwanted detuning due to the fabrication process can be corrected with a subsequent tuning process, which is explained in the following:
To get rid of such unwanted detuning, one can spectrally tune the single QD using its temperature dependence of the energy gap (which also affects the dielectric medium) or apply electric or magnetic fields to make use of the quantum confined Stark effect [66] (which not affects the optical properties of the cavity). Sometimes, this retuning possibilities are not enough to make up the fabrication processing contingented mismatches of the resonances. Another possibility to permanently retune the sample into resonance is to change the optical properties of the cavity by evaporation of another material onto the surface. Controlled to only evaporate on one side of a dielectric slab and not the walls of the air holes, for example, or uncontrolled by evaporating the whole surface of the sample. These changes will affect only the spectral properties of the confined field, but not of the QD.
An unmodified $L7$-type PhCC in a hexagonal lattice of air holes in a dielectric slab (GaAs) with a permittivity $\epsilon = 11.6281 (= 3.41^2)$ with lattice constant $a = 300$ nm, thickness-to-lattice constant ratio $t/a = 0.8$, air hole radius-to-lattice constant ratio of $r/a = 0.26667$ (80 nm) is used for the numerical investigation. The slab lies in the x-y-plane. Numerical data obtained from the simulation are then compared with experimental results [112]. To ensure numerical precision, the lower limit for the spatial sampling rate (including a subpixel averaging [54] with 15 points per pixel edge length) and the extension of the simulation domain are determined. In the top right part of Fig. 5.14, the strongest resonance within the first band gap is traced, showing the intensity of the electric field plotted over frequency in THz while increasing the spatial sampling rate from bottom to top, starting at 10 and incrementing by 1 (left). For a sampling rate of 12 points per lattice constant a and above, the simulation provides usable data. The bottom left side of Fig. 5.14 shows the dependency of the resonance of the simulation domain in x-direction (the y-direction is assumed to be constant for all calculations), starting at $11 \times a$ up to $29 \times a$. Strong deviations for small x-extensions for are observed, induced by the long size of the cavity itself ($8 \times a$), while the frequency is converged for extensions of $23 \times a$ and above. The spatial sampling rate and the size of the simulation domain in x-direction for the numerical analysis are determined to be $\Delta x = a/16$, $\Delta y = \sqrt{3}a/32$ and $l_x = 25 \times a$, respectively, to obtain reliable results. The z-direction has to be treated differently. There, a silicon dioxide (SiO_2) layer is used on the top side of the PhCC (the air holes are not affected inside), covering uniformly the whole sample. The evaporation

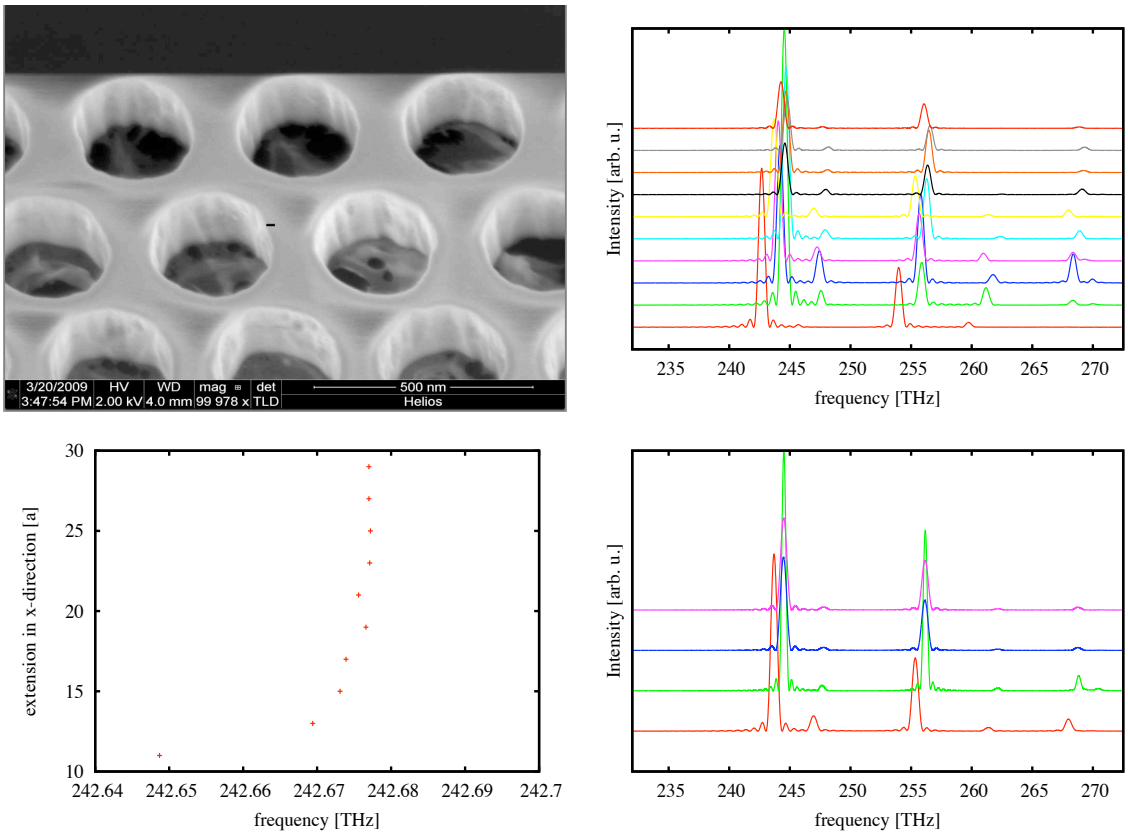

Figure 5.14: $L7$-type PhCC for permanent tuning with evaporated SiO_2 layers of different thickness. Top left: SEM image of the GaAs slab with e-beam written and wet-etched air holes in a hexagonal array with $r/a = 0.4167$ (125 nm). The image shows distinct deviations of the air holes from a perfectly circular shape, as well as rough walls. Top right: Determination of the minimum in-plane spatial sampling rate of a lattice constant for sufficient results. The intensity versus frequency in THz is plotted for different sampling rates, going from 10 (lower red) to 19 (upper red). A sampling of 12 points per lattice constant is found to be sufficient enough, 16 are chosen for the calculations to ensure numerical accuracy. Bottom left: Determination of the needed extension of the simulation domain in x-direction (extension in units of the lattice constant versus the resonance of the strongest mode). For the numerical calculation, a length of $25 \times a$ is chosen. Bottom right: Intensity (DFT) of the electric field (y)-component versus frequency in THz for different cell sizes inside the GaAs slab and additional SiO_2 layer. Red: uniform grid with $\Delta z = \Delta x$. Green: Non-uniform grid with a minimum $\Delta z = 5$ nm. Blue: Non-uniform grid with a minimum $\Delta z = 2.5$ nm. Magenta: Non-uniform grid with a minimum $\Delta z = 2$ nm. Due to the marginal difference between the different versions of the non-uniform grid, the minimum spatial cell size is chosen to be $\Delta z = 5$ nm.

process of the SiO_2 allows thin layers (thicknesses in the range of some nanometers), hence a detailed resolution in the computational region perpendicular to the slab is necessary to take the layers of different thicknesses properly into account. Therefore, a non-uniform grid in z-direction is used, reducing the grid edge length in the slab, including the SiO_2 layer, down to 5 nm (2.5 nm and 2 nm). Figure 5.14, bottom right, depicts the differences in the spectral response of the plain PhCC on the bottom right for the three cases of a nonuniform grid (green: 5 nm, blue: 2.5 nm, magenta: 2 nm), together with a uniform grid (red), spatially sampled with $\Delta z = \Delta x$. For the nonuniform grid, a discrepancy compared to the uniform grid

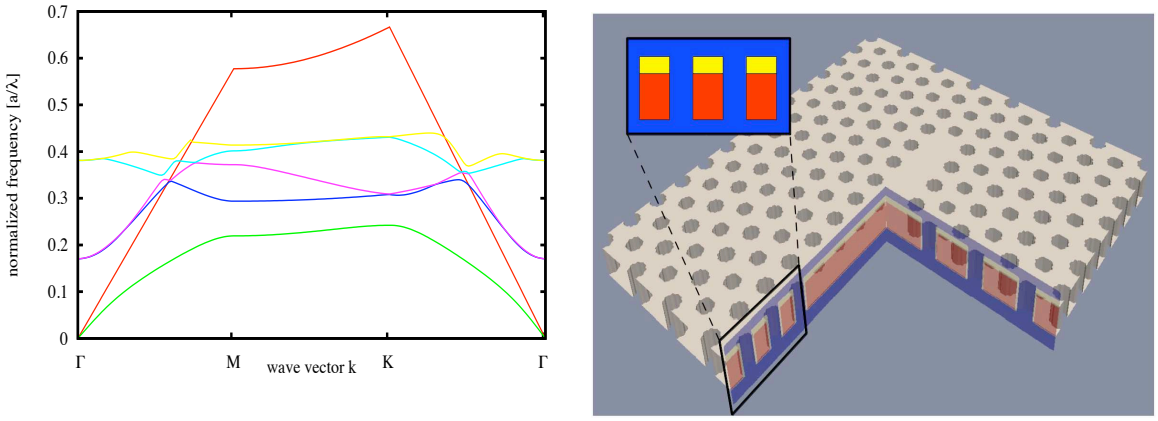

Figure 5.15: Left: Band structure for the PhC base structure (normalized frequencies vs. the wave vector). High-symmetry points in the irreducible Brillouin zone are marked. The first 5 bands (1: green, 2: blue, 3: magenta, 4: turquoise, 5: yellow), including light cone (red) are plotted. Note the band gap between the first two bands. For the band structure calculations, supercell of 4 unit lengths in z-direction is used. Calculations are performed with *MPB* [82]. Right: Geometrical setup. A *L*7-type defect is introduced in a PhC with a hexagonal lattice of air holes. Used parameters are $a = 300$ nm, slab thickness $t = 240$ nm ($=0.8a$) and air hole radius $r = 80$ nm ($= 0.26667a$). The cuts show the different permittivities of the dielectric material: blue: $\epsilon = 1$, red: $\epsilon_{\mathrm{GaAs}} = 11.6281 (= 3.41^2)$, yellow: $\epsilon_{\mathrm{SiO_2}} = 2.25$. The thickness of the SiO_2-layer is fixed for 50 nm for better visibility.

is visible. Since all versions of the nonuniform grid show the same behavior, the nonuniform grid with 5 nm spatial discretization is assumed to be converged and used for the numerical calculations for the PhCC with evaporated SiO_2 of different layer thickness. For the dielectric permittivity for the SiO_2 layer, $\epsilon = 2.25$ is used in the numerical evaluation.
The photonic band structure for the PhC is depicted in Fig. 5.15, left. Normalized frequencies are plotted over the wave vector, where high-symmetry points in the Brillouin zone are marked. Between the first two photonic bands. a gap emerges. The right side shows the geometrical setup. Note that only a section from the simulation volume is shown here for better visualization. The dielectric slab is shown in light-grey (see the defect area with the missing air holes). Cuts along the x- and y-direction show the permittivity distribution in more detail. Blue color has $\epsilon = 1$, red is the dielectric slab, and yellow marks the SiO_2 layer, whose thickness is varied to tune the resonance. Note that the SiO_2-layer is only on the top side, the holes are not filled.
It is expected, that the samples with evaporated SiO_2 layers will be red-shifted due to the extension of non-vacuum material in the z-direction (asymmetrically just at the top side), hence changing the conditions for the wave vector component k_z to be still confined. Also, the additional layer makes leakage of the field out of the cavity perpendicular to the slab easier, which will result in a drop of the Q-factor, as well as a drop in intensity. Above a certain thickness of the additional layer, a saturation effect is expected. Thus, the tuning range will be limited.

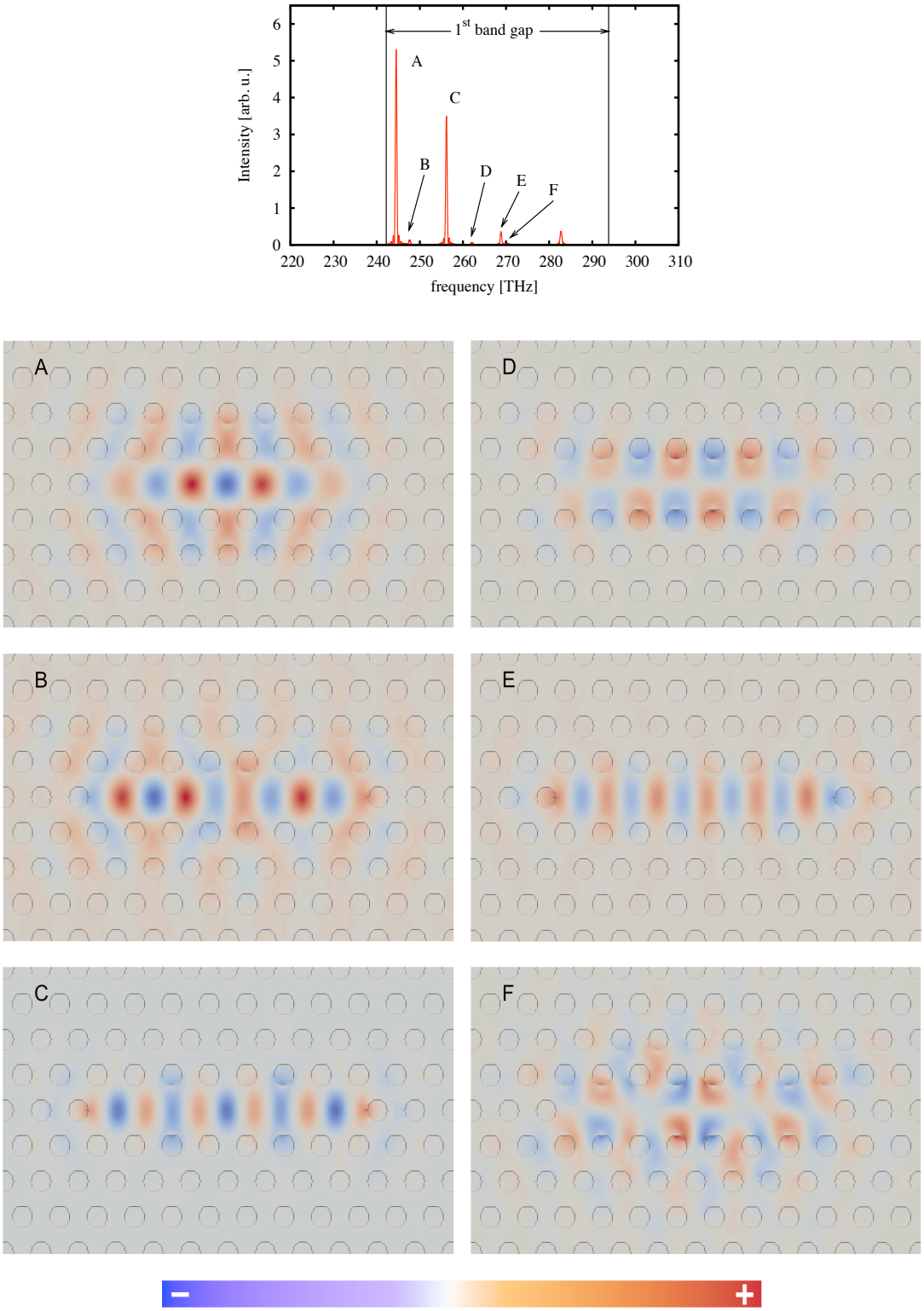

Figure 5.16: Spectrum (top) and spatiospectral response (bottom, normalized) of the geometrical setup in Fig. 5.15, right, without the additional SiO_2-layer. The labels A-C in the spectrum correspond with the left row, the labels D-F correspond with the right row. The color-coding is shown below. Grey circles show the air hole-slab interface.

Identification of the peaks in the spectral response with the corresponding spatiospectral response is given in Fig. 5.16. Intensity in arbitrary units is plotted over the frequency in THz in the top figure. Black vertical lines mark the edges of the 1st band gap. Capital letters label the six modes A-F of interest. The bottom part of Fig. 5.16 shows the spatiospectral response of the y-component of the electric field from the six modes in the TE-plane ($z = 0$). The patterns for the modes A-C are shown in the left row from top to bottom, while the right row shows the patterns for the modes D-F from top to bottom. The amplitude is color-coded (red: positive, blue: negative). Grey circles show the air holes. The modes A and C dominate the spectral response due to their high intensity.
In Figs. 5.17-5.21, numerical results with the modification of the slab are shown. Figure 5.17, top, shows the accumulated energy in the x-y- and x-z-plane without modification. The normalized intensity is color-coded (black: 0, white: 1.). Spatial coordinates are given in nm for both plots. As in the case of the $L3$-type PhCC, the energy is highly concentrated in the defect area (left). The logarithmic color scale chosen, reveals the evanescent parts, leaking out of the defect region mainly in a 30° angle. Note, that the accumulated energy distribution is clearly dominated by the fundamental mode, labeled with A in Fig. 5.16. Using different thicknesses of the SiO_2-layer, the normalized energy distribution at different cuts are depicted in the lower part of Fig. 5.17. The thickness of the additional layer is increased in steps of 10 nm (red: 0 nm, green: 10 nm, blue: 20 nm, magenta: 30 nm, turquoise: 40 nm, yellow: 50 nm, black: 60 nm, orange: 70 nm). In the first line, the left and right plot differ in linear and logarithmic scale of the z-axis, respectively, while in the lower line both plots have a linear z-axis. Cutting along $y = 0$ nm, $z = 55$ nm, the results are shown in the middle line. The effect of the additional SiO_2-layer is a drop in the total accumulated energy of 23% (peak intensity). The logarithmic scale shows no significant changes along the x-axis. More drastic changes are expected along the z-direction. The lower line shows a cut along $x = 0$ nm, $y = 0$ nm (left) and $x = 2260$ nm, $y = 0$ nm (right). The normalized accumulated energy is plotted over the z-coordinate (note the difference on the vertical axes). Black vertical lines mark the interfaces between the different dielectric media. At positive z-coordinates, the additional SiO_2-layer is located. Again, the different colors denote the different thicknesses of the layer. On the left, the accumulated energy is observed inside the defect region, where three facts attract attention. First, the accumulated energy drops with increasing SiO_2-layer thickness. Second, the distribution of the energy shows a slight asymmetry with more contribution at the interface between the PhC slab and the additional layer. Third, no gradient of the maximum with the layer thickness is observed. The first fact is clear, since the fields in the cavity are also located inside the additional layer. From there, due to the lower refractive index contrast, the fields can leak out of the GaAs defect region into the SiO_2 defect region due to a modification of the condition for total internal reflection. Thus, energy gets lost. The reason for the slight asymmetry is, that the additional layer increases the thickness of the basis slab, thus generating an effectively more thick slab. Including already the explanation for the latter fact, thus the strong spatial confinement in the defect region, the field and therefore the energy is still concentrated in the center of the GaAs slab, but the altered continuity condition at the interface to the additional layer allows more field in the SiO_2 layer.
Observing the energy more far away from the defect region, $x = 2260$ nm (right), the situation is substantially different. First, the intensity is five orders of magnitude smaller than in the defect region. Second, the asymmetry is more obvious with clearly visible discontinuous changes at the interfaces and third, a clear gradient with the layer thickness occurs, pointing towards the additional layer. The evanescent tail on the upper side of the device penetrates

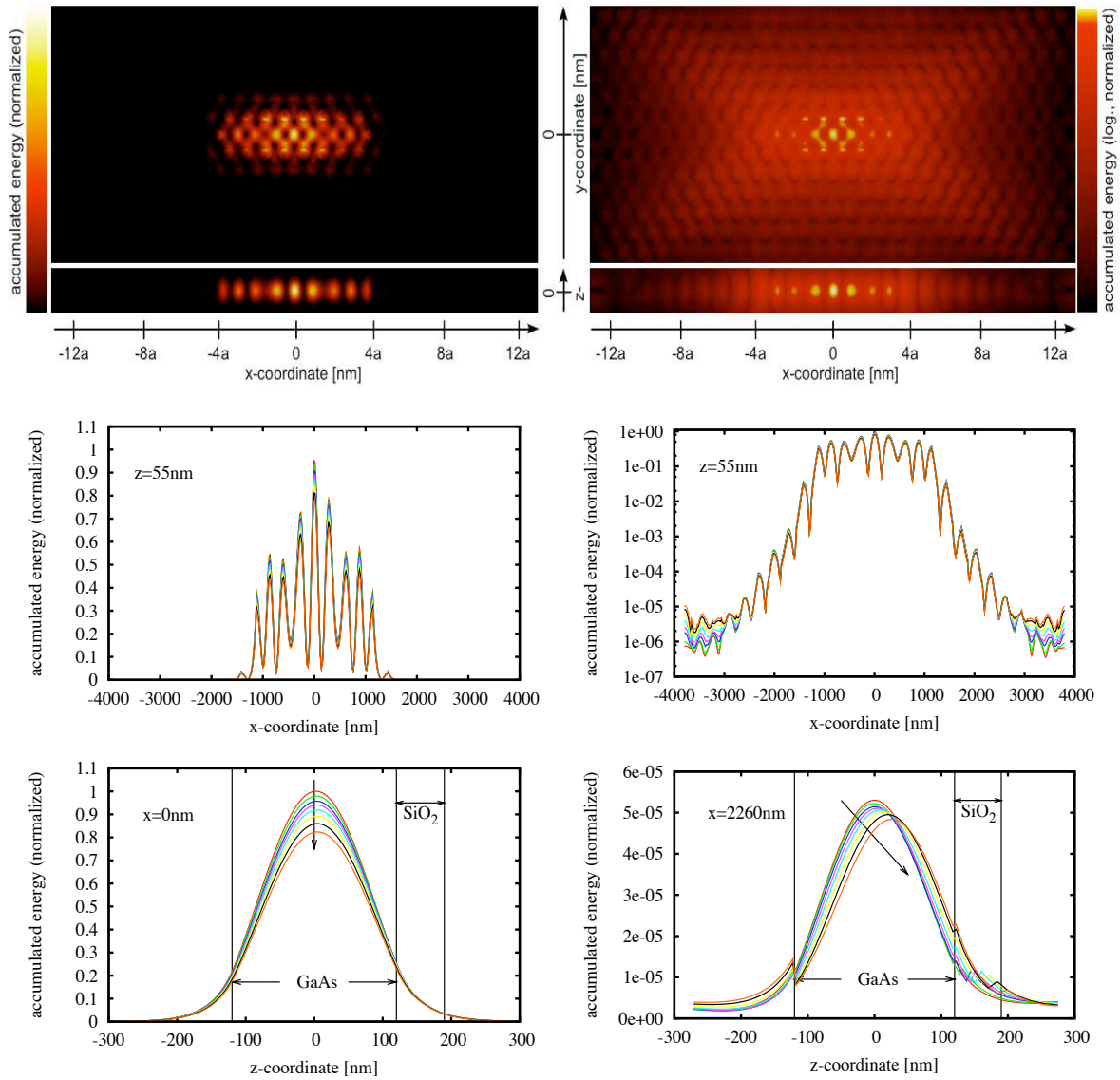

Figure 5.17: Accumulated energy distribution for the modified $L7$-type PhCC. Top: linear (left) and logarithmic scale (right) for the accumulated energy in the x-y- (upper) and x-z-plane for the unmodified sample. The strongest mode at 242.677 THz dominates the energy pattern. The logarithmic scale shows the evanescent parts, leaking out of the cavity. Middle: Cut along the x-axes at $y = 0$ nm and $z = 55$ nm in a linear scale (left) and a logarithmic scale (right). Bottom: Cut along the z-axes at $x = 0$, $y = 0$ (left) and $x = 2260$ nm, $y = 0$ (right, corresponding to $\approx 7.5333 \times a$) for the different thicknesses of the additional SiO_2 layer (from 0-70 nm). Vertical lines: GaAs slab thickness and the maximum SiO_2 thickness. Vertical (diagonal) arrows: displacement of the maximum of the acculumated energy with incrementing layer size.

deeper into the additional layer with increasing thickness due to weaker spatial confinement. Therefore, the maximum of the field is not located in the center of the basis slab consisting of GaAs, but also shifts to towards the SiO_2-layer.

The effect on the spectral shift of the fundamental mode is depicted in Fig. 5.18. In the upper graph, the frequency shift with increasing layer thickness is shown. On the left and right side,

the spectra for 0 nm and 70 nm SiO_2-layer thickness are plotted, respectively. The frequencies in THz are on the vertical axes, while the horizontal axis shows the intensity in arbitrary units. Capital letters mark the different modes within the first band gap (same labels mark the same modes as in Fig. 5.16, top), dotted lines and dashed arrows connect corresponding modes and are a guide for the eye. Both spectra are separated by the frequency shift (red crosses) with increasing layer thickness (top axis). With increasing layer thickness, the modes are collectively red-shifted. Due to the thicker slab, the wavelengths in z-direction increase. Also, saturation of the frequencies of the modes is observed for larger additional layers. In Fig. 5.17, bottom right, one can see the effect in more detail for mode A (mode B is also shown in the spectral region, but due to the small amplitude it is not clearly visible). The different colors correspond to different layer thicknesses of the additional SiO_2 layer (red: 0 nm, green: 10 nm, blue: 20 nm, magenta: 30 nm, turquoise: 40 nm, yellow: 50 nm, black: 60 nm, orange: 70 nm). For clarity, the left plot shows the spectral position of the peak maxima of modes A and B in THz (horizontal axis) with increasing layer thickness in nm (vertical axis). The saturation effect is explained with the evanescent tail of the confined modes in z-direction. As long as the coupling of the field to the vacuum is sufficiently large, the modes are red-shifted due to the leakage out of the basic GAs slab into the SiO_2-layer and further into the vacuum environment. As soon as the additional layer thickness exceeds a critical length l_C, the effect of a more thick layer vanished. Assuming the picture of a planar GaAs waveguide of finite thickness and infinitively extended in the x-y-plane, the field decays exponentially outside of the slab. With $\lambda = 337.07$ nm being the material wavelength of the fundamental mode for the unmodified PhCC system, shown in Fig.5.15, the field decays to $1/e$ at 62 nm away from the interface. Therefore, when the thickness of the additional layer exceeds this coherence length, the saturation takes place.

A clear shift for both modes with increasing layer thickness is observed. For larger additional layers, the peak position starts to saturate. However, the amplitudes and Q-factors drop further with saturated spectral peak position. Due to the presence of the field in the additional layer, the condition of total internal reflection is generally weakened because of the decreased refractive index contrast, first at the interface between the basic GaAs slab and the SiO_2-layer, and second at the interface the SiO_2-layer and the vacuum environment. This automatically leads to an increase in the cavity decay rate, since the fields leak more out of the basic slab. Hence, the Q-factor drops. Figure 5.19, left, shows the drop of the Q-factor on a logarithmic scale for the six modes, labeled with capital letters A-F, in dependence of the SiO_2-layer thickness (vertical axis).

The comparison with experimental data [112] is shown in the Figs. 5.20 and 5.21. The first Fig. compares the spectral response of the unmodified (left) and modified (54 nm additional layer of SiO_2, right), the latter compares the numerically obtained relative frequency shift (left) and drop in the Q-factor (right). In Fig. 5.20, the intensity of the y-component of the electric field in arbitrary units is plotted over the frequency in THz. The 1^{st} band gap is marked with black lines. Red shows the experimental data, green shows numerically obtained data. One observes a clear difference in the spectral position of the cavity modes for both cases. Inaccuracy in the fabrication process, as shown in Fig. 5.14, top left, leads to perturbation of the periodicity in the sample. The periodicity is the fundamental aspect of the PhC slab to provide best confinement. Also, deviations in the air holes around the defect affect the cavity resonance directly (see for example Fig. 5.7, top left). Nevertheless, a deviation of up to 10 THz is unusually large. From the numerical point of view, accuracy can mostly be increased with a more fine spatial grid. However, Fig. 5.14, top right and lower line, show that the

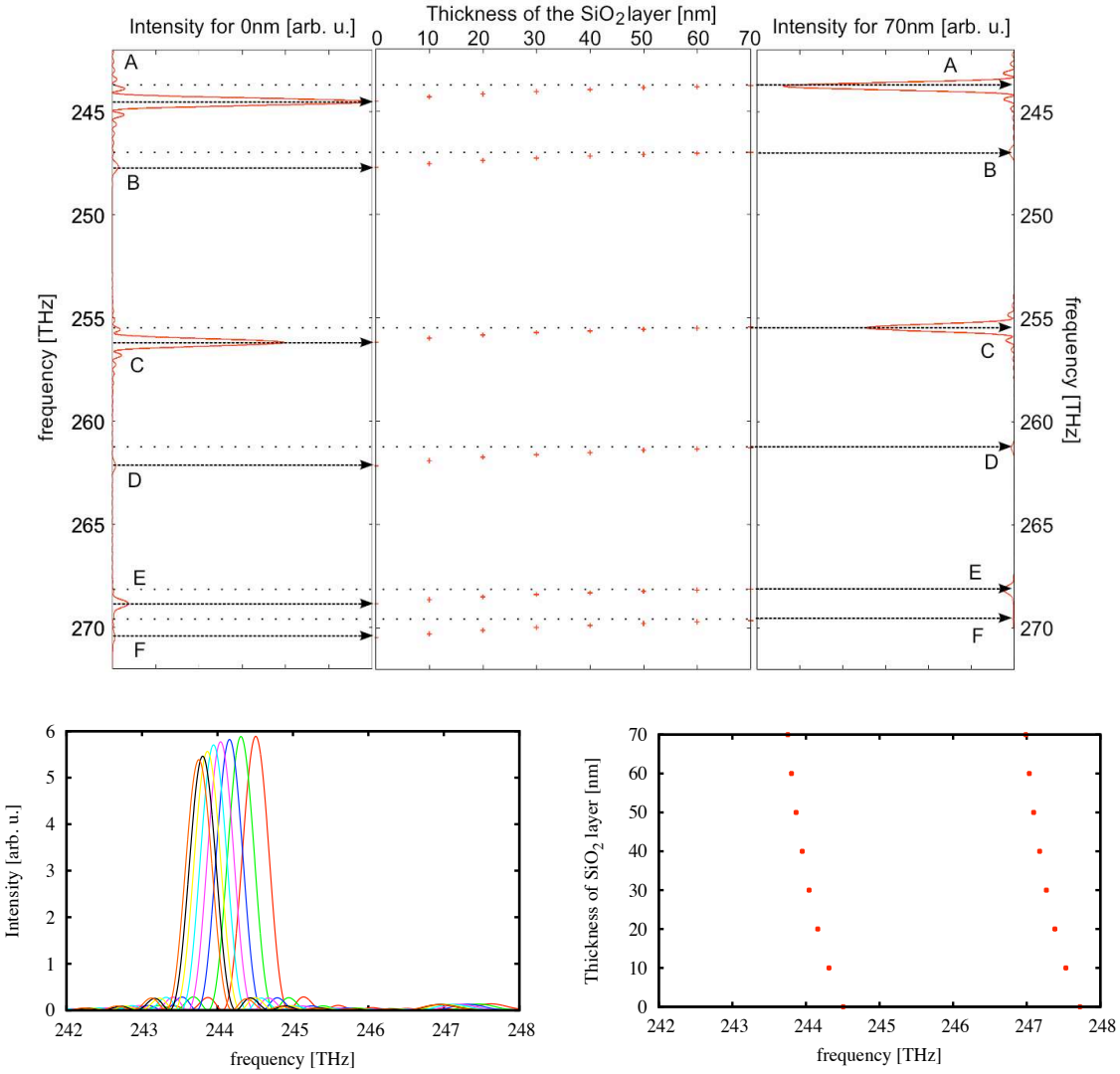

Figure 5.18: Spectral properties of the resonances with increasing additional SiO_2 layer thickness. Top: frequency shift of the strongest modes (intensity in arbitrary units, DFT) within the first band gap (for clarity and better visualization of the small red-shift, a smaller range is shown). The left side shows the spectral response for 0 nm thickness, the right side for a thickness of 70 nm. In between, the spectral displacement of the resonance with increasing layer thickness in 10 nm steps is depicted. The arrows serve for clarity, as well as the dotted lines, to visualize the red shift of the resonances. Bottom: Tracing the strongest mode. DFT intensity (left) and peak position (right) for different thicknesses. For large thicknesses, a saturation starts to take place.

computational volume, the spatial discretization as well as the nonuniform grid in z-direction, are checked to be converged. The frequencies of the cavity relative to each other show good agreement between the experiment and the FDTD simulation. For the frequency shift with increasing SiO_2-layer thickness, Fig. 5.21, left, shows the experimental data in red and the numerical data in green. Above a layer thickness of 40 nm, the experimental data shows a saturation of the shift. In the numerics, saturation starts above a thickness of 70 nm (not

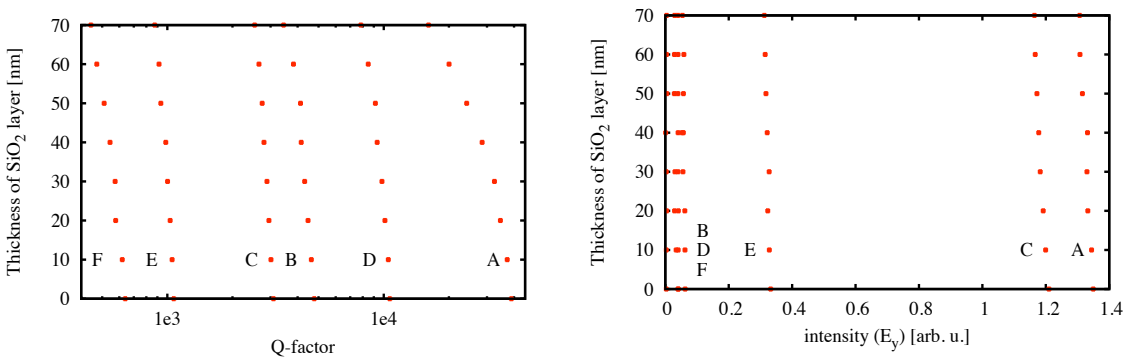

Figure 5.19: Left: drop of the Q-factor (horizontal axis, logarithmic scale) depending on the SiO_2 layer thickness in nm (vertical axis). Right: drop of the intensity of the cavity modes (horizontal axis, arbitrary units) in dependence of the SiO_2-layer thickness in nm (vertical axis). The capital letters label the modes corresponding to Fig. 5.18, top.

shown). Moreover, the experimental data exhibit a frequency shift of more than a factor 2. Again, disorder-induced perturbations in the sample due to inaccuracies in the fabrication process cause the difference. In general, the trend of the frequency shift agrees nicely. On the right side of Fig. 5.21, the Q-factors are compared. A difference is expected due to the differences in the frequencies of the modes, since $Q \propto f$. However, a factor of 2.6 separates the numerical data (green) from the experimental data (red). Since the simulation assumes perfect periodicity and a perfectly smooth surface on all interfaces, the numerically obtained Q-factors show the upper limit. Experimental data are naturally interfered by the already mentioned fabrication inaccuracies or dirtiness. Though the drop of the Q-factor is nice reproduced within the simulation.

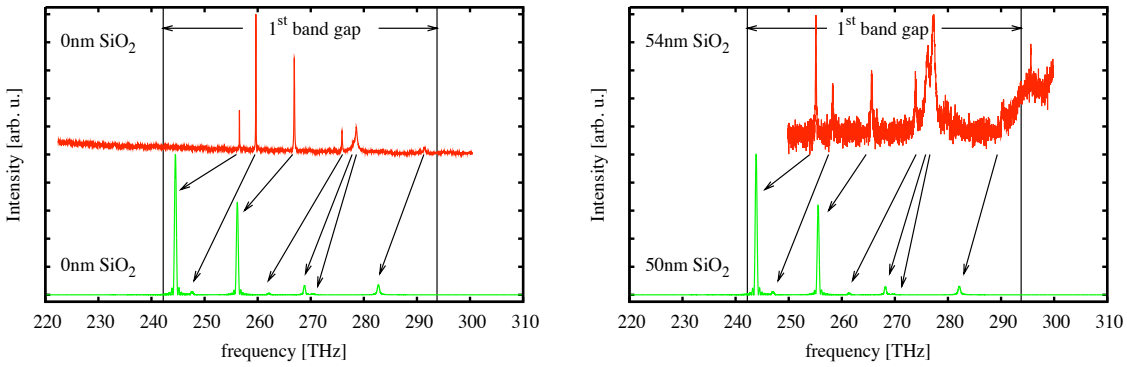

Figure 5.20: Comparison between the experimental (red) and the numerical (green) data. Left: unmodified cavity, SiO_2-layer thickness 0 nm. Right: modified cavity, SiO_2-layer thickness 54 nm (50 nm was used in the FDTD simulation). Intensity in arbitrary units over frequency in THz is shown. The black arrows assign the peaks in the experimental data with peaks in the numerical data. Vertical lines mark the upper and lower edge of the 1^{st} band gap. Note that the band gap stays unchanged under modification.

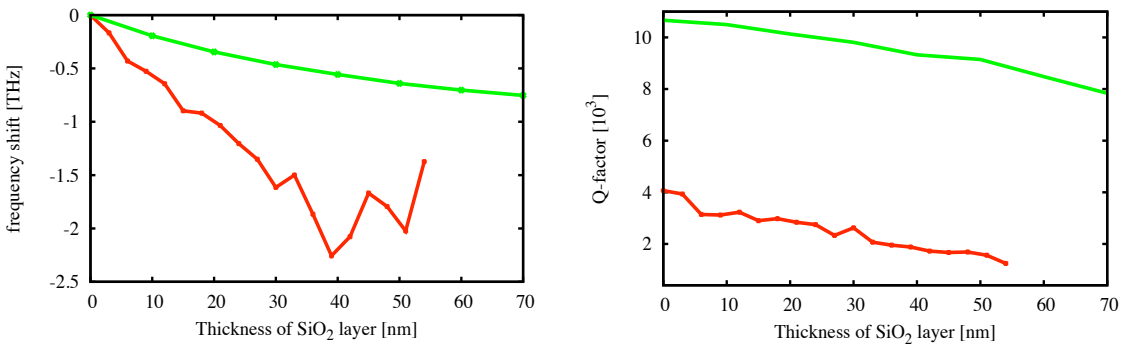

Figure 5.21: Comparison between the experimental (red) and the numerical (green) data. Left: the spectral shift in THz is plotted over SiO_2-layer thickness in nm. Right: drop of the Q-factor (labeled with D in Fig. 5.18) is plotted over SiO_2-layer thickness in nm. The trend of the spectral behavior is reproduced nicely.

Chapter 6

Coupled Systems

The investigation of coupled resonator systems is the content of this chapter. The focus lies on resonators in photonic band gap materials (PhCC) and resonators based only on TIR (microdisks). The first provide small effective mode volumes accompanied with high Q-factors, but the spatial extensions (several lattice constants) need to be large to ensure proper confinement in the plane of the PhC slab. Therefore, single devices in the regime of several micrometers are standard. The latter provide ultra-high Q-factors, accompanied with mode volumes of one order of magnitude larger and more, compared to PhCCs. Nevertheless, the size of a single device and therefore the capability for dense integration on chips makes it attractive. Applications for coupled resonator systems are fast semiconductor lasers [124], signal transmission [125], e.g. via coupled optical resonator waveguides (CROWs) and quantum information processing devices.
The embedding of QDs in a microresonator affects the optical properties of the microcavity only slightly due to its low crossection. The application range of such coupled systems is broad, covering single photon sources, lasing systems and quantum computing, just to mention some. Also, such systems are useful in current research to investigate the light-matter interaction in more detail.

6.1 Coupled Sub-μ Microdisk Resonators

The interaction between resonators based only on TIR is discussed here. For the sake of less computational effort, two-dimensional calculations of the sub-μ microdisk resonators are performed (see Sec. 4.1). Hence, the parameters for the simulations are a microdisk radius $R = 361$ nm and a dielectric permittivity of $\epsilon = 11.56$. Note that this model for the dielectric material does not include absorption. The regime of strong cavity-cavity interaction, thus the line splitting of the coupled system exceeds the line width of the isolated, uncoupled cavity, is investigated numerically. The computational domain has an extension of 745 cells in each, x- and y-direction, plus 20 cells of CPML (see Sec. 2.2.4). Square shaped cells with an edge length of $\Delta x = \Delta y = 7.35294$ nm and a simulation time of $t_{\text{sim}} = 2.5$ ps are sufficient to gain reliable results.

6.1.1 Strong Interaction Between Two Sub-μ Microdisks

The geometrical setup of a system of two coupled microdisk resonators is shown in the insets of Fig. 6.2. Different distances between the microdisks are taken into account. The detuning in frequency between the two microdisk resonators is performed via a radius variation of one microdisk, while the other microdisk has a constant radius, therefore the WGMs of the latter have constant frequency. Section 4.1.1 shows the frequency dependency of WGMs with radial mode order $M = 1$ and $M = 2$ and different azimuthal orders. Slight variations of the radius strongly affect the resonance of the WGMs. The WGM $\text{TE}_{1,10}$ will be in the focus for the investigation of the strong resonator-resonator interaction, since this mode provides a high Q-factor of $Q = 3.52 \times 10^6$ at a frequency $f = 555.742$ THz. Loss in perpendicular direction is not taken into account, since the simulation domain is two-dimensional (TE-plane) and periodic boundary conditions are applied in z-direction.
In Fig. 6.1, left, the spectral response of the coupled system (green) is shown, compared with the isolated, single MD (red). The intensity on a logarithmic scale is plotted over the frequency in THz. A reduced frequency range around the $\text{TE}_{1,10}$ WGM is shown. Both MDs are separated by the distance $d = 14.7$ nm. One observes a strongly asymmetric splitting

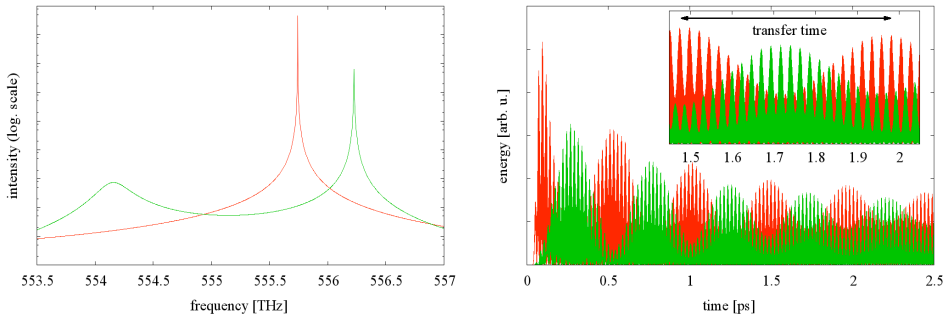

Figure 6.1: Beating between the odd and even eigenmode of two resonant MDs. Left: line splitting (green) of the coupled system. The isolated, single MD resonance of the $TE_{1,10}$ WGM is shown in red for comparison. Accompanied by the formation of an ultra-low-Q and ultra-high-Q mode, the single resonance splits asymmetrically into two new eigenmodes with even (low-frequency mode) and odd (high-frequency mode) symmetry, respectively. Right: electromagnetic energy transfer between the two MDs. Red: energy recorded in the right-placed MD. Green: energy recorded in the left-placed MD (see Fig. 6.3 for the mode patterns of the even and odd mode). The inset shows the beating on a shorter time scale to show the time needed to transfer the energy from one disk to the other (and vice versa).

of the MD resonance. Both peaks are separated by Δ =2 .0679 THz. This asymmetric line splitting is accompanied by an asymmetric loss spitting as well. Thinking about the coupling between a single QD and an optical mode (refer to Sec. 6.2 for the investigation of a single QD to a high-Q WGM in a MD), one expects a symmetric line and loss splitting due to the strong coupling between the oscillators. Here, the coupling between the closely spaced MDs induces the asymmetry in the line splitting, as will be explained later. The loss splitting finds its explanation in the radiation patterns of the even and odd eigenmode later, too.
On the right side of Fig. 6.1, the transfer of the electromagnetic energy between the two MDs is shown. The electromagnetic energy in arbitrary units is plotted over the time in ps. The red curve belongs to the right MD, green to the left MD (see Fig. 6.3 for the positioning of the disks and the corresponding mode patterns for the even and odd mode). The slight difference in the total amplitude of the energy results from the deformation of the mode pattern for the even mode (the field is more concentrated in the right-placed MD) due to the close spacing, hence the strong interaction, while the pattern for the odd mode has equal amplitude in both MDs. Therefore, the recorded energy in the left MD (green in Fig. 6.1, right) is lower. A clear beating between the two MDs is observed. The time needed to transfer the energy from one MD to the other equals the difference between two maxima (as denoted with a black arrow). For the transfer, the time is estimated to be t_{transfer} = 483.455 fs (averaged), which corresponds to a transfer frequency of f_{transfer} = 2.0684 THz and is in perfect agreement with the line splitting Δ =2 .0679 THz.

Figure 6.2 shows the line splitting (left) and the Q-splitting (right) of the coupled system for different distances. On the vertical axis, the detuning of one microdisk with respect to the second, fixed microdisk, is given as $1 - r/R$ in percent, where R is the radius of the fixed microdisk. This emphasizes the strong impact of a slight radius variation. Frequencies in THz are given on the horizontal axis. As a guide for the eye, the grey dashed line shows the isolated, single microdisk resonance of the WGM $TE_{1,10}$ at f = 555.742 THz. The different distances

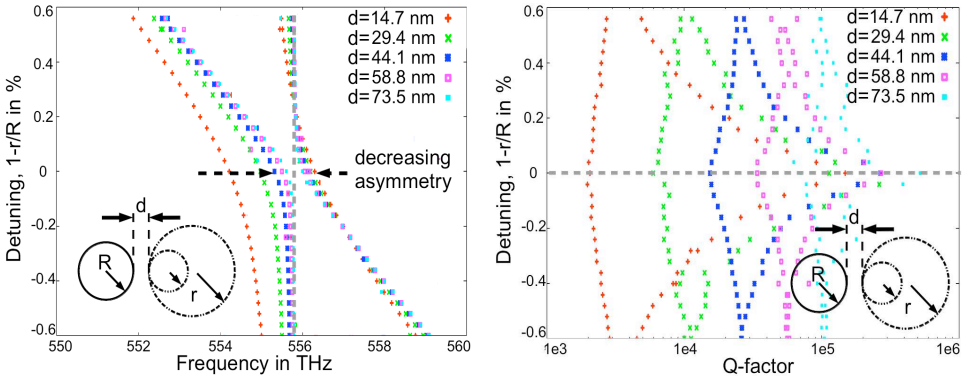

Figure 6.2: Coupling between two MDs. One MD is detuned with respect to the other, fixed microdisk via a radius variation, see inset. Left: Anticrossing of the coupled system for different spacings between the MDs, the detuning in $1-r/R$ in percent is shown on the vertical axis, the frequency in THz on the horizontal axis. The color-coding for different gap sizes is red: $d = 14.7$ nm, green: $d = 29.4$ nm, blue: $d = 44.1$ nm, magenta: $d = 58.8$ nm, turquoise: $d = 73.5$ nm. For small spacings, a strong asymmetry in the line splitting is observed. With increasing gap size, the asymmetry vanishes. Right: Q-splitting of the coupled system. On the vertical axis, the detuning is shown, while the horizontal axis shows the Q-factor on a logarithmic scale. The color-coding for the different gap sizes is the same like on the left side. For small spacings, the modes split asymmetrically into a ultra-low- and ultra-high-Q mode. For increasing spacing, the loss splitting decreases with decreasing asymmetry.

d are color-coded (red: $d = 14.7$ nm, green: $d = 29.4$ nm, blue: $d = 44.1$ nm, magenta: $d = 58.8$ nm, turquoise: $d = 73.5$ nm). At first, one notices the strong asymmetry of the eigenstates of the coupled system, which gradually decreases with increasing distance. For $d = 58.8$ nm and $d = 73.5$ nm, the line splitting is almost symmetric. This is explained with a tight-binding (TB) approach, as it is well-known for electronic systems in semiconductor physics [63, 64]. For CROWs, a TB approach is successfully applied to calculate the dispersion relation [79, 80]. The basis of the TB approach is the wave equation for one localized mode $\mathbf{E}_\Omega(\mathbf{r}, t)$ of an isolated, single cavity with eigenfrequency Ω. The mode is assumed to be real and orthonormal according to

$$\int d\mathbf{r}\, \epsilon_{r,0}(\mathbf{r})\, \mathbf{E}_\Omega(\mathbf{r}) \cdot \mathbf{E}_{\Omega'}(\mathbf{r}) = \delta_{\Omega\Omega'}\,, \tag{6.1}$$

where $\epsilon_{r,0}(\mathbf{r})$ denotes the dielectric profile of the single resonator. For a time-harmonic mode, the wave equation yields

$$\nabla \times [\nabla \times \mathbf{E}_\Omega(\mathbf{r})] = \frac{\epsilon_{r,0}(\mathbf{r})\Omega^2}{c^2}\mathbf{E}_\Omega(\mathbf{r}). \tag{6.2}$$

Describing the system of two coupled cavities, the eigenmodes with frequency ω of the coupled system are a superposition of the modes of the single defects, weighted with A and B:

$$\mathbf{E}_\omega(\mathbf{r}) = A\,\mathbf{E}_\Omega(\mathbf{r}) + B\,\mathbf{E}_\Omega(\mathbf{r}+\mathbf{r}'). \tag{6.3}$$

Here, $\mathbf{r}'$ is the displacement of the second resonator with respect to the first resonator. Equation (6.3) also fullfills eq. (6.1), but with $\epsilon_{r,0}(\mathbf{r}) = \epsilon_{r,0}(\mathbf{r}+\mathbf{r}')$ for the dielectric profile. Now, first one uses eq. (6.3) in eq. (6.2). After multiplication of $\mathbf{E}_\Omega(\mathbf{r})$, followed by multiplication of $\mathbf{E}_\Omega(\mathbf{r}+\mathbf{r}')$

from the left side, one spatially integrates over the whole space. Subsequent use of eq. (6.1) yields the new eigenfrequencies of the coupled system, depending on three parameters. The TB-frequencies are

$$\omega_{1,2}^2 = \Omega^2 \frac{1 \pm \beta_1}{1 \pm \alpha_1 + \Delta\alpha}. \tag{6.4}$$

and the TB-parameters α_1, β_1 and $\Delta\alpha$ are given by the integrals

$$\alpha_1 = \int d\mathbf{r}\, \epsilon(\mathbf{r})\, \mathbf{E}_\Omega(\mathbf{r}) \cdot \mathbf{E}_\Omega(\mathbf{r} + \mathbf{r}') \tag{6.5}$$

$$\beta_1 = \int d\mathbf{r}\, \epsilon_{r,0}(\mathbf{r} + \mathbf{r}')\, \mathbf{E}_\Omega(\mathbf{r}) \cdot \mathbf{E}_\Omega(\mathbf{r} + \mathbf{r}') \tag{6.6}$$

$$\Delta\alpha = \int d\mathbf{r}\ (\epsilon_r(\mathbf{r}) - \epsilon_{r,0}(\mathbf{r}))\ |\mathbf{E}_\Omega(\mathbf{r})|^2. \tag{6.7}$$

The overlap-type integral in α_1 induces the asymmetry in the mode splitting, enhanced by $\Delta\alpha$ at very short distances. $\Delta\alpha$ decays asymptotically to zero with the exponentially decaying field amplitudes of the resonant modes outside of the resonator. Hence, this quantity can often be neglected. Figure 6.3, left, depicts the accumulated energy of the coupled system on a logarithmic scale, while the middle and right show the mode patterns of the even and odd eigenmode, respectively, for a separation distance of $d = 14.7$ nm. As a guide for the eye, the black line depicts the MD-to-environment interface. As the accumulated energy in the coupled system shows, the $\mathrm{TE}_{1,10}$ is the dominant mode, since the energy distribution counts 20 lobes, corresponding to the 10 minima and 10 maxima in the field distribution. The occurrence of an even and odd mode confirms the fact of strong resonator-resonator interaction. Note the strong deformation of the field for the even mode, especially in the left-placed MD, compared with the odd mode. This is due to the strong interaction between the two resonators. For larger separation distances, this deformation vanishes.
Beside the line splitting, a loss splitting occurs for the coupled system. Asymmetric line and loss splitting is numerically investigated in [126] and experimentally proves in [114] for two coupled microdisk resonators whose isolated, single resonances are of the same radial mode order. In Fig. 6.2, right, the Q-factors of the eigenstates of the coupled system are shown on a logarithmic scale (horizontal axis). The color-coding for the distances is the same like in the left plot. As can be seen, for close positioned microdisk cavities, the Q splitting is largest, resulting in an ultra-low-Q mode (low-frequency mode, even field distribution) and an ultra-high-Q mode (high-frequency mode, odd field distribution). See Fig. 6.3 for the field distribution of the even (left) and the odd mode (right). For the ultra-low-Q eigenmode, the cavity decay time yields $T_{C,\downarrow} = 1.19$ ps (corresponding to a Q-factor of Q=2071), while the cavity decay time ultra-high-Q eigenmode is $T_{C,\uparrow} = 94.94$ ps (corresponding to a Q-factor of Q=165900). This is connected with an enhanced and suppressed radiation perpendicular to the coupling direction (the coupling direction is along the x-axis), respectively. Figure 6.4 shows the absolute value of the radiation pattern of the even (left) and the odd mode (middle) on a logarithmic scale for a resonator spacing of $d = 14.7$ nm. The color-coding is blue for low and red for high intensity. Substantial differences are observed between the even and odd case. The radiation of the even mode is only suppressed along the dark blue lines due to destructive interference. The selective mode patterns have a slightly asymmetric form. For the very short spacing of the resonators, the coupling between the microdisks is so strong, that

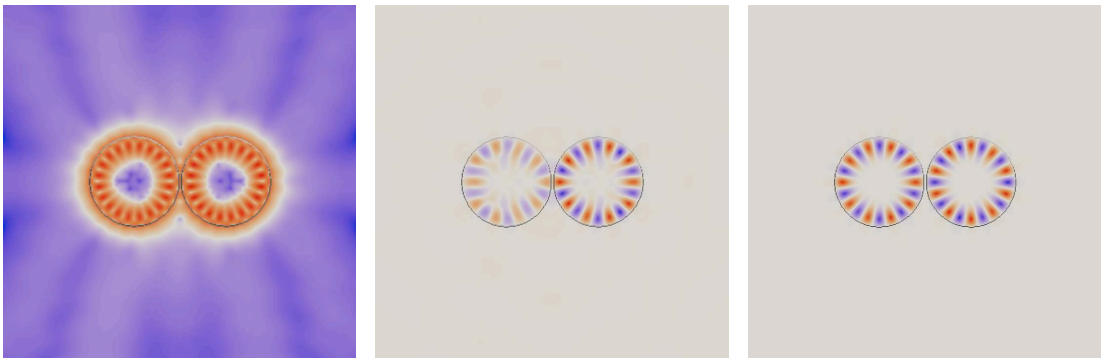

Figure 6.3: Spatiospectral response of the coupled MD system in the TE-plane (x-y-plane). The microdisk radius is $r = 361$ nm and the spacing between the MDs is $d = 14.7$ nm. Black lines show the interface of the MD to the vacuum environment. Left: Accumulated energy (normalized, logarithmic scale, red: high, blue: low). One can see, that the $TE_{1,10}$ WGM dominates the radiation pattern. Middle and right: mode patterns (normalized, linear scale) of the even (middle) and odd (right) eigenmode of the coupled system. The even mode has a deformed pattern, especially in the left-placed MD. Also the amplitude in the left MD is lower than in the right MD. For the odd mode, the amplitude is divided equally. Color-coding: red: +1, blue: -1.

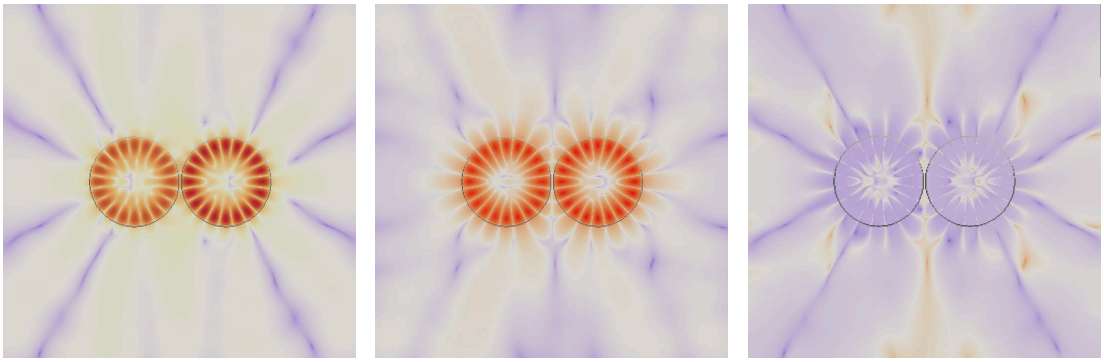

Figure 6.4: Intensity patterns (normalized, logarithmic scale, red: high, blue: low) for the even (left) and odd (middle) eigenmode of the coupled system. The odd mode has decreased radiation along the y-axis due to destructive interference of the patterns of the single MDs. Right: difference between even and odd intensity pattern. The enhanced radiation along the y-axis is clearly visible. Black circles denote the interface between the MDs and the vacuum environment.

the mode pattern is substantially altered. Due to constructive interference of the radiation patterns of the left and right microdisk, the intensity is high, especially along the y-direction. Therefore, the resonator decay time is reduced, hence the Q-factor is reduced. The intensity in y-direction is decreased for the odd mode compared to the intensity of the even mode. Destructive interference along the y-direction suppresses radiation and the resonator decay time increases. Thus, the Q-factor increases. For comparison, the left shows difference of the even and odd radiation pattern (logarithmic scale). A clear radiation perpendicular to the coupling direction (x-direction) is observed, which proves the assumption of suppression and enhancing of radiation due to destructive and constructive interference, respectively.

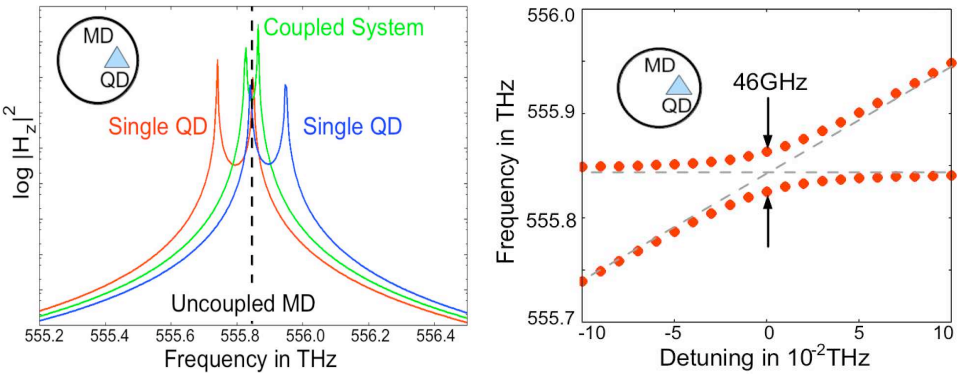

Figure 6.5: A single QD strongly coupled to the high-Q microdisk WGM $TE_{1,10}$. Left: Spectral response of the coupled system, the intensity on a logarithmic scale is plotted over the frequency in THz. Inset: geometrical setup (black circle: MD, blue triangle: QD). As a guide for the eye, the black dashed line denotes the isolated, single MD resonance $TE_{1,10}$. Red and blue: the QD is detuned to the MD resonance. Single peaks in the spectrum left and right show the QD resonances, while the MD resonance stays unchanged. Green: the QD on resonance with the MD resonance of $TE_{1,10}$. A clear line splitting around the isolated, single MD resonance is observed, and the VRS is $\Delta = 2g = 46$ GHz. Right: Anticrossing of the upper and lower polariton branch. Frequency in THz is plotted over the detuning of the QD in THz with respect to the MD resonance $TE_{1,10}$. Grey dashed lines are a guide for the eye, horizontal line: isolated, single MD resonance, diagonal line: QD resonance. A clear repelling of the upper and lower polariton branch can be seen, hence the QD is strongly coupled to the MD mode $TE_{1,10}$.

6.2 A Single Quantum Dot Strongly Coupled to a WGM of a Sub-μ Microdisk Resonator

For the numerical investigation, two-dimensional calculations are performed. As the electromagnetic resonator, the sub-μ microdisk resonator is used. For the coupling, the high-Q WGM $TE_{1,10}$ is chosen. Its resonance is at $f = 555.742$ with a Q-factor of $Q = 3.52 \times 10^6$. The QD is placed at a high-field position near the rim inside the microdisk. Spectrally, the QD frequency is variable to tune the QD into resonance with the WGM. Parameters for the QD are the dipole matrix element $\mu_y = 3$ eÅ and the phenomenological damping $\gamma_{\mathrm{QD}} = 0$. For the carrier wave functions, a Gaussian ellipsoid with a radius of $r = 30$ nm in x- and y-direction is used: $\Psi = C \cdot e^{-(x^2+y^2)/r^2}$. Initially, the QD is in the ground state, therefore $n_{\mathrm{QD}} = 0$. For the simulation, the amplitude of the exciting source is chosen small, so that no nonlinear effects occur.

Figure 6.5 shows the interaction between the high-Q resonator mode $TE_{1,10}$ and the QD. A scheme of the system can be found in the upper left corner, where the black circle shows the interface of the microdisk with the vacuum environment and the light-blue triangle shows the QD. On the left, the spectral response on a logarithmic scale is depicted, plotted over the frequency in THz. Black dashed line denotes the resonance of the isolated, single microdisk resonator. For a (red- and blue-) detuned QD, the WGM and the QD are not interacting. Therefore, the two peaks show the isolated resonances of the QD and the WGM. When the QD is on resonance with the microdisk WGM (green), a line splitting occurs, the VRS. The energy is periodically transferred between the quantum-mechanical and the optical resonator due to the strong coupling. In the quasi-particle picture, this is described with cavity-polaritons,

the upper and lower polariton branch. Detuning the QD further into the blue, the strong coupling vanishes and the two oscillators are not coupled any more (blue curve). In Fig. 6.5, the two polariton branches are shown. The emission frequency of the coupled system in THz is plotted over the detuning of the QD in THz with respect to the isolated, single WGM resonance. In the top left corner, the geometrical setup is sketched. In a system, which is not strongly interacting, the emission frequency would behave like the light-grey dashed lines. The vertical line stands for the WGM mode of the microdisk, while the diagonal line shows the variable QD frequency. At zero detuning, both lines cross. In the strong coupling regime, where the energy of the WGM is absorbed by the QD before it leaks out of the resonator and is re-emitted before it decays non-radiatively, the lines split up, depending on the Rabi frequency. Therefore, changing the frequency of a detuned QD into resonance, leads to an anticrossing between the WGM and the QD, the polariton branches. On resonance, the line splitting yields $\Delta = 46$ GHz. The splitting is quite small for such a high-Q mode, but the high Q-factor is compensated by a fairly large mode volume, compared to a $L3$-type PhCC, where the mode volume is below $(\lambda_0/n)^3$ (λ_0 is the vacuum wavelength of the resonance and n is the refractive index of the PhC slab [3, 4]). For microdisk devices, this value exceeds the effective mode volume of a PhCC [127]. Therefore, the interplay between the Q-factor and the effective mode volume restricts the line splitting to a value of several tens of GHz.

6.3 Coupled Photonic Crystal Cavities

In contrast to Sec. 6.1, photonic band gap materials are utilized here. The $L3$-type cavity, as introduced in Sec.5.2 is used for the numerical investigation. Therefore, three-dimensional calculations are performed to take into account all kinds of radiation loss. The PhCC is characterized by a hexagonal lattice of air holes in a purely dielectric slab. The lattice constant is $a = 300$ nm, the air hole radius $r = 0.3 \times a$, the slab thickness $t = 0.6 \times a$ and the dielectric permittivity of the slab is $\epsilon = 10.595$. The parameters are similar to [3] to obtain a TE-like photonic band gap in the desired frequency range. For the computational domain, the parameters are set to be $V_{\text{sim}} = 29 \times 14\sqrt{3} \times 2\,a^3$, $t_{\text{sim}} = 3$ ps, $\Delta x = \Delta z = a/16$ and $\Delta y = \sqrt{3/4}\Delta x$, if not mentioned otherwise. For more accurate calculations, an ϵ-averaging subroutine [54] with 10 points per cell length is used (see Sec. 2.2.3).

6.3.1 Strong Cavity-Cavity Interaction between Two Photonic Crystal Cavities

The investigated geometrical setup is depicted in Fig. 6.6, left, where the PhC slab is shown in grey. Two $L3$-type defects are aligned linearly next to each other. The next-neighbored air holes along the cavity axis are modified according to the investigations in Sec. 5.2. Therefore, the hole radius is shrunken to $r = 0.2 \times a$ and the center of the air hole is shifted outwards of the cavity centers by $s = 0.18 \times a$. The Q-factor of the fundamental mode for the isolated cavity is $Q = 41500$. Figure 6.6, right, shows the spectral response of the coupled cavity-system (green) around the fundamental mode frequency, compared with the spectrum of the isolated cavity (red). A slightly asymmetric line splitting around the fundamental mode frequency occurs. The eigenmodes of the coupled system, labeled with A and B, are spectrally separated by $g = 378$ GHz. For the isolated cavity with the mentioned modifications, the line width is $\gamma_C = 21$ GHz. Therefore, since the line splitting of the coupled system obviously exceeds the line width of the isolated system, strong cavity-cavity interaction is present. In the top right

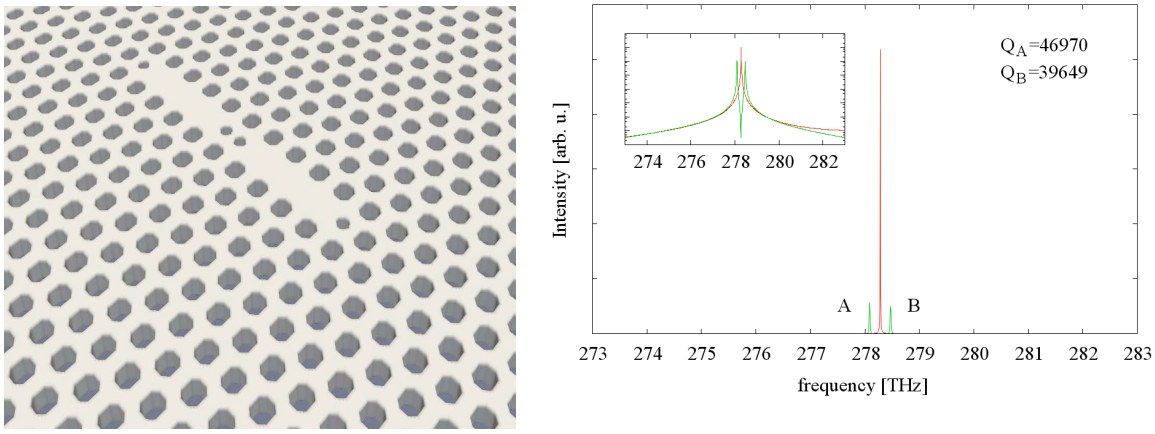

Figure 6.6: Geometry (left) and spectrum (right) for linearly aligned PhCCs. The spectrum shows intensity in arbitrary units over frequency in THz. Red: spectrum of an isolated single cavity. Green: coupled cavity response. The even and odd modes are labeled with A and B, respectively. The inset shows the spectrum on a logarithmic scale. In the top right corner, the Q-factors for the modes A and B are given.

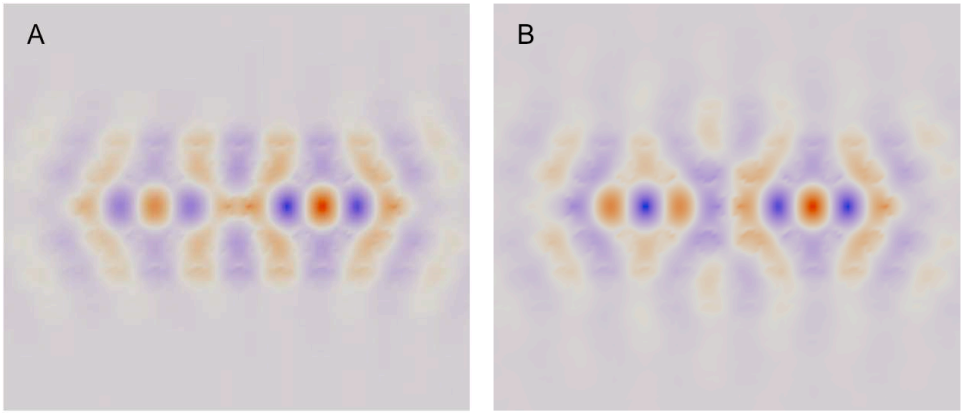

Figure 6.7: Mode patterns of the coupled cavity system with linear alignment. Left: even mode. Right: odd mode. The labels A and B refer to the frequencies in Fig. 6.6.

corner, the Q-factors for the even mode (Q_A) and the odd mode (Q_B) is given. Besides the line splitting in frequency, a Q-splitting occurs [128]. The splitting in loss is explained by the spatial FT of the mode patterns just above the PhCC slab. Larger components inside the light cone allow stronger leakage perpendicular to the slab. As shown in [128] for linearly aligned cavities, the Q-splitting is asymmetrically around the value of the isolated, single cavity Q-factor. Additionally, the spatiospectral response approves the strong interaction between the two cavities. In Fig. 6.7, the mode patterns are shown in the TE-plane ($z = 0$) with color-coded amplitude (red: positive, blue: negative). On the left, the even mode is depicted, while the right side shows the odd mode with color-coded amplitude (red: positive, blue: negative). Hence, the symmetric and asymmetric field distribution approve the strong cavity-cavity interaction. From the field distribution for the fundamental mode of the isolated cavity, Fig. 5.9, one sees, that the evanescent parts of the mode pattern penetrate the air hole lattice in a 30° angle with respect to the cavity main axis. For efficient field injection from one cavity into the other cavity,

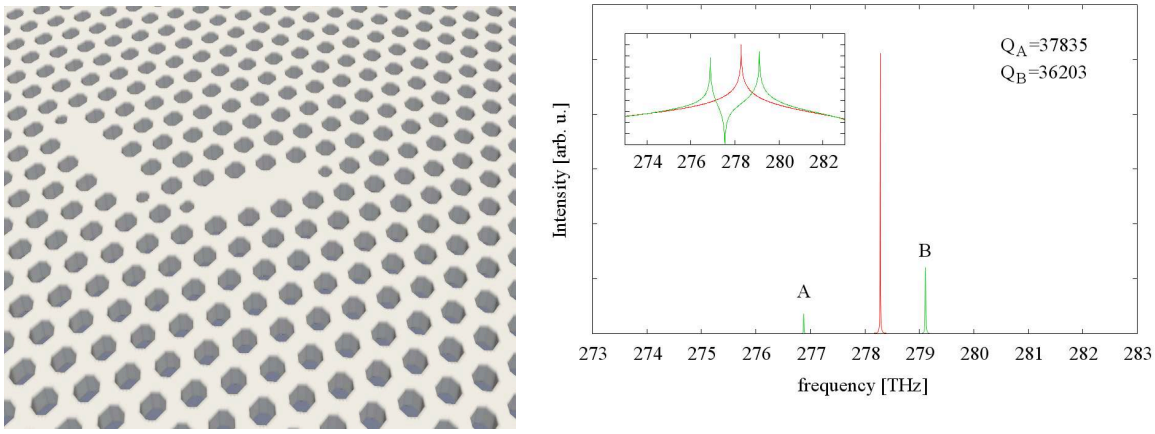

Figure 6.8: Geometry (left) and spectrum (right) for angle-aligned PhCCs. The spectrum shows intensity in arbitrary units over frequency in THz. Red: spectrum of an isolated single cavity. Green: coupled cavity response. The even and odd modes are labeled with A and B, respectively. The inset shows the spectrum on a logarithmic scale. In the top right corner, the Q-factors for the modes A and B are given.

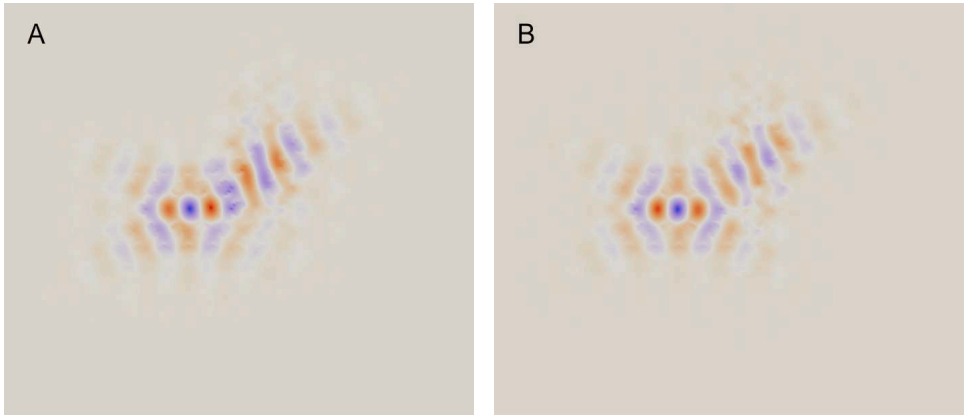

Figure 6.9: Mode patterns of the coupled cavity system with angled alignment. Left: even mode. Right: odd mode. The labels A and B refer to the frequencies in Fig. 6.8.

it is obvious to have maximum overlap between the single cavity mode patterns. Therefore, two more alignments of the coupled cavity system are investigated. First, the second cavity is aligned in a 60° angle with respect to the first cavity main axis to match the air hole lattice. Then, the second cavity is shifted away from the first cavity such, that the two centers of the cavities are connected with a virtual straight line, having a 30° angle with respect to the cavity axes. A scheme of the alignment is shown in Fig. 6.8, left. The second alignment scheme consists of two laterally aligned cavities, where the second cavity is shifted with respect to the first cavity such, that the centers of both cavities are again connected with a virtual straight line, having a 30° angle with respect to the cavity axes. See Fig. 6.10, left, for a scheme. Note, that the lateral alignment gives rise to the nearest alignment of the two cavities, regarding the distance between the centers, compared with the linear and angled alignment.
Figure 6.8, right, shows the spectrum of the coupled system for the angled alignment (green) compared with the spectral response of the isolated, single cavity. Intensity in arbitrary units

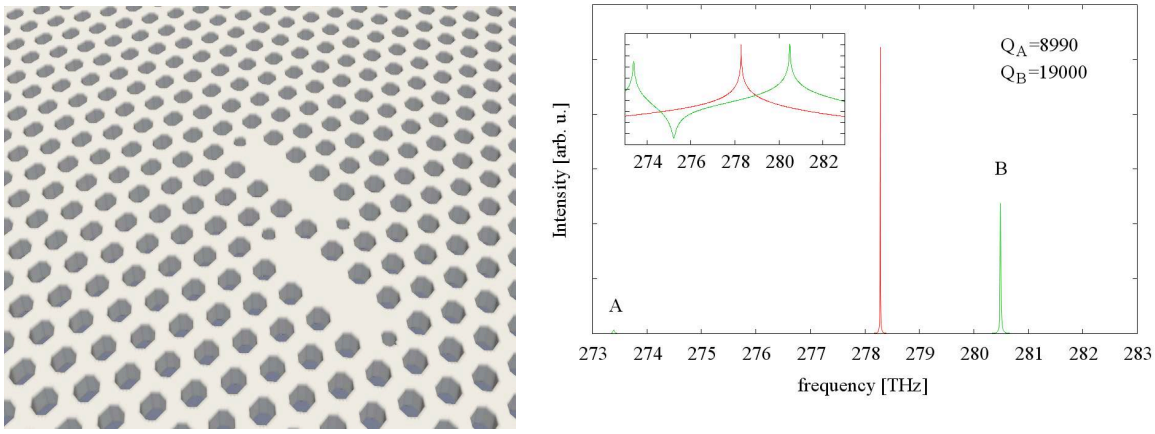

Figure 6.10: Geometry (left) and spectrum (right) for lateral aligned PhCCs. The spectrum shows intensity in arbitrary units over frequency in THz. Red: spectrum of an isolated single cavity. Green: coupled cavity response. The even and odd modes are labeled with A and B, respectively. The inset shows the spectrum on a logarithmic scale. In the top right corner, the Q-factors for the modes A and B are given.

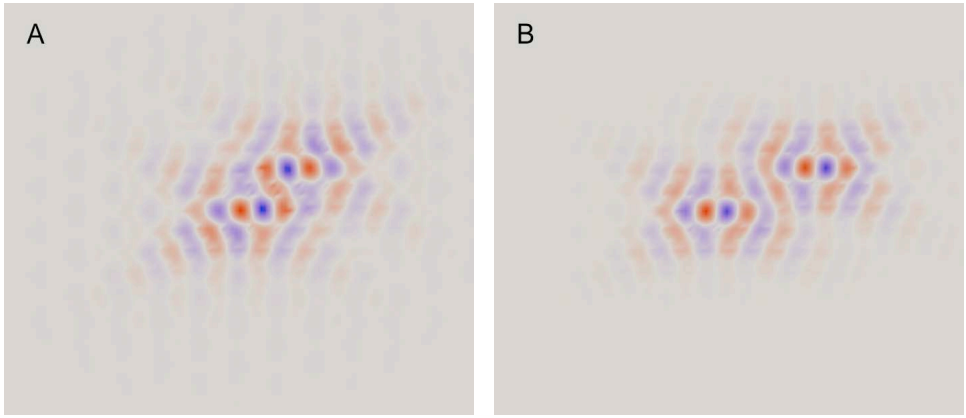

Figure 6.11: Mode patterns of the coupled cavity system with lateral alignment. Left: even mode. Right: odd mode. The labels A and B refer to the frequencies in Fig. 6.10.

is plotted over the frequency in THz. Like in the case of the linearly aligned cavities, a line spitting occurs, but the asymmetry is more pronounced. The even and odd eigenmodes are split by $g = 2.233$ THz, which is a factor of ≈ 6 more than in the case of linearly aligned cavities. Therefore, strong cavity-cavity interaction is at place. The mode patterns (color-coded, red: positive, blue: negative) of the eigenmodes of the coupled system are depicted in Fig. 6.9, where the even (left) and odd (right) field distribution according to the resonances A and B in Fig. 6.8 are shown. Despite the mode pattern is not developed so clearly, one can see, that the field injection is enhanced, because the line splitting is larger than in the linearly coupled case, thus the coupling is increased. The Q-factors here are slightly split, but for both eigenmodes of the coupled system, the values are below the Q-factor of the isolated, single cavity.

The case for laterally aligned cavities is shown in Fig. 6.10 schematically on the left. Regarding the center-to-center distance between the cavities, both cavities are closer to each other than

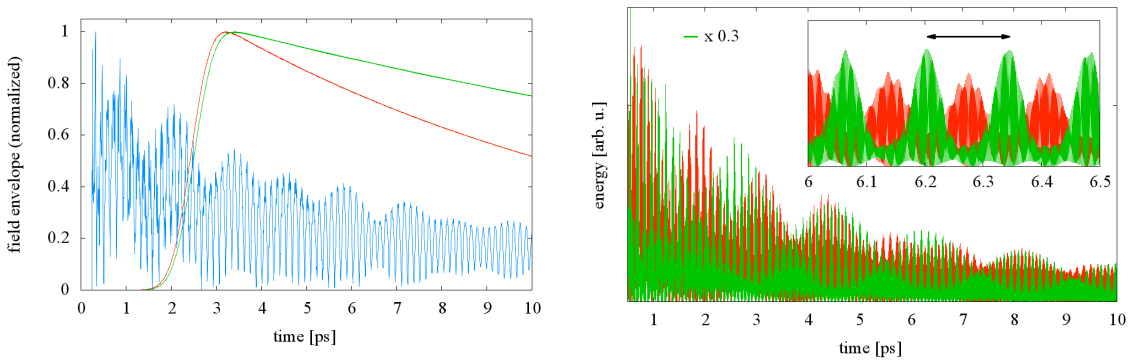

Figure 6.12: Left: Time signals of the coupled system for broadband excitation (blue, center frequency is the fundamental mode resonance) and narrowband excitation for the low-Q (red) and high-Q (green) eigenmode. Right: energy transfer between the two coupled PhCCs. Electromagnetic energy in arbitrary units is plotted over the time in ps. The red and green (multiplied by 0.3) curves are recorded in the centers of the two cavities. Inset: beating on short time scale.

in the two previous cases. Therefore, an increased coupling is expected, resulting in a larger line splitting. Figure 6.10, right, confirms this fact. The intensity of the coupled system (green) and, for comparison, of the isolated, single cavity (red), are plotted over frequencies in THz. A comparably large line splitting of $g = 7.099$ THz emerges. Due to the (spatially) exponentially decaying evanescent field, penetrating the neighboring cavity, the coupling strength between the cavities is enhanced due to increased spatial overlap of the single uncoupled mode patterns. This also explains the strong asymmetry in the line splitting due to eq. (6.4), which is induced by the overlap-type integral α_1, see eq. (6.7). The Q-factors for the even and odd mode are given in Fig. 6.10, too. Loss splitting is observed like in the case of the coupled MDs in Sec. 6.1.1. In [128], the splitting of the Q-factors is explained to be due to the radiation pattern perpendicular to the PhC slab plane, where the confinement is dominated by TIR, for the case of 2 linearly aligned $L3$-type defects in a PhC. Thus, the same argument as for the coupled MDs applies here. Constructive (destructive) interference of the radiation perpendicular to the slab cause the even and odd mode (compare Fig. 6.11 for the field distribution) to be less (stronger) confined. Figure 6.12 shows the time evolution of the field envelope (normalized) over ps, resulting from broadband excitation (blue, center frequency is the fundamental mode resonance) and narrowband excitation (red and green), resonant with the even and odd mode (low-Q and high-Q mode), respectively. The different Q-factors are clearly visible, since the even mode decays faster than the odd mode.

To see the transfer time of the electromagnetic energy from one cavity to the other, Fig. 6.12 shows the electromagnetic energy in arbitrary units over the time in ps. Each curve is recorded in the center of one of the cavities. The green curve is scaled by 0.3 since the amplitudes of the confined modes are slightly different. On the whole time scale, fast oscillations are visible, perturbated by the energy of the other cavity modes (see Sec. 3.1.2). Since the fundamental mode of the $L3$-type defect is the dominant mode, the beating between the two cavities can be seen even when the other modes are present. The inset shows the time from 6 ps to 6.5 ps. The distance between two maxima, indicated by the black arrow, is the transfer time, which is needed, to transfer the electromagnetic energy from one cavity to the other and back.

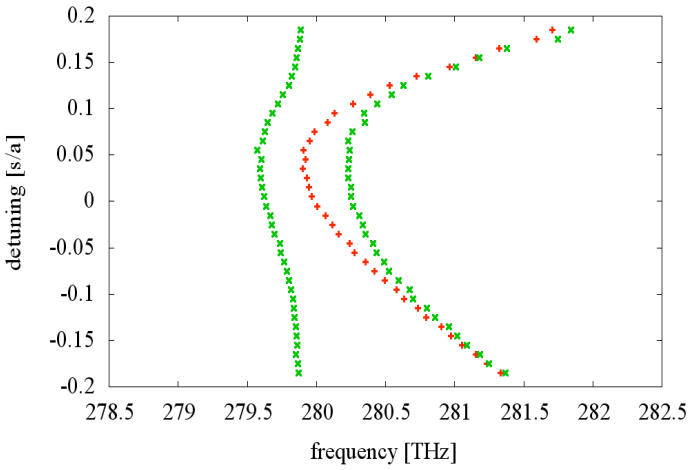

Figure 6.13: Avoided crossing of two strongly interacting PhCC cavities with a $L3$-type defect. Detuning in units of the outward shift of the outer air holes in s/a is plotted over the frequency in THz. Red: frequency-dependency of the isolated, single cavity. Green: frequency-dependency of the coupled system. The low-frequency branch corresponds to the fixed cavity. When zero detuning is approached, the fixed resonance is repelled by the approaching resonance of the cavity with the variable air hole position.

This time is estimated to be $t_{\text{transfer}} = 139.922$ fs, corresponding to a transfer frequency of $f_{\text{transfer}} = 7.146$ THz, equal to the line splitting.
For the purpose of investigating an avoided crossing between PhCC modes, two cavities are aligned laterally for enhanced field injection from one into the other cavity (see Fig. 6.10, left). One cavity has a fixed resonance. Here, the common parameters for the outer air hole shift is used, but the radius is unmodified (refer to Sec. 5.2). Therefore, the frequency of the fundamental mode is fixed to $f_C = 279.055$ THz with a Q-factor of $Q \approx 33000$. The second cavity is modified via the shift of the outer air holes, to spectrally tune the resonance through the resonance of the first, fixed cavity. Due to the air hole shift-dependent frequency shift of the cavity resonance (see Fig. 5.7), the variable resonance is expected to push the fixed resonance apart when the detuning between the cavities decreases. After the resonant case, the fixed mode is expected to return to its isolated frequency. Hence, no common avoided crossing, say anti-crossing, is expected here. Figure 6.13 shows the behavior of the coupled, detuned cavities. The detuning (vertical axis) is given in units of the air hole modification s/a, where 0 means being on resonance with the fixed cavity. Therefore, the vertical axis maps the resonance only indirectly. For better comparison, the single, isolated cavity resonance is shown in red. Frequencies in THz are given on the horizontal axis. As can be seen, the modes of the coupled system split around the isolated, single cavity resonance. When the detuning approaches 0, the branch of the fixed cavity is clearly pushed away. This clear avoided crossing emphasizes the strong cavity-cavity interaction.

Distance dependency of the coupled PhCCs is crucial, when one wants to integrate them in a dense manner on a chip. Therefore, the distant-dependent line splitting of two coupled

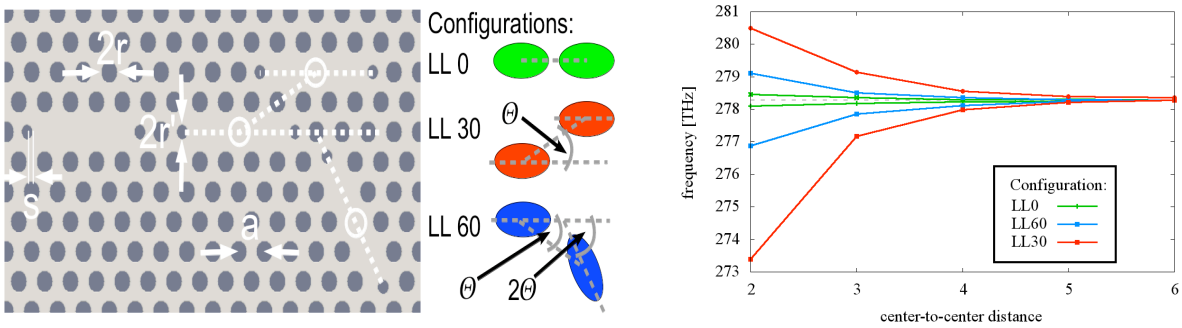

Figure 6.14: Left: Overview of the investigated alignments of the PhCCs. Right: distant-dependent line splittings of the alignments from the left. Same colors mean same alignment. The frequency in THz is plotted over the center-to-center distance between the cavities. A light-grey dashed line is a guide for the eye to show the resonance of the fundamental mode for the isolated, single cavity.

cavities, using the three investigated alignments, is depicted in Fig. 6.14. The left side shows the three alignment schemes. On the right side, frequency of the eigenmodes of the coupled system is plotted over the center-to-center distance. A grey-dashed line shows the isolated, single PhCC resonance of the fundamental mode. Red shows the frequencies of the even and odd eigenmodes (left and right branch, respectively) of the laterally aligned PhCCs, blue shows the angle-coupled PhCC eigenmodes and green shows the inline coupled cavities. As can be seen in the Figs. 6.6, 6.8 and 6.10, the line splitting is largest for the lateral alignment, with direct field injection due to the proper alignment. With increasing distance, the asymmetry in the line splitting vanishes, since the asymmetry-inducing term in eq. 6.4 gets less important due to less spatial overlap. The lateral alignment has the largest line splitting over the whole investigated distance range, therefore the coupling is largest in this case.

6.3.2 Strong Cavity-Cavity Interaction between Three Photonic Crystal Cavities: Pioneering more effective *CROW*s

In the previous Sec. 6.3.1, the focus lied on the coupling between two PhCCs, properly aligned for enhanced field injection into the neighboring cavity. Now, this scheme is expanded by introducing a third cavity. An interesting application is the CROW. Waveguides in PhCs are already investigated well, e.g. the $W1$ waveguide [129, 130], which is basically just a straight missing line in the air hole lattice. $W1$ waveguides exhibit, of course depending on a proper choice of the parameters (especially the ratio of the air hole radius and the lattice constant r/a), large bandwidths below the light line and also low loss [131]. However, an alternative to a $W1$ waveguide is a CROW, where for example the transmission is based on the coupling efficiency between the neighboring cavities.

Utilizing the laterally aligned cavities, since they exhibit the largest line splitting of the investigated alignments in the previous section, the addition of the third cavity can be done in different ways. First, the three cavities can be V-aligned. Second, the third cavity can be aligned such, that they are <-shaped. Third, the third cavity is aligned laterally with the same shift like the second cavity with respect to the first cavity, hence the three cavity-centers are

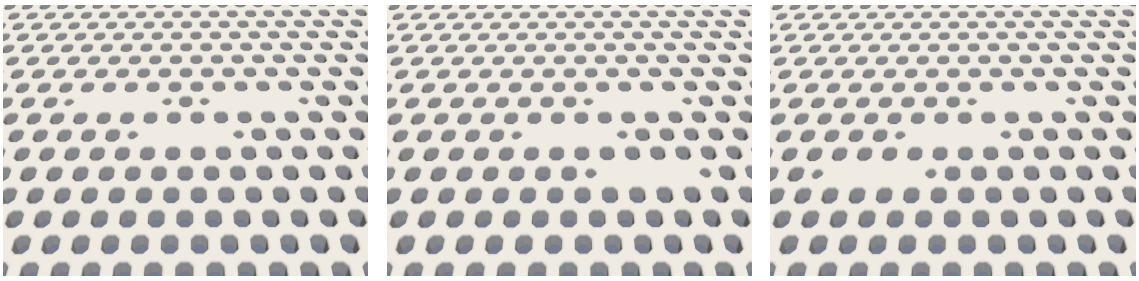

Figure 6.15: Geometries of the three cavities, making advantage of the lateral alignment for enhanced coupling. Left: V-aligned cavities. Middle: <-aligned cavities. Right: /-aligned cavities.

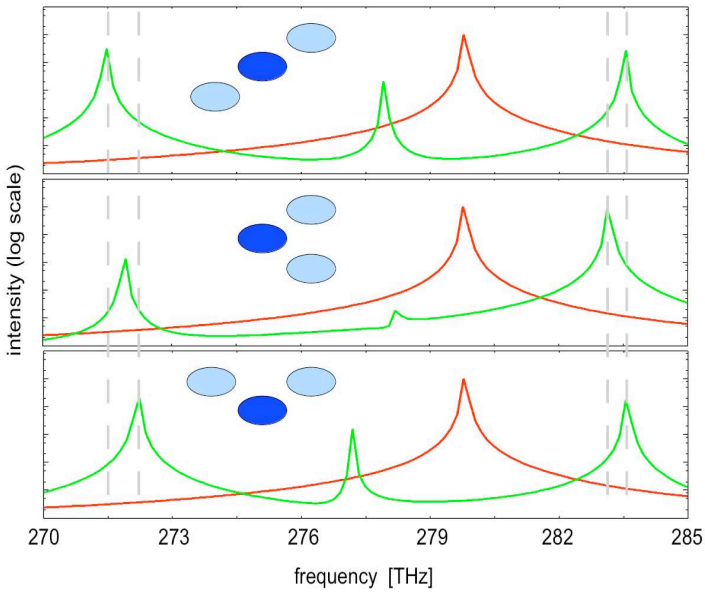

Figure 6.16: Spectral response from three coupled cavities in different alignments. Intensity on a logarithmic scale is plotted over the frequency in THz. The insets denote the coupling geometries (the dark-blue element contains the exciting light source). Red: isolated, single resonance of the fundamental mode. Green: response of the coupled system. Grey dashed lines are a guide for the eye, showing the eigenmodes at the most far (most close) frequency compared to the single cavity resonance.

connected via a virtual line, having a 30° angle with the cavity main axes. The three cavities are /-aligned. Figure 6.15 shows the different alignments (from left to right: V-, <-and /-aligned). Now, the spectral response is investigated, depending on the arrangement of the three cavities. In Fig. 6.16, the intensity on a logarithmic scale is shown over the frequency in THz. Red shows the isolated, single PhCC resonance of the fundamental mode for comparison, while green shows the spectral response of the coupled systems. In the insets, the corresponding alignments of the three cavities is shown. One observes, that the /-coupled geometry provides the largest line splitting, therefore the coupling is the largest. Thus, this geometrical alignment is preferable for CROWs, consisting of several coupled $L3$-type defect cavities in a PhC. For the case of V-coupled system, the line splitting clearly exceeds the one from the inline-coupled system, containing only two cavities, see Fig. 6.6. Note, that here the

distance between the top left and right cavities is larger. Equivalent spacing in the case of two linearly aligned cavities result in less efficient coupling. Therefore, the alignment proposed here is more efficient to transmit light along the cavity axis. The interaction between the corresponding cavities is larger than in the linearly aligned case, thus the coupling between the top left and right cavity is enhanced using the third cavity. The same applies for the case of the <-coupled cavities for light transmission perpendicular to the cavity axis. This is interesting, because the hexagonal character of the lattice dictates the alignment of a single defect. Light can be transmitted efficiently along different symmetry directions only by proper arrangement. A 90°-bend, for example, is problematic, because the hexagonal air hole lattice provides no useful alignment scheme for $L3$-type defects. Guiding light perpendicular to the cavity axis can be done efficiently with a <-aligned array.
The field patterns of the eigenmodes of the three-fold coupled system for the lateral alignment are depicted in Fig. 6.17, showing the y-component in the TE-plane (x-y-plane). From left to right, the plot shows the field amplitude $E_y(x, y, 0, \omega)$ (normalized, red: $+1$, blue: -1) in the TE-plane, the real-space intensity $|E_y(x, y, 0, \omega)|^2$ and the reciprocal space intensity $|E_y(k_x, k_y, 0, \omega)|^2$ (blue: low, red: high). From top to bottom, each pattern corresponds to the eigenmode of the upper spectrum in Fig. 6.16, thus the even mode at the frequency $f = 271.5$ THz with a Q-factor of $Q \approx 5500$, the center peak with vanishing amplitude in the center of the middle cavity at the frequency $f = 277.7$ THz with a Q-factor of $Q \approx 8800$ and the odd mode at the frequency $f = 283.6$ THz with a Q-factor of $Q \approx 17000$. The different Q-factors are explained with radiation patterns perpendicular to the slab. For the even eigenmode, constructive interference from all three cavities leads to increased energy loss, therefore to a low Q-factor. One also observes a long evanescent tails in the TE-plane, leaking into the air hole lattice of the PhC in a 30° angle with respect to the cavity main axis. The other eigenmodes have odd symmetry, hence leading to destructive interference in the perpendicular direction, which yields a larger Q-factor. Also, the spatial confinement is stronger due to a stronger decay of the evanescent tails.

6.4 A Single Quantum Dot Coupled to a Photonic Crystal Cavity

Till now, light-mediated coupling between optical resonators was investigated. Now, the isolated, single $L3$-type PhCC is extended with a quantum-mechanical oscillator, a QD. For this purpose, microscopic, dynamic equations of motion for the coherence and occupancy of the QD (see Sec. 2.5 for details) are evaluated numerically in every time step, using a RK-integrator (see Sec. A.1). Calculating the optical polarization field $\mathbf{P}(\mathbf{r}, t)$ of the QD, $\mathbf{P}(\mathbf{r}, t)$ is coupled back self-consistently to drive Maxwells equations (Sec. 2.5.1). Strong coupling between a single QD and an eigenmode of a microcavity is well-investigated [4, 117, 132]. The focus of this section, however, is the effect of a high-intensity excitation of the QD. It is well-known, that, when the energy of an exciting pulse is large enough, so-called Mollow triplets occur.

6.4.1 QDs under strong excitation: Mollow Triplets

Excitation with strong light fields yield additional peaks e.g. in a fluorescence or transmission spectrum [133, 134]. Regarding the picture of bare and dressed states (see Sec. 2.6) brings light into the situation. Assume an atom-like oscillator with one transition $\omega_L = \epsilon_{\text{gap}}/\hbar$ between the

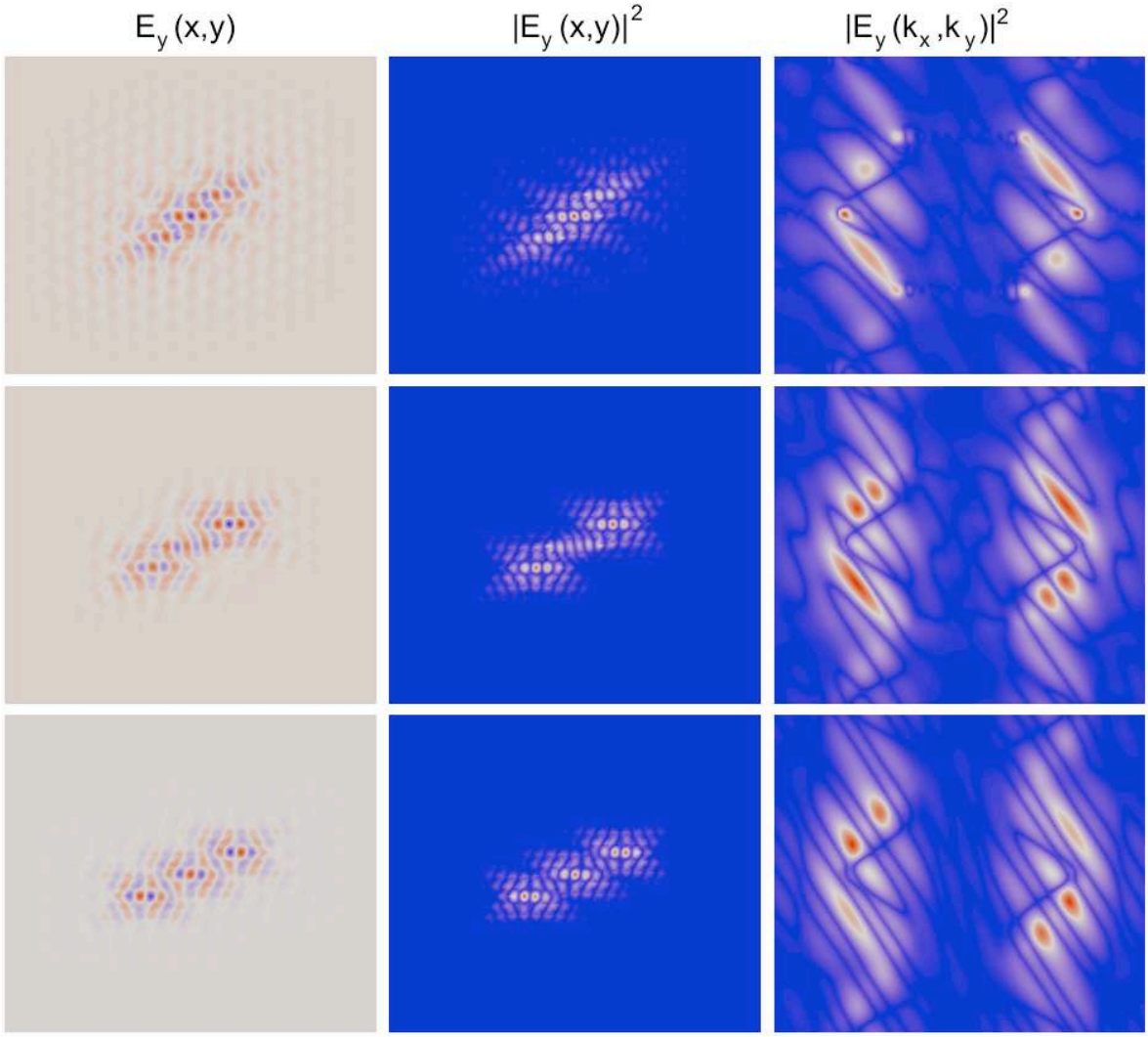

Figure 6.17: Spatiospectral response in the TE-plane from three laterally coupled cavities. Only the y-component of the coupled fundamental mode is shown. From left to right: Field amplitude (normalized, red: $+1$, blue: -1). Real-space intensity (blue: low, red: high). Reciprocal space intensity (blue: low, red: high). From top to bottom: even mode at $f = 271.5$ THz ($Q \approx 5500$). Center peak at $f = 277.7$ THz ($Q \approx 8800$). Odd mode at $f = 283.6$ THz ($Q \approx 17000$).

ground $|0\rangle$ and excited state $|1\rangle$. Bare and dressed states are described with a second quantum number, the photon number N, in addition to the quantum number of the atomic state. Thus, the full description of a state yields $|\, 0, N\rangle$, exemplarily for the ground state with N photons. Figure 6.18 shows the bare and dressed states schematically. Energy increases from bottom to top. Horizontal lines denote the states, bare states on the left and dressed states on the right. The transition frequency between the bared states is ω_L. However, the two bared states may have a detuning δ and are therefore degenerate for zero detuning. Illuminating the atom with an intense light field lifts the degeneracy. The bared states split by the Rabi frequency Ω_R, which is dependent of the intensity of the light field. Four transitions are possible:

- a transition connecting the dressed state with the atom in its ground state $|0\rangle$ while

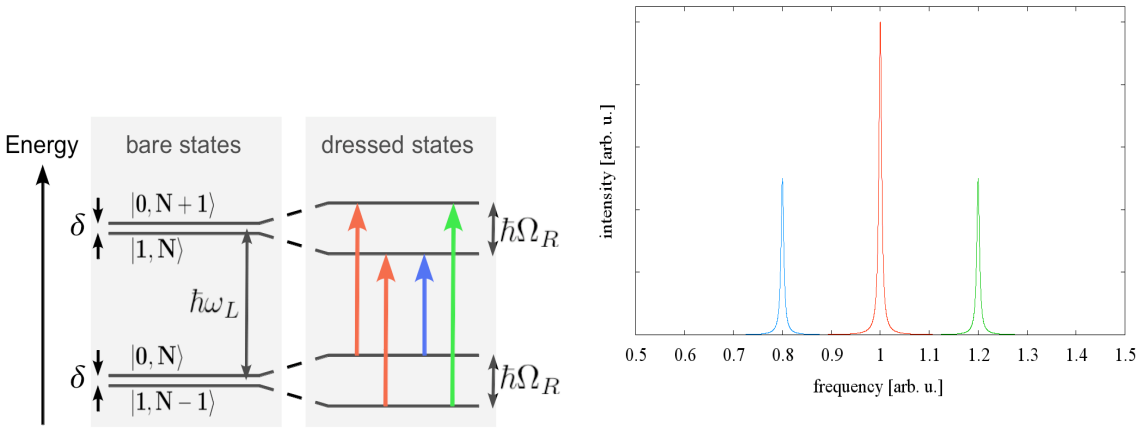

Figure 6.18: Left: energy levels from the quantum optics point of view. Bare states are separated by the gap energy $\varepsilon_{\mathrm{QD}} = \hbar\omega_L$ of the QD. Excitation with an intense laser pulse lifts the degeneracy of the bare states. Dressed states occur, split by the Rabi energy $\hbar\Omega_R$. Now, four transitions are possible. Right: Spectrum of a atom-like TLS under excitation with an intense laser pulse. The main peak belongs to the main transition (2x) in the scheme on the left. The upper and lower side band peak belong to the transition from $|1, N-1\rangle$ to $|0, N+1\rangle$ and from $|0, N\rangle$ to $|1, N\rangle$, respectively. Colors belong to the scheme on the left.

increasing the photon number N by 1 (red),

- a transition connecting the dressed state with the atom in its excited state $|1\rangle$ while increasing the photon number N by 1 (red),

- a transition connecting the atomic ground state to the atomic excited state without changing the photon number N (blue) and

- a transition connecting the atomic excited state and $N-1$ photons with the atomic ground state and $N+1$ photons (green).

These splittings yield three peaks in the spectrum. Two additional side peaks next to the central peak at ω_L, at $\omega = \omega_L \pm \Omega_R$ occur. These peaks have half the intensity of the central peak since they are each fed by one transition, while the central peak is fed by two transitions. A spectrum is shown in Fig. 6.18, right, to illustrate the Mollow triplet. The colors are equal to the colors of the transitions in the scheme on the left side. Lorentzian curves are used for the illustration. Since the Mollow triplet is intensity-dependent, placing a QD into a high-field position of a high-Q PhCC will lead to an increased Ω_R due to the strong spatial light confinement in the defect area and the small cavity decay rate. Therefore, one can control the splitting of the Mollow triplet with the Q-factor.
Since the dressed states are a picture from quantum optics, one is still able to see the splitting in a semiclassical approach, like the FDTD, where the electromagnetic field is treated classically and the QD is treated quantum-mechanically.

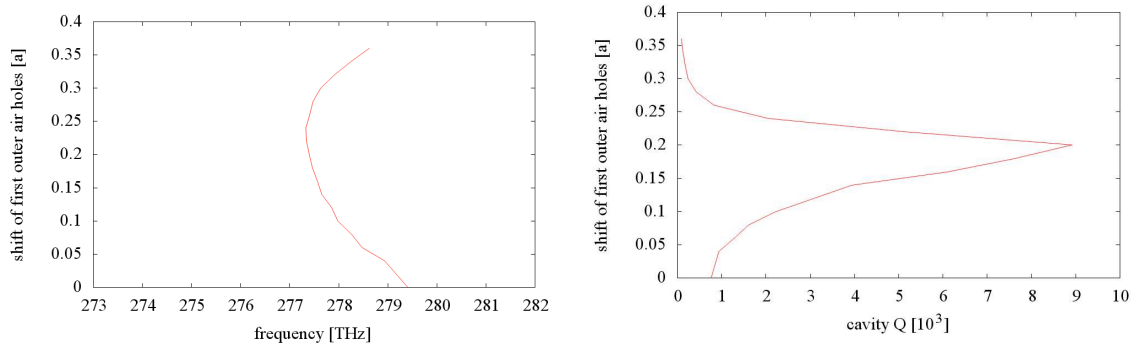

Figure 6.19: Left: air hole shift dependency (vertical axis, s/a) over frequency (horizontal axis, THz). Right: air hole shift dependency (vertical axis, s/a) over the Q-factor. Calculations are performed with a coarse grid with $\Delta x = \Delta z = a/10$, $\Delta y = \sqrt{3/4}\Delta x$. Similar to Fig. 5.7, top.

6.4.2 Mollow Triplets in a Coupled Cavity-QD System

For the investigations, a PhCC with a $L3$-type defect is used (similar to Sec. 5.2). The parametric set is a lattice constant of $a = 300$ nm, slab thickness-to-lattice constant ratio $t/a = 0.6$, air hole radius-to-lattice constant ratio $t/a = 0.3$ and a dielectric permittivity of $\epsilon = 10.595$, corresponding to GaAs at $T \approx 4$ °K [122]. For the purpose of a Q-depending Mollow triplet, the outer air hole modification is variable in the shift, but fixed in the radius ($r/a = 0.3$).
The fundamental mode is in the focus of this section. A spatiospectral response of the y-component of the electric field is shown in Fig. 5.5 for the unmodified defect area and in Fig. 5.9 for the modified defect area. A comparison shows, that the mode pattern is almost not changed. Especially the field maximum in the center of the defect area is not altered. Therefore, the QD is placed there. To describe the QD, the transition frequency is always chosen to be resonant with the cavity resonance, the dipole matrix element is $\mu_y = 3$ eÅ (since only the y-component of the fundamental mode has a field maximum in the center, the other dipole matrix elements are not taken into account) and the phenomenological dephasing is $\gamma_{\text{phen}} = 1$ ns^{-1}. For the spatial extension of the quantum dot, a Gaussian ellipsoid in all three dimensions is used. The radius is chosen to be fairly large with $r_{\text{QD}} = 50$ nm. In [85] it is shown, that the effect of the size of a QD in a square lattice on the radiative dephasing is negligible for extensions larger than 30 nm. Therefore, the size of the QD is not expected to have an noticeable influence. As initial conditions, the QD is assumed to be in the ground state. Otherwise, the situation would be non-physical due to a lack in surrounding fields.
The computational domain is set to $V_{\text{sim}} = 19 \times 9.5\sqrt{3} \times 2a^3$ and $t_{\text{sim}} = 10$ ps. For the sake of computational time and effort, the spatial discretization is set to be more coarse than in the previous cases, $\Delta x = \Delta z = a/10$ and $\Delta y = \sqrt{3/4}\Delta x$. Note that this slightly changes the spectral properties of the fundamental mode. Varying the position of the outer air hole results in Fig. 6.19, where the change in the resonance is shown on the left, and the change in the Q-factor is shown on the right side. The shift of the outer air holes is given in units of the lattice constant a. Frequencies on the left are given in THz. The general behavior of the frequency and the Q-factor remains with the coarse spatial grid. However, the resonance of the fundamental mode is at $f_C = 277.4$ THz with a cavity decay time of $T_C \approx 0.01$ ns,

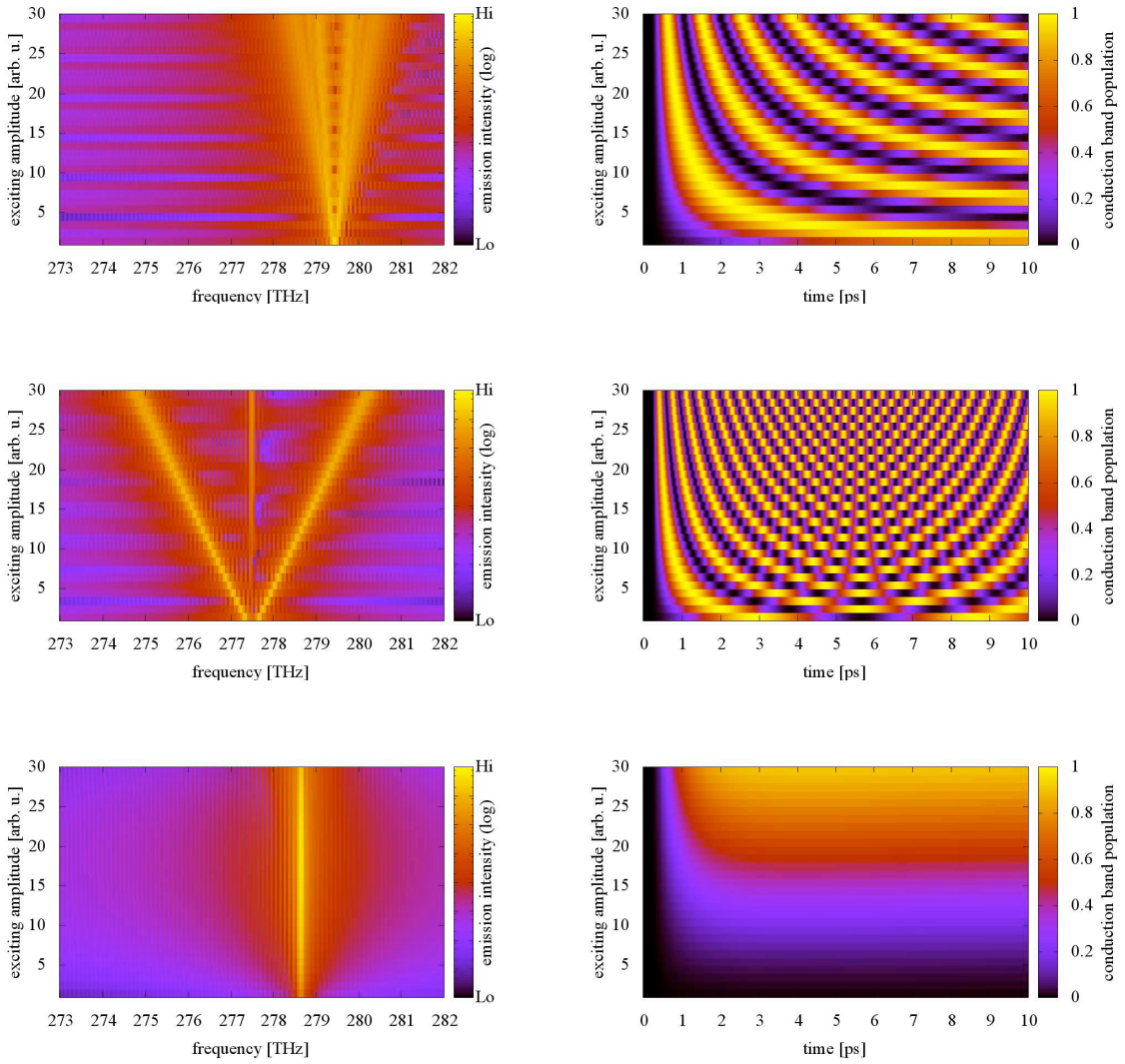

Figure 6.20: Left: Excitation amplitude (vertical axis) in arbitrary units over frequency in THZ (horizontal axis). The emission intensity of the QD is color-coded (logarithmic scale). Right: Excitation amplitude (vertical axis) in arbitrary units over time in ps (horizontal axis). The population of the conduction band of the QD is color-coded. From top to bottom: Shift of the outer air holes: $s/a = 0.02$ (top), $s/a = 0.2$ (middle) and $s/a = 0.38$ (bottom). The modification maps the Q-factor. Refer to Fig. 6.19 for the shift-dependent Q-factor.

corresponding to $Q = 8919$ for the optimal case with an air hole shift-to-lattice constant ratio $s/a = 0.2$.

Figure 6.20 is built up in the following manner: from top to bottom, the Q-factor of the cavity is gradually altered. De facto, the shift of the outer air holes maps the cavity Q-factor according to Fig. 6.19, right, as well as the frequency of the fundamental mode, left. The outer air holes of the cavity are shifted outwards by $s/a = 0.02$, $s/a = 0.2$ and $s/a = 0.38$ (from

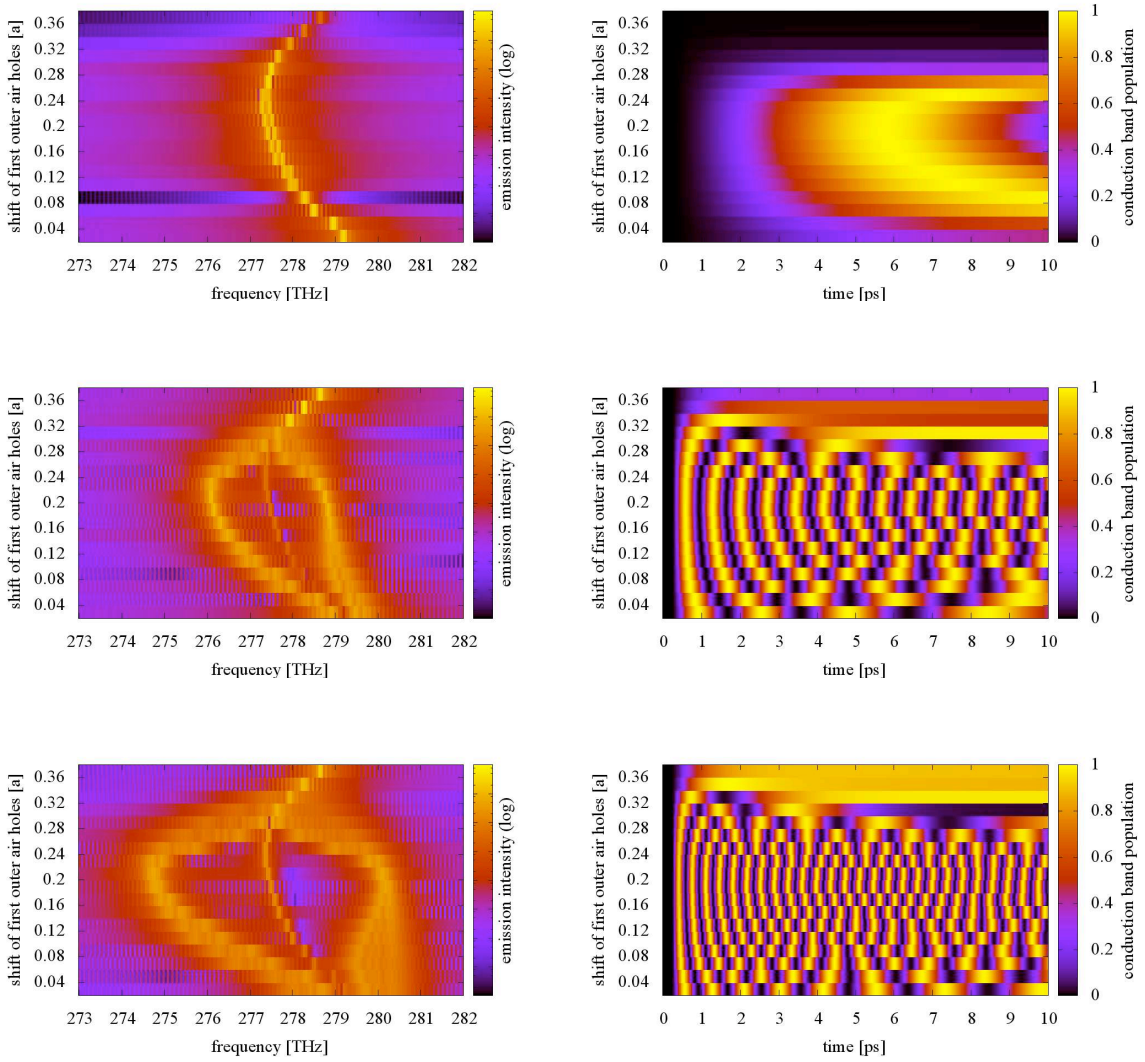

Figure 6.21: Left: Shift of the outer air holes from $s/a = 0.02$ to $s/a = 0.38$ (vertical axis) over frequency in THZ (horizontal axis). The emission intensity of the QD is color-coded (logarithmic scale). Right: Shift of the outer air holes from $s/a = 0.02$ to $s/a = 0.38$ (vertical axis) over time in ps (horizontal axis). The population of the conduction band of the QD is color-coded. The modification maps the Q-factor. Refer to Fig. 6.19 for the shift-dependent Q-factor. From top to bottom: Increasing intensity of the exciting laser pulse. The amplitudes refer to 1, 15 and 30 in Fig. 6.20.

top to bottom). On the left side, Fig. 6.20 shows the emission intensity of the QD (color-coded) on a logarithmic scale, depending on the exciting laser pulse intensity on the vertical axis in arbitrary units over the frequency in THz. The intensity is increased linearly from 1 to 30. On the right side, the temporal evolution of the conduction band population of the QD (color-coded) is shown for the corresponding cases. The exciting laser pulse amplitude is plotted on the vertical axis (in arbitrary units), while the time in ps is on the horizontal axis.

Starting from the first plot for the conduction band population for a outer air hole shift of $s/a = 0.02$, the Q-factor is fairly low ($Q = 755$). For lowest intensity, the exciting laser field is not able to invert the QD. Above, Rabi oscillations are observed. For increasing intensity, the Rabi frequency Ω_R increases linearly due to the linear dependence on the exciting field. The Q-factor is mapped in the population, too. Since the field decays exponentially in time in the cavity, the Rabi oscillations are dilated. In the spectrum for the coupled system, one can see the isolated cavity resonance at $f = 279.41$ THz for the lowest investigated amplitude. Increasing the amplitude of the exciting laser pulse lets the single resonance split. Population is built up in the QD and multiple Rabi flops are observed. Now, increasing the Q-factor of the cavity to $Q = 8919$ results in a clear Mollow triplet with narrow side band peaks, similar to Fig. 6.18 for the dressed state picture (note the resonance of the isolated, single cavity shift $f = 277.47$ THz according to Fig. 6.19 due to the modification). The population of the QD oscillates with an increased Rabi frequency Ω_R. With increasing Q-factor, the side bands of the Mollow triplets in the emission intensity of the QD become more narrow. Due to a more narrow line width of the cavity mode, the excitation of the QD is spectrally smaller, too, therefore the dressed states are excited more resonantly, yielding sharp side band peaks. This also is reflected in the conduction band population of the QD, which flops with a Rabi frequency $\Omega_R \approx 3$ THz, equal to the spectral shift of the side band peak frequency with respect to the main transition. Following the decrease of the Q-factor with larger shift of the outer air holes, one finds a decreased splitting of the Mollow triplet due to the lower Q-factor of the cavity. Also, the cavity field cannot fully invert the QD.
The situation in Fig. 6.21 is similar to Fig. 6.20. Here, the amplitude of the exciting pulse in arbitrary units is gradually increased from top to bottom (1, 15 and 30). The alignment of the subfigures is the same like in Fig. 6.20. On the left, the emission intensity of the QD is shown with frequencies in THz on the horizontal axis. The right side depicts the conduction band population of the single QD (color-coded), coupled to the cavity and the horizontal axis shows the time in ps. On the vertical axis, the shift s of the outer air holes is shown in units of the lattice constant a. Thus, this axis indirectly maps the cavity Q-factor, according to Fig. 6.19. Small and large shift means low Q-factors, while the optimal shift of the outer air holes is about $s/a = 0.2$. Generally, one sees the main transition line tracing the isolated, single PhCC resonance in Fig. 6.19. The QD transition is resonant with the cavity mode for all cases. For an exciting laser pulse amplitude of 10 and above, the Mollow triplet is clearly visible. Side band peaks reduce their width with increasing Q-factor of the cavity. For increasing amplitude, the side bands shift away linearly from the main peak, as it is expected.

Chapter 7

Conclusion and Outlook

Conclusion

Two different nano-scale sized structures are investigated within this thesis, using the Finite-Difference Time-Domain method for numerical evaluation of the three-dimensional Maxwells equations. Due to their different method to confine light in small spatial regions, both kinds of resonators have certain advantages where the other has disadvantages and vice versa. However, strong resonator-resonator interaction and also strong coupling between a single quantum dot, which is described with dynamic equations to calculate optical polarization field, is shown.
The effects of pertubating the perfectly circular shape of a microdisk resonator is investigated numerically, together with radius variations. Ellipticity and non-vertical side walls affect the resonances dramatically. Modifications of the mode patterns arise, resulting in stronger coupling to the environment, hence less confinement. The Q-factors are therefore affected strongly, too. One can also make advantage from these facts. An embedded quantum dot, for example, can be slightly detuned. Thus, by applying proper methods, the resonance can be adapted. Also, the spatial mode profile can be altered, to let the quantum dot be placed in a position with high field amplitude, when a proper modification is performed. Also, the coupling between different mode orders in a microdisk resonator can be analyzed well, because the resonance tuning using the mentioned parameters of the microdisk is comparably large. The effect of a uniaxial anisotropic environment is calculated, too. Even when the permittivity tensor elements exceed the permittivity of the resonator, confinement is still maintained. Additionally, anticrossing features between different mode orders are observed, resulting from the coupling between the different modes via the anisotropic environment. Experimental data of a microdisk resonator with radius $R = 3$ μm in a liquid crystal environment show a clear red-shift for all resonances in the investigated frequency range. A comparison with numerical data, using the uniaxial anisotropy to model the LC environment, is in good agreement.
For the purpose of strong interaction between photonic crystal cavities and strong coupling between single quantum dots and photonic crystal cavities, the optimization with the method of gentle confinement is discussed in detail. Effects of the modification of the first two neighbored air holes of a $L3$-type defect are investigated. The Q-factor is increased by one order of magnitude. Experimental data of a permanent tuning mechanism of a $L7$-type defect by evaporating a thin additional layer homogeneously only on the top surface of a photonic crystal cavity (without covering the air holes inside), are compared with numerical data. A red-shift in frequency and drop in the Q-factor and amplitude of the resonances are nicely reproduced by the simulations.
The coupling between microdisk resonators, photonic crystal cavities and quantum dots is investigated. For the microdisk-microdisk coupling, strongly asymmetric line and loss splitting emerges for small gap spacings between the resonators. A tight-binding approach, equivalent to the approach known from semiconductor physics, shows that the asymmetric line splitting results from an overlap integral-type tight-binding parameter, which decreases drastically with increasing gap size. The line splitting is explained by radiation patterns of the new eigenmodes of the systems, where constructive and destructive interference yield the low and high Q mode, respectively. The energy transfer between the resonators agrees perfectly with the line splitting. Strong coupling is observed for a single quantum dot coupled to a high-Q whispering gallery mode in a microdisk resonator. Placing the quantum dot in a high-amplitude position in the microdisk, a symmetric line splitting of 46 GHz occurs. When the quantum dot frequency is tuned through the microdisk resonance, repelling between the upper and lower polariton branch is observed. A more intense focus lies on the coupling using photonic crys-

tal cavities with $L3$-type defects. Analyzing the field pattern of the fundamental mode leads to alignment schemes for more efficient field injection between coupled cavities. The beating frequency between the two laterally aligned cavities agrees perfectly with the line splitting. Distant-dependent calculations are performed. It is shown, that the proposed alignment scheme also applies for three coupled cavities. Possible construction of waveguides, based upon photonic crystal cavities is proposed to efficiently guide light along different symmetry directions of the air hole lattice. Coupling a single quantum dot to a cavity mode in a photonic crystal under intense excitation is investigated at the last. Q-factor dependent simulations show the occurrence of Mollow triplets with increasing intensity of the exciting laser field.

Outlook

The recent progress in spectral mode tuning in optical resonators like microdisks and photonic crystal cavities is already far. Permanent tuning by direct modification and dynamic mode tuning by embedding a resonator in a liquid crystal environment have been shown. Also, the usage of a liquid crystal resonator yields a tuning range two orders of magnitude larger than using isotropic resonators. Finding a way for providing an anisotropic, dynamically tunable photonic crystal cavity is a big challenge. By Combining an anisotropic resonator with an anisotropic environment, the tuning range may be further increased. Also it may be possible to dynamically tune the cavity decay times, due to full control of the penetration depth of the mode patterns into the environment.
For the coupling between photonic crystal cavities and embedded quantum dots, it is also worth to investigate the coupling between multiple quantum dots in a single photonic crystal cavity. The knowledge of the energy transfer between the quantum dots can lead to new devices, new technologies in nanooptics and photonics. Also, for multiple coupled photonic crystal cavities and quantum dots in different cavities, which are spatially uncoupled but radiatively coupled via the confined electromagnetic modes in the coupled cavity system, can reveal interesting facts about the light-matter interaction and can give deeper insight into it, e.g. formation of new quasi-particles. Under strong excitation, side bands of Mollow triplets can be pushed towards resonances of other eigenmodes of the coupled system. The possibilities are merely unlimited due to the variety of possible combinations of these resonator systems. With this, a step towards quantum information processing with devices on a single chip can be done.

Appendix A

Numerical Methods

A.1 Runge-Kutta Algorithm

For the integration of the system of inhomogeneous, ordinary differential equations (ODE) of first order for the coherence and density of the nonlinear treated quantum dot, the *Runge-Kutta* algorithm of 4^{th} is used, since it is well established and of great stability. The integration steps will only be depicted shortly, a more detailed description can be found in [84].
Assume an inhomogeneous ODE in the form

$$\dot{y}(x) = f(y(x), x)\,. \tag{A.1}$$

Basically, the algorithm transforms the eq. (A.1) into an integral equation:

$$y(x+\Delta x) = \int_{x}^{x+\Delta x} f(y(\xi),\xi)d\xi \approx y(x) + \Delta x \sum_{i=1}^{j} \gamma_i f(y_i(x_i), x_i)\,, \tag{A.2}$$

where Δx is the discretization. In an explicit *Runge-Kutta* algorithm, $f(y_i(x_i), x_i) \approx k_i(y, x)$ is set. In 4^{th} those functions are given by the weightings γ_i:

$$\begin{aligned}
\gamma_1 k_1(y,x) &= \frac{1}{6} f(y,x) \\
\gamma_2 k_2(y,x) &= \frac{1}{3} f(y + \frac{k_1}{2}, x + \frac{\Delta x}{2}) \\
\gamma_3 k_3(y,x) &= \frac{1}{3} f(y + \frac{k_2}{2}, x + \frac{\Delta x}{2}) \\
\gamma_4 k_4(y,x) &= \frac{1}{6} f(y + \frac{k_3}{2}, x + \Delta x)\,.
\end{aligned} \tag{A.3}$$

A.2 Lagrange Interpolation

Since the *Runge-Kutta* integration algorithm, Sec. A.1, for the time-depending coherence and density equations of the QD, eqs. 2.58-2.59, needs the future time steps at $t + 0.5\Delta t$ and $t + \Delta t$, which are not provided by the FDTD algorithm, one needs to extrapolate these values from earlier time steps. One method for the extrapolation, actually used for interpolation, but also applicable for this purpose, is the *Lagrange* interpolation scheme, which is a polynomial interpolation scheme. In general, one creates a polynom $p(x)$ of order $(n-1)$, whose i^{th} element equals the function, which wants to be interpolated, at the i^{th} element.

$$p(x_i) = \sum_{j}^{n} l_{jn}(x_i) f(x_j) \,. \tag{A.4}$$

With $l_{jn}(x_i) = \delta_{ij}$, this condition is fulfilled. Hence, the coefficients $l_{jn}(x_i)$ take the form

$$l_{jn}(x) = \prod_{i=1, i\neq j}^{n} \frac{x - x_i}{x_j - x_i} \,. \tag{A.5}$$

For the extrapolation of the needed future time steps, it is enough to use a 3^{rd} order scheme, resulting in (for reasons of readability, the spatial indices are omitted)

$$\begin{aligned} E^{n+\frac{1}{2}} &= \frac{3}{8} E^{n-2} - \frac{5}{4} E^{n-1} + \frac{15}{8} E^{n} \\ E^{n+1} &= E^{n-2} - 3E^{n-1} + 3E^{n} \,. \end{aligned} \tag{A.6}$$

Appendix B

Parameters and Constants for the Numerical Simulations

B.1 Constants of Nature

List of the constants of nature in SI units.

Constant	Symbol [Dimension]	Value
Planck constant	h [Js]	6.626176×10^{-34}
reduced Planck constant	$\hbar$ [Js]	1.054589×10^{-34}
vacuum permeability	μ_0 [$\mathrm{Js^2C^-2m}$]	$4\pi 10^{-7}$
vacuum permittivity	ϵ_0 [$\mathrm{C^2J^{-1}m}$]	8.854188×10^{-12}
speed of light in vacuum	c_0 [$\mathrm{ms^{-1}}$]	2.997925×10^{8}

Table B.1: List of Constants of Nature.

B.2 Parameter List for the Quantum Dot

Parameter Quantum Dot	Sec. 6.2	Sec. 6.4
transition frequency ω_L [Hz]	varying	varying
dipole matrix element d_μ [eÅ]	3	3
phenomenological dephasing rate γ [Hz]	0	1×10^9
background ϵ	11.56	10.595
Gaussian ellipsoidal wave function radius x [m]	30×10^{-9}	50×10^{-9}
Gaussian ellipsoidal wave function radius y [m]	30×10^{-9}	50×10^{-9}
Gaussian ellipsoidal wave function radius z [m]	30×10^{-9}	50×10^{-9}

Table B.2: List of Parameters for the Quantum Dot.

B.3 Parameter List for the FDTD Simulations

Parameter	MD, Chap. 4+6	PhCC, Chap. 5+6
radius [m]	361×10^{-9} (3050×10^{-9})	- - -
lattice constant [m]	- - -	$a/16$ ($a/10$)
thickness [m]	$265 \times 10{-}9$ ($240 \times 10{-}9$)	$0.6 \times a$
air hole radius Δx [m]	- - -	$0.3 \times a$
spatial grid cell size Δx [m]	7.3529×10^{-9}	$a/16$ ($a/10$)
spatial grid cell size Δy [m]	7.3529×10^{-9}	$a/16$ ($a/10$)
spatial grid cell size Δz [m]	7.3529×10^{-9}	$a/16$ ($a/10$)
dielectric permittivity slab ϵ_{slab}	11.56	11.56
dielectric permittivity environment ϵ_{env}	1	1
simulation time t_{sim} [s]	5×10^{-12}	5×10^{-12} (1×10^{-11})
CPML cells	20	20

Table B.3: List of Parameters for the PhC Cavities and Microdisks.

CPML Parameter	Value
$\alpha_{\text{CPML, max}}$	0.05
$\sigma_{\text{CPML, max}}$	0.8
$\kappa_{\text{CPML, max}}$	5
m_{CPML}	3
$m_{\alpha_{\text{CPML}}}$	1

Table B.4: List of CPML Parameters. For more information, refer to [60].

Bibliography

[1] M. Shirane, S. Kono, J. Ushida, S. Ohkouchi, N. Ikeda, Y. Sugimoto, and A. Tomita. Mode identification of high-quality-factor single-defect nanocavities in quantum dot-embedded photonic crystals. *J. Appl. Phys.*, 101(073107), 2007.

[2] Y. Tang, A. M. Minatairov, J. L. Merz, V. Tokranov, and S. Oktyabrsky. Characterization of 2d-photonic crystal nanocavities by polarisation-dependent photoluminescence. *Proceedings of 2005 5th IEEE Conference on Nanotechnology*, 1:35 – 38 vol. 1, 2005.

[3] Y. Akahane, T. Asano, B.-S. Song, and S. Noda. High-q nanocavity in a two-dimensional photonic crystal. *Letters to Nature*, 425:944–947, 2003.

[4] T. Yoshie, A. Scherer, J. Hendrickson, G. Kithrova, H. M. Gibbs, G. Rupper, C. Eli, O. B. Shchekin, and D. G. Deppe. Vacuum rabi splitting with a single quantum dot in a photonic crystal nanocavity. *Letters to Nature*, 432:200–204, 2004.

[5] T. D. Ladd, F. Jelezko, R. Laflamme, Y. Nakamura, C. Monroe, and J. L. O'Brian. Quantum computers. *Nature*, 464(7285), 2010. Reviews.

[6] A. Grodecka, C. Weber, A. Knorr, and P. Machnikowski. Interplay and optimization of decoherence mechanisms in the optical control of spin quantum bits implemented on a semiconductor quantum dot. *Phys. Rev. B*, 73(12):125306, 2006.

[7] A. Grodecka and P. Machnikowski. Partly noiseless encoding of quantum information in quantum dot arrays against phonon-induced pure dephasing. *Phys. Rev. B*, 76(12): 205305, 2007.

[8] A. Grodecka, P. Machnikowski, and J. Lacak. Reducing pure dephasing of quantum bits by collective encoding in quantum dot arrays. *J. Phys.: Conf. Ser.*, 30(1):41, 2006.

[9] E. M. Purcell. Spontaneous emission probabilities at radio frequencies. *Physical Review*, 69, 1946.

[10] M. Pelton, J. Vučković, A. Scherer, and Y. Yamamoto. Three-dimensionally confined modes in micropost microcavities: Quality factors and pucrell factors. *IEEE Journal of Quantum Electronics*, 38(2):170–177, 2002.

[11] V. S. C. Manga Rao and S. Hughes. Single quantum-dot purcell factor and β factor in a photonic crystal waveguide. *Physical Review B*, 75(205437), 2007.

[12] L. Sanchis, M. J. Cryan, J. Pozo, I. J. Craddock, and J. G. Rarity. Ultrahigh purcell factor in photonic crystal slab microcavities. *Physical Review B*, 76(045118), 2007.

[13] B.-S. Song, S. Noda, T. Asano, and Y. Akahane. Ultra-high-q photonic double-heterostructure nanocavity. *Letters to Nature*, 4:207–210, 2005.

[14] D. K. Armani, T. J. Kippenberg, S. M. Spillane, and K. J. Vahala. Ultra-high-q micro-toroid on a chip. *Letters to Nature*, 421:925–928, 2003.

[15] G. Kithrova, H. M. Gibbs, M. Kira, S. W. Koch, and A. Scherer. Vacuum rabi splitting in semiconductors. *Nature Physics*, 2:81–90, 2006. Review article.

[16] A. A. Abdumalikov, O. Astafiev, and Y. Nakamura. Vacuum rabi splitting due to strong coupling of a flux qubit and a coplanar waveguide resonator. *Physical Review B*, 78(189502(R)), 2008.

[17] S. Gröblacher, K. Hammerer, M. R. Vanner, and M. Aspelmeyer. Observation of strong coupling between a micromechanical resonator in an optical cavity field. *Nature*, 460, 2009.

[18] S. Gröblacher, J. B. Hertzberg, M. R. Vanner, G. D. Cole, S. Gigan, K. C. Schwab, and M. Aspelmeyer. Demonstration of an ultracold micro-optomechanical oscillator in a cryogenic cavity. *Nature Physics*, 5, 2009.

[19] J. C. Sankey, C. Yang, B. M. Zwickl, A. M. Jayich, and J. G. E. Harris. Strong and tunable nonlinear optomechanical coupling in a low-loss system. *Nature Physics*, 6, 2010.

[20] J. D. Teufel, T. Donner, D. Li, J. W. Harlow, M. S. Allman, K. Cicak, A. J. Sirois, J. D. Whittaker, K. W. Lehnert, and R. W. Simmonds. Sideband cooling micromechanical motion to the quantum ground state. *arXiv:1103.2144v1 [quantum physics]*, 2011.

[21] Y. Li, J. Zheng, J. Gao, J. Shu, M. S. Aras, and C. W. Wong. Design of dispersive optomechanical coupling and cooling in ultrahigh-q/v slot-type photonic crystal cavities. *Opt. Express*, 18(23), 2010.

[22] Y.-G. Roh, T. Tanabe, A. Shinya, H. Taniyama, E. Kuramochi, S. Matsuo, T. Sato, and M. Notomi. Strong optomechanical interaction in a bilayer photonic crystal. *Physical Review B*, 81(121101(R)), 2010.

[23] E. Gavartin, R. Braive, I. Sagnes, O. Arcizet, A. Beveratos, T. J. Kippenberg, and I. Robert-Philip. Optomechanical coupling in a two-dimensional photonic crystal defect cavity. *Phys. Rev. Lett.*, 106(20):203902, 2011.

[24] F. R. K. Reinitzer. Beiträge zur kenntniss des cholesterins. *Monatshefte für Chemie*, 1888.

[25] O. Lehmann. über fliessende krystalle. *Zeitschrift für Physikalische Chemie*, 1889.

[26] K. A. Piegdon, S. Declair, J. Förstner, T. Meier, H. Matthias, M. Urbanski, H.-S. Kitzerow, D. Reuter, A. D. Wieck, A. Lorke, and C. Meier. Tuning quantum-dot based photonic devices with liquid crystals. *Opt. Express*, 18(8):7946–7954, 2010.

[27] M. Humar, M. Ravnik, S. Pajk, and I. Muševič. Electrically tunable liquid crystal optical microresonators. *Nature Photonics*, 3(10):595 – 600, 2009.

[28] Sir J. Pendry, D. Schurig, and D. R. Smith. Controlling electromagnetic fields. *Science*, 312(5514):1780–1782, 2006.

[29] U. Leonhardt. Optical conformal mapping. *Science*, 312(5781):1777–1780, 2006.

[30] A. Taflove and S. C. Hagness. *Computational Electrodynamics - The Finite-Difference Time-Domain Method, 3rd edition*. Artech House, Boston, 2005. 3rd Edition.

[31] A. F. Oskooi, D. Roundy, M. Ibanescu, P. Bermel, J. D. Joannopoulos, and S. G. Johnson. Meep: A flexible free-software package for electromagnetic simulations by the fdtd method. *Computer Physics Communications*, 181:687–702, 2010.

[32] J. B. Schneider. Understanding the finite-difference time-domain method, 2010. `www.eecs.wsu.edu/~schneidj/ufdtd`.

[33] L. Zschiedrich, S. Burger, B. Kettner, and F. Schmidt. Advanced finite element method for nano-resonators. *Proceeding of SPIE*, 6115, 2006.

[34] K. Kakihara, N. Kono, K. Saitoh, and M. Koshiba. Full-vectorial finite element method in a cylindrical coordinate system for loss analysis of photonic wire bends. *Opt. Express*, 14(23):11128–11141, 2006.

[35] T. Weiland. A discretization method for the solution of maxwell's equations for six-component fields. *Electronics and Communications AEUE*, 31(3):116–120, 1977.

[36] T. Weiland. Time domain electromagnetic field computation with finite difference methods. *International Journal of Numerical Modelling: Electronic Networks, Devices and Fields*, 9:259–319, 1996.

[37] R. Schuhmann and T. Weiland. Stability of the fdtd algorithm on nonorthogonal grids related to the spatial interpolation scheme. *IEEE Transactions on Magnetics*, 34(5): 2751–2754, 1998.

[38] F. Abelès. Recherches sur la propagation des ondes électromagnétiques sinusoïdales dans les milieux stratifiés. *Ann. Phys.*, 3(596):706, 1950.

[39] M. Born and E. Wolf. *Principles of Optics*. Cambridge, 2006. 7th Edition, 4th Printing.

[40] S. Teitler and B. W. Henvis. Refraction in stratified, anisotropic media. *J. Opt. Soc. Am.*, 60(6):830–834, 1970.

[41] L. Wang and S.I. Rokhlin. Stable reformulation of transfer matrix method for wave propagation in layered anisotropic media. *Ultrasonics*, 39:413–424, 2001.

[42] J.S. Hesthaven and T. Warburton. Nodal high-order methods on unstructured grids: 1. time-domain solution of maxwells equations. *J. Comput. Phys.*, 181:186–221, 2002.

[43] J. S. Hesthaven and T. Warburton. *Nodal Discontinuous Galerkin Methods: Algorithms, Analysis, and Applications*. Springer, 2007. 1st Edition.

[44] K. Stannigel, M. König, J. Niegemann, and K. Busch. Discontinuous galerkin time-domain computations of metallic nanostructures. *Opt. Express*, 17:14934–14947, 2008.

[45] X. Ji, T. Lu, W. Cai, and P. Zhang. Discontinuous galerkin time domain (dgtd) methods for the study of 2-d waveguide-coupled microring resonators. *J. Lightwave Technol.*, 23: 3864, 2010.

[46] G. Tang, R. L. Panetta, and P. Yang. Application of a discontinuous galerkin time domain method to simulation of optical properties of dielectric particles. *Appl. Opt.*, 49: 2827–2840, 2010.

[47] J. C. Maxwell. A dynamical theory of the electromagnetic field. *Philosophical Transactions of the Royal Society of London*, 155:459–512, 1865.

[48] J. D. Jackson. *Klassische Elektrodynamik*. Gruyter Berlin, 2006. 4th Edition.

[49] D. J. Griffiths. *Introduction to Electrodynamics*. Pearson Benjamin Cummings, 2008. 3rd Edition.

[50] K. S. Yee. Numerical solution of initial boundary value problems involving maxwell's equations in isotropic media. *IEEE Trans. Antennas and Propagation*, 14:302–307, 1966.

[51] C. Wiebeler, 2010-2011. private communication.

[52] Y.-P. Li S.-L. Qui. Q-factor instability and its explanation in the staircased fdtd simulation of high-q circular cavity. *Science*, 313, 2006.

[53] N. Okada and J. B. Cole. Simulation of whispering gallery modes in the mie regime using the nonstandard finite-difference time domain algorithm. *J. Opt. Soc. Am. B*, 27 (4):631–639, 2010.

[54] A. Farjadpour, D. Roundy, A. Rodriguez, M. Ibanescu, P. Bermel, J. D. Joannopoulos, S. G. Johnson, and G. Burr. Improving accuracy by subpixel smoothing in fdtd. *Optics Letters*, 31:2972–2974, 2006.

[55] A. F. Oskooi, C. Kottke, and S. G. Johnson. Accurate finite-difference time-domain simulation of anisotropic media by subpixel smoothing. *Optics Letters*, 34:2778–2780, 2009.

[56] G. Mur. Absorbing boundary conditions for the fintite-difference approximation of the time-domain method electromagnetic field equations. *IEEE Transactions on Electromagnetic Compatibility*, EMC-23(4):377–382, 1981.

[57] J. P. Berenger. A perfectly matched layer for the absorption of electromagnetic waves. *Journal of Computational Physics*, 114(2):195–200, 1994.

[58] Z.S. Sacks, D.M. Kingsland, R. Lee, and J.F. Lee. A perfectly matched anisotropic absorber for use as an absorbing boundary condition. *IEEE Trans. Antennas and Propagation*, 43:1460Ð1463, 1995.

[59] M. Kuzuoglu and R. Mittra. Frequency dependence of the constitutive parameters of causal perfectly matched anisotropic absorbers. *IEEE Microwave and Guided Wave Letters*, 6:447–449, 1996.

[60] J. A. Roden and S. D. Gedney. Convolutional pml (cpml): An efficient fdtd implementation of the cfs-pml for arbitrary media. *Microwave Optical Tech. Lett.*, 27(6):334Ð339, 2000.

[61] M. M. Nielson and I. L. Chuang. *Quantum Computation and Quantum Information*. Cambridge, 2004.

[62] J. D. Joannopoulus, S. G. Johnson, J. N. Winn, and R. D. Meade. *Photonic Crystals: Molding the Flow of Light*. Princeton University Press, 2008. 2nd Edition.

[63] H. Ibach and H. Lüth. *Festkörperphysik. Einführung in die Grundlagen*. Springer, 2002. 6th Edition (03/2002).

[64] N. W. Ashcroft and N. D. Mermin. *Festkörperphysik*. Oldenbourg, 2005. 2nd Edition (03/2005).

[65] O. Madelung. *Introduction to Solid-State Theory*. Springer, 1996.

[66] H. Haug and S. W. Koch. *Quantum Theory of the Optical and Electronic Properties of Semiconductors*. World Scientific Publishing, 2001.

[67] W. W. Chow and S. W. Koch. *Semiconductor - Laser Fundamentals*. Springer, 1999.

[68] T. Kuhn. *Density Matrix Theory of Coherent Ultrafast Optics and Kinetics of Semiconductors*, pages 173–187. Chapmann Hall, 1998. edited by E. Schöll.

[69] H. Haug and A.-P. Jauho. *Quantum Kinetics in Transport and Optics of Semiconductors*. Springer, 1996.

[70] C. Ell. *Microscopic Theory of Semiconductors*, chapter II. World Scientific, 1995.

[71] P. Y. Yu and M. Cardona. *Fundamentals of Semiconductors*. Springer, 1998.

[72] J. Sajeev. Strong localization of photons in certain disordered dielectric superlattices. *Phys. Rev. Lett.*, 58(23):2486–2489, 1987.

[73] E. Yablonovitch. Inhibited spontaneous emission in solid-state physics and electronics. *Phys. Rev. Lett.*, 58:2059, 1987.

[74] J. D. Joannopoulos, P. R. Villeneuve, and S. Fan. Photonic crystals. *Solid State Communications*, 102(2-3):165 – 173, 1997. Highlights in Condensed Matter Physics and Materials Science.

[75] J.-M. Lourtioz, H. B., V. Berger, J.-M. Gerard, D. Maystre, and A. Tchelnokov. *Photonic Crystals: Towards Nanoscale Photonic Devices*. Springer, 2008. 2nd Edition, Translated by M. P. de Fornel.

[76] J. Heebner, R. Grover, and T. A. Ibrahim. *Optical Microresonators: Theory, Fabrication and Applications*. Springer, 2008.

[77] S. Brandt and H. D. Dahmen. *Elektrodynamik: Eine Einführung in Experiment und Theorie*. Springer, 2005. 4th Edition.

[78] S. Blume. *Theorie Elektromagnetischer Felder*. Hüthig, 1991. 7th Edition, edited by Karl-Heinrich Wittich.

[79] M. Bayindir, B Temelkuran, and E. Özbay. Tight-binding description of the coupled defect modes in three-dimensional photonic crystals. *Phys. Rev. Lett.*, 84(10):2140–2143, 2000.

[80] D. Leuenberger, R. Ferrini, and R. Houdré. Ab initio tight-binding approach to photonic-crystal based coupled cavity waveguides. *J. Appl. Phys.*, 95(3):806–809, 2004.

[81] C. Meier, 2009-2011. private communication.

[82] S. G. Johnson and J. D. Joannopoulos. Block-iterative frequency-domain methods for maxwell's equations in a planewave basis. *Opt. Express*, 8(3):173–190, 2001.

[83] Q. Song, H. Cao, S. T. Ho, and G. S. Solomon. Near-ir subwavelength microdisk lasers. *Appl. Phys. Lett.*, 94(061109), 2009.

[84] W. H. Press, S. A. Teukolsky, W. T. Vetterling, and B. O. Flannery. *Numerical Recipes - The Art of Scientific Computing*. Cambridge, 2007. 3rd Edition.

[85] K. Zimmermann. Zur theorie der elektromagnetischen kopplung in periodischen quantenpunkt-strukturen. Diploma thesis, Technische Universität Berlin, 2003.

[86] R. Eichmann. *Lineare optische Eigenschaften dielektrisch strukturierter Halbleiter*. PhD thesis, Phillipps-Universität Marburg, 2002. PhD thesis.

[87] M. O. Scully and M. S. Zubairy. *Quantum Optics*. Cambridge, 2006. 5th Printing.

[88] C. C. Gerry and P. L. Knight. *Introductory Quantum Optics*. Cambridge, 2006.

[89] J. Bourassa, J. M. Gambetta, A. A. Abdumalikov, O. Astafiev, Y. Nakamura, and A. Blais. Ultrastrong coupling regime of cavity qed with phase-biased flux qubits. *Physical Review A*, 80(032109), 2009.

[90] T. Niemczyk, F. Deppe, H. Huebl, E. P. Menzel, F. Hocke, M. J. Schwarz, J. J. Garcia-Ripoll, D. Zueco, T. Hümmer, E. Solano, A. Marx, and R. Gross. Circuit quantum electrodynamics in the ultrastrong coupling regime. *Nature Physics*, 6:772–776, 2010.

[91] G. Günter, A. A. Anappara, J. Hees, A. Sell, G. Biasiol, L. Sorba, S. De Liberato, C. Cuiti, A. Tredicucci, A. Leitenstorfer, and R. Huber. Sub-cycle switch-on of ultrastrong light-matter interaction. *Nature*, 458(12):178–181, 2009.

[92] D. Ehmer. Mode calculations for one-dimensional photonic resonators. Bachelor thesis, Universität Paderborn, 2010.

[93] Q. Chen and D. W. E. Allsopp. One-dimensional coupled cavities photonic crystal filters with tapered bragg mirrors. *Optics Communications*, 281(23):5771–5774, 2008.

[94] D. Ehmer, 2010-2011. private communication.

[95] A. Lorenz. *Switchable Waveguiding in Photonic Liquid Crystal Structures*. PhD thesis, Universität Paderborn, 2010. PhD thesis.

[96] T. Ergin, N. Stenger, P. Brenner, Sir J. Pendry, and M. Wegener. Three-dimensional invisibility cloak at optical wavelengths. *Science*, 328(5976):337–339, 2010.

[97] I. I. Smolyaninov, V. N. Smolyaninova, A. V. Kildishev, and V. M. Shalaev. Anisotropic metamaterials emulated by tapered waveguides: Application to optical cloaking. *Phys. Rev. Lett.*, 102(21):213901, 2009.

[98] G. W. Grey, K. J. Harrison, and J. A. Nash. New family of nematic liquid crystals for displays. *Electronic Letters*, 9(6), 1973.

[99] S. Inui, N. Ilmura, T. Suzuki, H. Iwane, K. Miyachi, Y. Takanishi, and A. Fukuda. Thresholdless antiferroelectricity in liquid crystals and its application to displays. *J. Mater. Chem.*, 6(4), 1996.

[100] J. Li and S.-T. Wu. Extended cauchy equations for the refractive indices of liquid crystals. *J. Appl. Phys.*, 95(3):896–901, 2004.

[101] I.-C. Khoo and S.-T. Wu. *Optics and nonlinear optics of liquid crystals*, page 68. World Scientific Publishing Co. Pte. Ltd., 1993.

[102] R. Chen and H. Guo. Efficient calculation of matrix elements in low storage filter diagonalization. *J. Chem. Phys.*, 111(2):464–471, 1999.

[103] M. R. Wall and D. Neuhauser. Extraction, through filter-diagonalization, of general quantum eigenvalues or classical normal mode frequencies from a small number of residues or a short-time segment of a signal. i. theory and application to a quantum-dynamics model. *J. Chem. Phys.*, 102(20):8011–8022, 1995.

[104] V. A. Mandelshtam. On harmonic inversion of cross-correlation functions by the filter diagonalization method. *J. Theoretical and Computational Chemistry*, 2(4):497–505, 2003.

[105] V. A. Mandelshtam and H. S. Taylor. Harmonic inversion of time signals. *J. Chem. Phys.*, 107(17):6756–6769, 2003. See also erratum, ibid, vol. 109, no. 10, p. 4128 (1998).

[106] S. G. Johnson and M. Frigo. Implementing FFTs in practice. In C. Sidney Burrus, editor, *Fast Fourier Transforms*, chapter 11. Connexions, 2008.

[107] A. B. Matsko, A. A. Savchenkov, D. Strekalov, V. S. Ilchenko, and L. Maleki. Review of applications of whispering-gallery mode resonators in photonics and nonlinear optics. *IPN Progress Report 42-162*, 2005.

[108] B. R. Johnson, M. D. Reed, A. A. Houck, D. I. Schuster, Lev S. Bishop, E. Ginossar, J. M. Gambetta, L. DiCarlo, L. Frunzio, S. M. Girvin, and R. J. Schoelkopf. Quantum non-demolition detection of single microwave photons in a circuit. *Nature*, 6(9):663–667, 2010.

[109] Y.-P. Huang and P. Kumar. Interaction-free all-optical switching in $\xi^{(2)}$ microdisks for quantum applications. *Optics Letters*, 35(14):2376–2378, 2010.

[110] M. Soltani, S. Yegnanarayanan, and A. Adibi. Ultra-high q planar silicon microdisk resonators for chip-scale silicon photonics. *Optics Express*, 15(8):4694–4704, 2007.

[111] K. A. Piegdon, M. Offer, A. Lorke, M. Urbanski, A. Hoischen, H.-S. Kitzerow, S. Declair, J. Förstner, T. Meier, D. Reuter, A. D. Wieck, and C. Meier. Self-assembled quantum dots in a liquid-crystal-tunable microdisk resonator. *Physica E: Low-dimensional Systems and Nanostructures*, 42(10):2552–2555, 2010.

[112] K. A. Piegdon, 2009-2011. private communication.

[113] Lord Rayleigh. The problem of the whispering gallery. *Cambridge University, Cambridge UK*, 5:617, 1912.

[114] M. Benyoucef, J. B. Shim, J. Wiersig, and O. G. Schmidt. Quality-factor enhancement of supermodes in coupled microdisks. *Optics Letters*, 36(8):1317–1319, 2011.

[115] S. Declair, C. Meier, T. Meier, and J. Förstner. Anticrossing of whispering gallery modes in microdisk resonators embedded in an anisotropic environment. *Phot. Nano. Fund. Appl.*, 8(4):273 – 277, 2010.

[116] C. Meier. *Novel Photonic Materials*. Habilitation, Fakultät für Physik, Universität Duisburg-Essen, 2007.

[117] J. P. Reithmaier, G. Sęk, A. Löffler, C. Hofmann, S. Kuhn, S. Reitzenstein, L. V. Keldysh, V. D. Kulakovskii, T. L. Reinecke, and A. Forchel. Strong coupling in a single quantum dot-semiconductor microcavity. *Nature*, 432(141108):200–204, 2004.

[118] J. Wolters, A. W. Schell, G. Kewes, N. Nüsse, M. Schoengen, H. Döscher, T. Hannappel, B. Löche, M. Barth, and O. Benson. Enhancement of the zero phonon line emission from a single nitrogen vacancy center in a nanodiamond via coupling to a photonic crystal cavity. *Applied Physics Letters*, 97(141108), 2010.

[119] S. Noda, A. Chutinan, and M. Imada. Trapping and emission of photons by a single defect in a photonic bandgap structure. *Letters to Nature*, 407:608–610, 2008.

[120] Y. Tanaka, J. Upham, T. Nagashima, T. Sugiya, T. Asano, and S. Noda. Dynamic control of the q-factor in a photonic crystal nanocavity. *Letters to Nature*, 6:862–865, 2007.

[121] T. Uesugi, B.-S. Song, T. Asano, and S. Noda. Investigation of optical nonlinearities in an ultra-high-q si nanocavityin a two-dimensional photonic crystal slab. *Opt. Express*, 14(1):377–386, 2006.

[122] NSM. Nsm archive - optical properties of semiconductors. URL `http://www.ioffe.rssi.ru/SVA/NSM/Semicond/GaAs/optic.html`.

[123] Y. Akahane, T. Asano, B.-S. Song, and S. Noda. Fine-tuned high-q photonic crystal nanocavity based on a gentle confinement of light. pages 882 –883, 2004.

[124] H. Altug, D. Englund, and J. Vučković. Ultrafast photonic crystal nanocavity laser. *Nature*, 2(7):484–488, 2006.

[125] D. O'Brien, M. D Settle, T. Karle amd A. Michaeli, M. Salib, and T. F. Krauss. Coupled photonic crystal heterostructure nanocavities. *Opt. Express*, 15(3):1228–1233, 2007.

[126] S. Declair, T. Meier, and J. Förstner. Numerical investigation of the coupling between microdisk modes and quantum dots. *Physica Status Solidi C*, 8(4):1254–1257, 2011.

[127] K. Srinivasan, M. Borselli, and O. Painter. Cavity q, mode volume, and lasing threshold in small diameter algaas microdisks with embedded quantum dots. *Opt. Express*, 14(3): 1094–1105, 2006.

[128] K. A. Atlasov, K. F. Karlsson, A. R., B. D., and E. Kapon. Wavelength and loss splitting in directly coupled photonic-crystal defect microcavities. *Opt. Express*, 16(20): 16255–16264, 2008.

[129] P. Strasser, G. Stark, F. Robin, D. Erni, K. Rauscher, R. Wüest, and H. Jäckel. Optimization of a 60° waveguide bend in a inp-based 2d planar photonic crystal. *J. Opt. Soc. Am. B*, 25(1):67–73, 2008.

[130] D. Pergande and R. B. Wehrspohn. Polarization-dependent transmission properties of iosoi w1 photonic crystal waveguide. *Phot. Nano. Fund. Appl.*, In Press, Corrected Proof:–, 2011. doi: DOI:10.1016/j.photonics.2011.02.001.

[131] E. Dulkeith, S. J. McNab, and Y. A. Vlasov. Mapping the optical properties of slab-type two-dimensional photonic crystal waveguides. *Phys. Rev. B*, 72(3):115102, 2005.

[132] J. Kasprzak, S. Reitzenstein, E. A. Muljarov, C. Kistner, C. Schneider, M. Strauss, S. Höfling, A. Forchel, and W. Langbein. Up on the janes-cummings ladder of a quantum-dot/microcavity system. *Nature Materials*, 9:304–308, 2010.

[133] R. E. Grove, F. Y. Wu, and S. Ezekiel. Measurement of the spectrum of resonance fluorescence from a two-level atom in an intense monochromatic field. *Phys. Rev. A*, 15 (1):227–233, 1977.

[134] M. Florescu and S. John. Single-atom switching in photonic crystals. *Phys. Rev. A*, 64 (3):033801, 2001.

Danksagung

Jeder Frau und jedem Mann sei gedankt, die mich in den letzten drei Jahren auf dem Weg zu dieser Arbeit begleitet und geführt haben.
Besonderen Dank möchte ich meinem Doktorvater Dr. Jens Förstner aussprechen. Als sein erster Promotionsstudent war ich sicherlich kein leichter Schüler, der oft mit kleinen und auch großen Fragen und Problemen zu ihm kam. Weiterhin möchte ich Prof. Dr. Torsten Meier danken, der mich während meiner Arbeit immer unterstützt hat und als Zweitgutachter in kurzer Zeit viel zu lesen hatte.
Meinen Arbeitskollegen und der gesammten Arbeitsgruppe sowie der anderen Arbeitsgruppen der theoretischen und experimentellen Physik an der Universität Paderborn gilt ebenfalls besonderer Dank für die früchtetragenden Diskussionen und Unterhaltungen, Kaffeepausen und lustige Stammtischabende. Hervorzuheben sind mein Büronachbar Herr Dr. Matthias Reichelt und der mittlerweile in der Unendlichkeit der freien Marktwirtschaft entschwundene, ehemalige Kollegen Herr Dr. Christian Thierfelder, der mit seinem überragenden Wissen immer einen Rat wußte.
Desweiteren möchte ich meiner Familie danken, die mich in allen Lebenslagen unterstützt hat und immer die richtigen Ratschläge zur richtigen Zeit hatten. Insbesondere möchte ich meiner Mutter danken, die Dank mir in den letzten drei Jahren eine Menge grauer Haare mehr bekommen hat.
Besonderer Dank gebührt meiner Freundin Ania, die es in den letzten Monaten nicht leicht mit mir hatte, mir aber trotz alledem immer hilfreich zur Seite stand.
Nicht vergessen möchte ich meine Freunde, die ich in der ganzen Zeit nur selten besuchen konnte und dadurch teilweise der Draht zueinander verloren ging. Besonders hervorzuheben ist Herr Hagen Schäfer, der mich trotz der großen Entfernung häufig in Paderborn besucht und immer ein offenes Ohr hat.
Weiterer Dank gebührt der Deutschen Forschungsgemeinschaft DFG, die mir im Rahmen des Graduiertenkollegs GRK 1464 *Micro- and Nanostructures in Optoelectronics and Photonics* die Anfertigung dieser Arbeit erst ermöglicht hat.